Improved Ore Recovery in Burst Prone Ground using Destress Blasting

Isaac Vennes

Department of Mining and Materials Engineering

McGill University, Montreal, Quebec, Canada

April 2019

A thesis submitted to McGill University in partial fulfillment of the requirements of the degree of Doctor of Philosophy in Mining Engineering

Abstract

Destress blasting is a rockburst control technique where highly stressed rock is blasted to reduce the local stress and stiffness of the rock, thereby reducing its burst proneness. The technique is commonly practiced in deep hard rock mines in burst prone developments, as well as in sill or crown pillars which become burst-prone as the orebody is extracted. Large-scale destressing is a variant of destress blasting where panels are created parallel to the orebody strike with a longhole, fanning blast pattern from cross cut drifts situated in the host rock. The destress blasting practice reviewed in the literature showed varying levels of success, with the main criterion for success being the seismic response. This thesis therefore concentrates on quantifying the geomechanical effect of panel destress blasting based on the stress changes measured in the field after a destress blast.

This destressing strategy was implemented at Vale's Copper Cliff Mine (CCM) to create a stress shadow which encompasses the entire 100OB diminishing ore pillar. Destressing was done in 4 Phases, and ten uniaxial vibrating wire stress cells were installed in the diminishing pillar to monitor the stress changes. The geomechanical effect of panel destress blasting is then quantified with a pillar wide numerical model based on the measured stress changes. The destressing mechanism is simulated with a rock fragmentation factor (α) and stress dissipation factor (β). For the Phase 1 and Phase 2 blasts, it is shown that the best correlation between the numerical model and field measurements is obtained when the combination of α and β indicates that the blast causes high fragmentation (α =0.05) and high stress release (β =0.95) in the destress panel. It is also demonstrated that the burst proneness of the ore blocks in the panel stress shadow is reduced in terms of the brittle shear ratio (BSR) and the burst potential index (BPI).

For the Phase 3 blast however, a stress increase was detected in the expected panel stress shadow, which cannot be replicated with the previous model. The anisotropic destressing model is therefore explored. With this model, it is proposed that the degree of stiffness reduction and stress dissipation is influenced by the orientation of the in-situ principal stresses, whereby in the direction of major principal stress, σ_1, the rock fragmentation factor α_1 is likely to be larger than

the rock fragmentation factor α_2 in the direction of the minor in situ principal stress. Likewise, the stress dissipation factor β_1 in the major principal stress direction is likely to be less than β_2 in the minor principal stress direction.

The back analysis of the Phase 3 blast determined that the crown panel fragmentation factor in the orientation of σ_1 was much higher than the rock fragmentation factor in the σ_2-σ_3 plane, with a value of α_1 of 0.5 and a value of α_2 of 0.05. Therefore, the anisotropic stress release and fragmentation effect due to preferential fracture propagation was quantified, where the stress release and fragmentation normal to σ_1 is almost double the effect in the orientation of σ_1.

Sommaire

La méthode de tir de relaxation est une mesure de contrôle contre le coup de terrain. Le massif rocheux, lorsque que soumis à des fortes contraintes, est endommagé avec des explosifs afin de réduire sa rigidité et la magnitude des contraintes. Cette méthode est communément pratiquée dans des mines de roche dure profondes dans des galeries susceptibles aux coup de terrains, ainsi que dans des piliers de minerai en diminution. Le tir de relaxation à grande échelle en panneaux est une variante du tir de relaxation - où des panneaux parallèles à l'axe du gisement sont crées avec un patron de forage en éventail à partir de galeries situées dans l'éponte supérieure du gisement. Malgré de nombreuses années de recherche, la technique de tir de relaxation est toujours appliquée en utilisant une approche essai-erreur qui donne des résultats mitigés. L'effet du tir est souvent évalué selon la réponse sismique du tir. Cette thèse vise donc à quantifier l'effet géomercatique des tirs de relaxation en se basant sur les changements de contraintes mesurés sur le terrain après le tir.

Cette méthode a été employée en quatre phases à la Mine Copper Cliff (CCM) pour réduire les contraintes dans l'entièreté d'un pilier en diminution. Dix jauges de contraintes à fil vibrants ont été installées dans le pilier pour mesurer le changement de contrainte suivant le tir. L'effet mécanique du tir de relaxation a été quantifié avec les données d'un modèle numérique des changements de contraintes acquises à la suite du tir. La relaxation du panneau fut simulée avec 2 paramètres : le facteur de fragmentation (α) et le facteur de dissipation de contraintes (β). Pour les tirs de relaxation Phase 1 et Phase 2, une corrélation entre le modèle numérique et les données de changement de contraintes a été obtenue lorsque $\alpha = 0.05$ et $\beta = 0.95$, démontrant que le panneau fut complètement endommagé par le tir. Selon les indices BPI et BSR calculés dans l'ombre du pilier, l'analyse démontre en plus que les contraintes sont suffisamment diminuées dans le pilier pour réduire la propension du chantier aux coups de terrain.

Malgré le comportement observé dans les phases 1 et 2, une augmentation des contraintes dans l'ombre d'un panneau fut observée suite au tir de relaxation à la Phase 3. Or, le modèle anisotrope de relaxation a dû être employé. L'hypothèse de base du modèle anisotrope est que la direction de propagation des fractures attribuables au tir tend vers la direction de la contrainte

majeure principale. Le degré de fragmentation et de relaxation de contraintes est donc influencé par l'orientation de la contrainte majeure principale. Le facteur α_1, qui représente le facteur de fragmentation dans l'axe de la contrainte majeure principale (σ_1), s'avère plus bas que le facteur α_2, qui représente le facteur de fragmentation dans le plan normal à σ_1. Le même principe s'applique au facteur de relaxation de contraintes β - où il est fort probable que β_1 soit plus petit que β_2.

L'analyse régressive du tir Phase 3 démontre que facteur α_1 d'un des panneaux est beaucoup plus haut que le facteur α_2 (α_1 = 0.5, α_2 = 0.05). L'effet géomécanique de la propagation préférentielle des fractures a donc été quantifié. Dans le cas du tir Phase 3, l'effet de fragmentation et de relaxation du tir est presque doublé dans le plan normal à σ_1 par rapport à l'effet dans l'axe de σ_1.

Acknowledgements

I would like to thank first and foremost Dr. Hani Mitri, my thesis supervisor. I am grateful to him for his technical guidance, his professional advice, strategic planning skills, and his thoughtful encouragement which allowed me to complete this degree. Special thanks to him as well for having given me the opportunity of being part of the Mine Design Lab group. The financial support provided by MEDA, MITACS, and Vale is equally appreciated.

I would also like to thank Copper Cliff Mine Technical Services, notably Reddy Damodara Chinnasane, for their time devoted to the project. Copper Cliff mine operations also deserve thanks for providing the materials and manpower necessary for the project.

Finally, thanks to all my colleagues at the Mine Design Lab, Shahe, Atsushi, Hassan, Flavie, Kelly, and JT, for their help, technical advice, and friendship.

Contribution of Authors

The thesis includes 2 published manuscripts: chapter 4 is a journal article titled "Geomechanical effects of stress shadow created by large-scale destress blasting", chapter 5 is a journal article titled "Large scale destress blasting for seismicity control in hard rock mines: a case study". The literature review, numerical modelling, and analysis of results presented in these publications were conducted by the candidate. Both journal publications are co-authored by Hani Mitri in his capacity as thesis supervisor. Since chapter 5 is a collaborative publication with Vale Canada Ltd, it is co-authored by Mike Yao is his capacity as study supervisor representing Vale, and by Reddy Damodara Chinnasane due to his contributions to the study. Mr. Chinnasane installed all instruments at CCM and collected and prepared the all of the data from CCM used in the study. Mr. Chinnasane also composed the last paragraph of section 5.2 and provided Figure 5.6 in the manuscript of the second publication. In the thesis, Figures 3.1 and 3.2 were also prepared and provided to the candidate by Mr. Chinnasane. Excluding the above, all chapters and figures are original to the thesis and are wholly authored by the candidate.

Table of Contents

List of Figures

Chapter 1

Chapter 2

Chapter 3

List of Tables

Chapter 7

Chapter 1: Introduction

Despite more than a century of research, rockburst phenomena continue to persist in deep underground mines. Continuous improvements in rockburst control measures have been implemented in mines with destress blasting as one of the most promising techniques. However, destress blasting is still an art rather than a science, with varying methods of implementation and mixed levels of success. A literature review of destress blasting case histories reveals that little is being done in terms of understanding destress blasting through the application of constitutive models. Essentially, the stress changes caused by destressing in the rock to be destressed have not yet been quantified. This thesis will focus on Copper Cliff Mine (CCM) orebody OB 100/900, situated approximately 4000 feet (1,333 m) below surface, where a large-scale panel destressing program was conducted to reduce potential for burst of a diminishing ore pillar. Geological and geotechnical data was collected along with planned mining activities and stope geometric data. A 3-dimensional numerical simulation of destress blasting at CCM was carried out and validated based on in-situ stress change measurements. Two holistic destress blasting constitutive models were used in this study. The first is a rock fragmentation and stress reduction model, which reduces the stress and stiffness of the destressed rock with the parameters α and β. The second model is an anisotropic variant of the first model, which reduces the stress and stiffness with the same parameters, but which vary in magnitude with respect to the orientation of the major principal stress. The objective of this thesis is to validate these two holistic constitutive models, which when applied allows for the quantification of the geomechanical effects of destress blasting.

1.1 Rockbursts

Rockbursts occur when the rock has been loaded beyond its peak strength point, manifesting as a sudden and violent failure of rock. Natural tectonic stresses are disturbed by removal of rock such as mining. The creation of openings will result in high loads around them as the stresses reach a new equilibrium. If the loads in equilibrium exceed the strength of the rock, there is a potential for the occurrence of rockbursts. The proneness of rockburst depends mainly on strength of the rock, its stiffness, the magnitude of the load, and rate of excavation (rate of loading). Globally, the severity and intensity of rockbursts increases with mining depth.

Rockbursts were first recorded at an Indian gold mine in early 20th century (Blake 1972). Shortly after, in 1908, rockbursts were reported at Witwatersrand Mine, and defined as the "shattering" of pillars (Hedley 1992). The first recorded rockburst in Canada occurred during the 1930's, at mines in Kirkland Lake and Sudbury. In the 1970's, the application of bulk mining and the use of large underground openings in Canada only added to the problem (Hedley 1992)

Rockbursts pose a severe occupational hazard, resulting in 50 fatalities over the 4000 reported incidents in Ontario alone between 1960 and 1990 (Hedley 1992). Rockbursts also pose an operational hazard, such as the loss of production and cost of cleanup (Blake 1972). Destress blasting, the main subject of this thesis is a rockburst control method developed in the 1950's.

1.1.2 Rockburst Mechanisms

Figure 1.1 presents the rockburst classification proposed by Brown (1984).

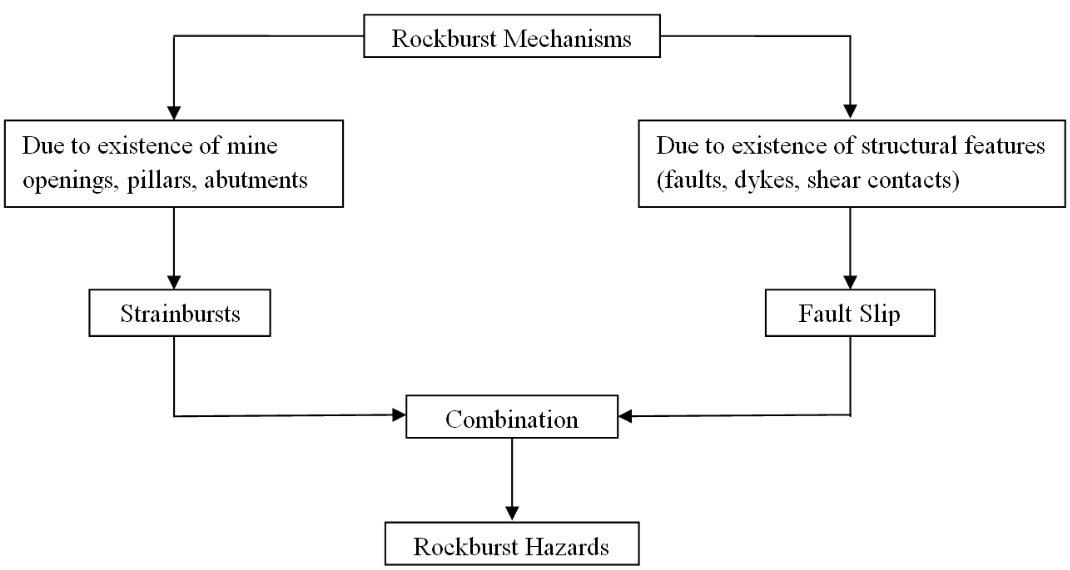

Figure 1.1: Rockburst mechanisms (Brown 1984)

Contributing factors to the occurrence of rockbursts are high stress, high rock stiffness, rapid mining rate, and large excavation area, among others. The rock itself must first be prone to brittle failure. Multiple criteria have been developed to assess the rockburst potential of rock. For example, the burstability of a specific rock type can be determined from the stress strain curve of a rock specimen (Aubertin and Gill 1988). Peng and Wang (1996) introduced the brittleness ratio, which is defined as the uniaxial compressive strength σ_c over the tensile strength σ_T, where a brittle and bursting rock has a ratio below 14.5. Finally, Wu and Zhang (1997) developed the failure duration index, which is the time between peak strength and total failure in a standardized UCS test. A failure duration below 50 ms would indicate a burst prone rock.

Once a rock is known to be burst prone, the next step is to determine the risk of rockburst by taking into account the in-situ geomechanical conditions of the rock mass. This can be done with criteria such as the energy release rate (ERR) (Cook 1978), the Burst Potential Index (BPI) (Mitri et al. 1999) and the Brittle Shear Ratio (BSR) (Castro et al. 1997), which are used to evaluate the burst potential of the in-situ rock based on its loading. The BPI was developed to account for the main limitation of the ERR, which is that it cannot recognize failure (Mitri et al., 1999). The BPI is the ratio between the mining-induced strain energy and the critical strain energy of intact rock, expressed as follows.

$$BPI = \frac{ESR}{e_c} \qquad [1.1]$$

where the energy storage rate (ESR) is the addition of strain energy over the pre-mining state and e_c is the critical strain energy determined from rock testing. On the other hand, the ESR was developed based on a study by Martin and Kaiser (1999), where the rock was found to undergo brittle shear as the ratio between the deviatoric stress and the uniaxial compressive strength exceeded 0.4 (Martin and Kaiser 1999).The BSR proposed by Castro et al. (1997), is expressed as:

$$BSR = \frac{\sigma_1 - \sigma_3}{UCS} \qquad [1.2]$$

Based on the above equation, the risk of strainbursts is deemed significant when the ratio exceeds 0.7. In addition, the incremental BSR, which is the change in BSR at each mining step, was found to correlate well with increased micro-seismicity on a mine-wide scale (Shnorhokian et al. 2014, Shnohorkian et al. 2015). In this study, the effectiveness of destress blasting will be evaluated with the BPI and BSR computed in the numerical model.

1.1.3 Rockburst control methods

Although the mechanisms of rockbursts are well understood, and the rockburst risk can be evaluated, rockbursts are still unpredictable. Therefore, much effort is put in reducing the risk of rockbursts or mitigating their effects. Figure 1.2 surveys the available rockburst control methods. These methods can either mitigate damage or reduce burst proneness of the ground, both reducing rockburst risk. First off, adopting a pillarless mining sequence, such as the Chevron mining sequence, can be used to avoid burst prone mining conditions such as a diminishing ore pillar. However, if mining in highly stressed, burst prone ground is unavoidable, destress blasting or destress slotting can both be adopted to transfer high stress away from mining. Nonetheless, destress blasting and destress slotting are still an art rather than a science, with results that are not fully predictable. As a contingency measure, rock supports, such as shotcrete, straps, wire mesh, and dynamic bolts, yield and absorb kinetic energy, mitigating rockburst damage.

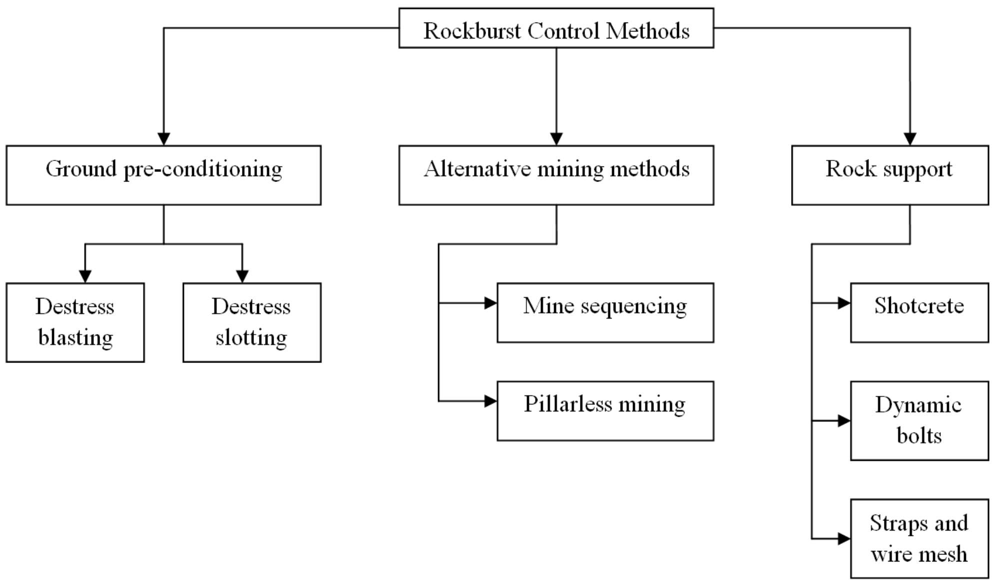

Figure 1.2: Rockburst control methods (Mitri 2001)

1.1.4 Destress blasting

Destress blasting involves the application of explosive energy to highly stressed zones with the purpose of fracturing the zone, thus reducing the stored stain energy (Mitri, 2001). The peak load is therefore transferred to another zone, ideally away from the mining face. Such reduction in peak load alone, given that all other parameters are constant, should reduce the burst potential of the rock. Destress blasting was first systematically practiced in the Witwatersrand gold mines in South Africa in the 1950's (Roux et al. 1957). The program was reported as successful, reducing the number and severity of rockbursts. In the late 1980's, destress blasting was revisited to mine longwalls in deep gold reefs such as Bloyvooruitzicht Mine and Western Deep Levels South Mine (Lightfoot et al. 1996). In Europe, destress blasting is used as a rockburst control method in Finland (Hakami et al. 1990), Poland (Wojtecki et al. 2017), and the Czech Republic (Konicek et al. 2013, Konicek and Waclawik 2018). In North America, destress blasting was applied in the Coeur d'Alene Mining district in Idaho (Boler and Swanson 1993). In Canadian mines, destressing was widely applied in sill pillars in thin, steeply dipping orebodies such as Campbell Mine (Makuch et al. 1987), Falconbridge Mine (Moruzi and Paseika 1964, Hedley 1992), Star-Morning Mine (Karwoski and McLaughin 1975), and Macassa Mine (Hanson et al. 1987) with mixed results. At

Creighton mine, destress blasting was applied to the development of sill drifts in a highly stressed ore pillar (Oliver et al. 1987, O'Donnell 1992). More recently, destress blasting of panels in the hanging wall has been applied to extract thick ore pillars, with the destressing of much larger volumes, such practiced at Brunswick Mine (Andrieux et al. 2003), Fraser Mine (Andrieux 2005), and presently at Copper Cliff Mine (CCM).

Destress blasting is understood to reduce the stress borne in rock by inducing fracturing, demonstrated to be along pre-existing fracture planes (Lightfoot et al. 1996). However, the exact mechanism of destressing along with its effects is not fully understood. Nonetheless, the induced fracturing is thought to have the positive effects that reduce burst proneness. First, fracturing reduces the stiffness of the rock (Blake 1972) as well as the load bearing ability. This effect is generally accepted and applied in numerical modelling back analyses (Tang 2000, Andrieux 2005, Boler and Swanson 1993, Blake 1972). The stress transfer occurs as a portion of the strain energy in the destressed rock is dissipated to the surrounding rock mass or rock support as strain energy. Secondly, an instantaneous reduction of stress occurs as the blast induced cracks propagate, and the stored strain energy is dissipated as fracturing energy (Tang and Mitri 2001). In addition, blast induced fractures tend to propagate in the direction of the major principal stress. For this reason, Saharan and Mitri (2009) proposed that the stress reduction factor vary depending on the direction of the destress blasthole with respect to the orientation of the principal stresses. The fracturing effect and the stress reduction effect are therefore directionally dependent.

The reviewed practice of destress blasting is based on site experience and trial and error, with varying levels of success. This success of a blast is usually evaluated with the seismic response of the blast. From energy balances developed for destress blasts (Knoteck et al. 1985, Hedley 1992), the energy released is compared to the input explosive energy (Konicek et al. 2013) or initial strain energy (Lightfoot et al. 1996) for a destress blast, sometimes as the sole criterion due to the lack of other conclusive results. Convergence measurements are also a popular criterion, but not the focus of back analysis. Back analysis with numerical modelling is seldom used. It is based on limited stress change data, with a simple elastic model where only fragmentation is taken into account (Andrieux 2005, Boler and Swanson, 1993). Finally, the difficulty of obtaining reliable in-situ stress measurements means the in-situ stress state prior to a destress blast is often assumed (Boler and Swanson, 1993).

1.2. Study Problem

Despite many years of research, destress blasting is still an art rather than a science. The reviewed practice is based on site experience and trial and error, with varying levels of success. This success is mainly evaluated based on the seismic response of the blast, sometimes as the sole criterion due to the lack of other conclusive results. Convergence measurements are also a popular criterion, but not the focus of back analyses. Back analysis with numerical modelling is seldom used and based on limited stress change data, with a simple elastic model where only stiffness reduction is considered. Finally, the difficulty of obtaining reliable in-situ stress measurements means the in-situ stress state prior a destress blast is often assumed. For these reasons, the geomechanical effects of destress blasting need to be quantified through back analysis based on measured stress changes following the blast. The constitutive model validated with the back analysis can subsequently be applied to assess the success of a destress blast.

1.3. Scope of Work

The scope of this work is large scale destress blasting in deep hard rock mines which aim to reduce stress in the mining region, consequently reducing the risk of strainbursts. The mine of interest is Copper Cliff Mine (CCM). The work will focus on the back analysis of destress blasts conducted at CCM. A numerical model of the 100/900 Orebody of CCM has been built. The destress blasts are simulated using the holistic constitutive models developed by Tang and Mitri (2001) and Saharan and Mitri (2009). With these models, the effect of the stress state prior to destress blasting, fracture propagation in the direction of the major principal stress, and instantaneous stress release due to fracture propagation will be examined. More importantly, with a quantified destressing effect, the safety of mining the pillars can be assessed in the model.

1.4 Thesis Outline

Chapter 2 is a literature review divided into 2 sections. The first section will cover destress blasting case studies divided into two categories: tactical destressing and strategic destressing. The second section will discuss the theory of destress blasting, which will provide a rationale for the holistic blast simulation model used in this study.

Chapter 3 presents the case study mine. It is divided into 4 sections. This first section discusses Copper Cliff Mine (CCM), the case study mine for this thesis. It describes the orebody known as 100OB where the destress blasting program was implemented. The second part explains in more detail the destress blasting program. The third part elaborates on the numerical model constructed for the simulation and analysis of the destress blasting effects. Finally, the fourth part discusses the instrumentation installed at CCM to monitor the effects of the destress blasting. This was used as a basis to validate the destress blasting constitutive models used in conjunction with the numerical model.

Chapter 4 is a journal article entitled "Geomechanical effects of stress shadow created by large scale destress blasting". In this chapter, a large-scale panel destress blasting program is applied to a simplified pillar model using the isotropic rock fragmentation and stress reduction constitutive model (Tang and Mitri, 2001). The aim was to determine if the panel destressing strategy sufficiently reduces stress in the pillar to reduce the burst proneness of the ore, which was evaluated with the brittle shear ratio (BSR). Finally, a rough estimate of a valid rock fragmentation factor and stress reduction factor was obtained by comparing the computed stress changes to the stress changes measured in large scale blasting case studies.

Chapter 5 is a journal article entitled "Large-scale destress blasting for seismicity control in hard rock mines – A case study". This chapter covers Phase 1 destress blast conducted at CCM. Tang and Mitri's (2001) model is used to simulate the destress blast. A validation methodology is established to compare the destress blast constitutive model parameters with the stress changes measured in-situ.

The focus of chapter 6 is the Phase 2 and Phase 3 destress blasts. In this chapter, Tang and Mitri's (2001) model is again adopted to simulate Phase 2 and Phase 3 blasts. It is shown that the stress redistribution following Phase 2 blast can be replicated with this model. However, the stress redistribution following the Phase 3 blast could not be explained with the isotropic model, i.e. one value for α, and one value for β in all directions. The anisotropic destressing model hypothesized by Saharan (2009) is therefore explored. Another issue that is examined here is the effect of slight variation of the orientation of the stress cell, where it was found that a slight variation in orientation could lead to different stress change results. It is shown that after accounting for possible stress cell orientation errors, the anisotropic model can replicate the measured stress changes after the Phase 3 blast

1.5 Contribution to Original Knowledge

In this study, 3D numerical modelling of large-scale destress blasting is attempted for the first time, considering a wide range of factors that have been previously rarely considered. The effects of destress blasting panel constitutive modelling parameters, mining depth, production sequence, and in-situ stress on the behavior of a diminishing ore pillar stability and burst potential have been adequately analyzed and described through a real-life case study of a steeply dipping, deeply seated ore deposit in a sublevel mining system of the Copper Cliff Mine.

Novel methodologies to consider the aforementioned factors in the 3D numerical modelling of a sequence of destress panels has been developed. In addition, a new methodology to derive the optimal destress blast constitutive model parameters through extensive back analysis has been developed using the data obtained from stress cells installed in the stress shadow zones in the diminishing ore pillar of the underground mine.

Chapter 2: Literature Review

2.1 Introduction

This chapter is divided in 2 sections. The first section will cover destress blasting case studies from the literature, categorized in two groups: tactical destressing and strategic destressing. The second section will discuss the theory of destress blasting, which will provide a rationale for the holistic blast simulation model used in this study.

The following case studies serve as the background to the methodology used to assess the Copper Cliff Mine destress blasts (see Chapter 3). Critical evaluation of each case study is presented. The Fraser Mine, Brunswick Mine, and Lazy Colliery case studies are presented in more detail and exemplify the practice of strategic destressing. On the other hand, Galena Mine, Bloyvooruitzicht Mine, and Western Deep Levels South mine are investigated in more detail to cover the successful application of tactical destressing.

2.2 Tactical destressing Case Studies

Tactical destressing involves directly pre-conditioning burst prone rock that is to be extracted. To achieve this, the rock ahead of the drift face, longwall, or pillar face is blasted in conjunction with a normal development or mining round. Once the rock is extracted, the new face will already have been damaged by the destress blast, reducing the risk of brittle, violent failure. However, the quantity of explosives required to damage the rock is much lower than the amount required to fragment it for extraction. Tactical destressing practice therefore tends towards small drill holes at large spacings, with low total explosive energy per targeted rock mass. The following case studies exemplify this practice.

2.2.1 Galena Mine (Boler and Swanson 1993)

Galena mine is a silver producing mine located in the Coeur d’Alene mining district in Idaho, USA. The mine employs overhand cut-and-fill mining method. The ore vein mined is near vertical and strikes N45°E. Bedding plane faults, striking N45°W, cutting the vein at 90°, are common. In addition, 70% of the stoping areas associated with the 29 largest seismic events all occur on a near vertical plane, striking N48°W. While the strike coincides with the faults mapped on surface, there was no major fault surface mapped that coincided with the locations of the seismic activity. Nonetheless, blocky structures with the same general trend in the area had the potential to accommodate slip. It is therefore reported that structural discontinuities play an important role in accommodating mining induced deformation.

The study investigated destress blast of the 46-99 stope, 1.5 km below surface, conducted on February 2, 1990. Destress blasting is typically used at Galena Mine when the following conditions are met.

- The overhand pillar reaches a critical height of 10-20 m
- The accelerometer array detects an increase in seismic activity.

As the pillar progressively thinned, an increase in micro-seismic activity was detected by an accelerometer array. Destress blasting of the 21 m high pillar was therefore undertaken. Eight 10 m boreholes and three 4 m boreholes (see Figure 2.1) were filled with a total of 125 kg of explosives. The direction of the major principal stress was measured from the borehole breakout of the vertical destress blast holes and observed to be parallel to the strike of the vein.

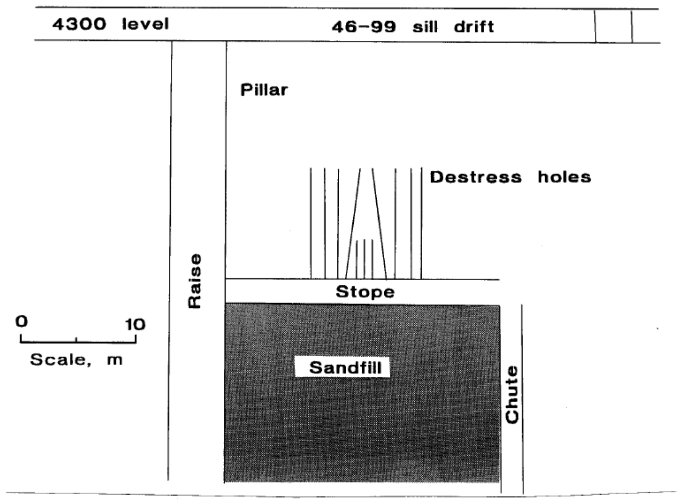

Figure 2.1: Section view of 45-99 stope during 1990 destress blast (Boler and Swanson 1993)

To monitor the stress changes caused by the destress blast, 8 uniaxial borehole pressure cells (BPC) were installed in 3 mutually perpendicular boreholes. The BPCs were aligned in the orientation of the principal stresses, assumed to be at +/- 45 degrees from the fault orientation.

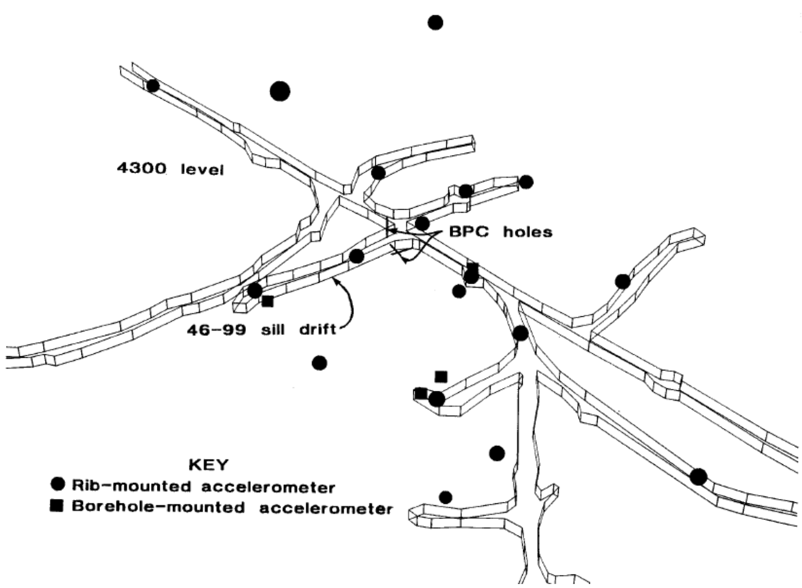

Figure 2.2: Perspective view of mine openings. Points of interest are the location of 46-99 sill drift and the BPC's (Boler and Swanson 1993)

The February 2, 1990 destress blast caused a stress increase in the order of 100 KPa in all BPC's, described as "noise level". In addition, no significant seismic ($M_L > 0.7$) event was detected that coincided with the destress blast of the pillar (a magnitude of 0.4 was recorded). However, multiple large seismic events occurred in the week following. Most notably, a large seismic event with a Gutenberg-Richter magnitude of 2.9 occurred 5 days after the destress blast. The five events recorded were all mapped to the fault plane.

However, it is unknown if the destress blast triggered these seismic events. First, the time delay was too large. Also, the stress drop measured by the BPC array would have coincided with a negligible unclamping of the fault. Finally, while a stress discontinuity between BPC array and the 45-99 stope was hypothesized, the hypothesis was deemed dubious as subsequent seismic events that would also have been shielded by the discontinuity yielded observable pressure changes.

Table 2.1: Destress Blast and post destress blast seismic event with $M_L \geq 0.6$ (Boler and Swanson 1993)

Date[1]	Time[2]	M_L	E, J	Damage	Comments
900202	144910	0.4	2.5×10^5	None reported	Destress blast.
900204	035210	1.2	4.0×10^6	Roof fall in stope	None.
900207	034500	2.9	1.4×10^9	5-6 cars muck down	Largest event in mine during 20-month period.
900207	122020	0.9	1.4×10^6	Track uplifted above stope	None.
900215	135421	0.6	5.0×10^5	None reported	Do.
900219	144603	1.2	4.0×10^6	. . do.	Event occurred 25 min after first production blast following destress.

E Energy.
M_L Local magnitude.
[1]Format of this field is yymmdd, where yy = year, mm = month, and dd = day.
[2]Format of this field is hhmmss, where hh = hour, mm = minute, and ss = second.

A 2D finite element method (FEM) analysis concluded that the modulus of elasticity of the destressed rock needed to be reduced by 80% to obtain the pre-mining major stress in the pillar. The subsequent change in stress around the pillar was not detected by the BPC's, suggesting that the stress change in the pillar was insignificant.

The conclusions of the study are that knowledge of approximate principal stress direction is essential to design an effective destress blasts. This is since blast induced cracks tend to propagate in the direction of the major principal stress. Since over-coring to determine the absolute stresses is impractical in most scenarios where destress blasting is required, the authors note that a more practical approach to determine the mining induced stresses would be to use numerical modelling and knowledge of the far-field stresses. In addition, observing borehole break-outs to determine the direction of the major principal stress should be done as often as possible. Finally, ground pressure and seismic monitoring are highly desirable to monitor destress blasting effectiveness.

While the study of the destress blast was well instrumented, Boler and Swanson (1993) noted a lack of knowledge of the stress state of the zone that was destressed. Nonetheless, significant work was done to explain the seismic events, but the cause of the fault slip is not known.

2.2.2 Bloyvooruitzicht Mine (Lightfoot et al. 1996)

Bloyvooruitzicht Mine is a deep gold reef located in South Africa. Destress blasting was implemented as part of the mining cycle. The report describes the destress blasting pattern for three stopes with their documented effects.

The 18-13W stope was preconditioned with 30 m long, 76 mm holes, fanned out from the dip gully (face parallel). However, holes deeper in the pillar could only be drilled 10 m due to high stress, which resulted in only 4 m of pre-conditioning. The noted effect of pre-conditioning was the extension of steep fractures.

The 30-24W stope was pre-conditioned with 10 m long, 76 mm holes, also fanned out from the dip gully. Frequent damage to the hole collar was noted. Also, the extraction of longwalls south of the pillar caused stress changes in pre-conditioned zones and caused an increase in seismicity. Subsequent rockburst led to a change in pre-conditioning strategy from face parallel holes to face perpendicular holes as shown in Figure 2.3.

The bulk of the report focuses on stope 17-24W. The site is a 40 m wide, 300 m long pillar. Shearing along the top and bottom of the pillar is observed, as well as closure in the back. The implementation of destress blasting in shown in Figure 2.3. A plan view of the pre-conditioning site is shown in Figure 2.4.

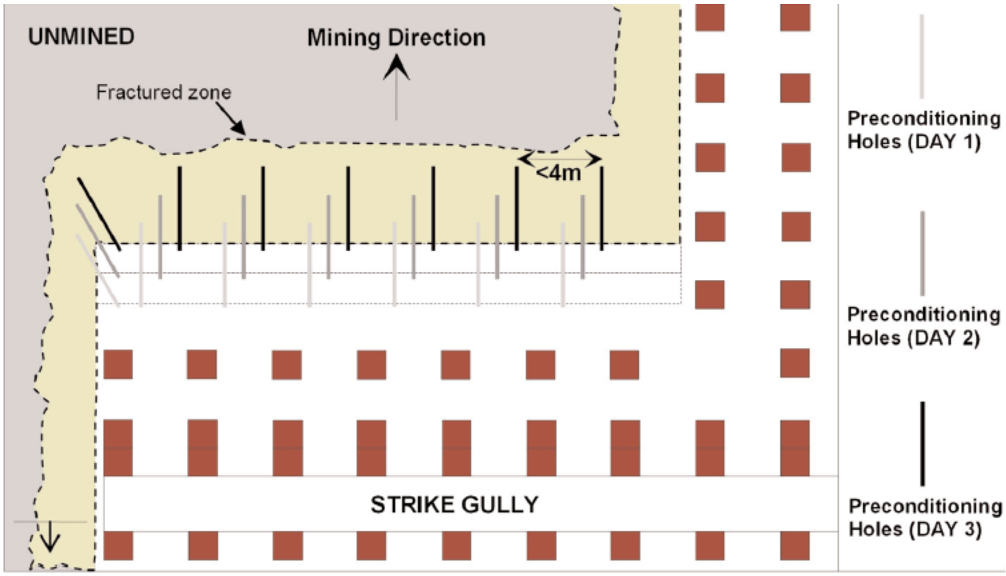

Figure 2.3: Pre-conditioning practiced in South African gold mines as described by Lightfoot et al. (1996). Unmined ore is destressed by blasting face perpendicular holes at each face advance (Mitri and Saharan 2006).

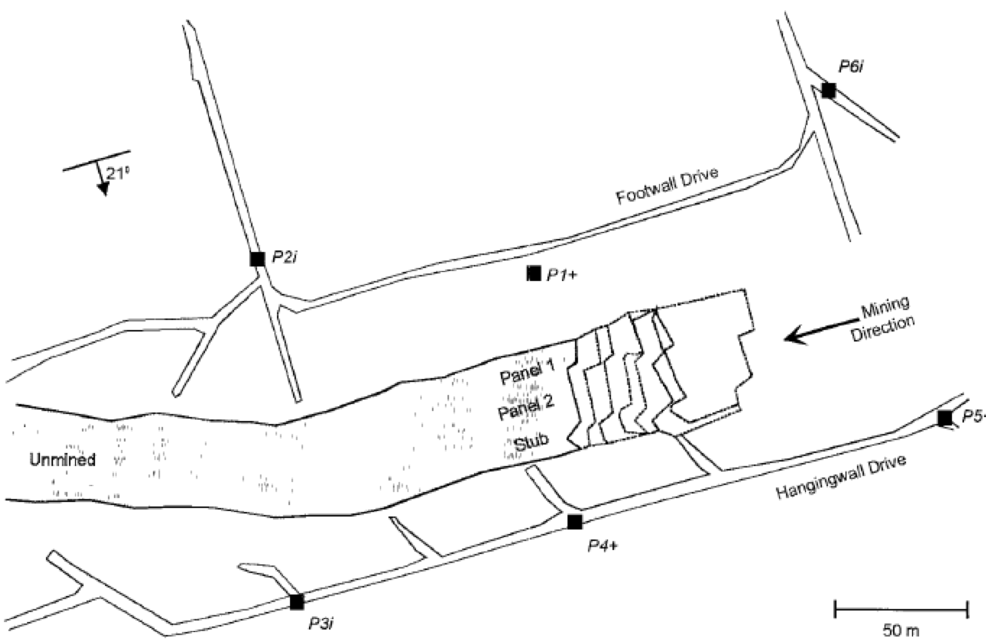

Figure 2.4: Plan view of pre-conditioning site (Lightfoot et al. 1996)

Six methods were used to assess the effects of pre-conditioning:

- Seismic analysis

- Convergence monitoring
- Ground motion monitoring
- Assessment of face dilation
- Analysis of mining induced fracturing
- Seismic tomography

Seismic monitoring, convergence monitoring, as well as fracture mapping yielded useful data that were used to validate the effectiveness of pre-conditioning. The data obtained from other monitoring methods was less conclusive overall.

To begin, 80% of the pre-conditioning blasts had the expected seismic efficiency of 1% to 2%. In addition, for 2 blasts, a separate seismic event was triggered; the recorded blast magnitude is 0.9, and the triggered event magnitude is 2.1. Finally, for 8 blasts, the combination of short holes, poor drilling, and little explosive resulted in low event magnitude and poor seismic efficiency. Spatial migration of micro-seismic events away from the location of the destress blasts was also observed; see Figure 2.5. It indicated the transfer of stress away from the pre-conditioned zone. It was also concluded that pre-conditioning too far ahead of the face is detrimental, as it either has no effect on the stress state at the face or can actively add to the load carried by the face. Holes with low induced seismicity therefore needed to be re-blasted to obtain the desired pre-conditioning effect. Figure 2.6 shows the blast event magnitude plot against the quantity of explosives in kg. Events between the two lines coincide with a seismic efficiency of 1-2% defined as follows (Lightfoot et al. 1996):

$$Seismic\ Efficiency = Wk/U_m \qquad [2.1]$$

where Wk is the seismic energy released, and U_m is the stored strain energy.

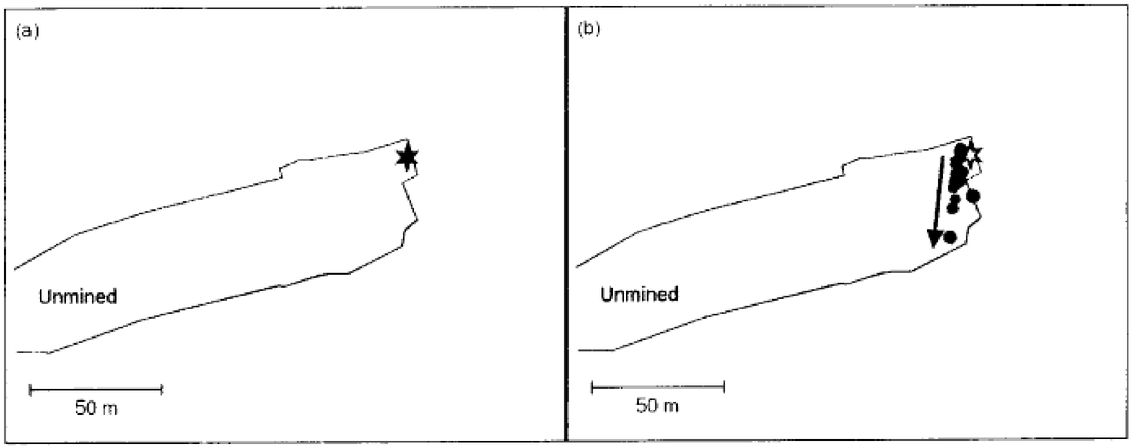

Figure 2.5: Preconditioning blast of November 26, 1992. (a) Location of recorded M = 0.7 blast event. (b) Trend of spatial migration of micro-seismicity away from blast event (Lightfoot et al. 1996)

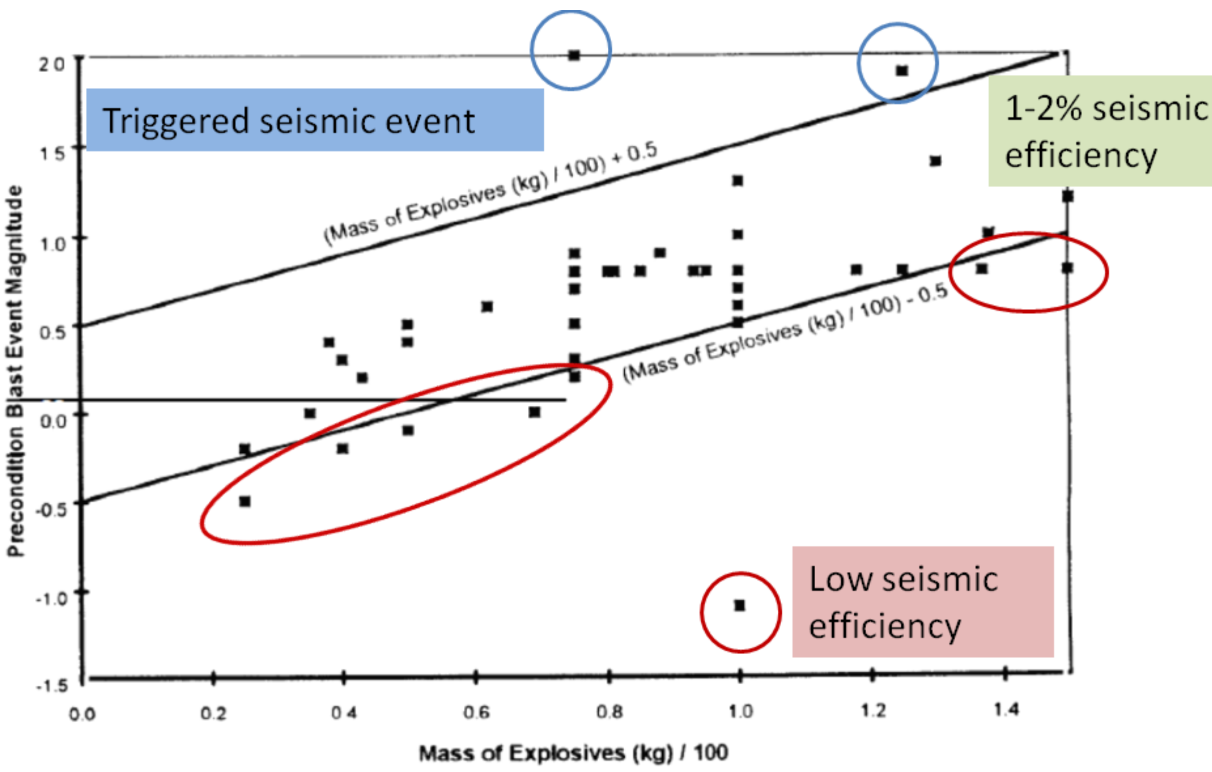

Figure 2.6: Blast event magnitude plot against quantity of explosives (modified from Lightfoot et al. 1996)

For fracture mapping, data was collected for strike, dip, frequency, and type of fracture. Six fracture groups were identified (I to VI) as listed in Table 2.2

Table 2.2: Summary of fracture groups (Lightfoot et al. 1996)

Fracture Group	Description
I	Steeply dipping face perpendicular joints
II	Intermediate dipping face perpendicular faults and joints
III	Steeply dipping shear zones 40˚ to panel face
IV	Steeply dipping face parallel joints
V	Steeply dipping joints 130˚ to panel face
VI	Shallow dipping faults 40˚ to panel face

The chronology of fracture formation was also established: fracture group III formed as a result of regional scale tectonism, groups I, II, IV, and VI formed due to mining induced stresses and group V due to tension immediately ahead of the face. Overall, no new fracture sets were created due to pre-conditioning. Instead, the relative proportion of steeply dipping fractures increased by 25%, with the relative proportion of shallow fractures decreased by 60%. Gouge-filled shearing was also observed for the steeply dipping fractures. Finally, a 3 m thick zone of intensified face parallel fractures was created ahead of the face. Pre-conditioning was therefore found to extend existing fractures rather than create new ones.

The daily convergence rate following production and pre-conditioning blasts were measured within 10 m of the face. It was observed that pre-conditioning has a greater effect on convergence than production blasts. In addition, a large variation in convergence rates was observed, tied to the performance of the destress blasts themselves. For ground motion, black boxes were installed at the face being pre-conditioned. However, the signal received by the boxes was too saturated and difficult to analyse. Dilation of the stope face was also assessed based on the degree of scaling required and the shake out of loose rock off the hanging wall. Digital photogrammetry was also used but deemed too time consuming at the time.

Overall, a 40% increase in face advance was achieved, with a reduced incidence of face bursts. The mechanism of pre-conditioning was found to be the extension of existing fractures based on fracture mapping. It was noted also that the transfer of stress is local and temporary. Pre-conditioning too far ahead of the face can have either no effect or can negatively affect the stress state of the rock mass by increasing the load on the face. Finally, the use of face perpendicular holes was more efficient than face parallel holes.

The main conclusion of the report for the purpose of large scale destress blasting is the finding that no new fracture sets are created after the destress blast. However, quantitative results in term of the stress state in the face are not reported. The main criterion used to assess the success of destress blasting is the seismic energy released. Convergence measurements are also conclusive.

2.2.3 Western Deep Levels South Mine (Lightfoot et al. 1996)

The Western Deep Levels South Mine is a deep South African gold reef where destress blasting is practiced as part of the mining cycle. As of 1996, 200 destress blasts were undertaken along with face advance. The mine used the same tools as Bloyvooruitzicht mine, but with different analysis methods.

- Seismic monitoring
- Convergence monitoring
- Fragmentation
- Analysis of stress induced fracturing

In addition, strain measurement for stress determination was attempted. The idea was to obtain a full stress profile ahead of the mining face before and after pre-conditioning. The strain gauges were to be placed 10 m to 15 m ahead of the face. However, hole collapse at 6 m to 7 m of depth prevented the installation of the instruments and the program was abandoned.

Seismicity was monitored with both portable monitoring systems and the mine wide monitoring system. Good correlation was obtained between the two systems and clustering in the stope vicinity was detected. 2000 events were detected over a period of 8 months, 500 of which had a magnitude greater than 0. The seismic b-value, which describes the distribution of the magnitudes of the seismic events, was calculated. A higher b-value indicates a higher frequency of small seismic events per large seismic event. The b-value increased for a single panel and this was taken as proof of successful destress blasting program. The results for other panels were inconclusive.

Daily convergence measurements were taken from 43 convergence ride stations. Convergence data correlated with the seismic data in that seismic events near the stope triggered a higher in-elastic convergence rate. However, this effect could only be detected relatively near the pre-conditioned panel, demonstrating the expected local effect of pre-conditioning.

The mechanism of pre-conditioning is described as an injection of gas opening existing fractures. Since the production blast occurs just after the pre-conditioning, it was expected that the production blast should be more efficient at breaking the face. This was indicated by the improved advance rates. Digital photogrammetry as a method to quantify fragmentation is discussed but not employed.

Finally, the fracturing obtained with pre-conditioning was analysed based on 600 individual mapped fractures prior to pre-conditioning and 500 individual mapped fractures after pre-conditioning (see Figure 2.7). Overall, fractures were found to be predominantly face parallel or face perpendicular, with steep dip both with or away from the mining face. Five fracture groups were identified. Similarly to Bloyvooruitzicht Mine, no new fracture groups were identified after pre-conditioning. Instead, the relative abundance of the fracture groups changed due to enhancement and re-mobilization of pre-existing fractures.

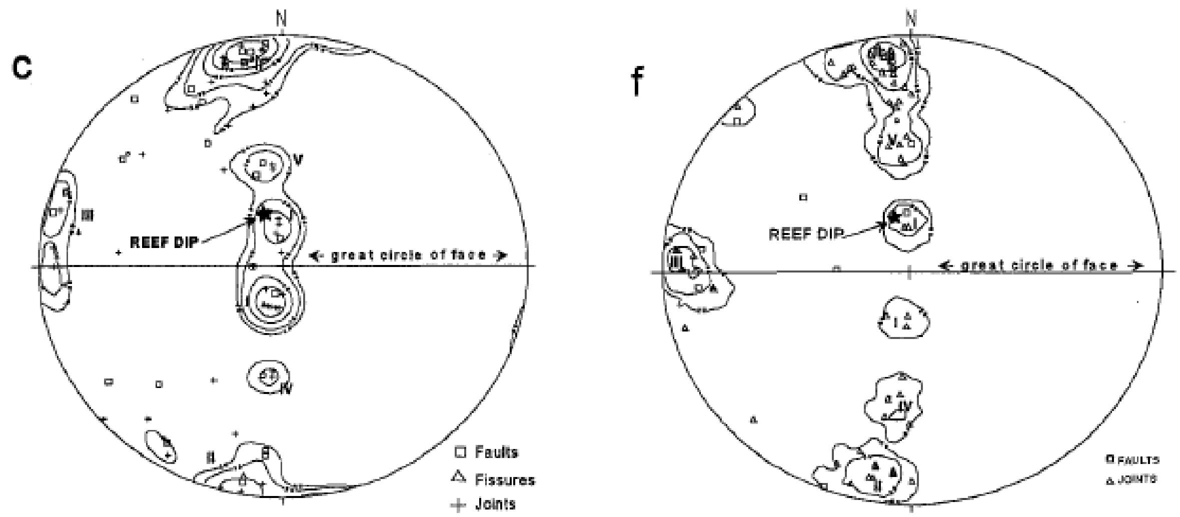

Figure 2.7: Stereonets of mapped fracture planes in normal (c) and pre-conditioned (f) ground (Lightfoot et al. 1996)

The results are similar conclusions to Bloyvooruitzhicht mine. In this case however, the criterion for success of destress blast mainly recorded seismicity. The seismic energy analysis was less conclusive. Again, the stress state of the face is assumed, and the main proof of success is the improved advance rate.

2.2.4 Macassa Mine (Hanson et al. 1987)

The orebody is a steeply dipping (75° dip) ore vein, 2-6 m wide. It is extracted with the cut-and-fill mining method. The crown pillar tended to rockburst-prone when their width approached 18 m or 60% of the stope was mined. A single line of destress blastholes with drilled in the mid-plane of the 58-40 crown pillar and loaded with ANFO. Seismic event locations and convergence before and after the blast where monitored. The monitoring indicated that pillar failure progressed from the exterior to the interior. In addition, most post-blast seismic activity occurred in the pillar, which is inconsistent with current understanding of the destress blasting mechanism. Convergence monitoring indicated partial destressing (50%) of the pillar.

A series of rockbursts occurred a year after the destress blast which severely damaged the adjacent drift. In the final analysis, destressing of the pillar improved conditions for the pillar itself but may have contributed to rockburst in the surrounding pillars.

2.2.5 Campbell Mine (Makuch et al. 1987; Hedley 1992; Mitri 2001)

The gold bearing orebodies at Campbell Mine are steeply dipping, 2-12 m wide, and mined to a depth of 1300 m. At deeper levels, the cut-and fill mining method is employed. Four destress blasts were done during the 1980’s, with the most successful one being the destressing of the crown and sill pillars on the 18 level.

The 4.5 m crown pillar was destressed with 45 mm holes, spaced 1.4 m, drilled to within 1.5 m of the overlying drift, over 45 m. The sill pillar above the level was also destressed, with 6 m long, 45 mm diameter holes, spaced 1.4 m over 25 m. Holes were loaded with ANFO. The blast was followed by increased micro-seismicity and rockbursts in the drift and sill pillar. Significant damage was observed in the back of 18 level. Drilling in the crown pillar was difficult due to fracturation. Nonetheless, the crown pillar was fully mined without further incidents. The sill pillar was abandoned as it lay below unconsolidated fill. In addition, a report by Makuch et al. (1987), concerned with the mathematical analysis of destress blasts conducted at Campbell Mine, proposed that destress blasting is most effective when the pillar is close to failure.

2.2.6 Creighton Mine (Oliver et al., 1987; O'Donnell 1992)

The 400 orebody at Creighton Mine is moderately dipping (65°), 65 m wide, 230 m strike, and mined to a depth of 2150 m. Levels are at 60 m intervals and the mining method used at the location and time of the destress blast case study was mechanized overhand cut-and-fill which created a crown pillar with high stress and rockburst problems as it reached a thickness of 30 m. To mine the crown pillar, the vertical retreat mining (VRM) method was introduced. A 6 m thick, backfilled, destress slot, striking North and cutting the pillar in two, was excavated to relieve the crown pillar.

Destress blasting was applied during the excavation of sill drifts in preparation for mining the ore blocks; refer to Figure 2.8. The sill drifts are 4.3 m x 3.7 m, with the inter-drift pillar being 3 m wide, obtaining a recovery of 67% to 75%. In-situ stresses were 100 MPa E-W, 79 MPa N-S, 62 MPa vertical. The ore had a UCS ranging from 175 to 250 MPa. 54 mm holes were drilled in the pillars and loaded with 0.9 to 1.5 m of ANFO. However, bursting continued after the destress blasts. Drift support was increased, and the pillars were re-blasted, yielding better results. Overall the correct procedure that was determined was to add stiffer resin grouted rebar in the backs when convergence stabilized, add high ribs and cable bolts for high spans, and use yielding support during the active phase.

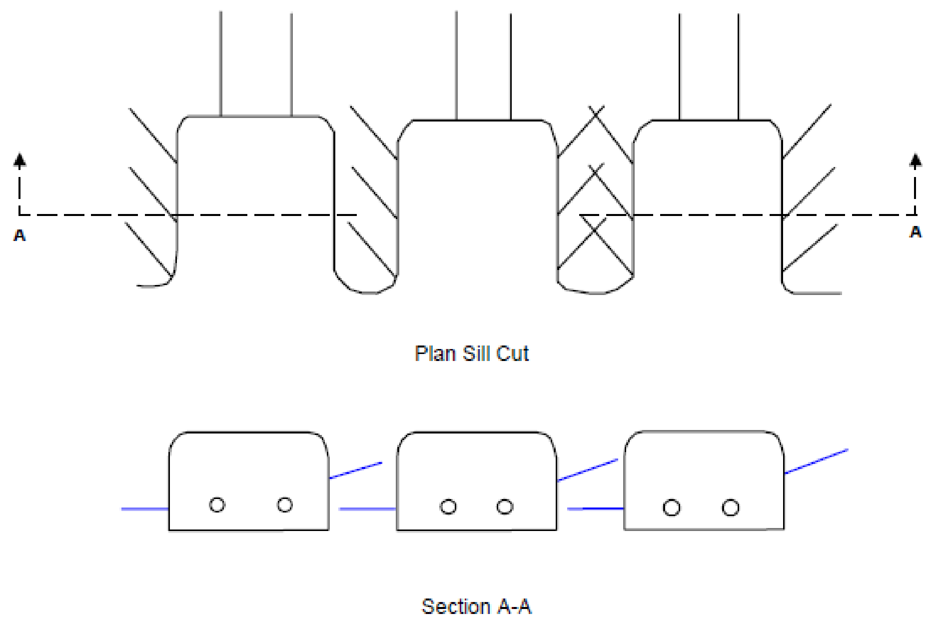

Figure 2.8: Destress blasting pattern for Creighton Mine sill drifts (O'Donnell 1992; Mitri 2001)

<u>2.2.7 Falconbridge Mine (Moruzi and Paseika 1964)</u>

Destress blast was carried out in the stope hanging wall. Critical strain energy of the destressed rock was known. Photo-elastic shear strain measurements and fracture observation on cores were conducted. A 15% increase in fractures in post-blast diamond cores was measured but deemed insignificant. Short- and long-term convergence measurements yielded more conclusive results. Overall, destress blasting was unsuccessful with little effect, as not enough energy was supplied (40 lb of ANFO in holes spaced 30 feet (9 m) apart).

2.2.8 Phyasalmi Mine (Hakami et al. 1990)

Destress blasting was conducted in the center plane of 10 m thick, 5 m wide stope pillars. The holes were 89 mm in diameter, 10 m long (broke through), with a spacing of 0.5 m to 0.8 m. Extensive instrumentation was used, such as rock bolt load cells, extensometers, endoscopes, seismographs, diamond drilling cores for RQD, and inspection holes.

Most of the results were inconclusive, excluding the following. The walls and backs of the drifts were damaged as there was no stemming (cratering was observed). Cracking was noted as perpendicular to the plane of the blastholes, in the direction of the major principal stress. Modulus and strength data of rock after destressing show significant destressing but only for 1 test. Inspection holes show breakouts after the blasts and RQD values mostly showed deterioration after blasting.

2.3 Strategic Destressing Case Studies

As seen in the previous section, the goal of tactical destressing is to directly precondition the rock to be mined. This is done by blasting ahead of a drift or a longwall in conjunction with the normal development or mining rounds. Once the first blasted round is extracted, the next face is already partially damaged, and the risk of violent brittle failure is reduced. On the contrary, strategic destressing does not directly blast the rock to be mined. Rather, the aim is to reduce the burst proneness of an entire mining region by strategically damaging rock at its periphery with the goal of creating a stress shadow in the area prone to burst. In consequence, strategic destressing tends to be large scale, where destressing of an entire mining region is achieved rather than the next cut only.

There are two variations of strategic destressing that can be found from the available case studies. In Canadian hard rock mines, the aim is to reduce stress in the mining region with large scale panels. Blasting these panels reduces their stiffness and releases stresses, causing high stress to wrap around the panel and lower stresses in the panel's stress shadow, and consequently the burst proneness. This practice is discussed in Brunswick Mine and Fraser Mine case studies. On the other hand, in deep longwall coal mines, the aim of destressing is to reduce the stiffness of overlying hard rock strata that are prone to violent collapse following the advance of the longwall. In this case, the roof is destressed with long blast holes in advance of mining to facilitate a more progressive collapse of the roof. This practice is exemplified by the Lazy Colliery case study.

<u>2.3.1 Brunswick Mine (Andrieux et al. 2000; Andrieux et al. 2003; Andrieux 2005)</u>

A large scale (27 Kt), choked, panel de-stress blast was conducted at Brunswick mine in October 1999. The 29-9 pillar, shown in Figure 2.9, needed destressing to act as a stress window, transferring high stress to a critical mining region. The blast was deemed successful. The case study was used to validate a classification system proposed by Andrieux and Hadjigeorgiou (2008) and a destressability index of "good" was introduced.

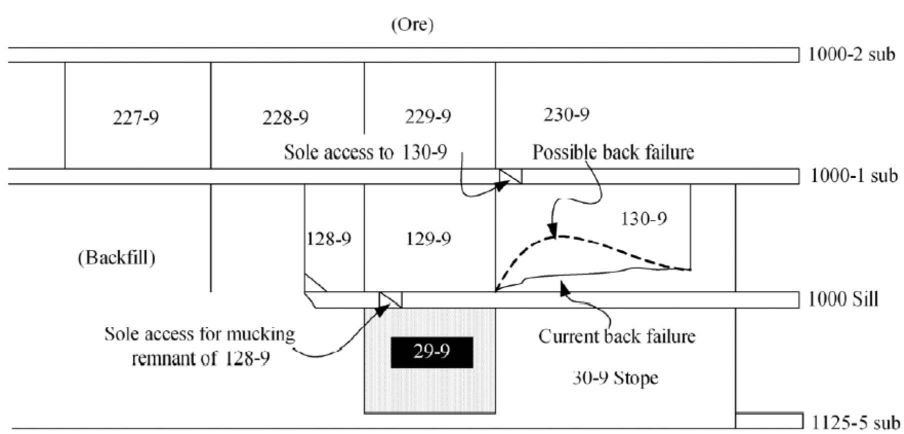

Figure 2.9: Overall view of area around 29-9 pillar (Andrieux et al. 2003)

The blast design was assessed with vibration contours in rock with software based on the Holmberg-Persson equation. A total of 32 blastholes were required using 1.25 density Emulsion corresponding to a total of 17,100 kg of explosives. The blast pattern consisted of two rows of parallel holes drilled in 29-9 pillar, with no free face as shown in Figure 2.10. The hole had an average charge length of 20 m. The blast holes were 165 mm in diameter to attain the required explosive energy. The spacing was 2.4 m by 2.4 m.

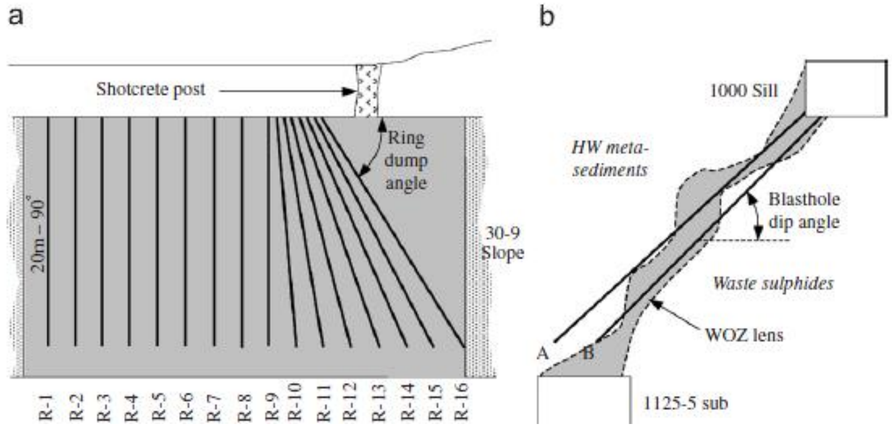

Figure 2.10: (a) Longitudinal section of the 29-9 pillar and (b) cross section at R-8. (Andrieux et al. 2003)

The following instrumentation and monitoring system were used to monitor the blast.

- Vibrating wire stress cells
- Mine wide seismic monitoring system
- Multi-point extensometers (MPBX)
- Borehole camera survey
- 2D seismic tomography (Figure 2.11)
- High frequency geophones

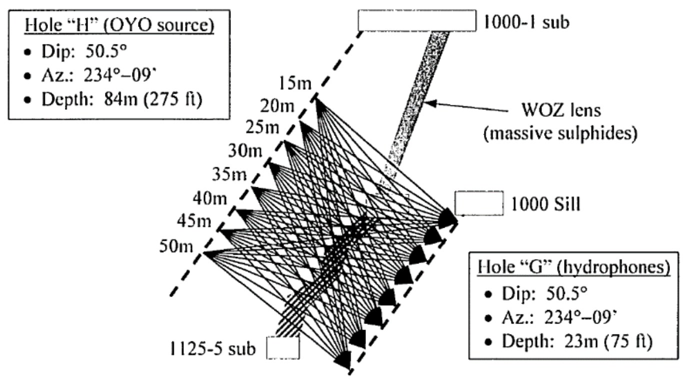

Figure 2.11: Setup of seismic tomography survey at Brunswick Mine (Andrieux 2005). The Oyo-Wappa mechanical seismic source was set up in the water filled borehole "H".

2-D seismic tomography survey was used to determine the change in fracturing before and after the blast. Vibration signals were generated at 5 m intervals in hole H and recorded with hydrophones in hole G (Figure 2.11). Localized damage zone was detected immediately below 1000 sill, but not on bulk of the pillar, yielding inconclusive results. Also, significant displacements occurred after the destress blast as can be seen from the plot in Figure 2.12. Higher displacements were measured at the bottom of the hole nearest to destress blast, indicating that the rock mass expanded near the blast. A stress drop was detected by the downhole gauge in the stress shadow. A minor stress increase was detected in the uphole gauge, indicating some stress wrapping. The results are consistent with a successful blast. However, the stresses were measured in only one direction. The effect of the re-orientation of stresses is therefore unknown. Figure 2.13 shows stress changes measured by the vibrating wire stress cells (Andrieux 2005)

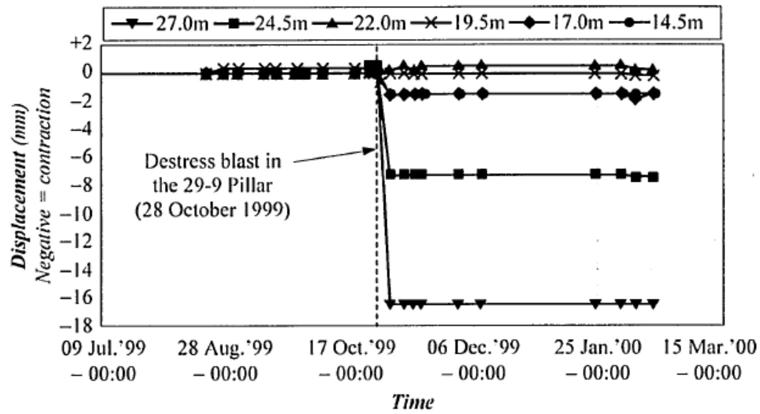

Figure 2.12: MPBX displacement results obtained after the destress blast in 29-9 pillar (Andrieux 2005)

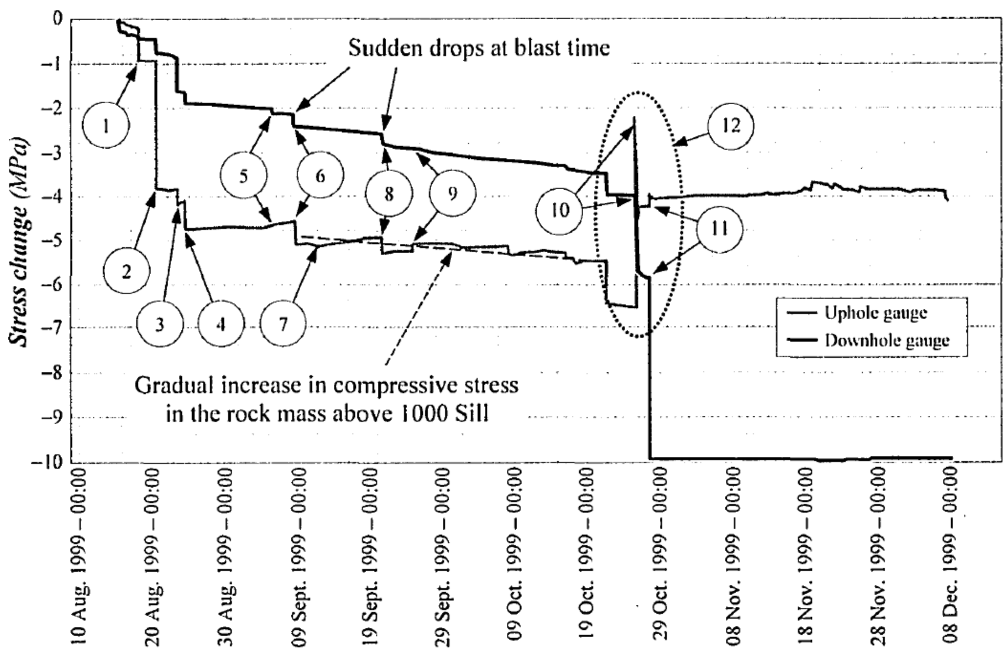

Figure 2.13: Stress changes measured by the Geokon vibrating wire stress cells (Andrieux 2005). Each measured stress change is denoted by the event ID of mining step or a seismic event which caused the stress change. Event ID 11 is the destress blast.

A 3DEC numerical model was built for a full-scale geomechanics study of the south end of the mine (Andrieux 2005). All previous mining was incorporated. Two methods were used to simulate the destress blast. First, reducing the modulus of elasticity of the destressed zone was attempted

(10% to 50% reduction range). The results did not provide a sufficient stress change as measured by the stress cells. However, a good match was obtained with the second method when the destressed rock was fully removed.

In this case, stress cell data seems to have given conclusive results. However, the cells were uniaxial, meaning that rotation of stresses is not measured. The full stress tensor after the destress blast in therefore unknown. Nonetheless, long term seismic analysis and convergence measurements also indicated a successful blast. However, the back analysis of the blast yielded unrealistic results, and the seismic tomography survey yielded no usable results.

2.3.2 Fraser Mine (Andrieux 2005)

A 10 kt, choked, destress blast was fired on 24 December 2001 at Fraser Mine. The level where the destress blast occurred was exploited with overhand cut-and-fill. Based on numerical modelling, the sill pillar was expected to fail as one or two cuts remained. Also, the mining rate was slowing due to increased seismic activity as the sill pillar thinned (cut #21 took twice as long as previous cuts).

The objective of the destress blast was to fracture the hanging wall and deflect high mining induced stress away from mining activity. The extraction of the next few cuts would be facilitated, nonetheless with the expectation that global failure of the sill pillar would be accelerated A Large scale, choked panel destress blast was attempted. The panel being destressed was 18 m high, 27.5 m wide, 3 m thick; refer to Figure 2.14. The targeted mass was 10,075 tonnes. The blasted rock was felsic gneiss.

Two parallel rows of holes were fanned from the drift and were drilled eastwards and upwards with no breakthrough (see Figure 2.15). There were 14 holes per row, with a spacing of 3 m by 3 m. The holes were 114 mm in diameter and loaded with bulk emulsion. A total of 4.4 tonnes of explosives was used, yielding 500 calories of explosive energy per kg of rock.

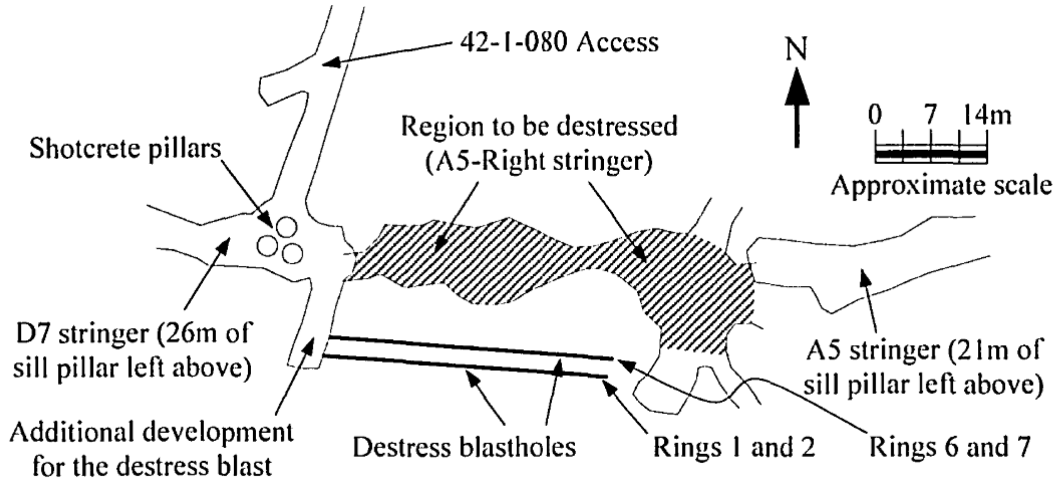

Figure 2.14: Plan view of area targeted by destress blast (Andrieux 2005)

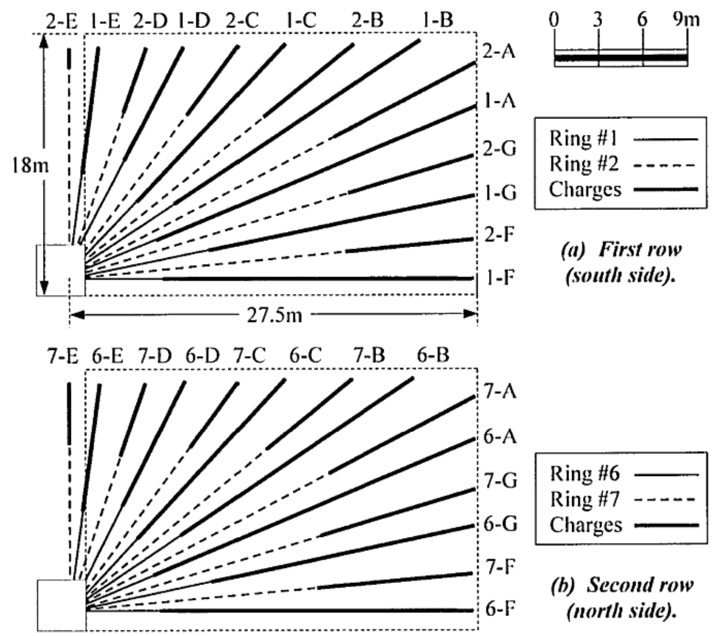

Figure 2.15: Destress blast pattern at Fraser Mine (Andrieux 2005)

The following instrumentation was used to analyze the destress blast:

- Vibrating wire stress cells
- Strain gauge in shotcrete pillar

- Multi-point extensometers (MPBX)
- High frequency geophones
- Mine wide seismic monitoring

Three vibrating wire stress cells were used. They were installed in boreholes drilled at 30° to 45° upwards from 42-1-80 access (see Figure 2.14 for the location of the drift). Two of the cells were in the expected destress blast stress shadow, one measuring an expected drop in stress in the horizontal direction (#1), the other measuring the change in vertical stress (#3). One cell was installed outside the stress shadow and expected to measure a stress increase (#2). Two six-point extensometers were used. Both were installed in vertical holes from the 42-1-80 access. Convergence was monitored with a strain gauge installed in a Shotcrete post in 42-1-80 access. Three surface mounted geophones, all with three recording axes, were installed 18 m, 42 m, and 230 m from the blast.

The blast-induced vibration data obtained was of good quality. Additional vibration data was recorded 3 seconds after the blast and inferred to be seismic events triggered by the blast. Moderate seismicity in the footwall side was recorded by the mine wide monitoring system in the following week. The cumulative stress drop due to the recorded seismic events was calculated based on the source volume and the moment magnitude ($\Delta\sigma = M_o/V$), with the highest drops occurring 4 hours after the destress blast. This indicated that the blast was successful at modifying the regional stress regime. The vibrating wire stress cell #1 recorded a 1.5 MPa stress drop immediately after the blast up to 6 MPa a week later. Stress cell #3 recorded a stress increase in the vertical direction. Little data was acquired from the extensometers due to improper installation. Permanent deformations were recorded however, indicating damage in the destressed zone. Finally, the strain gauge in the shotcrete post recorded a 20 tonne load increase. This downward movement of the strata after the destress blast was expected.

General conclusions were that the destress blast was successful, diverting stress away from the next cuts (as measured by the stress cells) and diverting them away to higher up in the sill pillar.

Like the Brunswick mine blast, the stress cells gave usable results. However, Andrieux (2005) notes that the stresses were uniaxial, and the full stress tensor is not measured.

2.3.3 Lazy Colliery (Konicek et al. 2013)

Destress blasting is widely implemented in the Czech Republic, with 2000 blasts done between 1990 and 2010 in the Upper Silesian Coal Basin (USCB). The subject of this case study is longwall mining of a thick coal seam in the Lazy Colliery. The Lazy Colliery is in the Ostrava Karivna coal field (OKC) in the UCSB. The cover depth is 700 m, and coal seams are 3.1 to 5.0 m thick. The longwall is extracted with a double drum shearer at panel lengths ranging from 109 m to 189 m. The coal at the Lazy Colliery can accumulate high strain energy. With a ratio of elastic deformation to total deformation greater than 0.8, and a UCS of 40 MPa, the coal is susceptible to rockbursts. Also, the roof strata consist of massive sandstone with a UCS ranging from 70 to 120 MPa.

The longwall face of panel 140914 (Figure 2.16) in coal seam 504 was determined to be at high risk of rockbursts; the edges of the overlying extracted and caved coal seams 512 and 530, with goaf heights of 58 m and 75 m respectively, are located over the panel, transferring high stress to the longwall face. Destressing of the competent interburden rock was therefore undertaken to reduce the occurrence of rockbursts.

The goal of the destressing program was to reduce the strength and massiveness of the overlying strata by creating a network of fissures. The horizon to be destressed was 20 m above the coal seam, and it was targeted with long boreholes that were drilled from the gate roads. The borehole lengths ranged from 40 m to 100 m, drilled upwards with an angle ranging from 12° to 37°; see examples in Figures 2.17 and 2.18. The boreholes were 93 mm in diameter and spaced 10 m along the gate road to meet the required amount of explosives. The holes were loaded with explosives over 63% to 85% of their lengths, with sand stemming ranging from 14 m to 25 m. The explosive used was a gelatine type explosive Perunit 28E with a heat of explosion of 4100 kJ/kg.

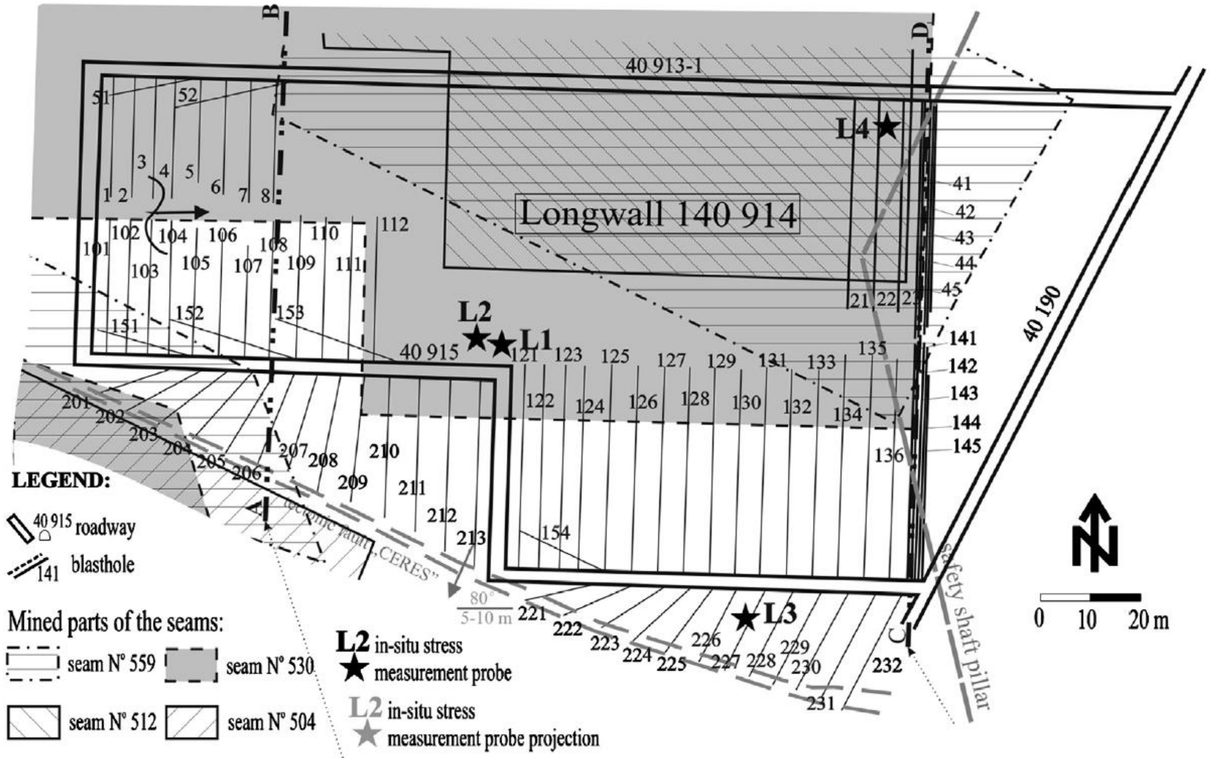

Figure 2.16: Longwall panel 140 914 plan view (Konicek et al. 2013)

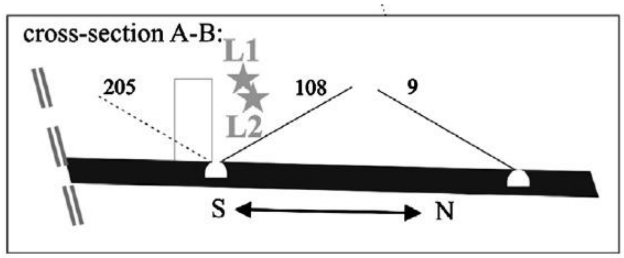

Figure 2.17: Cross-section A-B, along the strike of the longwall. Destress blast holes shown in the section are holes 108 and 9. L1 and L2 show the position of the CCBM stress cells (out of plane). (Konicek et al. 2013)

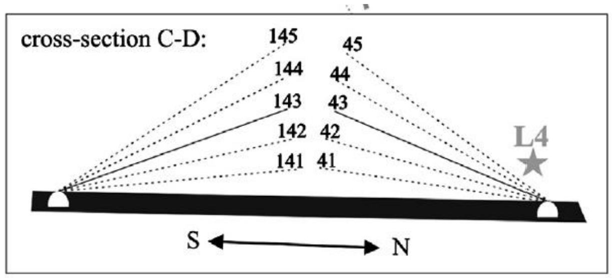

Figure 2.18: Cross-section C-D, along the strike of the longwall. Destress blast holes shown in the section are holes 141-145 and 41-45. L4 is the position of a CCBM stress cell (out of plane). (Konicek et al. 2013)

To evaluate the effectiveness of the destress blast, the seismic effect of the destress blasts was calculated based on the seismic energy released by the destress blast (Konicek et al. 2013). The seismic effect is derived from the energy balance established for OKC (Knoteck et al. 1985):

$$E_1 = E_{VT} + E_{pr} + E_{pot} + E_{kin} \quad [2.2]$$

$$E_2 = E_r + E_{kin} + E_{seismic} + E_{NM} \quad [2.3]$$

where:

$E_1 = initial\ energy$
$E_{VT} = explosive\ energy$
$E_{pr} = released\ deformation\ energy$
$E_{pot} = change\ in\ potential\ energy$
$E_{kin} = kinetic\ energy$
$E_2 = resulting\ energy$
$E_r = fragmentation\ energy$
$E_{seismic} = Seismic\ energy$
$E_{NM} = not\ measured$

By assuming that the change in potential energy and kinetic energy are 0, and by introducing the coefficient K, the balance can be reduced to:

$$E_{seismic} = K\left(E_{VT} + E_{pr}\right) \tag{2.4}$$

The factor K can be determined statistically based on individual sets of measurements (denoted with i) where K is minimum; in other words, the factor K is determined from a fully confined blast with no displacements, meaning no release of strain energy (E_{pr} is 0):

$$K = \min(K_i) \; where \; K_i = \frac{E_{seismic^i}}{E_{VT^i}} \tag{2.5}$$

The efficiency of the elastic deformation release can therefore be expressed as:

$$SE = \frac{E_{seismic}}{KE_{VT}} \tag{2.6}$$

or

$$SE = \frac{E_{OKC}}{K_{OKC}Q} \tag{2.7}$$

where:

$E_{OKC} = seismic\ energy\ calculated\ from\ monitoring\ system$

$K_{OKC} = combined\ coefficient\ for\ OKC$

$Q = explosive\ charge\ in\ kg$

The coefficient K_{OKC} was measured to be 2.1 based on a large-scale field study covering 1000 cases at OKC (see Figure 2.19). The seismic effect was then evaluated for 18 destress blasts. Overall, the seismic effect measured for all 18 blasts ranged from 3.6 to 53. The seismic effects of the blasts were categorized from very good to excellent.

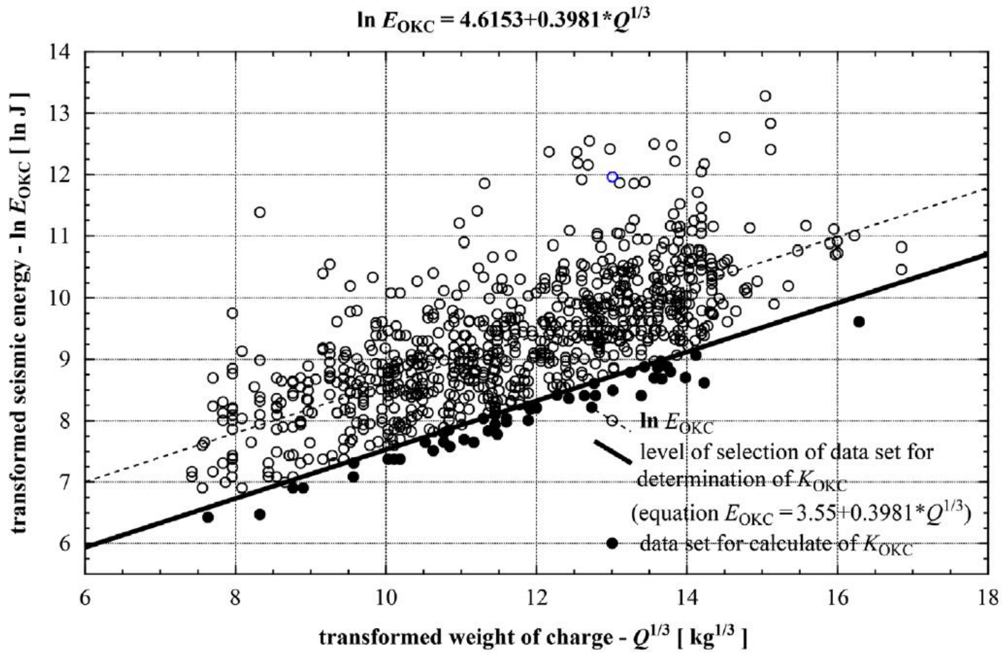

Figure 2.19: Relation between transformed data of seismic energy and weight of the charge (Konicek et al. 2013). Data set for the determination of K_{OKC} is denoted in black.

In-situ stress measurements were also conducted with the conical ended borehole monitoring (CCBM) method and the conical ended borehole overcoring (CCBO) method. Due to the conical shape of the sensor, the entire stress tensor could be obtained. The CCBO's were used to obtain an absolute, one time, stress measurement while the CCBM's were used to monitor long term stress changes. The CCBM could also measure the change in the orientation of the stress tensor.

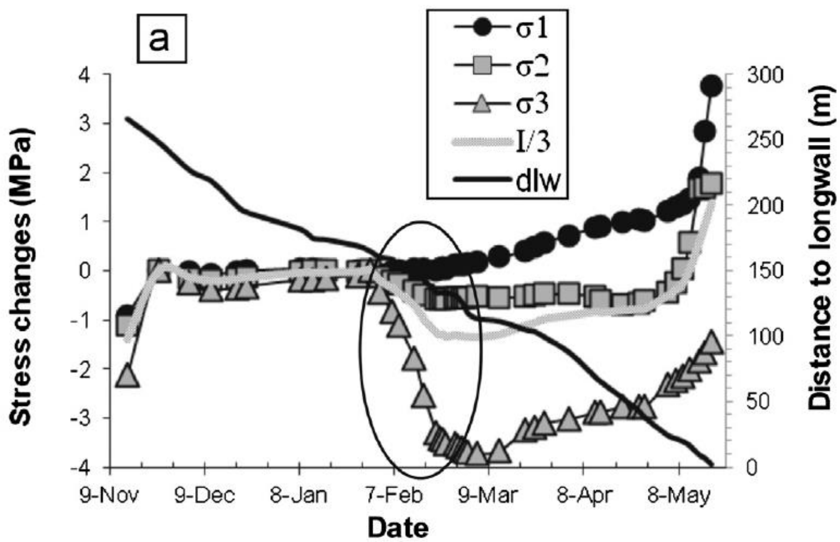

Figure 2.20: Stress variation measured by CCBM L3 (Konicek et al. 2013)

The stress cells were used to monitor the mining induced stress as the longwall advanced (see Figure 2.20). A reduction in the zone of influence of the site from the calculated 93 m to the measured 50 m indicated that the competency of the overlying strata was reduced by blasting. Also, a drop in the minor principal stress was measured following the destress blast on the 28th of January 2007, showing the stress release characteristic of destress blasting.

The efficiency of the adopted destress blasting was evaluated mainly in terms of the seismic effect. Since all the blasts released at least 3 time more energy than the explosive energy, the destress blasting effect was deemed very good in the energy release point of view. However, the actual stress tensor in the roof prior and following the destress blast is not reported. From the CCBM measurements, it is reported that only the minor principal stress decreased following the destress blast. This loss of confinement, in terms of brittle shear ratio or BPI, leads to an increase in burst proneness. Nonetheless, the authors report that the 300 m longwall panel was extracted without any further rockbursts following the destress blasting program.

2.3.4 Star-Morning Mine (Karwoski and McLaughin 1975)

The Star-Morning mine a deep silver mine located in the Coeur d'Alene district, Idaho. The orebody is a sub-vertical, narrow ore vein, mined with overhand cut-and-fill. A destress blasting trial was done in two adjacent panels, totalling 75 m in length, 24 m in height. For one panel, destress blasting was conducted in the ore, while it was conducted outside the ore in the other. 100 mm diameter holes were fanned from the crosscut, parallel to the ore vein. It was observed that better results were obtained when destress blasting was conducted inside the ore. A 50 mm halo of powdered rock was observed around the 100 mm blast holes, increasing the diameter to 200 mm. No radial cracking occurred. However, the destressed rock seemed more fractured due to possible extension of existing fractures due to blasting.

2.4 Case Study Review Conclusions

Destress blasting is used as a last resort, when burst prone structures cannot be avoided by changing the mining sequence or geometry. Destress blasting is applied in two general mining scenarios as follows.

1) Development of drifts, raises, and shafts. At increased depths, very high stresses occur at the face of an advancing drift. Continuous destressing is therefore needed as the face advances. Destress is implemented at each advance round. This practice is widely applied to mining longwalls in South Africa but also practiced when drifting in highly stress pillars at moderate depth in Canada.
2) Pillars: In North America, destressing is mostly applied in sub-vertical ore deposits for the extraction of remnant pillars in longhole mining or sill pillars and crown pillars in cut-and-fill mining. The highly stressed pillar is either directly destressed or the hanging wall is destressed so that the ore pillar is in the stress shadow of the destressed zone.

In addition, the practice can be divided in two broad types:

1) Tactical destressing, which involves directly pre-conditioning burst prone rock that is to be extracted.

2) Strategic destressing, where the aim is to reduce the burst proneness of an entire mining region by strategically damaging rock at its periphery to create a stress shadow in the area prone to rockburst.

The contrast between strategic and tactical destressing is emphasized the most when comparing the explosive energies of the destress blast per ton of ore blasted rock (see Figure 2.21). Strategic destress blasting case studies apply explosive energies exceeding 200 cal/kg, while tactical destress blasting case studies stay between 10 cal/kg and 100 cal/kg.

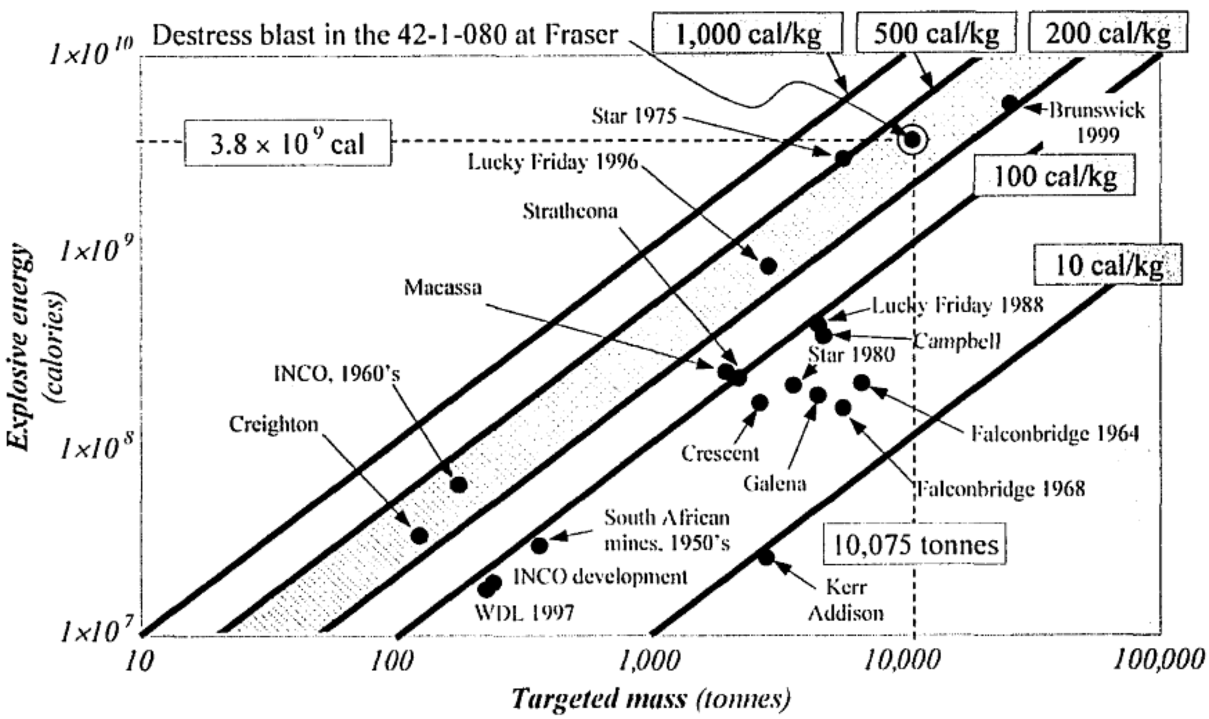

Figure 2.21: Explosive energy in calories vs. the targeted mass of destress blasting (Andrieux 2005)

To measure the success of a blast, the following criteria are typically used:

- Monitoring of seismicity, where the triggering of a significant seismic event by destress blasting is the main indication of success, as well as a reduction in the frequency and magnitude of seismicity over the long term.
- Measurement of displacement and convergence coherent with expected destressing

- Measurement of stress changes coherent with expected destressing effect.
- Measurement of seismic energy from rock bursts and destress blasting (informative but difficult exercise)
- Mining advance rate, or frequency of delays.

The application of destress blasting has seen varying levels of success. This success is mainly evaluated based on the seismic response of the blast, sometimes as the sole criterion in lack of other conclusive evidence. Convergence measurement is also a popular criterion. Back analysis with numerical modelling is seldom used and is done with only simple models.

In addition, the state of stress prior to destressing is usually unknown and must be assumed. Destressing in low stress ground may just cause transfer of more energy to the high stress ground, and high stress is often assumed based on seismic history. Blast induced fracture propagation in a non-hydrostatic stress field is also unaccounted for (Saharan 2009). In this case, the orientation of the major principal stresses will affect the blast induced fracture propagation, and therefore the overall effect of the destress blast.

Therefore, the stress change effect of destressing needs to be quantified with a holistic model in order to further investigate the effectiveness of destressing. This holistic model can then be used to assess the success of a destress blast based on measured and computed stress changes.

2.5 Destress Blasting Theory

Destress blasting is the application of explosive energy to highly stress zones to fracture rock, thus reducing the stored stain energy. The peak load is transferred to another zone, ideally away from mining. This reduction in peak load alone, given all other parameters are constant, will reduce the burst proneness of the rock.

2.5.1 Destress Blasting Mechanisms

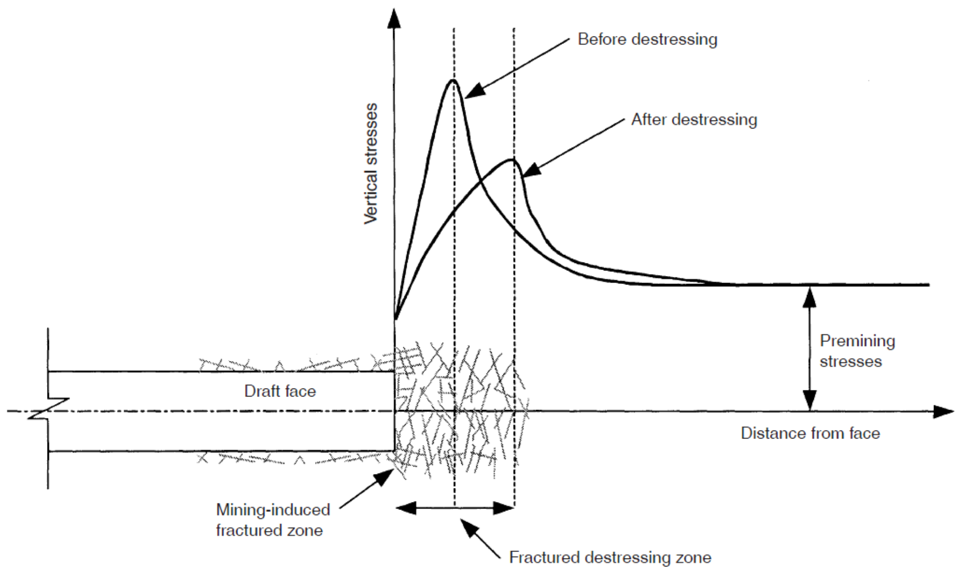

Figure 2.22: Stress distribution resulting from of an ideal destress blast (Tang and Mitri 2001)

As shown in Figure 2.22, destress blasting is understood to reduce the stress in the rock by inducing fracturing, demonstrated to be along pre-existing fracture planes (Lightfoot et al. 1996). However, the exact mechanism of destressing along with its effects is not fully understood. Nonetheless, the induced fracturing is thought to have the following positive effects that reduce burst proneness:

Modification of rock mass properties: the fracturing reduces the stiffness of the rock (Blake 1972) as well as the load bearing ability. This effect is generally accepted and applied in numerical modelling back analyses (Blake 1972; Boler and Swanson 1993; Tang 2000; Andrieux 2005). A portion of the strain energy in the destressed rock is transferred to the surrounding rock mass or rock support due to the relative reduction in the stiffness of the destressed zone.

Dissipation of stress: an instantaneous release of stresses from the rock due to blast induced damage. Essentially, strain energy is consumed to fracture the rock (Tang and Mitri 2001), releasing stress.

Modification of failure mechanism: destress blasting mobilizes the rock mass along pre-existing fractures, equivalent to plastic strain. As rockbursts are normally associated to brittle elastic rock failure, a destressed zone will yield gradually rather than fail suddenly as a rockburst (Saharan 2004)

Point 2 can be examined based on the energy balance of a destress blast (Cook 1967, Salomon 1974):

$$W_t + U_m = U_c + W_r \tag{2.8}$$

- $W_t = change\ in\ potential\ energy$
- $U_m = stored\ strain\ energy\ in\ mined\ material$
- $U_c = increased\ strain\ energy\ in\ surrounding\ rock$
- $W_r = released\ energy$

Applied to a destress blast, the additional energy components are required (Hedley 1992):

$$W_t + U_{m1} + Ex = U_c + U_{m2} + U_f + W_r \tag{2.9}$$

- $U_{m1} = stored\ strain\ energy\ before\ destressing$
- $U_{m2} = stored\ strain\ energy\ in\ after\ destressing$
- $Ex = explosive\ energy$
- $U_f = energy\ consumed\ in\ fracturing\ the\ rock$

Based on this energy balance, Hedley (1992) concludes that stored strain energy in the pillar is used in the fracturing process, and the volume of the blasted rock mass is theoretically reduced.

Mitri (2001) describes the reduction in volume for a confined blast as follows. Shearing on pre-existing, favorable failure planes initiated by the explosive blast is observed as the presence of gouge zones in the pre-existing planes (Lightfoot, Kullman et al. 1996; Mitri 2001). As the fully confined rock approaches failure, its volume decreases due to Poisson effect (the Poisson ratio of rock is smaller than 0.5). At failure, this reduction ceases and rock goes plastic with a Poisson ratio approaching 0.5. The presence of gouge in the fractures implies plastic failure, which further indicates a reduction of volume which gives the desired softening effect. Microcracking (dilation) caused by blast opposes this, increasing volume and stress.

However, ejection of material is not accounted in the above analyses. Destress blasting should aim for a swell of 5-15% (Liu 2013), which is equivalent to the swell of a “frozen” production blast. In this case, displacement of rock for a mass destress blast must be allowed for, preferably with a void underneath the blast. This ejection of material from the panel is argued to cause additional wall convergence and reduced panel load bearing capacity (Andrieux 2005).

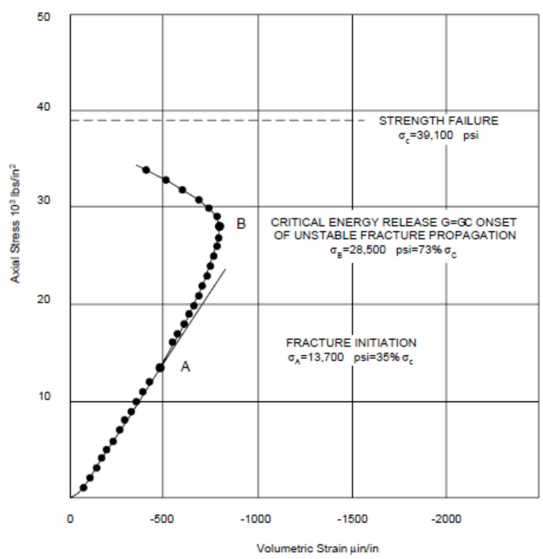

Figure 2.23: Stress strain curve of norite (Klaus 1970)

In addition, stress can rebuild as the consolidation (volumetric reduction) of the rock ceases (Mitri 2001).This is consistent with effect of plasticization from Figure 2.23; for a fully confined rock, the bulk modulus increases with increasing stress. The rock is therefore able to support more stress. This is valid as long as the dilation of the failed rock is prevented (the rock is kept fully confined). Fully confined destressing therefore needs to be done when stress is near failure. This is commonly practiced: In South Africa, destressing is practiced 3-5 m ahead of the face (Lightfoot et al. 1996), and in North America, ore pillars are destressed as they attain critical thickness (Boler and Swanson 1993). If the rock is destressed too early, stresses will rebuild as mining continues to advance.

2.5.2 Holistic effects and simulation of destress blasting

As shown in the previous sections, destress blasting is still an art rather than science. There is a wide range of destress blasting practices, mostly based on-site experience. Over the past 25 years, multiple modelling techniques have been proposed to holistically simulate destress blasting, notably Saharan (2009) and Tang (2000). Both models will be applied to the back analysis of the Copper Cliff Mine destress blast to shed light on destress blasting mechanism. Establishing input parameters for these models will also help with the prediction of the performance of future blasts. The theory and application of these simulation techniques is overviewed below.

Rock fragmentation (Blake 1972)

- Static, linear elastic model
- Apply a rock fragmentation factor (α) to damaged zone

With this model, the only factor considered is the reduction in rock mass stiffness due to blast induced damage. The factor α applied varies between 0 and 1, with a factor close to 0 representing a fully damaged rock mass, and a factor close to 1 representing poor quality destressing or an undamaged rock mass.

Rock fragmentation and stress reduction (Tang and Miti 2001)

- Static, linear elastic model
- Apply rock fragmentation factor (α) to damaged zone
- Apply stress reduction factor (β) to damaged zone

Tang expanded on Blake's fragmentation factor by adding the stress reduction factor to account for the strain energy that is instantaneously released by the blast as either seismic energy or used to fracture the rock. This release of stresses in a blasted rock mass is explained theoretically with Hedley's (1992) destress blast energy balance. The stress reduction factor β ranges from 0 to 1, where 0 represents no stress dissipation, e.g. poor quality destress blast, and 1 represents 100% stress dissipation suggesting complete damage of the destress zone.

Anisotropic rock fragmentation and stress reduction (Saharan 2009)

- Static, linear elastic model
- Apply transversely isotropic rock fragmentation factor (α_1, α_2,) to damaged zone
- Apply transversely isotropic stress reduction factor (β_{ij}) to damaged zone

This model was introduced by Saharan (2009), who postulates that fragmentation and stress reduction is anisotropic due to the tendency of fractures to propagate in the direction of the major principal stress. The overall hypothesis is that there will be a lower stress release and rock fragmentation effect in the direction of the major principal stress. Saharan and Mitri (2009) proposed the following model.

$$\beta_{ij} = \left(\frac{(\sigma_{ij}\ before\ destress\ blasting) - (\sigma_{ij}\ after\ destress\ blasting)}{\sigma_{ij}\ before\ destress\ blasting}\right) \times 100\% \qquad [2.10]$$

where,

- β_{ij} is the stress relaxation to σ_i at measuring point on the j^{th} Cartesian plane.
- σ_{ij} is the i^{th} major principal stress at measuring point on the j^{th} Cartesian plane.
- i is the principal stress identifier (1,2,3)
- j is the Cartesian plane identifier (x, y, z)

Under isotropic stress conditions, all blast induced fractures are mode 1 tensile cracks. However, the tensile stress perpendicular to the pre-loading axis is suppressed under anisotropic stress conditions, favoring the initiation of mode II fractures propagating in the direction of the major principal stress. Yang and Ding (2018) conducted a caustics experiment to determine the behavior of blast induced cracks under loading. Uniaxial static stress on an Acrylic glass plate was varied from 0 to 9 MPa. A hole in the center of the plate was loaded with 180 mg of lead azide and detonated. Two pertinent observations were made.

- Initial static stress load generates different stress concentrations around the borehole, with the maximum tensile stress located on major principal stress axis.

- Increasing the level of stress concentration decreases propagation time, increases tendency for propagation to occur in the direction of σ_1, increases severity of mode II fractures, and increases deflection angle of crack.

When a pre-existing crack was introduced in the plate, it was found that that blast induced cracks still extend preferentially in the direction of σ_1. Under isotropic stress conditions, all cracks are mode I. However, stress anisotropy on the specimen increases the severity of mode II cracking, with longer cracks propagating in the direction σ_1. Pre-existing cracks facilitate crack propagation, but cracks will still preferentially propagate in direction of σ_1. The same experimental setup was used to study the wave propagation in a jointed medium (Yang et al. 2016). It was found that cracks did not propagate across a pre-exiting fractures. The same pattern was observed where blast induced fractures could only propagate from the tips of the pre-existing fractures in the direction of the major principal stress.

Multiple numerical modelling studies have been conducted to investigate blasting induced crack propagation in rocks, reporting similar behavior. Zhu et al. (2007) found partial reflection and transmission across cracks filled with unconsolidated soil as joint material, with no crack propagation across joints. The presence of air in a joint further reduces amplitude of transmitted stress waves. Ma et al. (2008) varied uniaxial loading of their model up to 50 MPa, where all fractures propagated in the major principal stress direction. The effect was detectable with a deviatoric stress of just 2 MPa.

These studies suggest that pre-existing fracture orientation may not be the dominant factor in the preferential orientation of blast induced fractures, and therefore the overall destressing effect. However, it is not yet clear to what extent preferential fracture propagation will affect the stress release and rock fragmentation as a whole for a destress blast. The effect first needs to be quantified, and it is hoped that a back-analysis blast induced stress change will be able to discriminate between the isotropic and anisotropic models. This will further shed light on the effect of the stress state prior to blasting on the success of a destress blast. These aspects are presented in Chapter 6.

Chapter 3: Case Study Mine

This chapter is divided into 4 sections. This first section discusses Copper Cliff Mine (CCM), the case study mine for this thesis. It describes the orebody known as 100OB where the destress blasting program was implemented. The second part explains in more detail the destress blasting program. The third part elaborates on the numerical model constructed for the simulation and analysis of the destress blasting effects. Finally, the fourth part discusses the instrumentation installed at CCM to monitor the effects of the destress blasting. This was used as a basis to validate the destress blasting constitutive models used in conjunction with the numerical model.

3.1 Copper Cliff Mine

Copper Cliff Mine is an underground hard rock metal mine located in Copper Cliff near Sudbury, Ontario, Canada. The mine is currently operated by Vale Canada Ltd and is exploiting multiple orebodies. The orebodies of interest are 100OB and 900OB. These are described below.

3.1.1 100OB and 900OB

The 100 and 900 orebodies are both steeply dipping and pipe shaped, extending 1300 m vertically and around 150 m horizontally. The orebodies are near each other, with narrow zones of sulphides linking the two. The 100OB is composed of massive to heavily disseminated inclusions of sulphide mineralization, with a sharp contact between the ore and host rock. The 900OB on the other hand consists of erratic sulphide stringers and lenses with some disseminated mineralization. The main host rock for the orebodies is predominantly massive quartz diorite, which is primarily composed of amphibole, biotite and chlorite.

3.1.2 Geological Structures

The geological structure with the most influence on the 100 and 900 orebodies is the 900OB Cross Fault. The fault strikes at 100°, dips at 45° to the north, and cuts through the 100OB between the 2430 level (2430L) to the south, and the 3000 level (3000L) to the north. Major damage to the access ramp following a 3.8 Mn seismic event attributed to the Cross Fault on September 11, 2008, resulted in stope abandonment. In addition, The mining sequence between levels 3050 and 3400 needed to be revised due to rock bursting attributed to the cross fault. However, a recent study by Sainoki et. al (2017) with an orebody-wide numerical model encompassing the cross fault showed that shear movements along the fault are aseismic. In addition, no large seismic events occurred due to the cross fault from 2006 to 2014. Given that the 900OB Cross Fault lies outside the likely boundary of the diminishing ore pillar model of this study, it is not considered in the destress blasting back analysis.

On the other hand, there are many non-persistent or discontinuous olivine and quartz diabase dykes that cross cut the 100 and 900 orebodies near the diminishing ore pillar being studied in this thesis. The most significant is a stiff quartz diabase trap dyke that lies between the two orebodies in the mid to upper region and intersects the 900OB South of 100OB. To the North, a soft Olivine Diabase Dyke intersects 100OB near the diminishing ore pillar. The trap dyke and Olivine Diabase Dyke are therefore both included in the diminishing ore pillar numerical model.

3.1.3 100-900OB Mining Sequence

The 100OB diminishing ore pillar was formed by two mining fronts:

- Bottom up mining front from 3500L to 3050L from September 1999 to October 2009
- Ongoing bottom up mining front from 4200L to 3710L starting in 2004

As of April 2014, 17 stopes remained in 100OB between levels 3880 and 3500. On the other hand, 900OB was mined bottom up first from 3500L to 3000L from February 2000 to February 2003, and then from 4050L to 3710L from April 2007 to November 2010. The remaining stopes in 900OB between 3880L and 3500L are not planned to be mined, as it was decided to mine 100OB completely before going on to 900OB. A 15 m crown pillar was to remain between 3500L and 3550L spanning across both 100OB and 900OB. However, after the implementation of destress blasting in 100OB, the crown pillar between 3550 and 3500L in 100OB is now planned be mined. From this point forward, the 100OB pillar refers to all stopes between 100OB that are planned for production. The pillar consists of 7 “crown stopes” between 3500L and 3550L, 9 “sill stopes” between 3710L and 3550L, and 2 “still stopes” between 3880L and 3710L. The sill stopes are mined with the vertical retreat method (VRM), while the crown stopes are mined with upholes from 3550L (URM). The drilling horizon for the sill stopes is 3550L and muck is drawn from 3710L. For the crown stopes, the stope is mucked and drilled from 3550L. Figure 3.1 shows the state of the diminishing ore pillar before destressing and the planned mining methods.

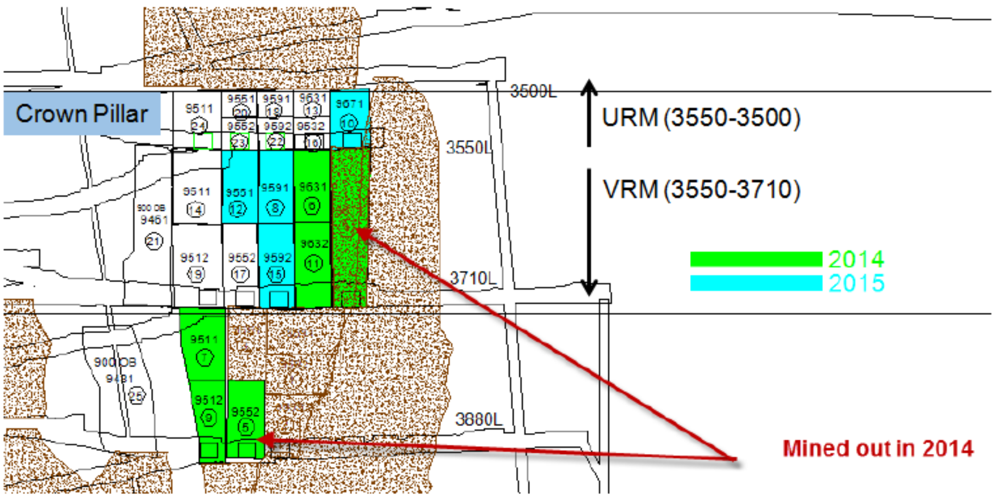

Figure 3.1 State of diminishing ore pillar in January 2015. Planned mining sequence shown in the figure was revised

3.1.4 Stress Conditions in the Diminishing Ore Pillar

The state of stress in the diminishing pillar is estimated based on borehole breakouts and the breakout pattern of the stope cave at the local latitude of 9710 sill. The major principal stress is estimated to have a plunge of 10°, and an azimuth of N78°W, oriented nearly perpendicular to the orebody strike. The intermediate principal stress is found to have a trend of N12˚E. The minor principal stress is assumed to be due solely to overburden weight and is nearly vertical. The magnitude of the principal stresses is estimated with the Sudbury regional stress empirical equations.

Based on a linear elastic boundary element (BEM) analysis conducted in 2012, it was determined that the crown stopes between levels 3500L and 3550L should be mined in tandem with the sill stopes on 3710L. The mining sequence would also need to be a retreat away from the 9710 sill cave at the North end of the orebody. The other sequence that was explored was a retreat from the stiff Trap Dyke at the South end of the orebody. However, it was found that mining 100OB diminishing pillar did not significantly affect the stress state in the trap dyke. Therefore, mining away from the cave towards the stiff trap dyke was determined to be the proper sequence in order to reduce the stresses in the production area. The overall mining sequence is therefore a retreat from North to South, alternating between the crown and sill stopes.

The BEM analysis also determined that the stresses close to mining were high, but not extremely high compared to the uniaxial strength of the rock. However, mining in the region has been historically difficult, with squeezing drill-holes and seismicity experienced when mining from both 3500L and 4050L. A dynamic support system has therefore been widely implemented in all active mining areas in 100OB. Due to the even more severe stress condition that would occur in the diminishing ore pillar, the destress blasting program described in the following sections was implemented.

3.2 Overview of the Destress Blasting Program

3.2.1 Overall Strategy

The aim of the destress blast program implemented at CCM was to create a stress shadow which encompasses all the stopes in the 100OB diminishing ore pillar. To begin, the sill drifts on 3550L, 3710L, and 3880L were extended into the hanging wall as shown in Figure 3.2. From there, rings of blastholes parallel to the orebody strike were drilled to form a series of panels which would completely shield the diminishing ore pillar in the E-W direction. These panels will be destressed in 4 phases as mining of the diminishing ore pillar progresses. As of April, 2019, the first three phases have been fired. Figure 3.2 shows a plan view of the 100OB pillar with the destress panels.

Figure 3.2: Plan view of 3550 Level showing destress blasting rings in the hanging wall (in purple). Sill drifts are extended across the orebody to the hanging wall (in green).

3.2.2 Planned mining sequence of 100OB Diminishing pillar

Figure 3.3 shows the nomenclature for the pillar stopes. Stopes are numbered based on the local latitude of the sill drive which accesses them. For a stope to be mineable, its corresponding destress panel needs to have been blasted. Table 3.1 lists the stopes that are shielded by each of the 4 destress phases. Due to the N-S retreat of the mining sequence, the destress phases occur relatively early in the total sequence to stay in advance of the planned North-South mining retreat. The overall mining sequence with each destress phase implemented is provided in Table 3.2.

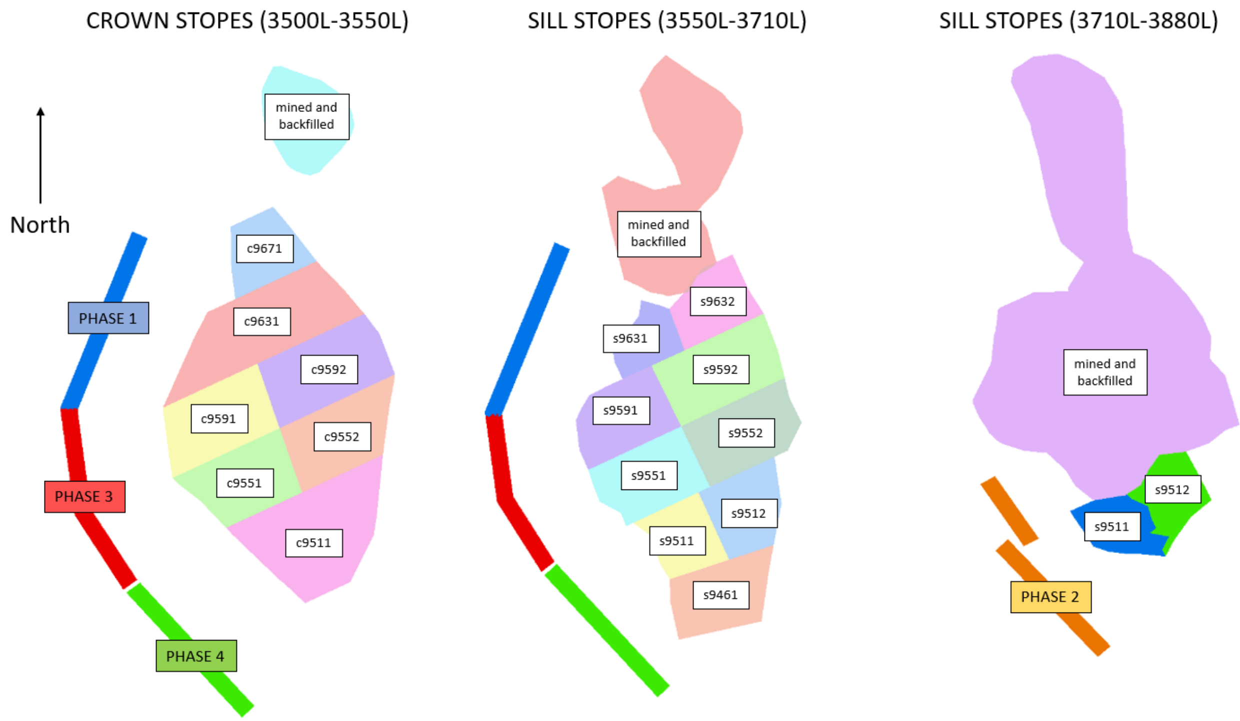

Figure 3.3: Planned stope numbering.

Table 3.1: Destress phases and corresponding stopes

Phase 1	Crown	9671, 9631
	Sill	9631, 9632
Phase 2	Crown	
	Sill	9511*, 9512*
Phase 3	Crown	9591, 9592, 9551, 9552
	Sill	9591, 9592, 9551, 9552
Phase 4	Crown	9511
	Sill	9511, 9512, 9461**

*On 3880L

** Cancelled

Table 3.2: Original planned mining and destressing sequence for diminishing pillar at the moment of the Phase 3 blast. Date of executed steps in sequence as of April 2019 is also provided. Destress blasts are included in the sequence as “mining steps”

Mining Step	Stope Name	Mining Method	Top Sill	Date Crown Blast/Destress Blast
1	Phase 1			21-Sep-15
2	9631	VRM	3710	05-Jan-16
3	Phase 2			31-Mar-16
4	9511	VRM	3880	15-May-16
5	9671	URM	3550	20-Jun-16
6	9512	VRM	3880	08-Oct-16
7	Phase 3			06-Feb-17
8	9591	VRM	3710	06-Dec-17
9	Phase 4			
10	9632	VRM	3710	03-Mar-18
11	9551	VRM	3710	
12	9631	URM	3550	30-Sep-18
13	9592	VRM	3710	
14	9591	URM	3550	
15	9552	VRM	3710	
16	9511	VRM	3710	
17	9592	URM	3550	
18	9512	VRM	3710	
19	9551	URM	3550	
20	9552	URM	3550	
21	9511	URM	3550	

The destress blast panels consist of both up and down blast holes with 2 rings of 114 mm diameter holes with a spacing of 1.8 m between the rings. The blast holes are collared such that a toe spacing of 2.6 m is maintained between the holes within the ring. Furthermore, the blast hole rings are staggered to maintain a spacing of 2.4 m between the nearest rings. The blast parameters for the Phase 1, Phase 2, and Phase 3 blasts are provided in Table 3.3

Table 3.3: Blast parameters for phase 1, phase 2, and phase 3 blasts

	Phase 1	Phase 2	Phase 3
Hole Diameter	114 mm		
Hole Length	6-32 m	3-35 m	5-36 m
Total charge	23484 kg	21319 kg	24948 kg
Delay	18 ms	18 ms	18 ms
Max charge per delay	223 kg	264 kg	306 kg
Toe Spacing*	2.6 m	2.8 m	2.8 m
Ring Spacing	1.8 m		
Collar	Adjusted to maintain toe spacing		

*measured from charge toe rather than hole toe

3.2.2 Phase 1 blast

Phase 1 blast is composed of 2 panels as shown in Figure 3.4. The first panel is drilled from 3550L, from sills 9670 and 9630. From each of these sills, there is a ring of upholes and downholes, covering the entire pillar crown and half of the pillar sill. The downhole ring and uphole ring are staggered such that a toe spacing of 2.4 m is maintained between the nearest rings. The downhole rings cover 30 m of vertical distance, while the upholes cover 15 m. The panel is roughly 32 m wide and 50 m high. The approximate targeted mass is 20 kt. The second panel consists of 2 uphole rings from 3710L, covering both 9670 sill stopes and 9630 sill stopes. The panel is roughly 34 m wide and 28 m high. The targeted panel mass is estimated at 10 kt. Phase-1 destress blast required approximately 3000 m of drilling for both up and down holes, with a total targeted mass of 30 kt. Based on the design, the amount of emulsion yields an average energy of 493 cal/kg and 513 cal/kg for up and down holes, respectively.

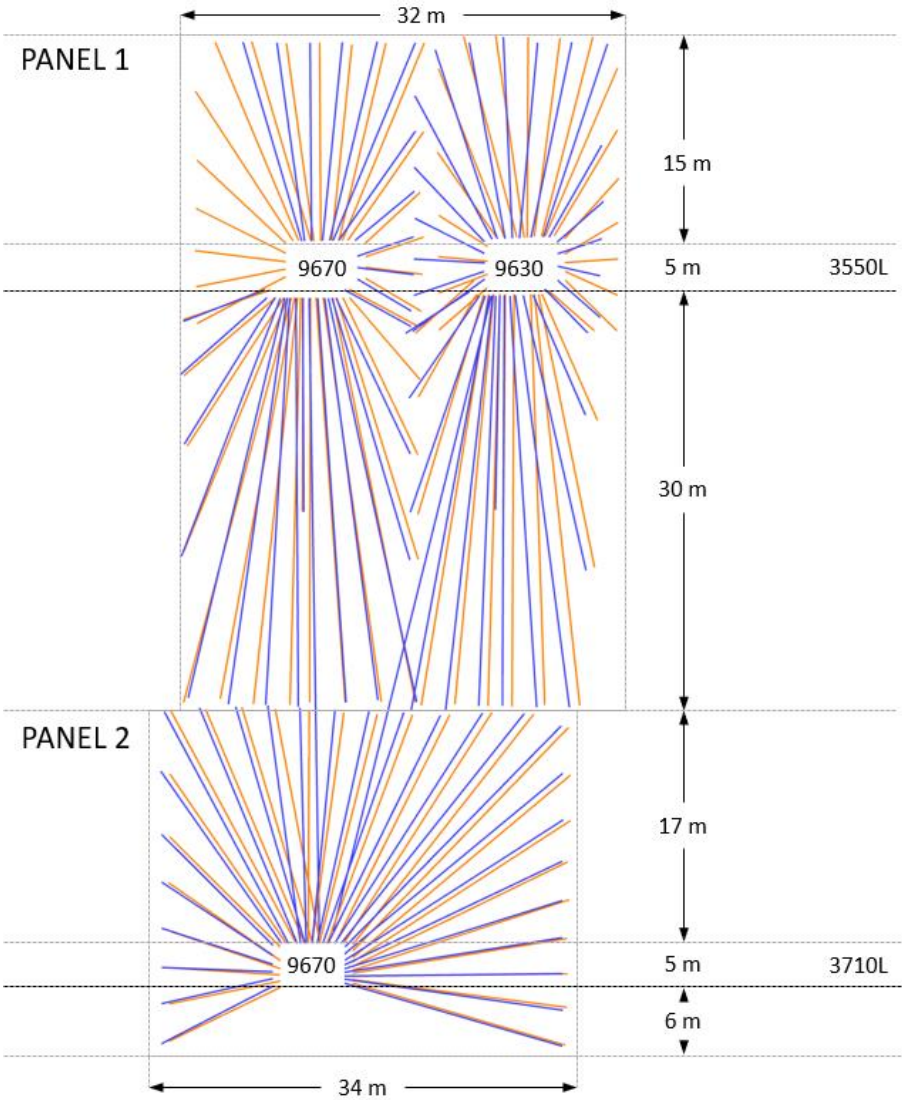

Figure 3.4: Phase 1 destress blast, looking East. Annotated measurements are in the plane of the destress blasts. Parallel blasthole rings are shown in blue and in orange.

3.2.3 Phase 2 Blast

Panel 1 is drilled from sills 9550 and 9510 on 3710L. The panel consists of 2 parallel rings of upholes and 2 parallel rings of downholes from each drift as shown in Figure 3.5. The panel extends 15 m upwards and 30 m downwards, targeting 12 kt of rock. The blast rings are 2.4 m apart along the strike of the drift. Staggered 1 m behind Panel 1 in 9550 sill is Panel 2. Panel 2 is composed of 2 rows of destress holes extending 15 m N-W, parallel to Panel 1. The targeted mass is approximately 8 kt. Finally, Panel 3 consists of mostly upholes from 9510 sill on 3880 level. The panel is 20 m high and has a strike length of 27 m. The 2 rings of holes target around 5.5 kt or rock. The total Phase 2 targeted mass is approximately 25 kt.

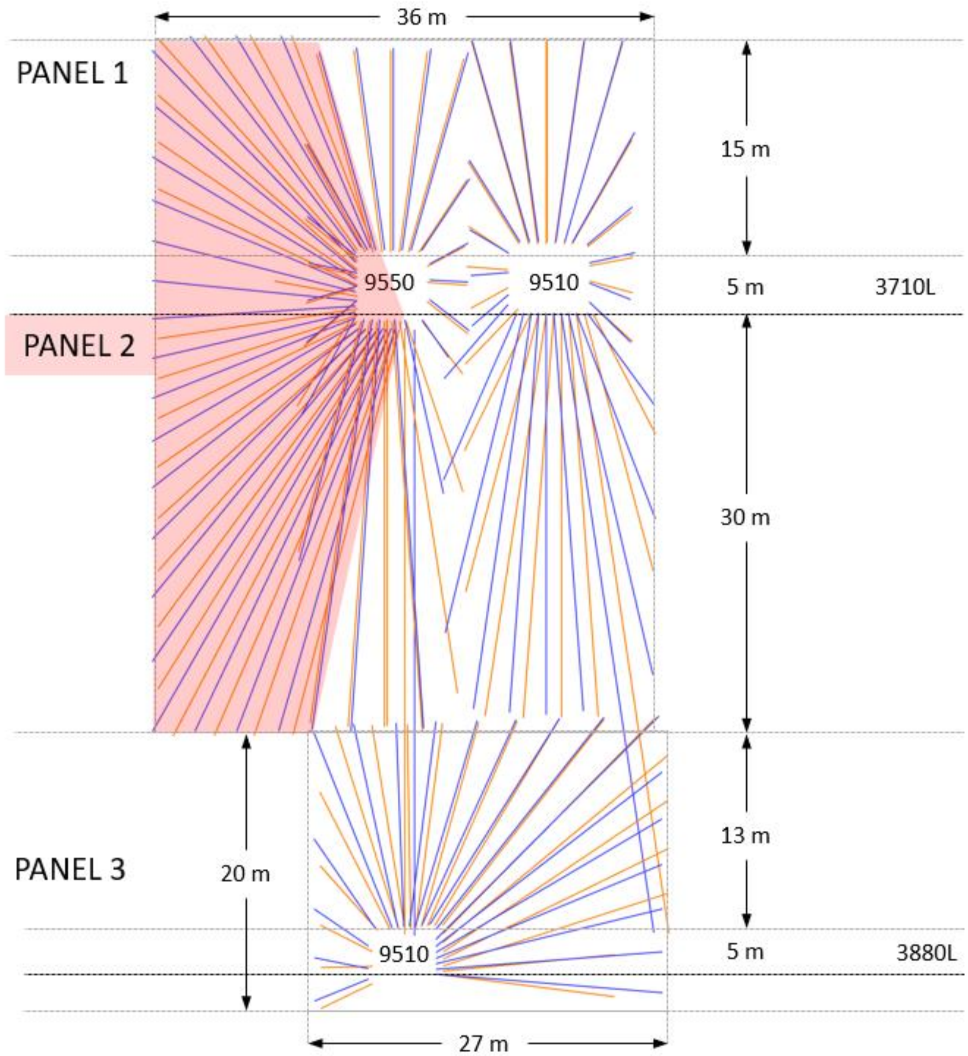

Figure 3.5: Phase 2 destress blast, looking North-East. Annotated measurements are along the strike of the destress blast panels. Parallel blasthole rings are shown in blue and in orange.

3.2.4 Phase 3 blast

The first panel is drilled from 3550L, from sills 9590 and 9550. In each sill, there is a pair of uphole rings covering the entire crown portion of the pillar in height. A second pair of downhole rings in each sill is staggered 8 m behind the uphole rings, covering most of the height of the sill stopes. The remaining portion of the sill stopes at the bottom is either covered by the Phase 2 blast or the second Phase 3 panel. The strike of the first panel changes as it wraps around the remnant pillar. The total strike length of the panel is 36 m; see Figure 3.6. With a height of 60 m, it targets 23 kt of rock.

The second panel is drilled with 2 rings of up-holes from 3710L, from 9590 sill. It spans 14 m across and is 18 m high, targeting approximately 2.6 kt of rock.

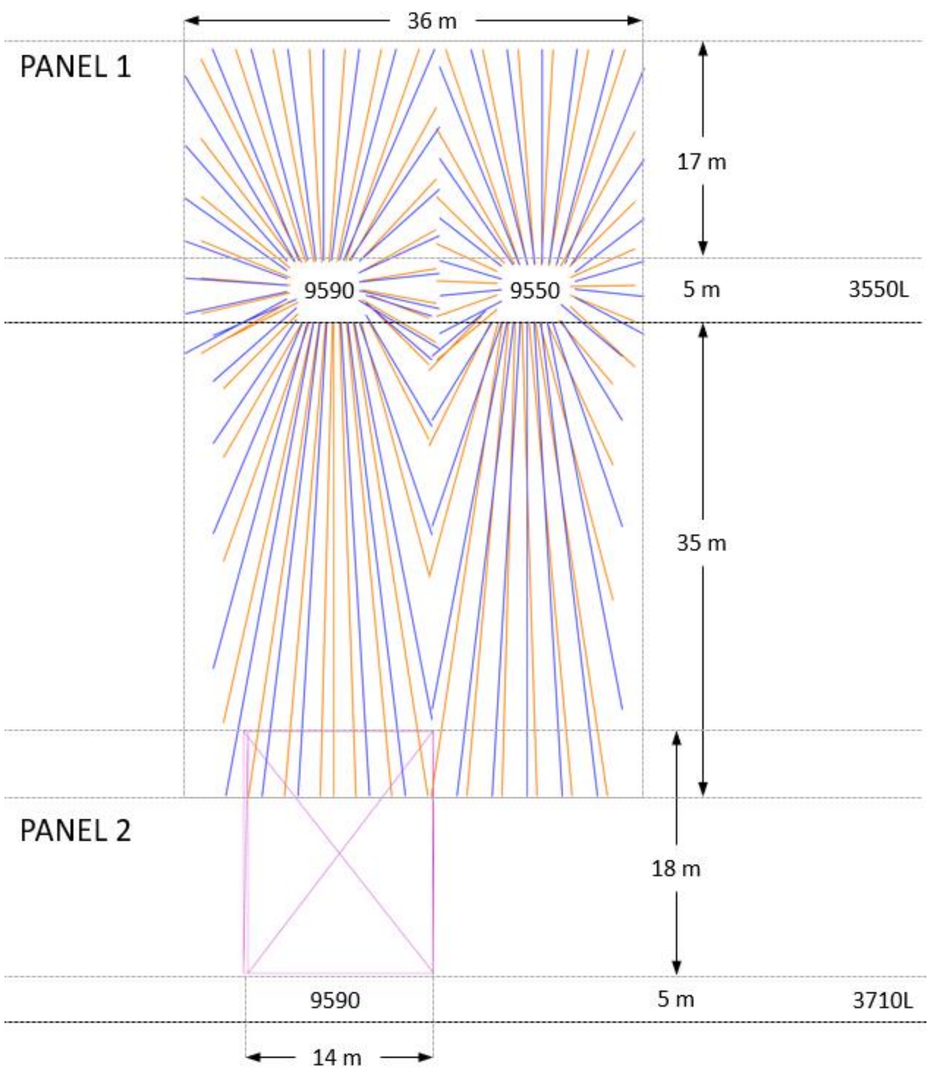

Figure 3.6: Phase 3 destress blast, looking North-East. Annotated measurements are along the strike of the destress blast panels. Parallel blasthole rings are shown in blue and in orange.

3.3 Model Construction

In this section, the numerical model that was built to validate the destress blasting constitutive models is described. In this study, the finite difference software FLAC3D was used. The numerical model is referred to as the “pillar-wide model”. The scope of the model is the 100OB diminishing ore pillar and the destress panels, with no other geological domains or orebodies considered when sizing the model. The topics discussed in this Chapter are model loading, applied elastic properties, applied plastic properties, boundary extent analysis, mesh sensitivity analysis, final geometry, and finally ore extraction sequence leading up to the diminishing ore pillar. Figures 3.8 to 3.10 show the final model geometry.

3.3.1 Model Loading

The numerical model’s x-axis corresponds to the E-W axis, the y-axis corresponds to the N-S axis, and the z-axis corresponds to elevation. The far-field stresses at CCM vary with depth, and are found with the Sudbury regional stress equations:

$$\sigma_1(MPa) = 10.82 - 0.0407D\ (m) \quad [3.1]$$

$$\sigma_2(MPa) = 8.68 - 0.0326D\ (m) \quad [3.2]$$

$$\sigma_3(MPa) = 0.0292D\ (m) \quad [3.3]$$

where D is the depth below ground surface. The model is constrained in the z-direction on the bottom boundary, with all other faces free to displace in all directions. The model x-faces and y-faces are loaded in the x-direction and y-direction, respectively. Overburden stress is applied to the top boundary. Since the x-faces and y-faces boundaries are free, the Poisson self-compression effect does not need to be considered. The major principal stress (σ_1) azimuth is N78˚W and the plunge was simplified to be horizontal to make the minor principal stress vertical. The stresses applied to the x-face and y-face model boundaries are calculated as:

$$\sigma_x(MPa) = 10.80 - 0.0406D\ (m) \quad [3.4]$$

$$\sigma_y(MPa) = 8.67 - 0.0327D\ (m) \quad [3.5]$$

$$\sigma_{xy}(MPa) = -0.225 + 0.000847D\ (m) \quad [3.6]$$

$$\sigma_{yz}(MPa) = 0 \quad [3.7]$$

$$\sigma_{xz}(MPa) = 0 \quad [3.8]$$

where "D" is the depth below surface in meters and a negative stress indicates compression. The vertical stress applied to the top surface is found to be:

$$\sigma_z(MPa) = 0.0292D\ (m) \quad [3.9]$$

The stresses calculated above are directly applied to their respective boundaries.

3.3.2 Model Elastic Properties

The model consists of 4 rock types, with elastic properties shown in Table 3.4. The rock mass stiffness is applied to the model, which is reduced from the intact stiffness based on the GSI (Hoek et al. 2002).

Table 3.4: Elastic Material Properties

	E_{intact} (GPa)	$E_{rockmass}$ (GPa)	ν	γ (kN/m^3)
Host Rock	48	24.96	0.18	28.5
Orebody	52	27.6	0.19	36.3
Trap Dyke	60	N/A	0.22	28.5
Olivine Diabase Dyke	N/A	10	0.25	28.5
Backfill	N/A	2	0.3	20

3.3.3 Rock Mass Failure Envelope

The UCS values provided by Copper Cliff Mine were used to calculate the burst potential index (BPI) (Mitri et al. 1999), brittle shear ratio (BSR) (Castro et al. 1997), and the post peak properties for the plastic analysis in Appendix 1. The relevant properties are shown in the Table 3.5. These include the intact uniaxial compressive stress (UCS), intact Hoek and Brown failure envelope parameters (m_i, s, a), rock mass rating (RMR) and disturbance factor "D". The Olivine Diabase Dyke is strongly sheared and soft. It is therefore not expected to fail in a brittle manner. The UCS and Hoek and Brown parameters are therefore not needed to calculate its burst proneness. Similarly, the only properties required for the backfill are its elastic properties provided in Table 3.5.

Table 3.5: Hoek and Brown failure envelope parameters

	UCS (MPa)	m_i	s	a	RMR	D
Ore	140	24	1	0.5	65	0
Host Rock	122	25	1	0.5	65	0
Trap Dyke	220	15	1	0.5	100	0
Olivine Diabase Dyke	N/A	N/A	N/A	N/A	N/A	N/A
Backfill	N/A	N/A	N/A	N/A	N/A	N/A

3.3.4 Model Boundary Extent Analysis

The size of the model was established with a parametric study where a simplified pillar with the same approximate dimensions was mined out. The model is linear elastic and the applied properties and stresses are given in Table 3.4 and 3.5. The zone of influence (1% change) of the 100-900 Orebody pillar was determined. The boundary was deemed far enough if it lies outside the orebody zone of influence. The final boundaries were set 160 m away from the 100-900 OB pillar.

3.3.5 Model Mesh Sensitivity Analysis

The surfaces of the geological units were generated with Rhino 5 (McNeel 2015) The final tetrahedral mesh was generated with Kubrix (Itasca 2016). The required mesh density of the 100-900 Orebody, panel, and external boundary surfaces were determined with a mesh sensitivity analysis, conducted with a simplified pillar model. The density of the mesh around the boundary was increased, forcing Kubrix to generate more zones between the surfaces given a constant mesh grading factor and external boundary mesh density. The tested combinations and results are given in Table 3.6 and illustrated in Figure 3.7.

Table 3.6: Tested combinations of boundary mesh

Model #	Stope Mesh maximum edge length	External Boundary maximum edge length
1	3 m	30 m
2	3 m	18 m
3	1.5 m	18 m
4	1.5 m	15 m

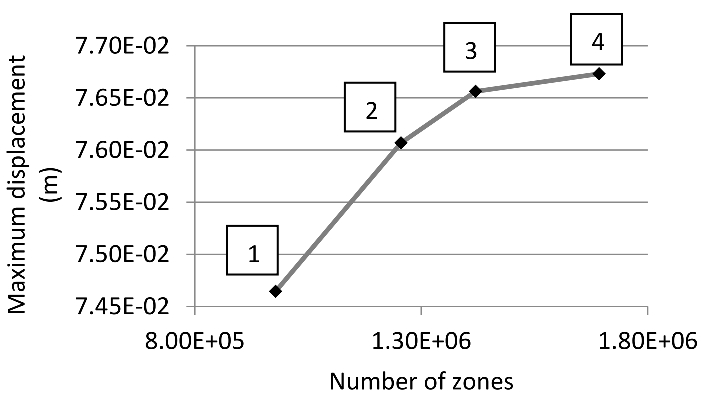

Figure 3.7: Mesh sensitivity analysis with simplified model

A maximum edge length of 1.5 m for the stopes and a maximum edge length of 15 m for the external boundary were therefore selected for the 100-900OB Pillar model. The maximum mesh edge length of the other surfaces was then chosen based on the desired mesh density in the geological units (e.g. the mesh density of the panel surfaces was increased, while the mesh density around previously mined stopes was decreased). Table 3.7 shows the maximum edge length applied to the various surfaces in the model. These parameters yield a 3D numerical model with 4,000,000 zones.

Table 3.7: Applied maximum edge length for each model surface

Kubrix Surface	Maximum Edge Length (m)
Outer boundary	15
Panels	0.75
Stopes	1.5
Mined ore	3
Drifts	3
Trap Dyke	10
Olivine Diabase Dyke	10

3.3.6 Final model geometry

Overall, the 3D model is composed of 4 geological domains: Ore, Host rock, Olivine Diabase Dyke, and Trap Dyke. The ore domain is further split between the previously mined and backfilled stopes and the remaining stopes as shown in Figure 3.8. The mine developments in the footwall between 3880L and 3400L were then extracted. The following sections describe the final geometry of each model feature.

a) Olivine Diabase Dyke and Trap Dyke

The dyke geometry provided by CCM was not modified. Grid point spacing on the dykes was defined in Rhino by setting a maximum triangle edge length when re-meshing the surface triangles.

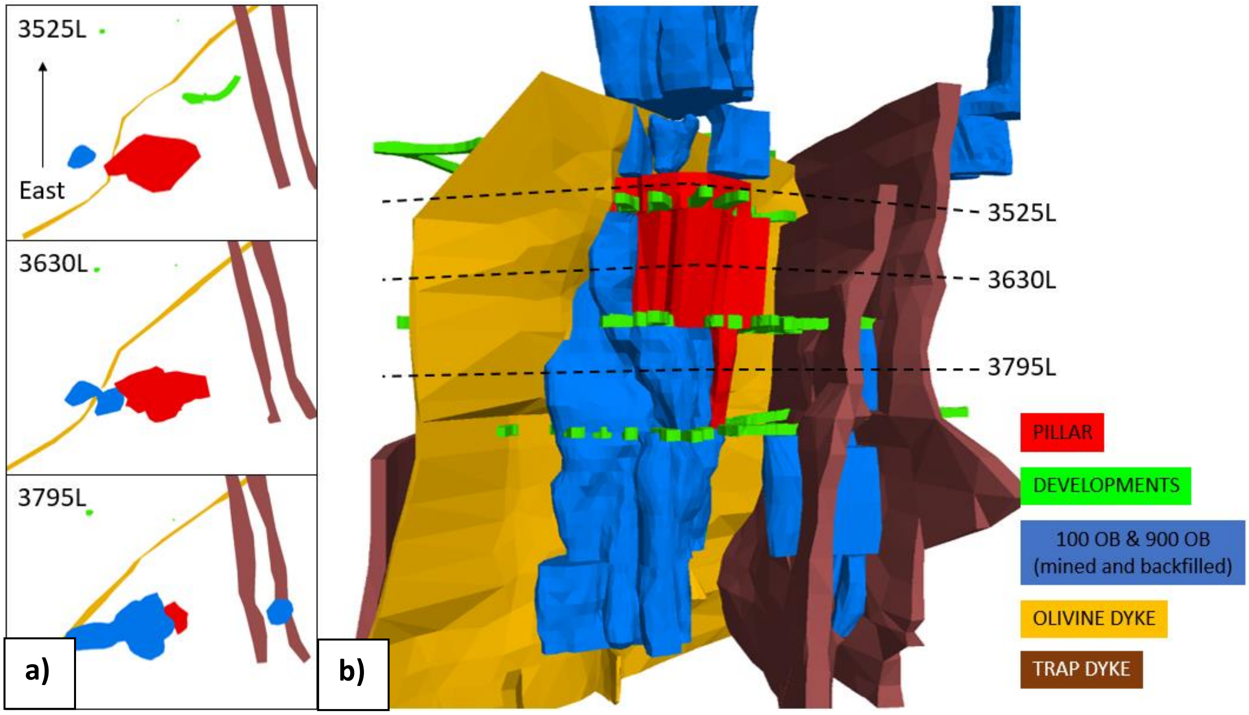

Figure 3.8: Final model geometry for Olivine Diabase Dyke and trap dyke. a) Plan section views of 3525L, 3630L, 3795L. b) Elevation view of 100OB. The Olivine Diabase Dyke intersects the ore pillar and the mined out 100-OB between 3880L and 3500L. The trap Dyke is entirely to the south of 100OB and intersects 900OB.

b) 100-900OB

Stope as-built were provided by CCM for all previously mined stopes in 100OB and 900OB. The as-built surfaces for adjacent stopes were merged and simplified. To achieve this, the combined as-built of all stopes were cut vertically every 10 m, and a simplified polyline was drawn manually at each section outlining all stopes. The drawn sections were then lofted to produce a single “as-built” for all adjoining stopes. The resulting geometry for the mined stopes is shown in Figure 3.9. Grid point spacing on the mined stopes was defined in Rhino by setting a maximum triangle edge length when re-meshing the surface triangles.

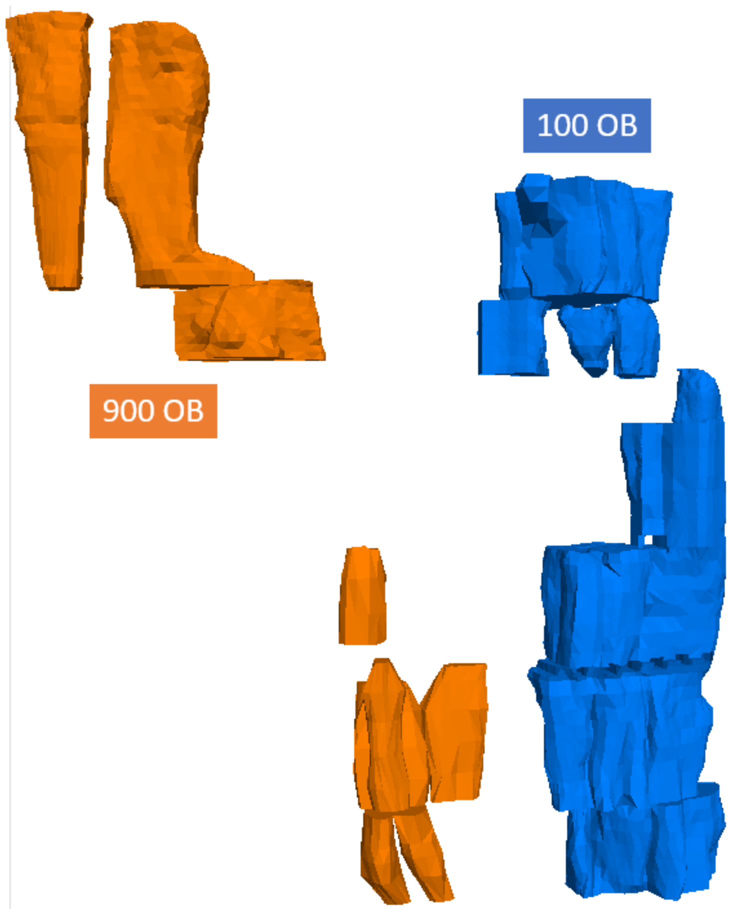

Figure 3.9: Final geometry for mined out stopes in 100OB and 900OB, looking west

c) Stopes

All planned stopes are implemented in the model based on their planned geometries. Stopes mined with upholes from 3550L are referred to as "crown stopes", while stopes mined with the VRM method from 3710L are referred to as sill stopes. A section view of the final stope geometry and their numbering scheme is provided in Figure 3.10. Not shown are two sill stopes (s9511 and s9512) located between 3710L and 3880L.

d) Destress panels

The destress panels were built based on the provided destress blastholes. It is assumed that the destress blasthole damage zone is 16 times the diameter of the hole. With two rows of 100 mm diameter blastholes, this yields a panel thickness of 3 m. The final panel geometries are shown in Figure 3.10.

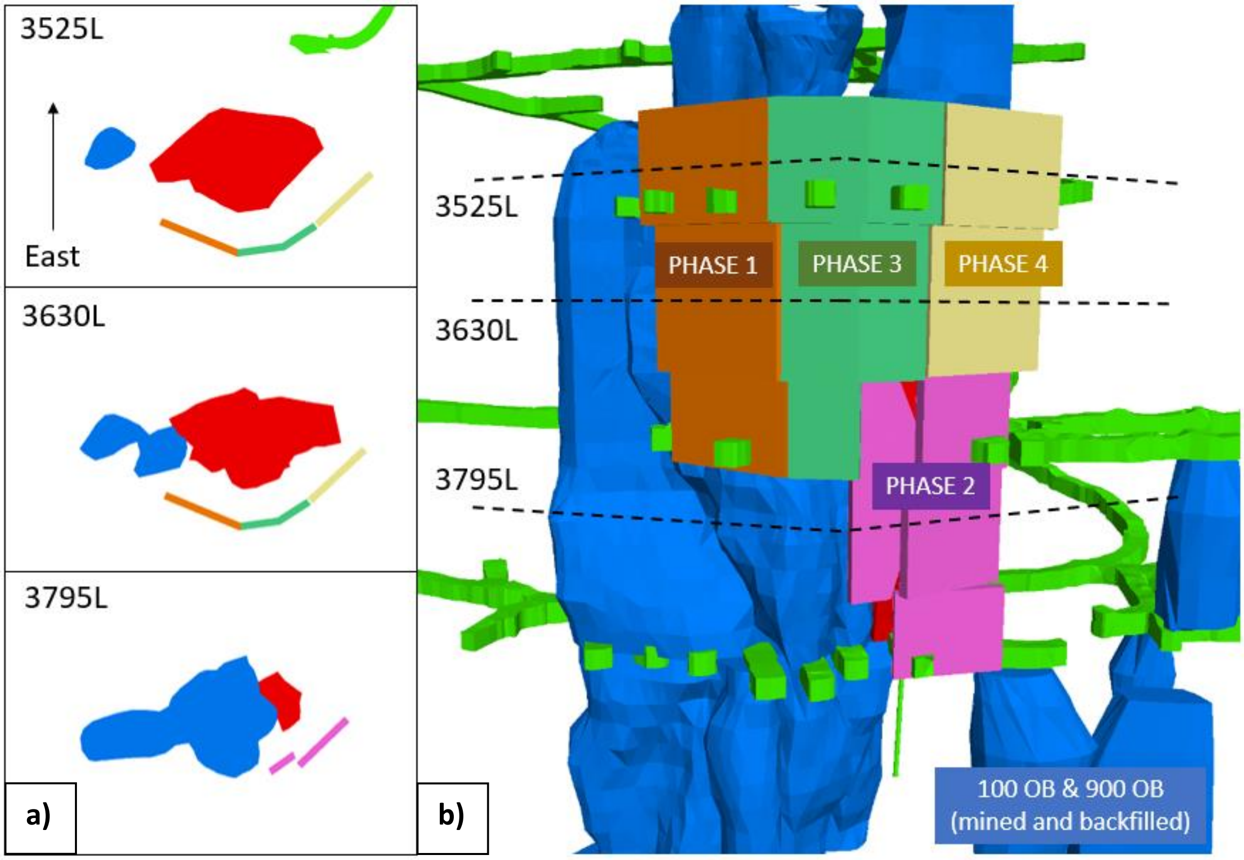

Figure 3.10: Destress panels. Remaining ore (in red) is shielded from high stresses in the E-W direction once all panels are blasted.

d) Drifts

Production levels 3880, 3710, and 3550 are included in the models, with a geometry based on the as-builts provided by CCM. Sill drifts were also built in the model based on the as-built provided in December 2016. No developments constructed after this date are included in the model. The ramp is modelled between levels 3880 and 3500.

3.3.7 Planned stope as-builts

During the extraction of the ore pillar, stope as-built were made available by CCM after the construction of the final model. For Stopes s9631 and c9671, the planned geometry differed from the as-built captured with a Cavity Monitoring System (CMS). New stope as-builts cannot be implemented, as it would require a reconstruction of the entire model at the surface construction stage. Complete node renumbering would be required, making comparison of models based on zone numbering impossible. Therefore, ore pillar stope as-builts are implemented with a loop command which finds all zones in the final model whose centroids are within the CMS as-built. A comparison between the stope as-built for s9631 and the planned geometry is shown in Figure 3.11. This technique was applied to all stopes extracted between the Phase 1 blast and Phase 3 blast.

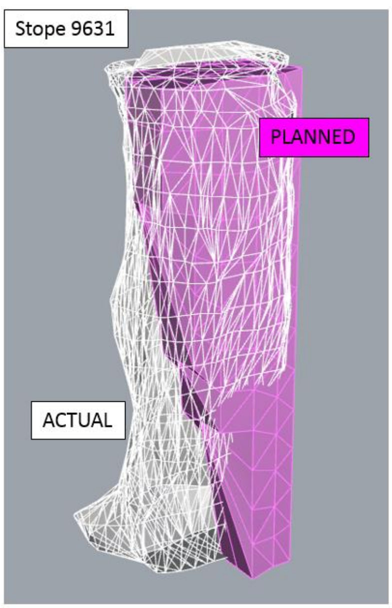

Figure 3.11: Comparison of stope as-built acquired by CMS and the planned stope geometry of s9631.

3.4 Pillar Instrumentation

Eight uniaxial stress cells were installed by CCM in the ore pillar before Phase 1 destress blast and two additional stress cells were installed before the Phase 2 blast, after extracting stope 9631. The stress cells were preloaded with a wedge and platen assembly to approximately 7-8

MPa during the installation. The stress cell measurements were set as initial as soon any stress change was measured. Subsequent readings were then analyzed with reference to the initial reading to determine the changes in stress from that point onwards. The stress cells were installed in vertical holes in the roof and floor of the sill drifts, in the North-South or East-West direction. The orientation of the stress cells and their location is provided in Table 3.8. The position of the uphole and downhole stress cells installed from 3550L are shown in Figures 3.12 and 3.13. SC6 is located in a horizontal hole in 9550 sill, on 3550L. The locations of the uphole cells installed from 3710L are shown in Figure 3.13. The locations of SC9 and SC10 with respect to developments on 3710L are shown in Figure 3.14.

Table 3.8: Uniaxial stress cell locations

#	Name	Direction	Location
SC1	9670-Sill_CN3800_UH-NS	N-S	3550L, Stope 9671, 6 m vertical uphole
SC2	9670-Sill_CN3801_UH-EW	E-W	3550L, Stope 9671, 6 m vertical uphole
SC3	9550-Sill_CN3797_UH-EW	E-W	3550L, Stope 9551, 6 m vertical uphole
SC4	9550-Sill_CN3798_UH-NS	N-S	3550L, Stope 9551, 6 m vertical uphole
SC5	9550-Sill_CN3802_DH-EW	E-W	3550L, Stope 9551, 7.5 m vertical downhole
SC6	9550-Sill_CN3804_WH-NS	N-S	3550L, 9550 Sill, side hole trending West
SC7	9590-Sill_CN3799_UH-EW	E-W	3550L, Stope 9591, 6 m vertical uphole
SC8	9590-Sill_CN3803_DH-EW	E-W	3550L, Stope 9591, 7.5 m vertical downhole
SC9	9400-Sill_CN4187_UH-NS	N-S	3710L, 9400 Sill, 6 m vertical uphole
SC10	9400-Sill_CN4188_UH-EW	E-W	3710L, 9400 Sill, 6 m vertical uphole

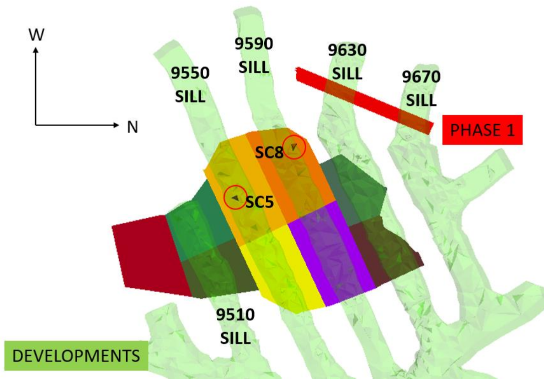

Figure 3.12: Locations of downhole stress cells installed from 3550L with respect to the Phase 1 panels. Downhole cells were installed 6 m below the floor of 3550L.

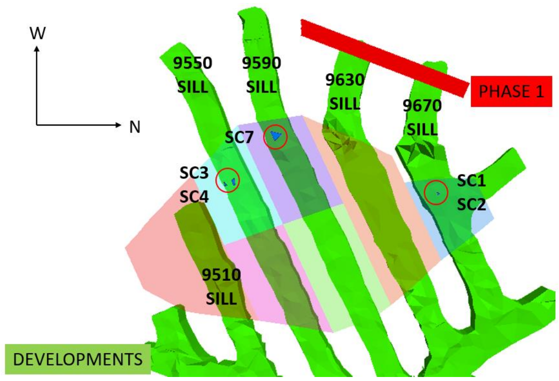

Figure 3.13: Locations of uphole stress cells installed from 3550L with respect to the Phase 1 panels. Uphole stress cells were installed 7.5 m above the roof of the 3550L.

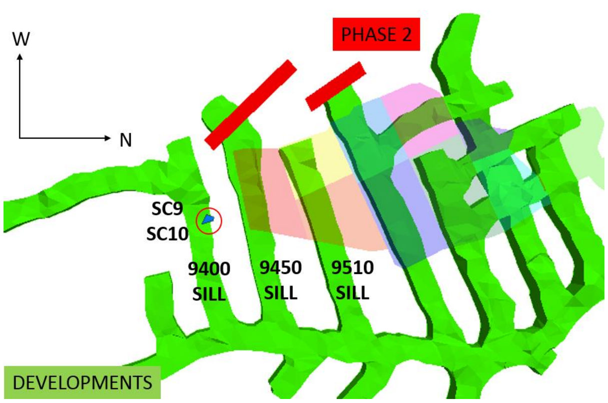

Figure 3.14: Locations of SC9 and SC10 with respect to developments on 3710

Chapter 4: Geomechanical effects of stress shadow created by large-scale destress blasting

Isaac Vennes, Hani Mitri

Department of Mining and Materials Engineering, McGill University, Montreal, H3A 0E8, Canada

Received 30 April 2017; received and revised from 10 August 2017; accepted 11 September 2017

Chapter resume: In this chapter, the journal article "Geomechanical Effects of stress shadow created by large scale Destress Blasting" is presented. The article is a parametric study conducted in Flac3D where a panel destress panel program is implemented in a simplified pillar model. The goal of the parametric study is to verify the back-analysis methodology that will be applied to Copper Cliff Mine (CCM) in Chapters 5 and 6. The Copper Cliff Mine (CCM) pillar wide model used in Chapter 5 and Chapter 6 is linear-elastic, and the validation is based on immediate stress changes measured in the pillar. The reduction of burstability of the ore pillar due to these immediate stress changes is evaluated in the model based on the brittle shear ratio (BSR) and the burst potential index (BPI). The overall goal of Chapter 4 parametric study is therefore to verify if the reported reduction of burstability in the stress shadow from the panel destressing case studies can be related to a reduction of stress in the stress shadow evaluated with the BSR and the BPI.

The stress changes in the stress shadow detected at Brunswick Mine and Fraser Mine are 4.0 MPa and 1.5 MPa respectively in the direction of the major principal stress. The magnitude of stress changes measured in the field following destress blasting are low with respect to the magnitudes of the far field stresses, owing to either the distance between the blast and the location of the sensor or to a low panel destressing effect. The first step of the parametric study is therefore to approximate the destressing effect that provides the same stress changes measured in the Brunswick and Fraser Mine case studies.

With the approximated model input parameters, the BSR in the stress shadow is evaluated over the subsequent mining sequence. The mass of ore where BSR>0.7 is measured and termed "ore at risk". A significant reduction of ore at risk over the pillar mining sequence indicates that the reduced burst proneness in the panel stress shadow can be partially attributed to the immediate decrease of stress in the shadow.

Contribution of authors: All numerical modelling and analysis was conducted by the candidate. The paper is co-authored by Hani Mitri in his capacity as Ph.D. supervisor.

Geomechanical effects of stress shadow created by large-scale destress blasting

Abstract: This study aims to determine if large-scale choked panel destress blasting can provide sufficient beneficial stress reduction in highly-stressed remnant ore pillar that is planned for production. The orebody is divided into 20 stopes over 2 levels, and 2 panels are choke-blasted in the hanging wall to shield the ore pillar by creating a stress shadow around it. A linear elastic model of the mining system is constructed with finite difference code FLAC3D. The effect of destress blasting in the panels is simulated by applying a fragmentation factor (α) to the rock mass stiffness and a stress reduction factor (β) to the current state of stress in the region occupied by the destress panels. As an extreme case, the destress panel is also modeled as a void to obtain the maximum possible beneficial effects of destressing and stress shadow. Four stopes are mined in the stress shadow of the panels in 6 lifts and then backfilled. The effect of destress blasting on the remnant ore pillar is quantified based on stress change and brittle shear ratio (BSR) in the stress shadow zone compared to the base case without destress blasting. To establish realistic rock fragmentation and stress reduction factors, model results are compared to measured stress changes reported for case studies at Fraser and Brunswick mines. A 1.5 MPa immediate stress decrease was observed 20 m away from the panel at Fraser Mine, and a 4 MPa immediate stress decrease was observed 25 m away at Brunswick Mine. Comparable results are obtained from the current model with a rock fragmentation factor α of 0.2 and a stress reduction factor β of 0.8. It is shown that a destress blasting with these parameters reduces the major principal stress in the nearest stopes by 10–25 MPa. This yields an immediate reduction of BSR, which is deemed sufficient to reduce volume of ore at risk in the pillar.

4.1 Introduction

4.1.1. Overview of strainbursts and destress blasting

Rockbursts are seismic events where the rock suddenly and violently fails in a brittle manner after being strained beyond its elastic limit. Brown (1984) categorized rockbursts based on two underlying mechanisms. On one hand, strainbursts are caused by high stress due to the existence of mine openings and the readjustment of stresses due to excavation, with event Richter magnitudes ranging from -0.2 to 3.5 (Ortlepp 1992). On the other hand, fault slip bursts are caused by a violent renewed movement along an existing fault, with Richter magnitudes ranging from 2.5 to 5. Fault slip bursts can be mining induced, where the trigger for the fault slip is stress readjustment along the fault due to mining activities.

The subject of this paper is destress blasting, which is a strainburst control technique. Ortlepp (1992) categorized strainbursts based on their source mechanism, presented in order of event Richter magnitude: superficial spalling (–0.2 to 0), face buckling (0 to 1.5), pillar or face crush (1 to 2.5), and shear rupture through an intact rock mass (2 to 3.5). Contributing factors to the occurrence of strainbursts are high stress, stiff strata, rapid mining rate, and large excavation area. More recently, Sainoki et al. (2016) demonstrated that the fracture network significantly alters the stress state, generating burst prone conditions.

Rockburst risk and rockburst damage can be reduced with the following methods. The first is by reducing the mining rate to limit the energy release associated with each mining step (Mitri et al., 1999). The mining sequence can also be adjusted such that the stress concentration in remnant ore pillars is minimized, or the volume of ore at risk is minimized (Shnohorkian et al. 2015). Afterwards, the damage caused by rockbursts to mine openings can be mitigated with the use of dynamic rock supports, shotcrete, straps, and wire mesh. Finally, in the case where high energy release per mining step is unavoidable, as is the case with deep mining, ground preconditioning techniques such as destress blasting and destress slotting can be used (Mitri, 2001)

When practicing destress blasting, explosives are used to fracture the rock. This lowers the stiffness and releases the stored strain energy in the blasted region. This technique can be directly applied to the rock in the face to be extracted such as in drift development and crown pillar destressing in overhand cut-and-fill mining. It can also be applied in panels near the zone to be mined to create a stress shadow as illustrated in Figure 4.1. The former technique was applied at Galena Mine (Boler and Swanson, 1993), Bloyvooruitzicht Mine (Lightfoot et al., 1996), Western Deep Levels South Mine (Lightfoot et al., 1996), Macassa Mine (Hanson et al., 1987) and Campbell Mine (Makuch et al., 1987) with mixed results. The latter technique was applied in Star

Morning Mine (Karwoski and McLaughin, 1975), Fraser Mine (Andrieux, 2005) and Brunswick Mine (Andrieux et al., 2003; Andrieux, 2005). Section 2 discusses these case studies and their findings.

<u>4.1.2. Review of destress blasting case studies</u>

Destress blasting or preconditioning of ore was applied at Galena Mine (Boler and Swanson, 1993) after the crown pillar decreased to critical height of 10–20 m or once the arrays of microseismic accelerometers detected an increase in seismic activity. A 21 m overhand pillar was directly destressed with 125 kg of explosives across eight 10 m blastholes and three 4 m blastholes. The stress change was monitored with 8 borehole pressure cells in the footwall. The detected stress drop was only in the order of 0.1 MPa and hence was considered as measurement noise. A numerical modeling back analysis concluded that an 80% drop in pillar stiffness would be required to destress the pillar to pre-mining stress levels. Based on the measured stress drops, the stress change in the pillar was deemed insignificant.

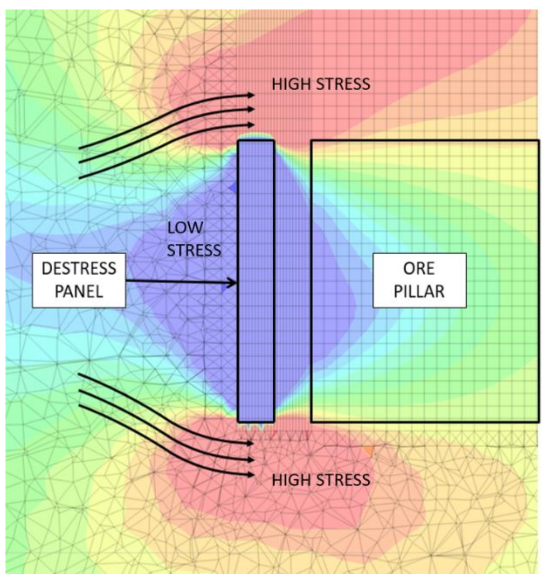

Figure 4.1 Example of a destress panel for the creation of stress shadow in the pillar

At Bloyvooruitzicht Mine (Lightfoot et al., 1996), continuous destressing of the mining face was implemented in the mining cycle with good results. The rock 4 m ahead of the face was pre-conditioned with 10 m-long 76 mm-diameter holes. In this case study, 80% of the blasts had an expected seismic efficiency of 1%–2%, with 2 blasts triggering seismic events of magnitude 2.1. Migration of seismic events away from the pre-conditioned zone indicated a stress transfer away from the mining face. Overall, the face advance rate was increased by 40%; and based on seismic data, the preconditioning program was deemed successful. Western Deep Levels South Mine also employed this technique, with drift convergence data showing an increased rate of in-elastic drift closure near the pre-conditioned face.

At Macassa Mine (Hanson et al., 1987), destress blasting was conducted once the crown pillar attained a critical height of 18 m. The pillar was destressed with a line of destress holes in the mid plane of the pillar. Most post-blast seismicity occurred in the pillar, but convergence monitoring indicated only partial destressing.

Similarly, at Campbell Mine, the 4.5 m crown pillar was destressed with 45 mm holes, spaced 1.4 m over the 45 m stope strike, drilled to within 1.5 m of the overlying drift. The sill pillar above the level was also destressed, with 6 m-long 45 mm-diameter holes, spaced 1.4 m over 25 m. The blast was followed by increased micro-seismicity and rockbursts in the drift and sill pillar itself.

As opposed to direct ore preconditioning, panel destressing consists of blasting relatively large volumes of rock (> 10,000 tonnes) in the hanging wall of the orebody, such that the ore to be mined in bulk lies in the stress shadow of the destress panel. In this case, panel destress blasting aims to reduce the risk of rockbursts by reducing the magnitude of the major principal stress in the ore to be mined. This strategy has been applied to Star Morning Mine (Karwoski and McLaughin, 1975), Brunswick Mine (Andrieux et al., 2003; Andrieux, 2005) and Fraser Mine (Andrieux, 2005). The two latter applications were deemed successful based on recorded stress changes, seismicity, and measured displacements.

A comparison between large-scale (< 10,000 tonnes) direct destressing and panel destressing was conducted at Star Morning Mine (Karwoski and McLaughin, 1975). The sub-vertical, narrow ore vein is mined with overhand cut-and-fill. A destress blasting trial was done in two adjacent stopes, totalling 80 m in length and 24 m in height. For one stope, destress blasting was conducted in the ore, while in the other stope, it was conducted outside the ore (to create a stress shadow). 100

mm-diameter holes were fanned parallel to the orebody from the crosscut to the ore vein, with a toe spacing of 2–3 m. Better results were obtained when destress blasting was conducted inside the ore, based on monitoring of seismic activity during ore extraction.

In the case of Fraser Mine (Andrieux, 2005), a 10,000-tonne choked destress blast was fired on December 24, 2001. The level where the destress blasting took place was exploited with overhand cut-and-fill. Based on numerical modeling, the sill pillar was expected to fail when one or two cuts remained, and the mining rate was slowing due to increased seismic activity as the sill pillar became thinner. The objective of the destress blasting was to fracture the hanging wall and deflect high mining induced stress away from mining activity. The extraction of the next few cuts would therefore be facilitated, nonetheless, with the expectation that global failure of the hanging wall would be accelerated, a choked panel destress blasting was attempted. The panel being destressed was 18 m high, 27.5 m wide, and 3 m thick. The targeted mass was 10,075 tonnes. Two parallel rows of holes were fanned from the drift, and were drilled eastwards and upwards without breakthrough. There were 14 holes per row, with a spacing of 3 m by 3 m. The holes were 114 mm in diameter, and loaded with bulk emulsion. A total of 4.4 tonnes of explosives was used, yielding 2100 J of explosive energy per kilogram of rock. Three uniaxial stress cells were installed, and a sudden decrease of 1.5 MPa in the major principal stress was recorded in the stress shadow, 25 m away from panel. The same stress cell measured a stress decrease of 6 MPa a week later. Permanent deformation was also measured with vertical extensometers, indicating damage in the destressed zone. General conclusions were that the destress blasting was successful, diverting stress away from the next cuts to higher up in the sill pillar

At Brunswick Mine (Andrieux et al., 2003; Andrieux, 2005), at 27,000 tonne choked panel destress blasting was conducted in October 1999. A remnant ore pillar needed destressing as it transferred high stress to a critical mining region. The blast pattern consisted of two rows of 16 parallel holes without free face. The holes had an average charge length of 20 m. The blastholes were 165 mm in diameter to attain the required explosive energy. The blasthole pattern was 2.4 m by 2.4 m. The holes were loaded with a 1.25 g/cc density emulsion corresponding to a total of 17,100 kg of explosives. A sudden 4 MPa stress drop in the direction of the major principal stress was measured 20 m away in the downhole gage, located in the stress shadow. A minor stress increase was detected in the uphole gage, indicating some stress wrapping, consistent with a successful blast. A numerical modeling back analysis was conducted, where the modulus of elasticity of the panel was reduced by 10%–50%. The results did not give sufficient stress change compared to the stress cell measurements. However, a good match was obtained when the destressed rock was fully removed.

The above-mentioned three case studies show that compared to ore preconditioning case studies where destressing was directly applied to the ore, the panel destressing strategy targets a greater mass of rock (> 10,000 tonnes), uses larger holes (> 100 mm), and yields more explosives per targeted mass (800–2100 J/kg).

Also, experience at Fraser Mine and Brunswick Mine show that the magnitude of the sudden and long-term stress decrease in the stress shadow is small in proportion to the mining induced major principal stress. In addition, the Brunswick Mine back analysis results show that the rock fragmentation factor should be lower than 0.5 and close to 0, with the best match obtained when the panel was extracted from the model. This suggests that the simulation of stress dissipation in the destressed panel was not accounted for in the numerical modeling study. Therefore, even if it appears that the destressing effect is at its theoretical maximum, the stress changes observed are still small with respect to the mining induced stresses. This study aims in part to determine if this small stress change is sufficient to reduce the rockburst potential of the ore.

However, the destressing effect of the panel on the ore needs to be replicated in the simplified model. A parametric study is therefore conducted where the rock fragmentation factor (α) and the stress dissipation factor (β) of the panel are varied, and the computed stress changes are compared to the measured stress changes at Fraser and Brunswick Mine. The theory behind these factors is discussed in Sections 4.3 and 4.4.

4.2 Geomechanical effects of destressing

Destress blasting is understood to reduce the stress in the rock by inducing fractures, demonstrated to be along pre-existing fracture planes by the presence of gouge in pre-existing joints (Lightfoot et al., 1996). The induced fracture set is thought to have multiple effects that reduce burst proneness. Firstly, the induced fractures reduce the stiffness of the rock (Blake, 1972) as well as the load bearing ability. Secondly, as the blasting-induced cracks propagate, the stored strain energy is dissipated as seismic energy (Tang and Mitri, 2001), resulting in an instantaneous reduction of stresses in the rock. Finally, destress blasting mobilizes the rock mass along pre-existing fractures, equivalent to plastic strain. As rockbursts are normally associated with brittle elastic rock failure, a destressed zone will yield gradually rather than fail suddenly in the form of rockburst (Saharan and Mitri, 2009). However, when examining the effectiveness of panel destressing with a linear elastic model, the failure mechanism inside the panel is not relevant to the bursting condition of the ore pillar. Therefore, only the former two effects need to be considered in this study.

In addition, Mitri (2001) described that as rock approaches elastic limit, its volume decreases due to the Poisson's effect. This volume reduction stops as the rock fails and its Poisson's ratio increases to 0.5 (in perfect plasticity). The reduction of volume of the blasted rock is therefore implied by the presence of gouge which indicates that plastic failure has occurred. However, micro-cracking in rock due to blasting will dilate the rock, but the net overall effect is still reduction of volume of pre-conditioned rock according to Andrieux et al. (2003) and Lightfoot et al. (1996), who used this as a criterion to assess the success of a destress blasting, both with and without available stress change data. The authors believe that this is still a debatable issue and that to date, there is no conclusive evidence about the volume decrease of the destressed rock.

Finally, the panel will be under higher stress when choked than if it could displace, since dilation of the rock is resisted by the surrounding wall rocks of the panel. However, dilation of panel is not modeled in this study, as the material properties of the panel remain elastic. It is therefore possible that the stresses in the panel are underestimated.

4.3 Simulation of destress blasting

4.3.1 Modeling technique

Multiple techniques have been developed to simulate the effect of destress blasting, starting with the rock fragmentation factor α (Blake, 1972), which reduces the Young's modulus of the rock targeted by the destress blasting. Tang and Mitri (2001) expanded Blake's fragmentation factor by adding the stress dissipation factor β to consider the strain energy that is instantaneously released by the blast as seismic energy and consumed to fracture the rock. Tang (2000) deemed the inclusion of β necessary for considering case studies where α is unrealistically low; whereas a realistic range for α is 0.4 – 0.6, combined with $\beta > 0.4$. Finally, Saharan and Mitri (2009) proposed that α and β should vary differently in the 3 principal stress directions, since blasting-induced fractures tend to propagate in the direction of the major principal stress.

In this study, the technique described by Tang (2000) is applied to the destress panels. Six combinations of α and β are tested, with the assumption that $\alpha + \beta = 1$. The most optimistic combination with the highest rock fragmentation and stress reduction tested is $\alpha = 0$ and $\beta = 1$, which is equivalent to the panel material being extracted. The combination with the lowest stress reduction and rock fragmentation tested is $\alpha = 0.8$ and $\beta = 0.2$. A base case model without destress blasting is also run ($\alpha = 1$, and $\beta = 0$). The parameters α and β are assumed isotropic, i.e. the same in all 3 principal stress directions.

To simulate a destressed panel, the modulus of elasticity is reduced in the panel by the factor α which ranges from 0 to 1:

$$E_{\text{destress}} = E\alpha \qquad [4.1]$$

In addition, the residual stress tensor in the targeted zones is given by the following equation:

$$\{\sigma_D\} = \{1 - \beta\}^T \{\sigma\} \qquad [4.2]$$

where β ranges from 0 to 1, and

$$\{\sigma\}^T = (\sigma_{xx}, \sigma_{yy}, \sigma_{zz}, \sigma_{xy}, \sigma_{yz}, \sigma_{xz}) \quad [4.3]$$

The balanced stress state in the panel prior to destressing is replaced with the residual stress state $\{\sigma_D\}$ defined by Equation 4.2 This removes a portion of the strain energy in the panel proportional to the factor β, causing an imbalance between the model boundary work and strain energy in model. A new equilibrium is reached after solving the model where the final stress tensor in the panel lies between the initial stress tensor and the residual stress tensor.

4.3.2 Panel geometry

The total mass targeted by a destress blasting can be estimated based on the drill hole diameter. With 2 rows of blastholes, and assuming that the damage zone is equal to 16 times the blasthole diameter, the targeted mass M_e can be estimated as (Andrieux, 2005):

$$M_e = 2(16d)HL\rho_r \quad [4.4]$$

where *d* is the blasthole diameter, *H* is the height of the panel, *L* is the strike length of the panel, and ρ_r is the density of the rock. The explosive energy applied in reported destress blasting case studies ranges from 40 J/kg to 2100 J/kg (Andrieux, 2005). Since most applications of destress blasting aim to directly pre-condition the rock to be extracted, the applied explosive energy is low and the drill hole diameter is small: 43–54 mm for Creighton Mine (Oliver et al., 1987; O'Donnell, 1992), 45 mm for Campbell Mine (Makuch et al., 1987), and 35–63.5 mm for Macassa Mine (Hanson et al., 1987).

However, panel destressing case studies all lie on the high end of this range (200 - 500 cal/kg, 1 cal = 4.148 J) with large blasthole diameters ranging from 115 mm for Star Morning mine (Karwoski and McLaughin, 1975) and Fraser Mine (Andrieux, 2005) to 165 mm for Brunswick Mine (Andrieux et al., 2003). According to Equation 4.4, the targeted panel thickness based on the reported blasthole diameters ranges from 3.7 m to 5.3 m. In this study, a 3 m-panel thickness is assumed, equivalent to two rows of 89 mm-diameter blastholes.

4.4 Evaluation of strainburst potential

The first step of the study is to confirm the need for destress blasting. For a linear elastic numerical model, the available criteria are either based on energy or stress state. Multiple methods based on energy calculations have been proposed such as the energy release rate (ERR) (Cook, 1966), and the burst potential index (BPI) (Mitri et al., 1999).

ERR is the kinetic energy released per mining step, calculated based on the energy balance of elastic material. Adding the ERR to the energy storage rate (ESR) increment for the mining step yields the total energy available ($W + U_m$), where W is the increase in potential energy and U_m is the strain energy of the removed material. The ERR is therefore reduced as number of mining steps is increased, reducing the volume of rock removed per mining step and therefore reducing U_m. For destressing, the ERR will also be reduced as a stress decrease in the ore means that the removed strain energy U_m also decreases, reducing the total energy available. However, the ERR alone does not play a role in the rock mass critical strain energy, and therefore cannot evaluate failure, nor the need for destressing.

On the other hand, the BPI considers the critical strain energy and can therefore be used as a criterion to evaluate the need for destressing. It is expressed as (Mitri et al., 1999):

$$BPI = \frac{ESR}{e_c} \qquad [4.5]$$

where ESR is the total strain energy in the rock; and e_c is the elastic strain energy capacity, which is defined as

$$e_c = \int_0^{\varepsilon_{\mathrm{el}}} \sigma d\varepsilon \qquad [4.6]$$

where ε_{el} is the elastic limit strain, and σ is the uniaxial compressive strength (UCS) of rock. However, lacking a failure envelope and with only the UCS available, the calculation of e_c is limited to the uniaxial loading condition. Therefore, Equation 4.5 is only applicable to stope and drift faces and not to the interior of the pillar.

Finally, another criterion for this study is the brittle shear ratio (BSR) (Castro, 1997), which is expressed as

$$BSR = \frac{\sigma_1 - \sigma_3}{UCS_{intact}} \quad [4.7]$$

where σ_1 and σ_3 are the major and minor principal stresses, respectively. The above-mentioned criterion was developed based on a study by Martin and Kaiser (1999), where rock was found to undergo brittle shear as the ratio of the deviatoric stress to the UCS exceeded 0.4, and the risk of strainbursts deemed significant when the ratio exceeded 0.7. Therefore, ore zones in the model with a BSR exceeding 0.7 are termed 'at risk'.

Considering the above-mentioned review, this study uses the BSR as a criterion to evaluate burst prone conditions in the pillar. Furthermore, as the numerical model is capable of modeling sequences, it is possible to calculate the change in BSR due to destress blasting by comparing the values before and after destressing.

4.5 Model construction

4.5.1 Model geometry

Pillar and panel zones are built manually with finite difference numerical modeling software FLAC3D. Host rock and other ore zones that are not in the pillar are generated with KUBRIX (Itasca, 2016). The pillar hanging wall and footwall are vertical. The pillar consists of 20 stopes on 2 levels, with 10 stopes per level. On each level, there are 5 stopes along the orebody strike, 2 across the orebody thickness. The orebody is mined transversally, such that the stope strike length is along the orebody thickness. The stope dimensions are 12 m × 15 m × 30 m (strike length × thickness × height). The destress panel dimensions are 15 m × 3 m × 60 m (orebody strike x thickness × height). The model boundary is set 160 m away from the pillar, such that the pillar extraction causes a stress change smaller than 1% at the boundary. For the mesh sensitivity analysis, the zone size in the pillar is kept constant at 1 m × 1 m × 1 m, while the boundary surface mesh is varied from 8 m × 8 m to 15 m × 15 m. Monotonic convergence of maximum displacement is obtained at 10 m × 10 m boundary mesh (see Figure 4.1). This yields an optimal model with 1,500,000 zones. The panel zones are 0.25 m along the panel thickness, 1 m along the panel strike, and 1 m along the panel height

4.5.2 Model material properties

The numerical model is linear elastic. The elastic material properties are shown in Table 4.1, along with the UCS of the intact rock. The properties are provided by a case study mine.

Table 4.1: Material properties.

Material	Young's modulus (GPa)	Poisson's ratio	Unit weight (MN/m^3)	UCS_{intact} (MPa)
Ore	27.6	0.28	0.037	140
Host rock	37.8	0.24	0.029	150
Backfill	2	0.3	0.024	N/A

4.5.3 Model loading

Pre-mining stresses in the model are calibrated to match the stress-depth relationship used at Copper Cliff Mine Equations 4.8-4.10, yielding a similar stress-depth relationship to that of the Canadian Shield proposed by Herget (1987):

$$\sigma_3 = \sigma_{ZZ} = 0.029z \qquad [4.8]$$

$$\sigma_1 = \sigma_{YY} = 10.825 + 0.032z \qquad [4.9]$$

$$\sigma_2 = \sigma_{XX} = 8.687 + 0.024z \qquad [4.10]$$

where *z* is the depth.

The model external *X*-faces are constrained in the *X*-direction, and external *Y*-faces are constrained in the *Y*-direction. The bottom face is constrained in the *Z*-direction, and the top boundary is free, with applied overburden stress. The far-field stresses in the *X*- and *Y*- directions are initialized in all zones. The initial stresses are the principal stresses with the major principal stress perpendicular to the orebody and panel strike, i.e. in the *Y*-direction.

4.5.4 Mining sequence

To set up the ore pillar shown in Figure 4.2, the orebody is mined from bottom to top in 10 stages, with vertical lifts matching the stope heights, which range from 30 m to 40 m. The ore above the pillar is mined first. After each lift, the void is backfilled. The ore pillar is mined from hanging wall to footwall in the *Y*-direction (see Figure 4.3 and Figure 4.4), and longitudinally in the *X*-direction (see Figure 4.4), starting with bottom level stopes and going upwards in the z-direction. Stopes are numbered from 1 to 10 and suffixed with “L” for lower stopes on the 2000 m level and “U” for upper stopes on the 1940 m level. For the parametric study, 2 panels are destressed simultaneously, and the first 4 stopes shown in Figure 4.2 are mined in the stress shadow. Stopes are mined in the following order: 1L, 2L, 3L, and 1U. Each stope is mined in six 5 m lifts (Table 4.2).

Table 4.2: Pillar mining stages.

Mining stage	Description
1	Initial pillar
2	Destressing of panels 1 and 2
3-8	Extraction of stope 1L
9-14	Extraction of stope 2L
15-20	Extraction of stope 3L
21-26	Extraction of stope 1U

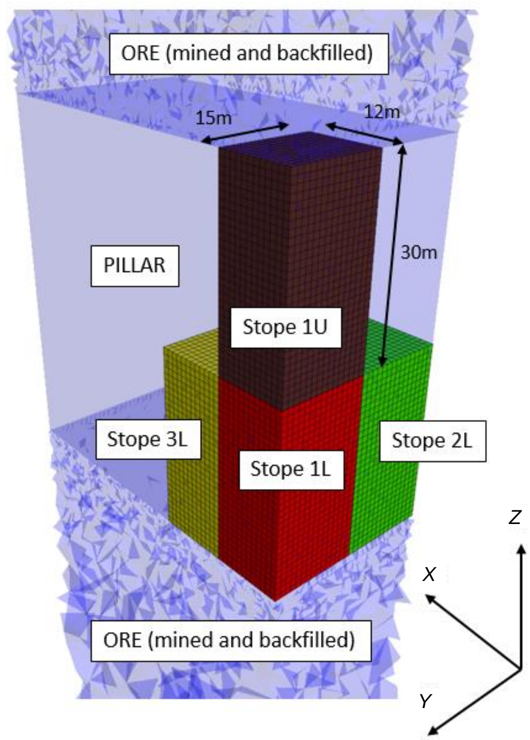

Figure 4.2 Model view of stopes mined.

4.6 Results and discussion

The effect of panel destressing is quantified in terms of the stress drop over the strike of the hanging wall stopes and in terms of ore at risk defined herein as the zones having BSR > 0.7. To begin, the computed stress in the *Y*-direction in pillar is 80 MPa following the extraction of upper and lower orebody representing past mining activities, as shown in Figure 4.5. With an initial pillar BSR due to mining induced stresses at 0.2, there is no immediate need to destress.

However, after the extraction of first 4 stopes, 11.4% of the remaining ore is at risk, equivalent to 36,000 tonnes.

The stress in the *Y*-direction following a destress blasting with a rock fragmentation factor α of 0.1 and a stress dissipation factor β of 0.9 is shown in Figure 4.6. The variation of major principal stress in the stress shadow for varying destress blasting input parameters is shown in Figure 4.7. The stress decrease in proportion to the initial stress in the stope is shown in Figure 4.8.

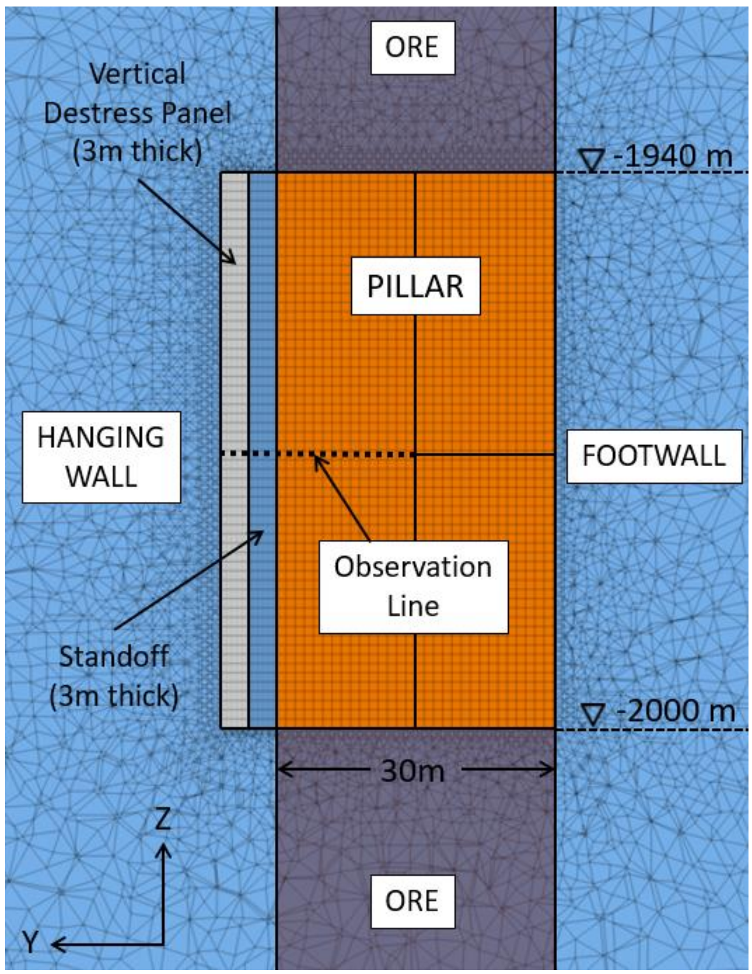

Figure 4.3 Model elevation view along orebody thickness.

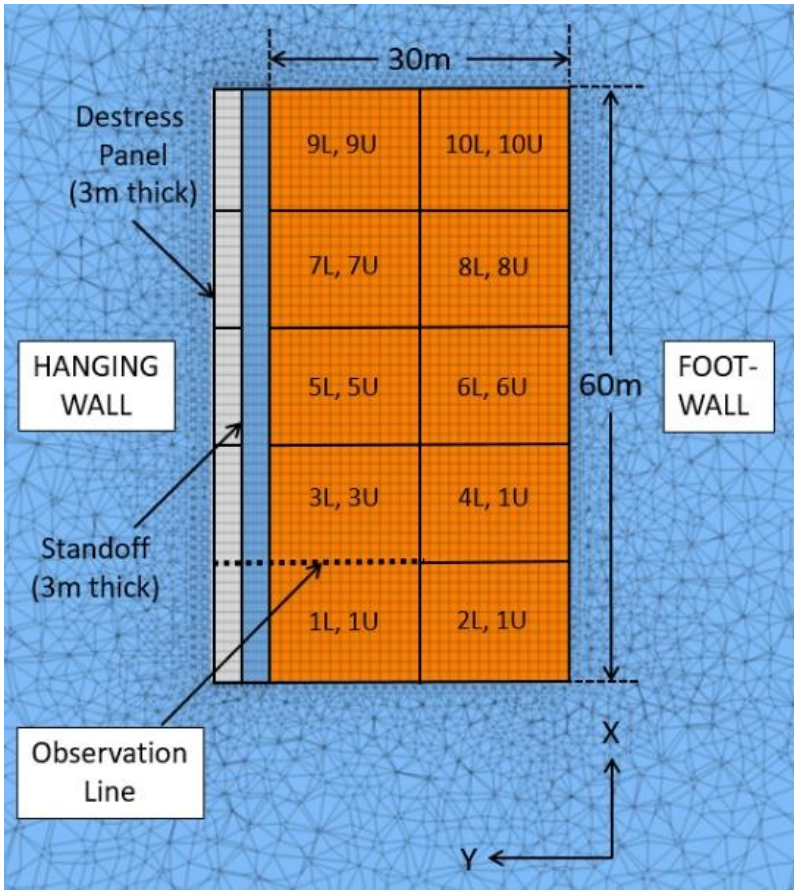

Figure 4.4 Plan view of the modeled ore pillar and destress panel.

For a high rock fragmentation and stress reduction effect ($\alpha = 0.1$, and $\beta = 0.9$), immediate stress drop of 10–25 MPa is obtained in the hanging wall stopes 1L, 1U, 3L and 3U, which represents a 10%–30% stress change. Immediately after the destress blasting, the volume of ore at risk in the stress shadow is reduced by 10%. After extracting 4 stopes in the stress shadow, the destress blasting reduces the volume of ore at risk by 50%, from 16% of the remaining ore in the stress shadow to 8% of the remaining ore in the stress shadow (Figures 4.9 and 4.10). On the other hand, for a low rock fragmentation and stress reduction effect ($\alpha = 0.8$, and $\beta = 0.2$), the resulting stress reduction is below 3 MPa (4% stress change). The destress blasting yields an immediate 2% reduction of ore at risk. After 4 stopes, the destress blasting reduces ore at risk by 5%.

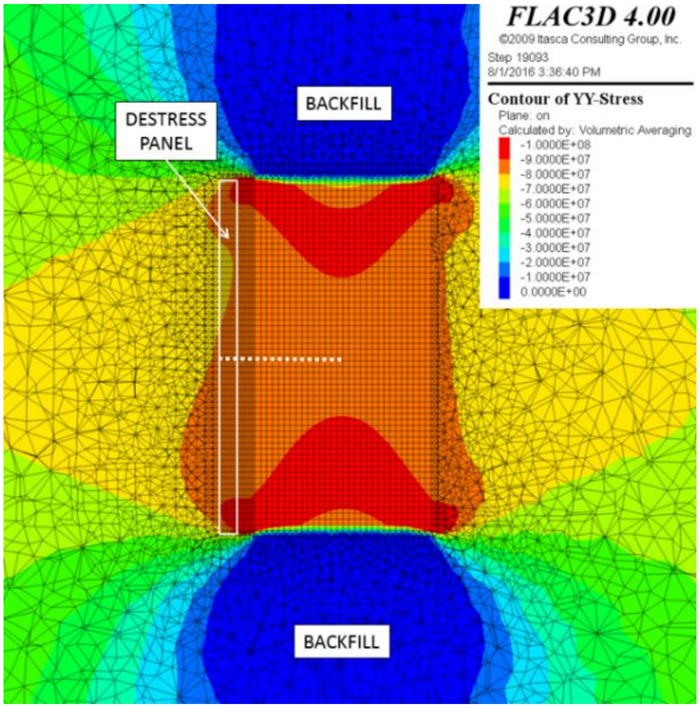

Figure 4.5 Stress state in the pillar before destressing. Stress state taken in plane of observation line shown in Figure 4.4. Stress contour in Pa

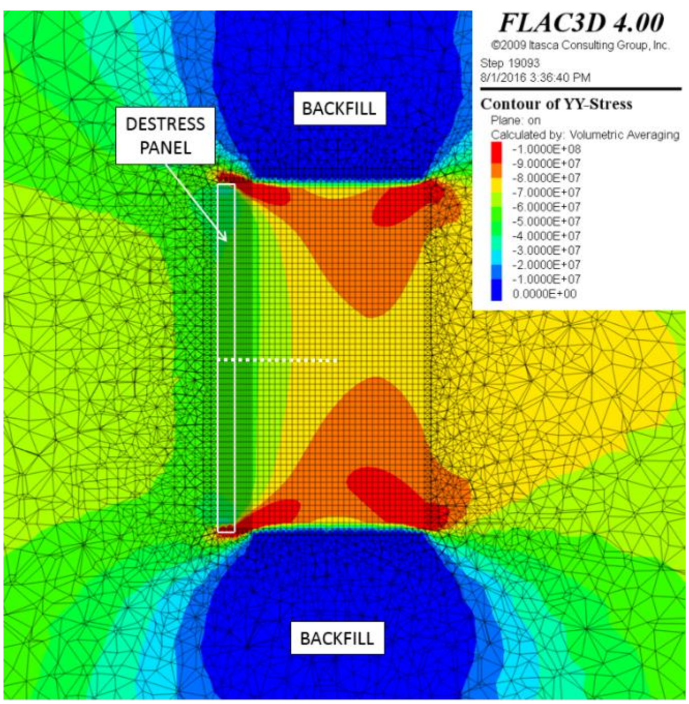

Figure 4.6 Stress state in the pillar after distressing when α = 0.1 and β = 0.9. Section taken in plane of observation line shown in Figure 4.4. Stress contour in Pa.

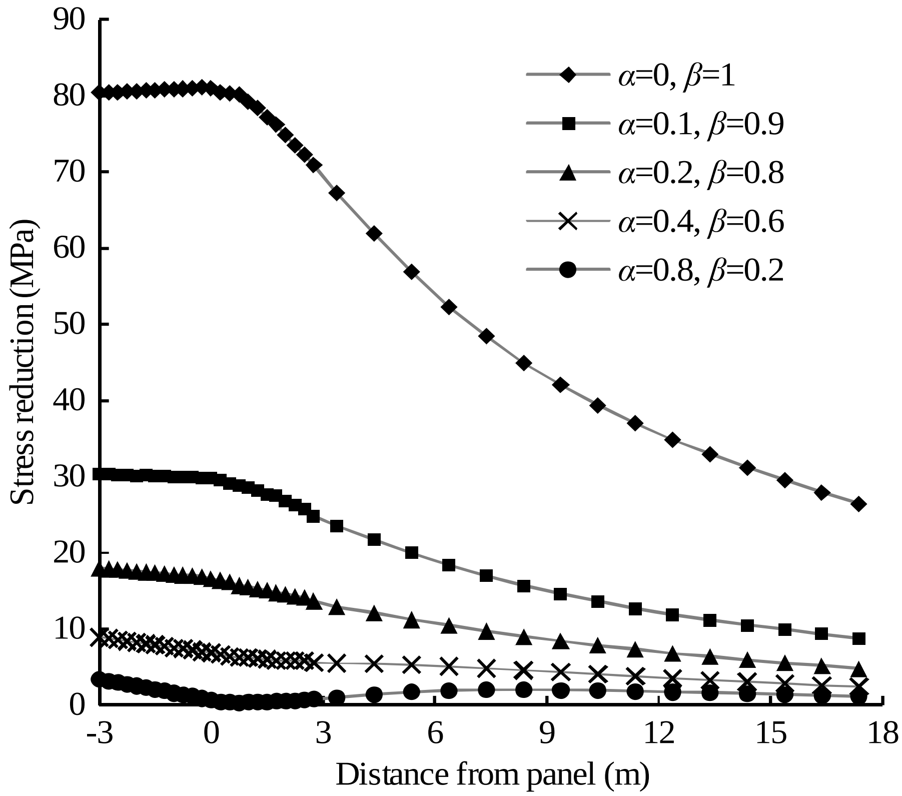

Figure 4.7 *Y*-stress drop due to destress blasting along stope strike.

For all tested destressing parameters, the destressing effect is barely noticeable immediately after the blast with ore at risk method (see Figure 4.11 and 12). Since the bulk of the pillar BSR is well below 0.7, the destress blasting stress reduction in the shadow does not necessarily translate into a reduction of ore at risk. However, once multiple stopes are extracted and the BSR at the stope skin increases, the effect of destress blasting on the ore at risk is more prominent. After the extraction of stopes 1L, 2L, 3L and 1U, the volume of ore at risk is reduced by 50% when α = 0.1 and β = 0.9, equivalent to a mass of 18,000 tonnes of ore. The reduction mostly occurs in stope 3U, as shown in Figures 4.13 and 4.14.

These results can be qualitatively compared to the successful destress blasting case studies of Brunswick and Fraser mines, where a 4 MPa drop at approximately 20 m and a 1.5 MPa drop at approximately 25 m were measured in the direction of the major principal stress immediately after the destress blasting. This suggests that $0.2 < \alpha < 0.4$ and $0.6 < \beta < 0.8$. Applied to the parametric study, these parameters yield an immediate stress drop of 13–5 MPa in the stopes 1L, 3L, 1U and 2U. Over the extraction of the first 4 stopes, the ore at risk is reduced 8%–36% in the stress shadow.

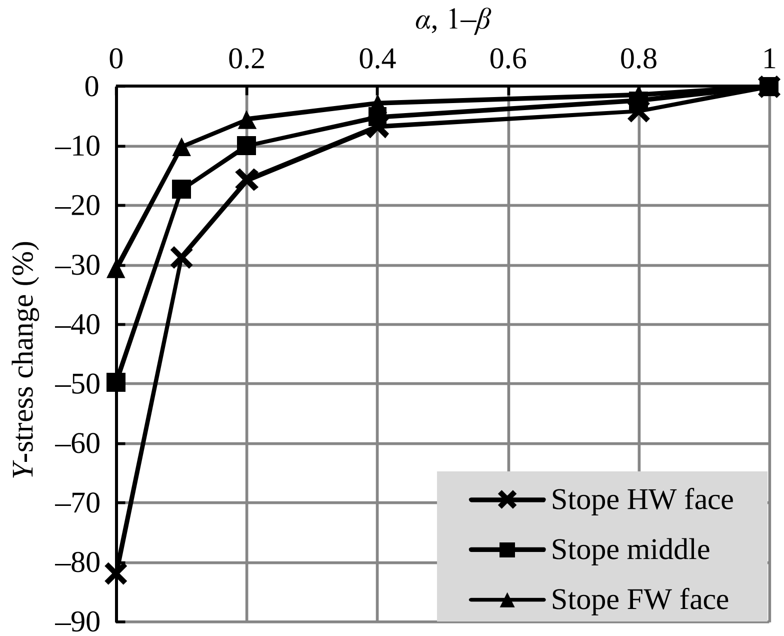

Figure 4.8 *Y*-stress change in hanging wall stope.

Overall, the application of the rock fragmentation factor and stress reduction factor to the destress panels in an elastic model can replicate the immediate stress changes measured in the field. By measuring the volume of ore at risk in the pillar using the BSR criterion, it is shown that the immediate stress change due to destressing has a beneficial effect on the ore to be mined.

However, further validation is required to address the limitations of the elastic analysis. To begin, failure of the pillar and the subsequent stress change are not considered. For example, the stabilized stress change after destress blasting at Brunswick Mine was measured to be 6 MPa 2 weeks after the blast, up from 1.5 MPa immediately after the blast, and plastic deformation of the drifts was noted. At Bloyvooruitzicht Mine, micro-seismic events migrating away from the mining face indicated redistribution; convergence data correlated with the seismic data, whereas seismic events near the stope triggered a higher in-elastic convergence rate. These effects are not captured by the elastic model, and it is not established if long-term post-peak behavior of the pillar in the case of panel destressing is beneficial.

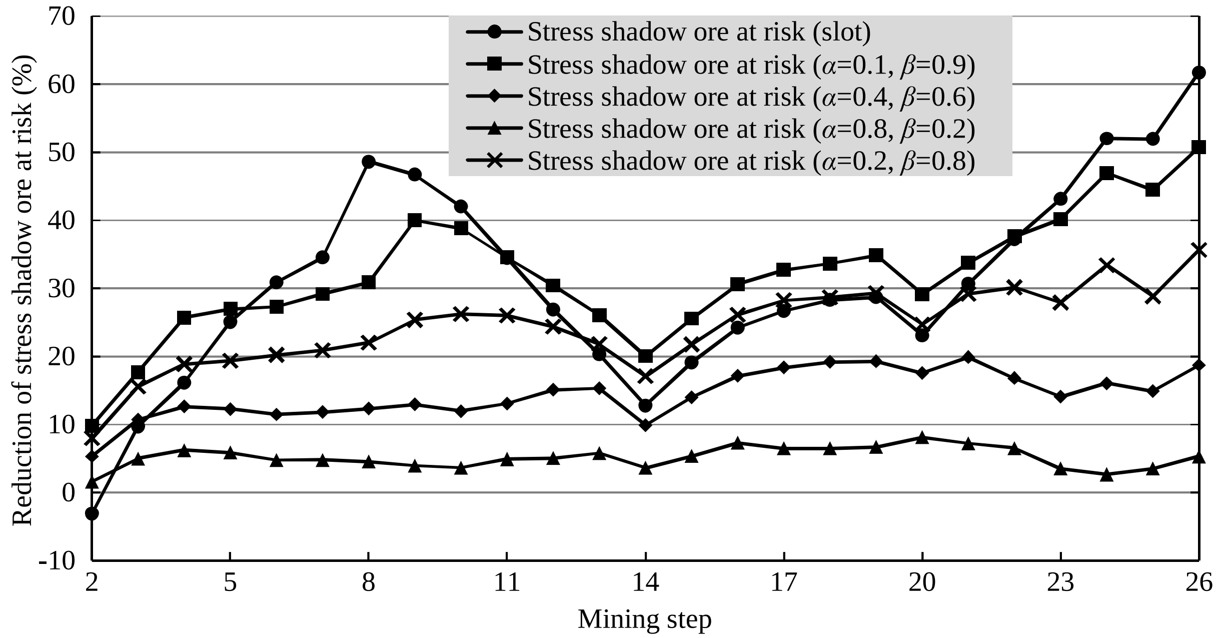

Figure 4.9 Ore at risk reduction in stress shadow with respect to scenario without destress blasting. Mining step descriptions are provided in Table 4.2.

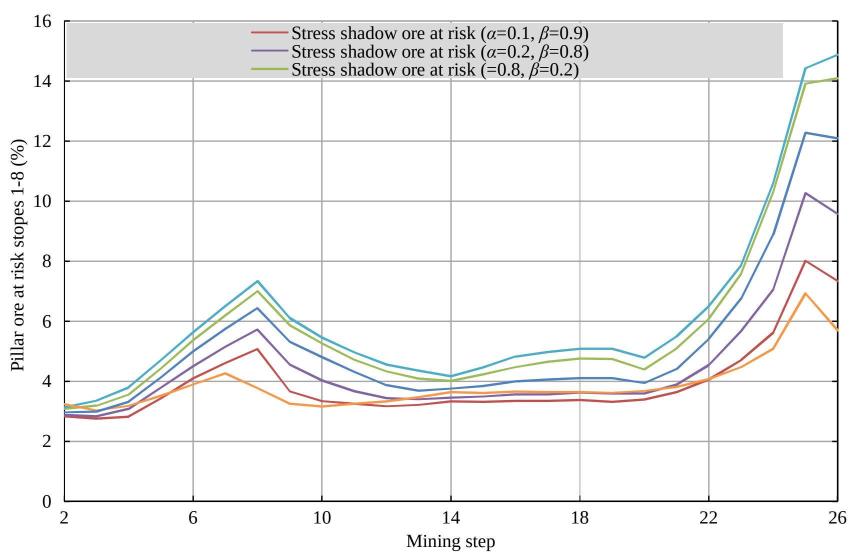

Figure 4.10 Ore at risk in stress shadow. Mining step descriptions are provided in Table 4.2.

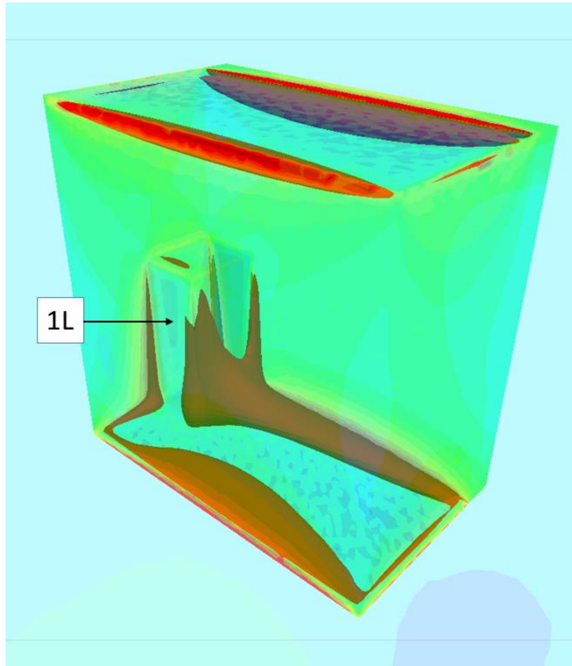

Figure 4.11 BSR shells after extraction of stope 1L. Ore at risk contour (BSR>0.7) in red. High ore at risk in stope 3L.

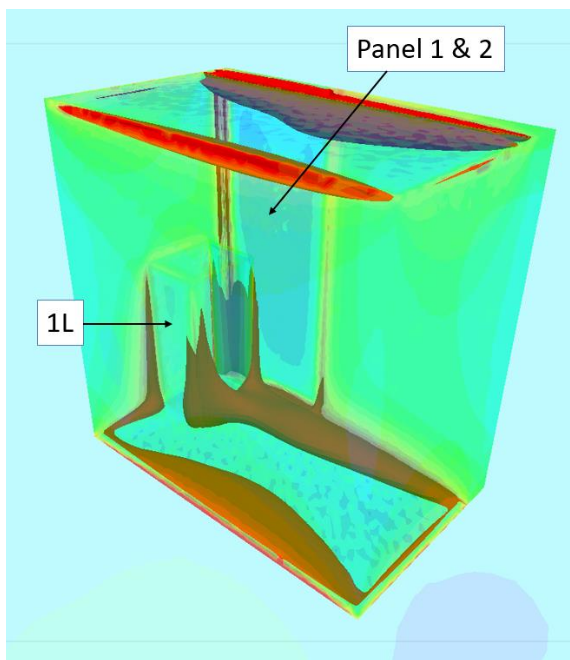

Figure 4.12 Ore at risk after destressing (α = 0.1, and β = 0.9) and extraction of stope 1L. Reduction of ore at risk in stope 3L not apparent.

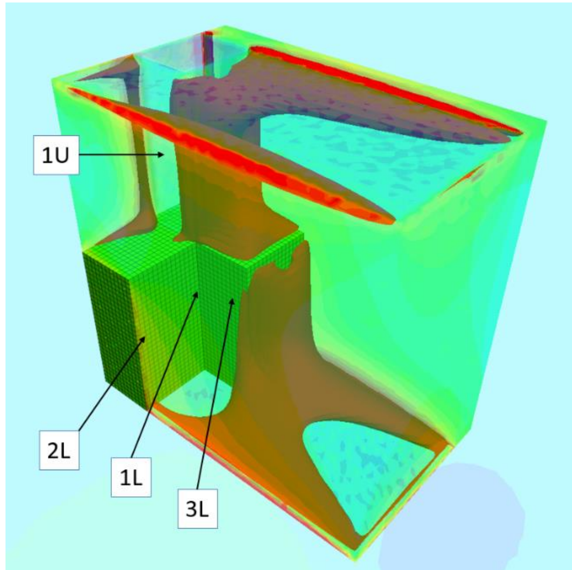

Figure 4.13 Ore at risk in stope 3U without destressing after extraction of stopes 1L, 2L, 3L and 1U.

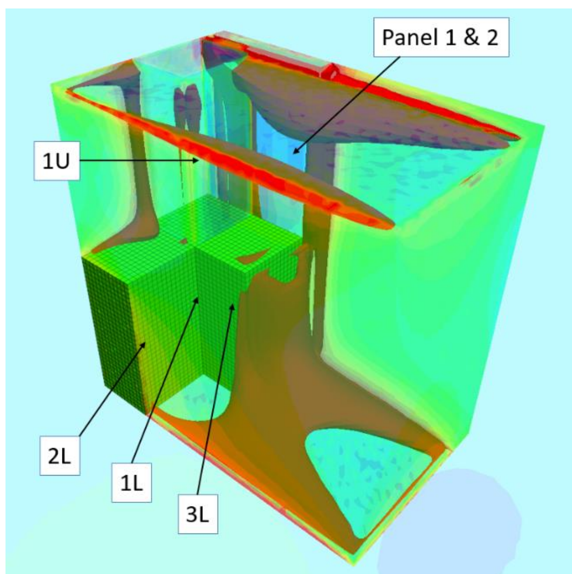

Figure 4.14 Reduced ore at risk in stope 3U after destressing (α = 0.1, and β = 0.9) and extraction of stopes 1L, 2L, 3L and 1U.

Finally, it is assumed in the parametric study that the initial or field stress σ_1 is normal to the destress panel. The effect of the orientation of σ_1 with respect to the destress panel is not investigated herein. Furthermore, the destressed modulus of elasticity and stress release are assumed to be isotropic. According to Saharan and Mitri (2009), the destressed rock mass may not necessarily behave as isotropic and different rock fragmentation factors ought to be used in the post-destress analysis. These results therefore reflect a best-case scenario for a panel destressing program.

4.7 Conclusions

In this study, panel destress blasting is shown to reduce the volume of ore at risk in a highly stressed ore pillar by 8%–36% in the stress shadow, given an obtained rock fragmentation factor below 0.4 and a stress reduction factor above 0.6. These values are realistic when compared to the observed immediate stress changes at Brunswick Mine and Fraser Mine following a panel destress blasting, where 800–2100 J/kg of explosive energy was applied. Panel destressing can therefore be an effective tool to reduce risk to operations when mining the ore pillar in bulk.

4.8 Conflict of interest

The authors wish to confirm that there are no known conflicts of interest associated with this publication and there has been no significant financial support for this work that could have influenced its outcome.

4.9 Acknowledgement

This work is financially supported by a joint grant from MITACS Canada and Vale Canada Ltd. The authors are grateful for their support. The views and opinions expressed in this article are those of the authors and do not necessarily reflect the official position of the supporting organizations.

4.10 References

Andrieux P, Brummer R, Liu Q, Simser B, Mortazavi A. Large-scale panel destress blast at Brunswick mine. CIM Bulletin 2003; 96(1075): 78–87.

Andrieux P. Application of rock engineering systems to large-scale confined destress blasts in underground pillars. PhD Thesis. Laval University; 2005.

Blake W. Rock-burst mechanics. Quarterly of the Colorado School of Mines 1972; 67: 1–64.

Boler FM, Swanson PL. Seismicity and stress changes subsequent to destress blasting at the Galena Mine and implications for stress control strategies. U.S Department of the Interior, Bureau of Mines; 1993.

Brown ET. Rockbursts: Prediction and control. Tunnels & Tunnelling 1984;93: 90-93.

Castro LAM, Grabinsky MW, McCreath DR. Damage initiation through extension fracturing in a moderately jointed brittle shear rock mass. International Journal of Rock Mechanics and Mining Sciences 1997; 34(3–4): 110.e1–110.e3.

Cook NGW. The design of underground excavations. The 8th U.S. Symposium on Rock Mechanics (USRMS). American Institute of Mining, Metallurgical, and Petroleum Engineers Inc.; 1966. p. 167–93.

Hanson D, Quesnel W, Hong R. Destressing a rockburst prone crown pillar: Macassa Mine. Division Report MRL 87-82(TR). Ottawa, Canada: Canmet ENERGY, Natural Resources Canada; 1987.

Herget G. Stress assumptions for underground excavations in the Canadian Shield. International Journal of Rock Mechanics and Mining Sciences & Geomechanics Abstracts 1987; 24(1): 95–7.

Itasca. KUBRIX. Minneapolis, USA: Itasca Consulting Group; 2016.

Karwoski WJ, McLaughin WC. Rock preconditioning to prevent rockbursts - report on a field demonstration. U.S. Department of the Interior, Bureau of Mines; 1975.

Lightfoot N, Kullman DH, Toper AZ, Stewart RD, Gronder M, Rensburg ALJ van, Longmore PJ. Preconditioning to reduce the incidence of face bursts of highly stressed faces. Pretoria, South Africa: Safety in Mines Research Advisory Committee (SIMRAC); 1996.

Makuch A, Neumann M, Hedley DGF, Blake W. Destress blasting at Campbell Red Lake Mine. Report SP 87-8E. CANMET, Elliot Lake Laboratory; 1987.

Martin CD, Kaiser PK, McCreath DR. Hoek-Brown parameters for predicting the depth of brittle failure around tunnels. Canadian Geotechnical Journal 1999; 36: 136-151

Mitri HS. Practitioner's guide to destress blasting in hard rock mines. 2nd edition. Department of Mining and Metallurgical Engineering, McGill University; 2001.

Mitri HS, Tang B, Simon R. FE modelling of mining-induced energy release and storage rates. Transactions of South African Institute of Mining and Metallurgy 1999; 99(2): 103–10.

O'Donnell JDP. The use of destress blasting at Inco's Creighton Mine. In: MASSMIN 92. Johannesburg: SAIMM; 1992. p. 71–4.

Oliver P, Wiles T, MacDonald P, O'Donnel D. Rockburst control measures at Inco's Creighton Mine. In: Proceedings of the 6th Conference on Ground Control in Mining, West Virginia, 1987.

Ortlepp WD. Invited lecture: The design of support for the containment of rockburst damage in tunnels – an engineering approach. In: Kaiser PK, McCreath DR, editors. Proceedings of the International Symposium on Rock Support. A.A. Balkema; 1992. p. 593–609.

Saharan MR, Mitri HS. Simulations for rock fracturing by destress blasting, as applied to hard rock mining conditions. Saarbrucken, Germany: VDM Verlag; 2009.

Sainoki A, Mitri HS, Yao M, Chinnasane D. Discontinuum modelling approach for stress analysis at a seismic source: Case study. Rock Mechanics and Rock Engineering 2016; 49(12): 4749–65.

Shnorhokian S, Mitri HS, Moreau-Verlaan L. Stability assessment of stope sequence scenarios in a diminishing ore pillar. International Journal of Rock Mechanics and Mining Sciences 2015; 74: 103–18.

Tang B. Rockburst control using destress blasting. PhD Thesis. McGill University; 2000.

Tang B, Mitri HS. Numerical modelling of rock preconditioning by destress blasting. Proceedings of the Institution of Civil Engineers – Ground Improvement 2001; 5(2): 57–67.

Chapter 5: Large scale destress blasting for seismicity control in hard rock mines – A case study

Isaac Vennes[a], Hani Mitri[a], Damodara Reddy Chinnasane[b], Mike Yao[b]

a) Department of Mining and Materials Engineering, McGill University, Montreal, Canada

b) Copper Cliff Mine, Vale Canada Ltd, Sudbury, Canada

Submitted to IJMST and under Revision as of April 24, 2019

Chapter resume: In this chapter, the journal article "Large scale destress blasting for seismicity control on hard rock mines – A case study" is presented. The journal article covers the back analysis of the "Phase 1" destress blast at Copper Cliff Mine (CCM), which is the first of 4 destress blasts that are planned to destress the 100OB diminishing pillar. The article starts with a review of available large scale strategic destress blasting case studies. The review shows that panel destressing applied in steeply dipping metal mines aims to directly reduce the stress magnitudes in the stress shadow, while strategic destressing applied in deep longwall coal mines aims to reduce the rigidity of overlying strata. The methodology based on stress changes presented in Chapter 4 is therefore applicable to the CCM large-scale panel destressing case study.

Then, the back analysis of the CCM panel destressing program is conducted with a pillar wide numerical model in Flac3D, where the holistic constitutive model proposed by Tang and Mitri (2001) is applied to the Phase 1 panel. The theory behind the constitutive model is discussed in Chapter 2. The numerical model geometry, loading, and material properties are presented in Chapter 3. The methodology presented in Chapter 4 is adopted and expanded; In chapter 4, the most valid input parameters range is approximated based on other panel destressing case studies, while in Chapter 5, stress change data is available enabling a more rigorous back analysis.

The first step of the analysis is to find the destress blast model input parameters that provide the best match with the measured stress change data from the field, keeping the panel thickness constant. It is demonstrated in Appendix 4 that changing the input parameters in the panel provides the same stress change effect as varying the panel thickness. Therefore, only the constitutive model input parameters need to be varied, and an underestimation of the targeted mass is compensated for by reducing the rock fragmentation factor. The most conforming combination of α and β is found by measuring the distance between the computed stress change contours and the position of the stress cells. With the validated input parameters, the second step of study is to determine if the computed stress shadow in the model significantly decreases the brittle shear ratio (BSR) or the burst potential index (BPI) of the stress shadow stopes. The chapter covers the burst proneness of the pillar over the extraction of the first stope mined after Phase 1. The burst proneness results over the entire mining sequence is provided in Appendix 3.

Contribution of authors: All numerical modelling and analysis were conducted by the candidate. The paper is co-authored by Hani Mitri in his capacity as Ph.D. supervisor, and by Mike Yao in his capacity as industry supervisor representing Vale. Instrumentation at the mine site was installed by Reddy Damodara Chinnasane, who then collected and prepared the data.

Large scale destress blasting for seismicity control in hard rock mines – A case study

Abstract: Destress blasting is a rockburst control technique where highly stressed rock is blasted to reduce the local stress and stiffness of the rock, thereby reducing its burst proneness. The technique is commonly practiced in deep hard rock mines in burst prone developments, as well as in sill or crown pillars which become burst-prone as the orebody is extracted. Large-scale destressing is a variant of destress blasting where panels are created parallel to the orebody strike with a longhole, fanning blast pattern from cross cut drifts situated in the host rock. The aim of panel destressing is to reduce the stress concentration in the ore blocks or pillars to be mined. This paper focuses on the large-scale destress blasting program conducted at Vale's Copper Cliff Mine (CCM) in Ontario, Canada. The merits of panel destressing are examined through field measurements of mining induced stress changes in the pillar. The destressing mechanism is simulated with a rock fragmentation factor (α) and stress dissipation factor (β). A 3-dimensional model is built and validated with measured induced stress changes. It is shown that the best correlation between the numerical model and field measurements is obtained when the combination of α and β indicates that the blast causes high fragmentation (α =0.05) and high stress release (β =0.95) in the destress panel. It is demonstrated that the burst proneness of the ore blocks in the panel stress shadow is reduced in terms of the brittle shear ratio (BSR) and the burst potential index (BPI).

5.1 Introduction

In the past 20 years, large-scale destressing has been applied successfully in both coal and hard rock mines. A review of the few available case studies of large scale destress blasting is made in the following section. While in principle all destress blasting programs aim to reduce the potential of rockburst, its application is primarily one of two types, namely rigid roof destressing for stiffness reduction of the overlying strata in longwall coal mining, and panel destressing in hard rock mines for stress reduction in the ore pillars to be mined.

A feature of a rockburst prone coal mine is the proximity of the working face to thick and rigid host rock stratum (Brauner 1994, Konicek et al. 2011), where abrupt caving of stiff overlying strata could result in dynamic loading of the mine, posing a serious threat to the safety of the working face. Instances where this rockburst mechanism is found is in retreat longwall mining at the Lazy Colliery in the Czech Republic (Konicek et al. 2013)(Konicek and Waclawik 2018), and retreat room and pillar during pillar recovery (Singh et al. 2011) where it is necessary to fracture the roof periodically as the coal mining face advances. Reduction of stress at the face itself is not explicitly sought. The depth of the Lazy Colliery is 700 m, with coal seams that are 3.1 to 5 m thick. The longwall face is prone to rockbursting as it tends to accumulate high strain energy due to a stiff massive sandstone roof. The goal of the destressing program is therefore to reduce the strength and massiveness of the roof strata by creating a network of fissures. The destress horizon is targeted with long boreholes that are drilled from the gate roads. The entire length of a panel is destressed in roughly 20 stages averaging 5 drill holes per stage. The seismic effect parameter developed by Konicek et al. (2013) is the primary means of evaluating the effectiveness of a destressing stage, with most blasts yielding at least a very good seismic effect. Based on stress change measurements from compact conical ended borehole monitoring (CCBM) probes, the range of influence of the site is measured to have decreased, demonstrating that the competency of the overlying strata was reduced by blasting. The longwall panel was extracted without any further rockbursts following the destress blasting program. A variation of the Lazy Mine destressing technique was applied in the Polish part of the Upper Silesian Coal Basin, referred to as torpedo blasting (Wojtecki et al. 2017). In contrast to the Lazy Mine, the charge per stage is much lower ranging from 288 kg to 576 kg due to the lower charge length. Based on the seismic effect, most stages provided at least a very good destressing effect.

Panel destressing practice in hard rock mines is exemplified by 2 Canadian case studies. For these mines, the relative stiffness of the ore and host rock is not necessarily a major factor, and the purpose of destressing is primarily to create a stress shadow that shields the ore to be mined from high stress. At Fraser Mine (Andrieux 2005), the objective of the destress blast was to directly reduce stress in the ore sill pillar being mined out. The extraction of the subsequent cuts was therefore facilitated, but with the expectation that global violent failure of the sill pillar would be accelerated. To create a destress panel, two rows of 14 blast holes were fanned from a cross cut drift, yielding a 10,000 tonne panel with an average explosive energy of 385 cal/kg of targeted mass. The blast took place in December 2001, and vibrating wire stress cells recorded a horizontal stress decrease perpendicular to the panel, and a vertical stress increase in the stress shadow. Similarly, a large scale (27,000 tonne mass), choked, panel destress blast was conducted at Brunswick mine in October 1999 (Andrieux 2005, Andrieux et al. 2003). The blast pattern consisted of two parallel rows of 16 holes drilled pillar, with no free face. The blast pattern yielded an explosive energy per kilogram of targeted mass of 200 cal/kg. A stress drop was detected by the downhole gauge in the stress shadow, and a minor stress increase was detected in the uphole gauge. In both above-mentioned case studies, the measured stress changes indicated stress wrapping around the panel.

Overall, the Lazy Colliery case study demonstrates a successful destress blasting program where the goal is to fracture stiff overlying strata to facilitate its caving. A lower density of explosives is required compared to the Canadian case studies. The explicit goal of the blasts was not to reduce the major principal stress at face since the global failure of the roof is expected to occur as the mining face advances. The purpose is rather to reduce the dynamic effect of caving when it inevitably occurs. On the other hand, for the Canadian case studies, stress decrease was the explicit goal. Accelerated failure of the hanging wall was not an objective of the program but rather an accepted consequence of destress blasting. The blasts were choked as well, but with much higher explosive energy density. In the case of Fraser Mine, the numerical modelling back analysis where the panel material was simulated as a cavity (after destressing) conformed the most with in-situ measured stress cell changes, indicating that high displacement of panel material contributed to the high stress release.

The blast parameters of the case studies presented above are summarized in Table 5.1. The focus of this paper is Copper Cliff Mine (CCM), whose destress blasting program follows the philosophy of Fraser and Brunswick Mine destress blasts. Details of the destressing program at CCM will be presented in section 2. The merits of destress blasting are examined through field measurements from uniaxial stress cells installed in the ore pillar, seismic data, and a mine-wide 3D numerical model of the destress panel and remnant pillars. The destressed zones in the model are simulated with the rock fragmentation factor, α, and the stress reduction factor, β. The model is validated based on the stress cell field measurements and the best conformity between the models and the stress cell measurement.

Table 5.1: Large scale destress blast parameters

	Blasthole Φ (mm)	Toe spacing (m)	Average length (m)	Average charge length (m)	Charge per Delay (kg)	Pattern
Lazy Colliery (Konicek et al. 2013)	75	10	40-100	26-75	1550-3450	Single row, along strike of gate road, 12^{o}-37^{o} dip.
Lazy Colliery (Konicek and Waclawik 2018)	93	10	47-100	19-80	700-3100	Single row, along strike of gate road, 4^{o}-35^{o} dip.
Polish USCB (Wojtecki et al. 2017)	76	6	45	15	288-576	Single row along strike of gate road, 45^{o} dip
Fraser Mine (Andrieux 2005)	114	3	23	13	473 (maximum)	28 holes in 2 rows, fanned from drift perpendicular to orebody strike
Brunswick Mine (Andrieux et al. 2003)	165	2.4	27	20	607 (maximum)	32 holes in 2 rows, along strike of drift parallel to orebody strike, 45^{o} downwards

5.2 Case Study Mine

The case study mine is Copper Cliff Mine (CCM), located in Copper Cliff near Sudbury, Ontario, Canada. The mining method employed is longhole open stoping with Vertical Retreat Mining (VRM). The orebody of interest, 100 OB, is pipe-shaped and nearly vertical, extending 1200 m vertically and 150 m horizontally. The ore consists of inclusions of massive to disseminated sulphide mineralization, while the massive quartz diorite host rock is composed of amphibole, biotite, and chlorite. Two geological structures are present near the orebody: a strongly sheared olivine diabase dyke and a stiff quartz diabase dyke. Ore below 3880L was mined out in a bottom-up, center out sequence, ending in March 2009. Ore above 3500L was mined in the same sequence, with the last stope mined in October 2009, leaving a remnant pillar between 3880L and 3500L under high mining induced stress (Figure 5.1).

Based on a separate numerical modelling study, it was determined that the proper sequence to reduce stress in the remnant ore is a North-South retreat from the Olivine Diabase Dyke, alternating between the sill stopes and crown stopes. Nonetheless, the rockburst potential of the sill pillar was still known to be high based on computed mining induced stresses and increased seismic activity being experienced. A dynamic support system has been widely implemented in all active mining areas and rockburst control techniques were explored.

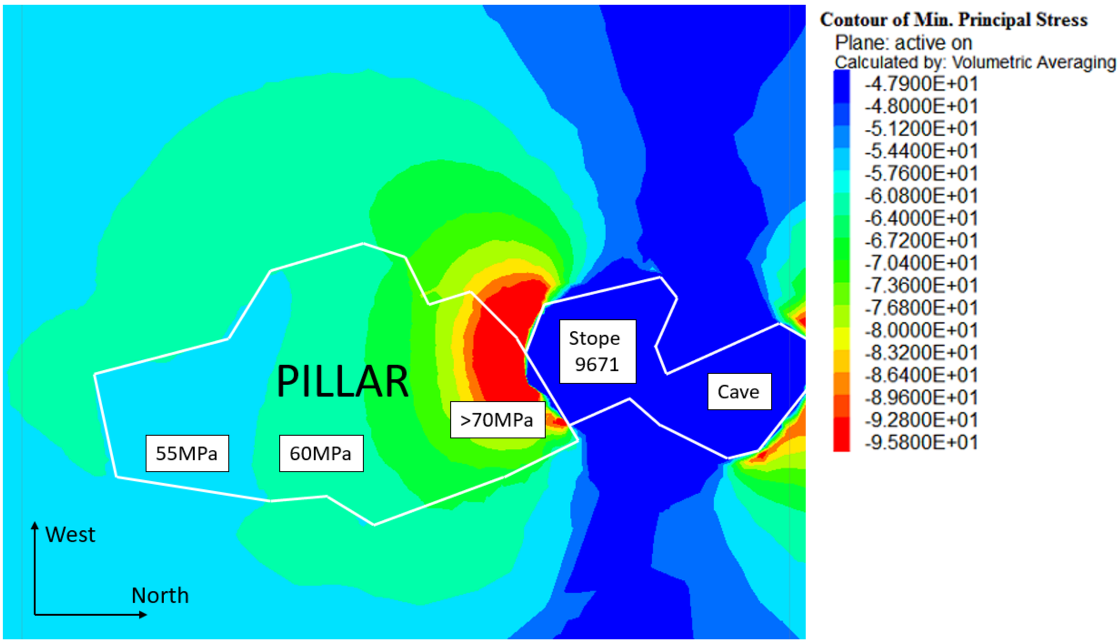

Figure 5.1: Mining induced stress in the 100OB pillar (outlined in white) in November 2014, before destressing is implemented. Contours are in MPa. In red are zones with a computed stress greater than 95 MPa.

The ore pillar is composed of 18 stopes between 3880L and 3500L. There are 11 “sill stopes” between 3550L and 3880L, and 7 “crown stopes” between 3550L and 3500L. The sill stopes are mined with the VRM method, while the crown stopes are mined with upholes from 3550L. The drilling horizon for the sill stopes is 3550L and muck is drawn from 3710L. For the crown stopes, the stope is mucked and drilled from 3550L (Figure 5.2).

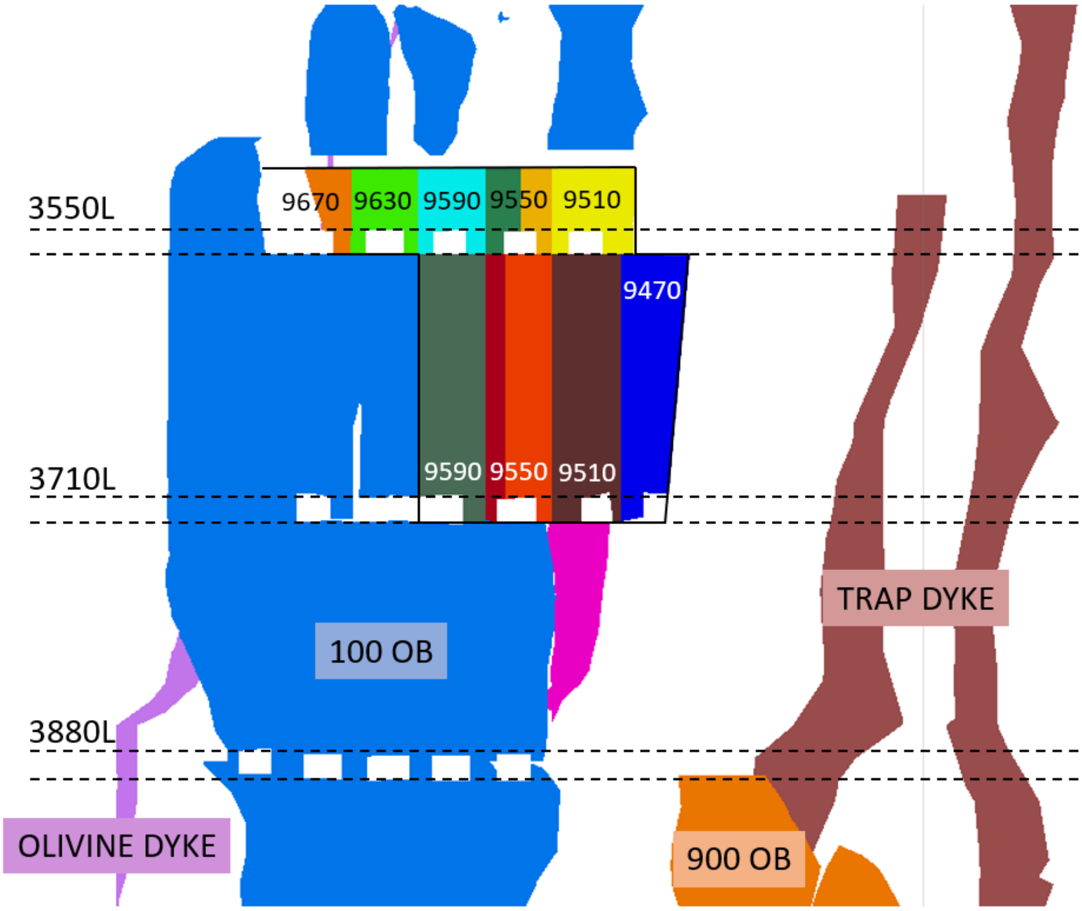

Figure 5.2: Section view of the remnant pillar before destressing

To drive stress away from active stopes in the pillar, a panel destressing program is implemented in 4 phases (Figure 5.3). The panels are drilled and blasted from extensions of the stope cross-cuts that drive across the orebody into the hanging wall. The overall extraction sequence of the pillar, including the destressing phases, is provided in Table 5.2. The stope nomenclature is explained in Figure 5.4. The scope of this paper is the Phase 1 panels that were blasted on September 21, 2015, and the extraction of stope 9631 that took place from October 2016 to January 2017. A plan view of the Phase 1 blast with respect to stope 9631 is shown in Figure 5.5.

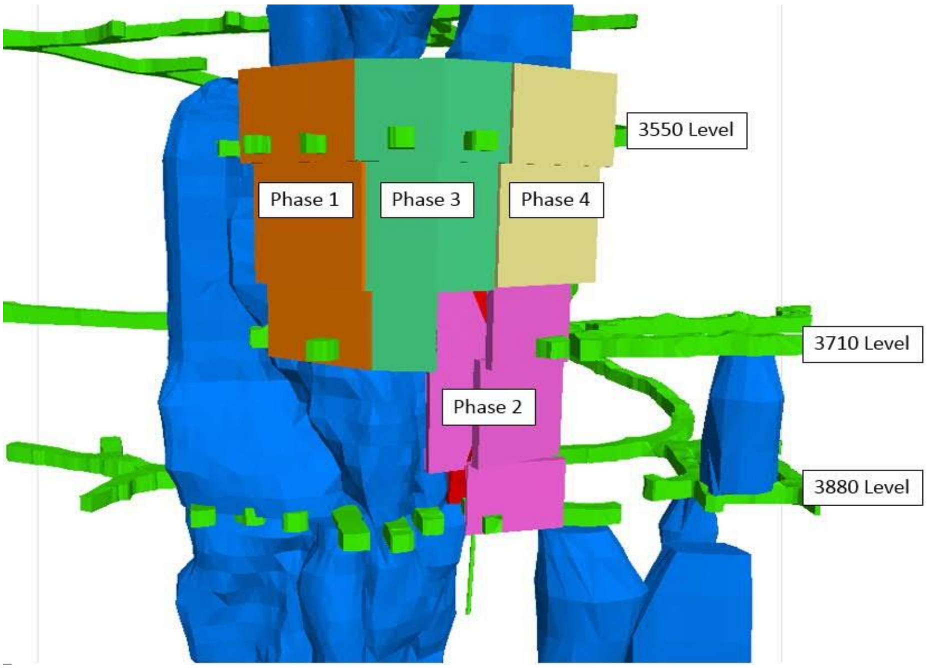

Figure 5.3: Planned destress panels at CCM, looking East. Mined and backfilled stopes are shown in blue, mine developments are shown in green. Planned stopes in red are completely shielded by the destress panels.

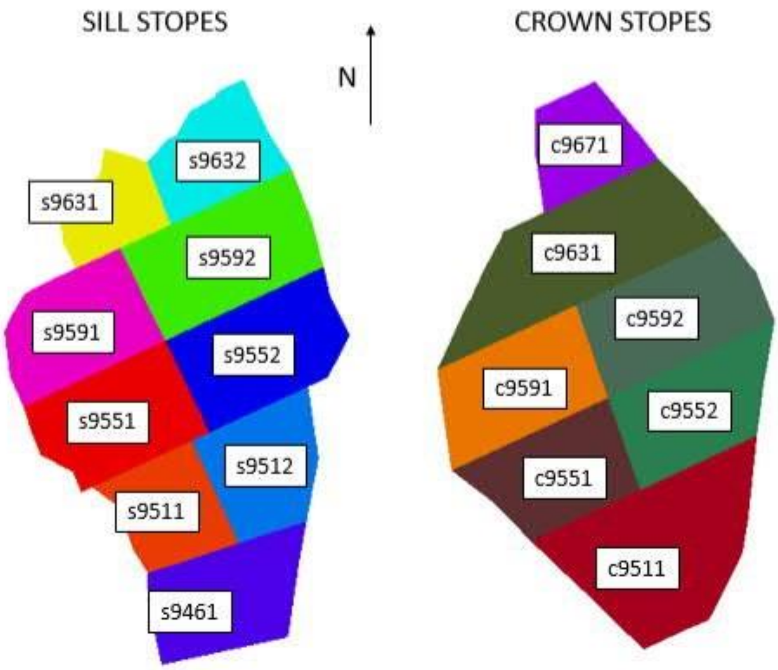

Figure 5.4: Plan views of sill stopes and crown stopes in the 100-900 OB remnant pillar. Crown stopes are located between 3500L and 3550L. Sill Stopes are located between 3550L and 3710L.

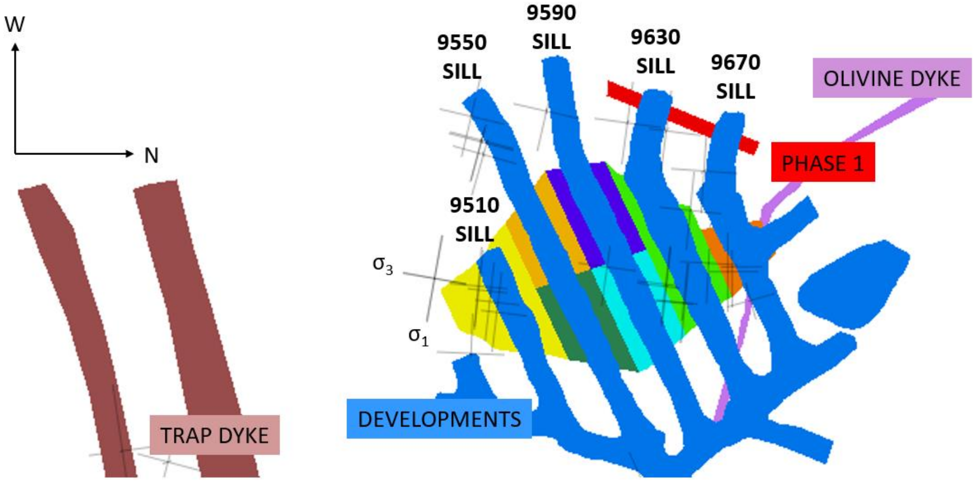

Figure 5.5: Plan view of Phase 1 blast on 3550L

Table 5.2: Planned Mining Sequence

Mining Step	Stope	Mining Method	Level
1	Phase 1		
2	9631	sill	3710
3	Phase 2		
4	9511	sill	3880
5	9671	crown	3550
6	9512	sill	3880
7	Phase 3		
8	9591	sill	3710
9	Phase 4		
10	9632	sill	3710
11	9551	sill	3710
12	9631	crown	3550
13	9592	sill	3710
14	9591	crown	3550
15	9552	sill	3710
16	9511	sill	3710
17	9592	crown	3550
18	9512	sill	3710
19	9551	crown	3550
20	9461	sill	3710
21	9552	crown	3550
22	9511	crown	3550

The destress blast panels consist of both up and down holes with 2 rings of 114 mm diameter holes with a spacing of 1.8 m between the rings. An isometric view of typical drill pattern of up and down holes is shown in Figure 5.6. The up and down holes are collared such that a toe spacing of 2.6 m is maintained between the holes within the ring. Furthermore, the up hole and down hole rings are staggered such that a 2.4 m spacing is maintained between nearest rings. The Phase 1 destress blast required approximately 3000 m of drilling for both up and down holes. The holes were loaded with emulsion of 23,484 kg using 370 detonators with a maximum charge of 223 kg per delay. However, the collars of both up and down holes were not loaded up to a length of 2 to 3 m. The holes were fired center out with 18 ms delay between the holes. Based on the design, the amount of emulsion yields an average energy of 493 cal/kg and 513 cal/kg for up and down holes respectively.

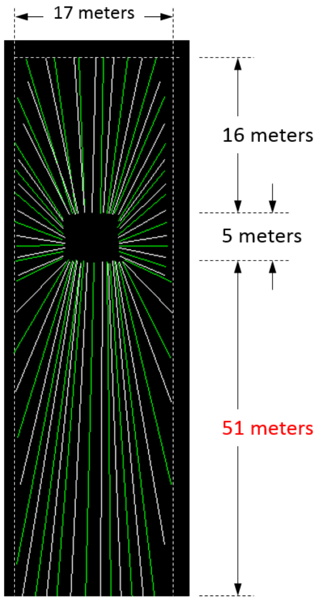

Figure 5.6: Elevation view of the two rings (one in white, one in green) of upholes and downholes from 3550L

5.3 Methodology

The Phase 1 destress blast is simulated holistically with the rock fragmentation factor (α) and stress reduction factor (β). The destress blast simulations are then validated based on uniaxial stress cell data, where the most conforming combination of α and β is retained. The first stope in the sequence (stope 9631) is then mined. The burst proneness of the ore in the stress shadow is quantified with burst potential index (BPI) and the brittle shear ratio (BSR). The incremental BSR and BPI are also evaluated.

5.3.1 Pillar instrumentation

Eight uniaxial stress cells were installed by CCM in the ore pillar before the Phase 1 destress blast. The stress cells were preloaded with a wedge and platen assembly to approximately 7-8 MPa during the installation. The stress cell measurements was set as initial as soon as any stress change was measured. Subsequent readings were then analyzed with reference to the initial reading to determine the changes in stress from that point onwards. The stress cells were installed in vertical holes in the roof and floor of the sill drifts, in the North-South or East-West direction. The orientation of the stress cells and the measured stress change for Phase 1 destress blasts and the extraction of stope 9631 are shown in Table 5.3. The position of the uphole and downhole stress cells installed from 3550L are shown in Figures 5.7 and 5.8. Stress cell 6 is located in a horizontal hole in 9550 sill, on 3550L.

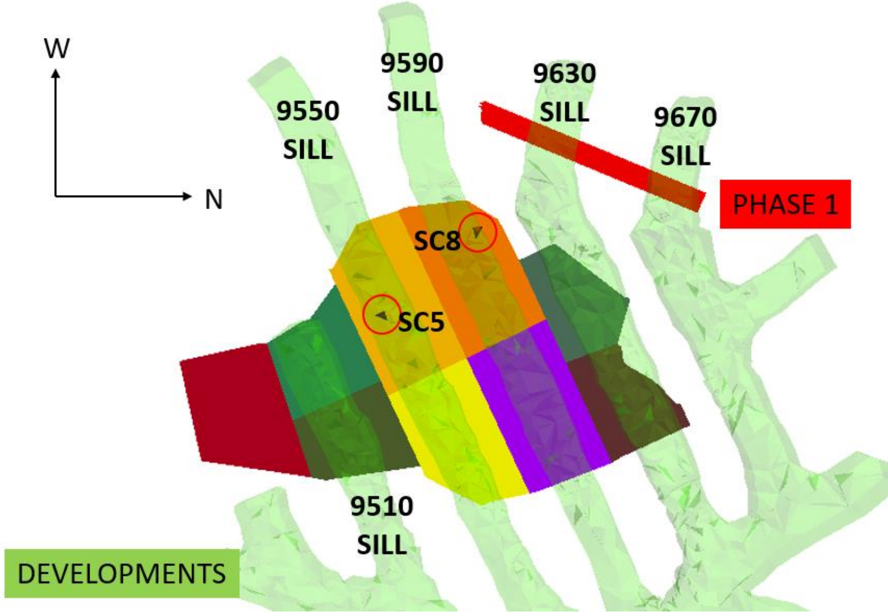

Figure 5.7: Position of downhole stress cells installed from 3550L with respect to the Phase 1 panels. Downhole cells were installed 6 m below the floor of 3550L.

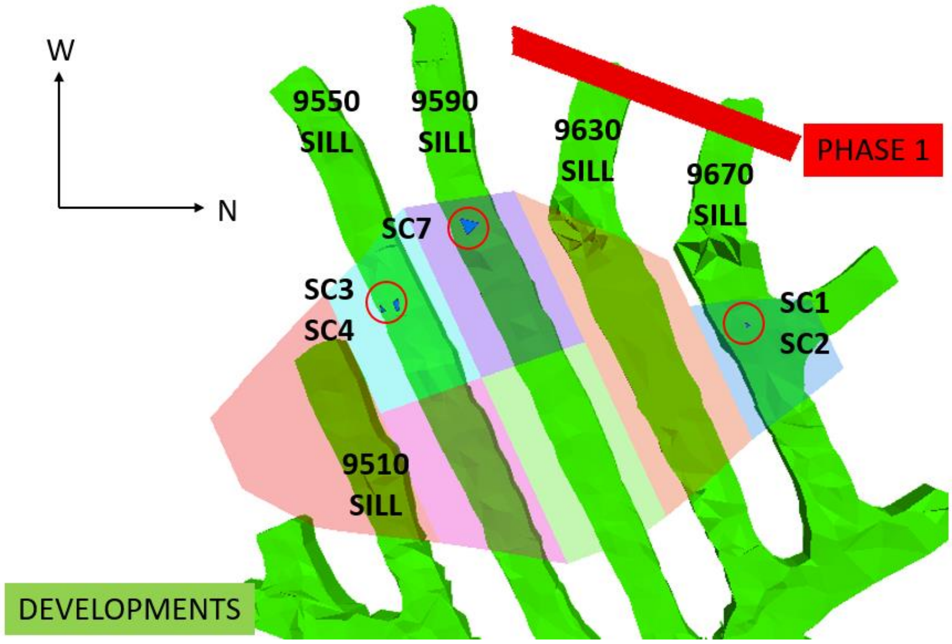

Figure 5.8: Position of uphole stress cells installed from 3550L with respect to the Phase 1 panels. Uphole stress cells were installed 7.5 m above the roof of the 3550L.

Table 5.3: Measured stress changes for phase 1 blast

#	Name*	Direction	Measured Stress Change (MPa)	
			Immediate	Stabilized
1	9670-Sill_CN3800_UH-NS	YY	-1.17	-1.20
2	9670-Sill_CN3801_UH-EW	XX	-3.17	-3.19
3	9550-Sill_CN3797_UH-EW	XX	-0.53	-0.30
4	9550-Sill_CN3798_UH-NS	YY	-0.50	-0.44
5	9550-Sill_CN3802_DH-EW	XX	-1.68	-1.62
6	9550-Sill_CN3804_WH-NS	YY	-0.32	-0.13
7	9590-Sill_CN3799_UH-EW	XX	-6.20	-6.40
8	9590-Sill_CN3803_DH-EW	XX	-1.80	-1.62

*UH denotes an uphole cell, DH denotes a downhole cell. The first number in the cell name is the drift latitude. Stress cell 6 is installed in a horizontal hole.

Stress measurements were logged more frequently a few hours prior and after major production and destress blasts. Otherwise, the readings were logged at least once a day to once a week depending on the rate of change and mining activity in the area. The reported "immediate" stress changes in Table 5.3 is the difference between the last stress measurement before the blast and the first stress measurement after the blast. This immediate stress change is assumed to represent only the elastic stress redistribution caused by the stress release and stiffness reduction of the panel. Therefore, the computed stress changes in the numerical model after the destressing step can be directly compared to the measured immediate stress change. Subsequent stress changes that are measured in the hours to days following a blast are understood to be caused by progressive yielding of the rock mass, which eventually stabilizes as seismic activity subsides. Stabilized stress changes for Phase 1 are reported 29 days after the blast. Given that the model is linear elastic, the stabilized stress changes are not used for model validation.

5.3.2 Numerical model

In the present study, a 3D model of the remnant pillar in the 100OB is constructed in Rhino and discretized in Kubrix. The destress blasting program is simulated with Flac3D. Figure 5.9 shows the final model geometry excluding the Trap Dyke and Olivine Diabase Dyke.

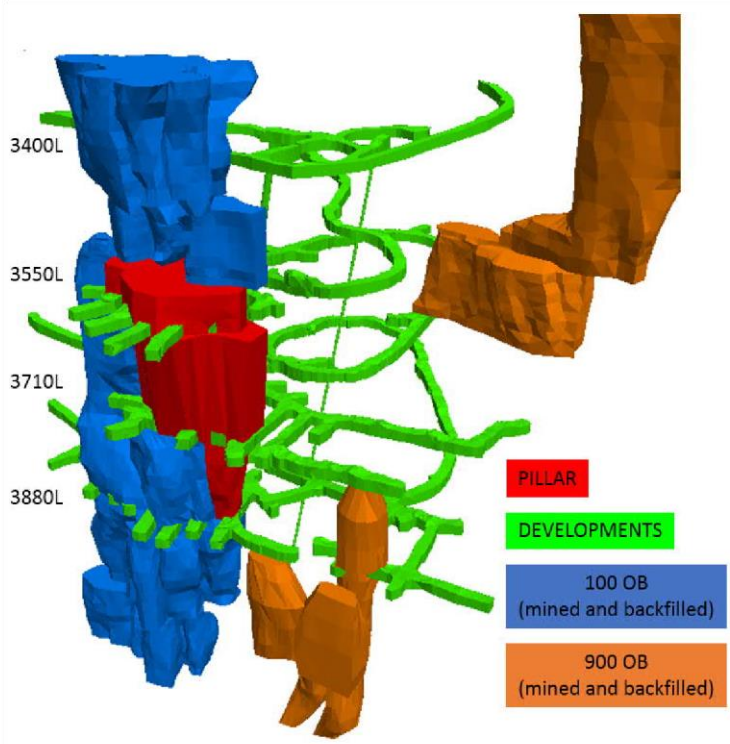

Figure 5.9: 3D numerical model of the remnant ore pillar in 100OB.

The model surfaces were constructed in Rhino and exported to Kubrix to generate a 3-dimensional grid for Flac3D. For unmined stopes, the stope boundaries built in Rhino were based on the planned geometries. On the other hand, for mined stopes the surfaces obtained with a laser Cavity Monitoring System (CMS) were used and simplified. Similarly, drift as-builts were used to build the mine developments such as the ramp, 3550L, 3710L, and 3880L. The panels were also constructed in Rhino based on provided drill hole patterns. To find the panel geometry, it was assumed that a destress blast hole damage zone is 16 times the hole diameter (Andrieux 2005). Therefore, with 2 rings of blast holes, the total panel targeted mass "M_e" can be estimated as:

$$M_e = 2(16d)HL\rho_r \qquad [5.1]$$

where d is the blasthole diameter, H is the height of the panel, L is the strike length of the panel, and ρ_r is the density of the rock. The resulting panel thickness is 3 m.

A mesh sensitivity analysis was conducted in a simplified pillar model. Different grid point spacings were applied to each domain surface depending on the desired accuracy. The final grid spacing for the panels and the stopes was set at 0.75 m and 3 m respectively, where higher accuracy was needed. Model boundary grid spacing was set at 25 m, and geological domain boundary grid spacing was set at 10 m.

The elastic material properties and rock mass characterization parameters obtained from previous laboratory results are shown in Table 5.4. The rock mass properties for each geological unit are calculated from the intact properties with the Hoek and Brown failure criterion parameters. For the ore and host rock, the rock mass stiffness applied to the model is calculated based on a GSI of 60. For the Trap Dyke, a GSI of 100 is assumed. No intact data is available for the Olivine Diabase Dyke. However, since the Olivine Diabase Dyke is strongly sheared, it is unlikely to undergo brittle failure, and the failure envelope parameters are therefore not needed.

Table 5.4: Elastic material properties and Hoek and Brown failure envelope parameters

	Elastic Properties				Hoek and Brown Failure Envelope					
	E_{intact} (GPa)	$E_{rockmass}$ (GPa)	ν	γ (kN/m^3)	GSI	m_i	m_b	s	a	σ_c (MPa)
Host Rock	48	24.96	0.18	28.5	60	25	5.99	0.0117	0.503	150
Orebody	52	27.6	0.19	36.3	60	24	5.75	0.0117	0.503	140
Trap Dyke	60	N/A	0.22	28.5	100	15	15	1	0.5	220
Olivine Diabase Dyke	N/A	10	0.25	28.5	N/A					
Backfill	N/A	2	0.3	20						

The bottom boundary is constrained in the z-direction, while all other faces free to displace in any direction. The in-situ stress varies linearly with depth, and is given by the empirical Sudbury regional stress equations:

$$\sigma_1(MPa) = 10.82 + 0.0407D\ (m) \qquad [5.2]$$

$$\sigma_2(MPa) = 8.68 + 0.0326D\ (m) \qquad [5.3]$$

$$\sigma_3(MPa) = 0.0292D\ (m) \qquad [5.4]$$

where D is the depth below ground surface, σ_1 in the major principal stress in the N12˚W direction, σ_2 is the intermediate stress in the N78˚E direction, and σ_3 is vertical minor principal stress. The model is loaded with external boundary tractions, yielding different in pre-mining stresses in each geological domain in relation to the rock mass stiffness (Shnorhokian et al. 2014). The model x-faces and y-faces are loaded in the x-direction and y-direction respectively, and with shear stress boundary tractions in the x-y direction. Overburden pressure is applied to the top boundary.

5.3.3 Numerical simulation of destress blasting

Destress blasting is understood to have 3 effects on the targeted mass, which are the reduction of targeted mass stiffness due to fragmentation, the dissipation of stress due to fracture propagation, and the modification of the failure mechanism from brittle elastic to plastic yielding. In this paper, the first two effects are modelled holistically with the rock fragmentation factor (α) and the stress reduction factor (β). This methodology has been applied to single blastholes (Sainoki et al. 2016a) to assess the effectiveness of drifts destressing. The size of the damage zone was determined with a blast damage model. It was shown that for drift destressing pattern, the assumption that face is uniformly destressed too optimistic and overestimates the volume of blast zones. However, drift destressing typically uses small diameter holes, with a low hole density in the blast pattern (Comeau et al. 1999). In the case of panel destressing, a much higher explosive energy per targeted mass is applied, with a pattern hole density and hole diameters of a production blast. The assumption of uniform fragmentation and stress release in targeted mass is therefore valid. A previous parametric study (Vennes and Mitri 2017) of panel destressing strategy in a simple pillar showed stress change magnitudes obtained with uniformly destressed panels can replicate the measured stress changes at Brunswick and Fraser Mine.

To begin, the rock fragmentation factor introduced by Tang and Mitri (2001) considers the reduction of stiffness of the targeted mass due to blasting. The modulus of elasticity is reduced in the panel by the factor α which ranges from 0 to 1:

$$E_{destress} = E\alpha \qquad [5.5]$$

In addition, Tang and Mitri (2001) proposed equation 5.6 to estimate the Poisson ratio due to softening of the rock mass:

$$\upsilon_{destress} = \upsilon * (2 - \alpha) \quad [5.6]$$

If the solution to equation 6 is greater or equal to 0.5, the Poisson ratio is set to 0.49. Tang and Mitri (2001) also introduced the stress dissipation factor, which represents an instantaneous release of stresses due to the blast. The residual stress tensor in the targeted zones is given by the following equation:

$$\{\sigma_D\} = \{1 - \beta\}^T \cdot \{\sigma\} \quad [5.7]$$

where β ranges from 0 to 1, and where

$$\{\sigma\}^T = \left(\sigma_{xx}, \sigma_{yy}, \sigma_{zz}, \sigma_{xy}, \sigma_{yz}, \sigma_{xz}\right) \quad [5.8]$$

The balanced stress state in the panel prior to destressing is replaced with the residual stress state [σ_D] defined by equation 5.8. This removes a portion of the strain energy in the panel proportional to the factor β, causing an imbalance between the model boundary work and the total strain energy in model. A new equilibrium is reached after solving the model where the final stress tensor in the panel lies between the initial stress tensor and the residual stress tensor. Table 5.5 shows the tested combinations of α and β for Phase 1 destress blast. It is assumed that α + β = 1.

According to Liu et al. (2005), choke destress blasting should aim for a swell factor of 5-15%, which will release ground stresses but keep fragmented “frozen” rock in-situ. However, the computed panel volume will be reduced for all possible combinations of α and β. Given that panel volumetric reduction is desirable and that the targeted material will swell, rock must be ejected from the panel to obtain the destressed panel stress state. At CCM, the stope crosscuts from which the panels are drilled acted as a void, and ejected material in the panel access drifts was observed. However, the holistic simulation approach used for destressing does not directly consider rock displacement, but it can replicate the effect of rock displacement by further reducing the panel stiffness. Therefore, the destressed modulus of elasticity is not the actual field modulus of the panel, but instead a reflection of the effect of both fragmentation and ejection of material from the panel.

Table 5.5: Tested combinations of “α” and “β”

Model #	α	β
1	0.05	0.95
2	0.1	0.9
3	0.2	0.8
4	0.3	0.7

5.3.4 Evaluation of pillarburst potential

The pillarburst potential of the ore pillar needs to be assessed before and after destressing to evaluate if the panel destressing strategy sufficiently reduces the stress in the pillar to ensure safe mining. The brittle shear ratio (BSR) and burst potential index (BPI) are both suitable parameters for this study. To begin, the brittle shear ratio (BSR) (Castro et al. 1997), is expressed as:

$$BSR = \frac{\sigma_1 - \sigma_3}{UCS_{intact}} \qquad [5.9]$$

where σ_1 and σ_3 are the mining induced major and minor principal stresses. In a study by Martin and Kaiser (1999), rock was found to undergo brittle shear as the ratio between the deviatoric stress and the uniaxial compressive strength exceeded 0.4, and the risk of strainbursts was deemed significant when the ratio exceeded 0.7. Ore zones in the model with a BSR exceeding 0.7 are therefore termed ‘at risk’.

On the other hand, the Burst Potential Index (BPI) relates the energy storage rate of the rock to its’ critical strain energy, whereas a BPI of 100% is initially assumed to be the threshold for high risk of rockburst. It is expressed as (Mitri et al. 1999):

$$BPI = \frac{ESR}{e_c} \qquad [5.10]$$

where ESR is the total strain energy in the rock, and e_c is the elastic strain energy capacity. Since the model is loaded with the boundary traction method, all zones in the model have zero stress under zero strain. Therefore, the ESR of a zone “i” is calculated based on the total stress and total strain in a zone:

$$ESR_i = \frac{1}{2} \cdot \begin{bmatrix} \sigma_{11} \\ \sigma_{22} \\ \sigma_{33} \end{bmatrix}_i^T \cdot \begin{bmatrix} \varepsilon_{11} \\ \varepsilon_{22} \\ \varepsilon_{33} \end{bmatrix}_i \quad [5.11]$$

To calculate the critical strain energy of the ore, host rock, and Trap Dyke, the energy at failure of a triaxially loaded specimen was calculated analytically. The axial load at failure was calculated with the generalized Hoek and Brown failure criterion for an intact specimen (Hoek et al. 2002):

$$\sigma_1 = \sigma_3 + \sigma_{ci} \left(m_i \frac{\sigma_3}{\sigma_{ci}} + s \right)^a \quad [5.12]$$

Hooke's law was used to calculate the axial and radial strain at failure under triaxial loading, where $\sigma_{11} = \sigma_l$, $\sigma_{12} = \sigma_{23} = \sigma_{13} = 0$, and $\sigma_{22} = \sigma_{33} = \sigma_r$. The ESR of the specimen at failure can then be calculated analytically with equation 5.13, and treated as the critical strain energy of the rock under triaxial conditions.

$$e_c = \frac{1}{2} \cdot (\sigma_{11}, \sigma_{33}, \sigma_{33})^T \cdot (\varepsilon_1, \varepsilon_{33}, \varepsilon_{33}) = \frac{1}{2E} \left({\sigma_{11}}^2 + 2{\sigma_{33}}^2 - 2\upsilon(2\sigma_{11}\sigma_{33} + {\sigma_{33}}^2) \right) \quad [5.13]$$

The critical strain energy for the Olivine Diabase Dyke is not calculated as the material is too soft to fail in a brittle manner. Also, the BPI is only valid in compressive zones at risk of brittle shear failure. Therefore, for zones in a low stress regime where $\sigma_3 < 0$, the BPI is set to 0.

5.3.4 Validation of destress blasting model

The stress change results from the stress cells and the model are not compared directly since the magnitude of the stress change error between the model and the stress cells does not adequately reflect model conformity. Model conformity is instead evaluated by measuring the distance error "D" between the stress cell and the computed stress change contour with the same stress change. The distance error is calculated in the model by finding the closest zone in the stress cell where the computed stress change is within +/- 0.1 MPa of the measured stress change. This process is illustrated in Figure 5.10. In this case, the effect of high contour density at the stress cell location is mitigated.

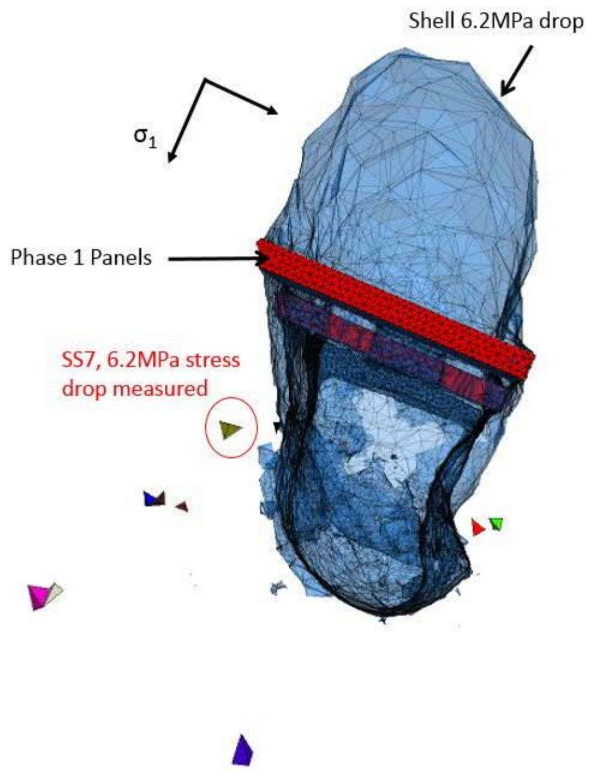

Figure 5.10: Comparison between model stress changes and measured stress changes after destressing the Phase 1 panels (in red). SS7 (in yellow) read a 6.2 MPa stress decrease in the N-S direction. The shell (in blue) shows where the computed stress changes in N-S equal -6.2 MPa. A small distance between the cell and the contour indicates good conformity between the numerical model and the stress change data.

5.4 Results

5.4.1 Evaluation of destress blast input parameters

To begin, the holistic modelling approach described in Section 3.3 must be validated with the measured stress changes. Conformity between the stress measurements and the model is based on “D”, defined as the distance between the stress cell and the closest zone in the model with a computed stress change equal to the stress cell measurement. Figure 5.11 shows the stress change shells superposed with their respective stress cells. For stress cells 2, 5, and 7, the best match is obtained with model 1. On the other hand, stress cell 8, which read a stress change of -1.5 MPa in the N-S direction, does not present a clear trend because the shell of a 1.5 MPa stress decrease intersects to position of the stress cell in all 4 models. The stress cell is therefore not well situated to measure the destressing effect of the Phase 1 blast, and by itself would have yielded inconclusive results.

	α = 0.05 β = 0.95	α = 0.1 β = 0.9	α = 0.2 β = 0.8	α = 0.3 β = 0.7
Stress Cell 2 9670- Sill_CN3801 Uphole E-W Direction Δσ = -3.17 MPa				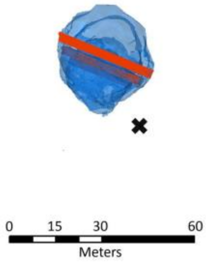
Stress Cell 5 9550- Sill_CN3802 Downhole E-W Direction Δσ = -1.68 MPa	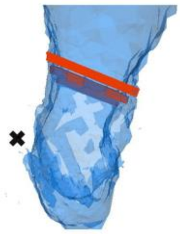			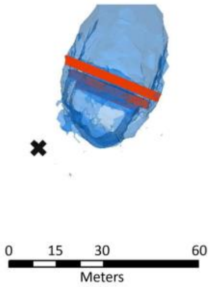
Stress Cell 7 9590- Sill_CN3799 Uphole E-W Direction Δσ = -6.20 MPa	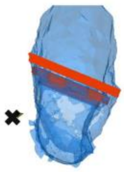			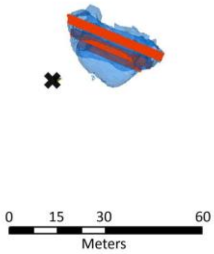
Stress Cell 8 9590- Sill_CN3803 Downhole E-W Direction Δσ = -1.80 MPa				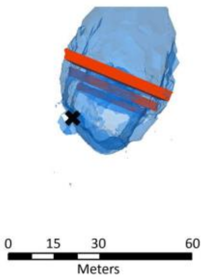

Figure 5.11: Comparison of Phase 1 blast stress change shells with the positions of stress cell 2, 5, 7, and 8. The position of the stress cell is marked by a black cross.

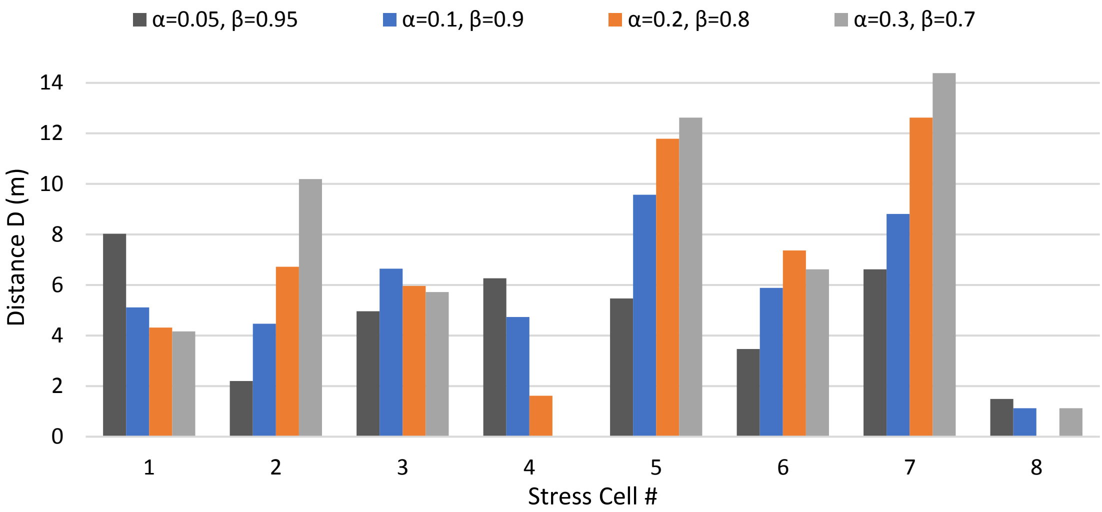

Figure 5.12: Distance "D" (y-axis) obtained for stress cells 1 to 8 (x-axis). Results for models 1-4 are plot for each stress cell (4 bars per point on the x-axis).

Figure 5.12 shows the distance "D" results for all stress cells for models 1 to 4. Stress cells 2, 5, 6, and 7 show a trend towards a high destressing effect, while stress cells 1 and 4 show a trend towards a lower destressing effect. Stress changes for cells 3 and 8 are not sensitive to destress blast input parameters, due to the positioning effect demonstrated in Figure 5.11 for stress cell 8.

Finally, Figure 5.13 presents the spread of the D values for the 4 destressing models. Model 1 has the lowest median D value and the lowest maximum D value. Considering the measured data from all other stress cells, model 1 is the most valid. This indicates that the panel is highly fractured, with the rock stiffness reduced from 25 GPa to 1.25 GPa and a stress reduction of 95%. Therefore, the merits of the destress blasting program conducted at CCM will be evaluated with $\alpha = 0.05$ and $\beta = 0.95$ as destress blast input parameters.

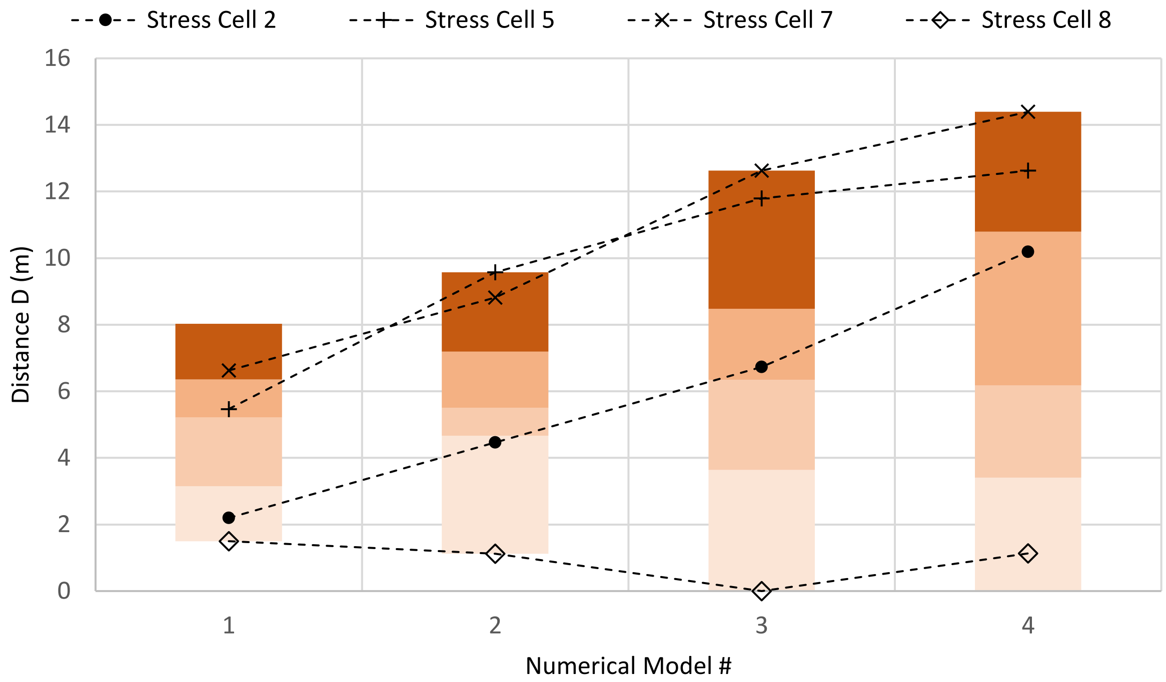

Figure 5.13: Distance "D" obtained for models 1-4. The graph shows the quartile spread obtained with the 8 stress cells for each model.

5.4.2 Evaluation of the merits of destress blasting

The abundance of stress change data obtained with the stress cells in the pillar provided a unique opportunity to validate the rock fragmentation factor and stress reduction factor constitutive models for a large-scale panel destress blast. In section 4.1, the most suitable combination of destress blasting parameters was determined to be $\alpha = 0.05$ and $\beta = 0.95$.

In this section, the first stope in the extraction sequence (stope 9631) is mined after destressing Phase 1 with these parameters. An overview of the modelled scenarios is given in Table 5.6. Stope 9631 is mined in 6 lifts bottom up. The final lift is named as "Crown Blast", where the top half of the stope in terms of height is blasted. The stope is backfilled after the ore from the crown blast is mucked. The rockburst potential of the stope, and the stress shadow stopes are then evaluated with the BSR and BPI for each stope lift. The BSR and BPI are observed along two planes intersecting the stope (see Figure 5.14).

Table 5.6: Stope extraction mining steps

Mining Step	Scenario 1:	Scenario 2: No Destressing
1	Undisturbed	Undisturbed
2	Destress Blast	N/A
3	Lift 1	Lift 1
4	Lift 2	Lift 2
5	Lift 3	Lift 3
6	Lift 4	Lift 4
7	Lift 5	Lift 5
8	Crown Blast	Crown Blast

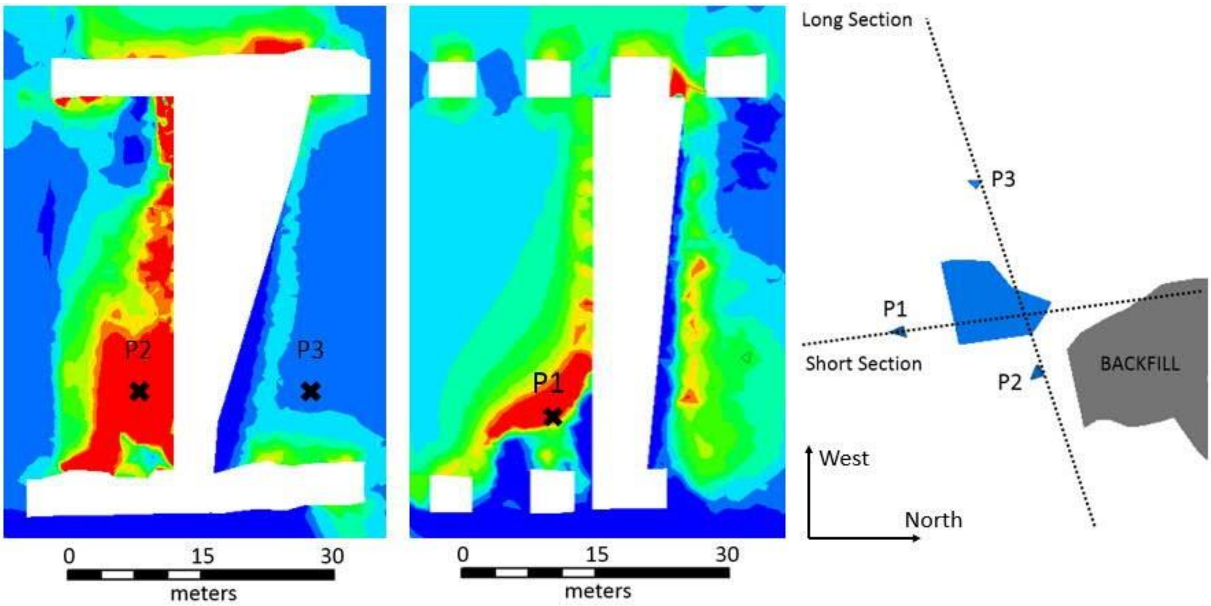

Figure 5.14: Section views of stope 9631 after the Crown Blast. Contours show the BPI, where a BPI>0.25 is in red. Observation points 1 is shown in the short section. Observation points 2 and 3 are shown in the long section.

On these sections, 3 observation points were identified. The BPI and BSR for points 1 and 2 is plotted in Figures 5.15 and 5.16. The graphs shows that for all points, destressing reduces the BPI and BSR over all mining steps. At point 1, the BSR is lowered from 0.58 to 0.52 before mining, and from 0.7 to 0.63 after mining. For point 2, the BSR is also reduced, with a BSR 0.93 before destressing, and a BSR of 0.87 after destressing. At the final mining step, destressing reduced the BSR from 0.98 to 0.93. Point 3, under low deviatoric stress, also measures a significant BSR reduction. The same pattern is observed with the BPI, where the greatest reduction in burst potential is measured at point 2, from 51% to 44% after mining stope 9631.

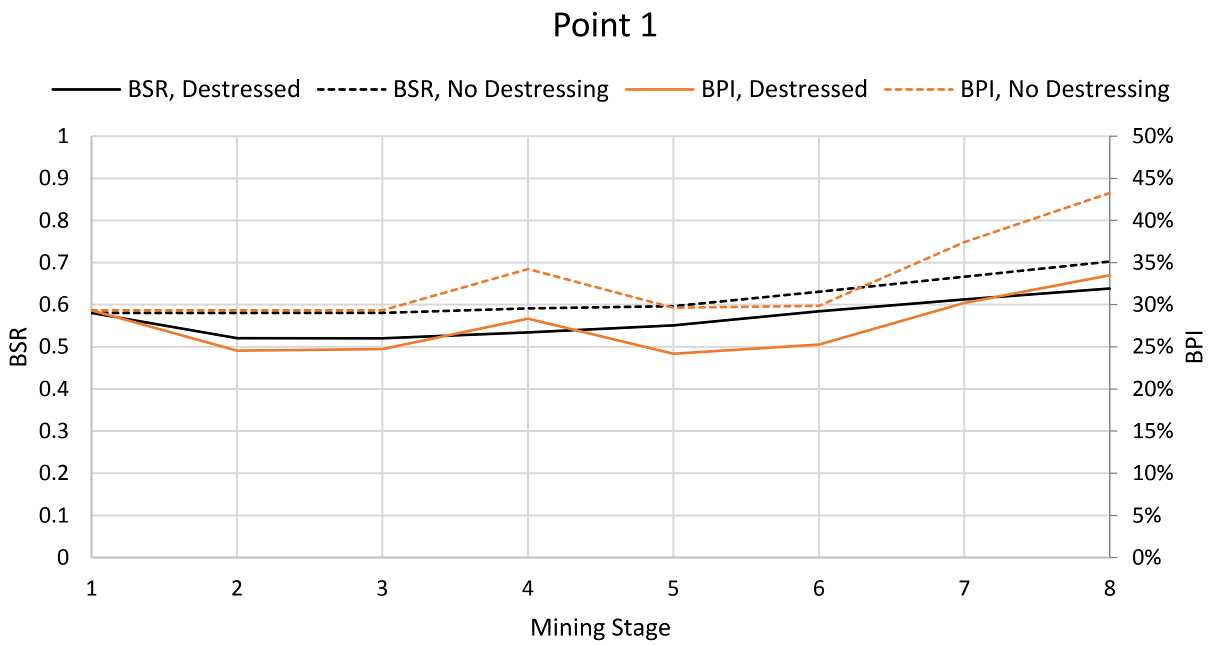

Figure 5.15: BSR and BPI at observation point 1. Step 2 is the destressing step. Step 8 is the crown blast.

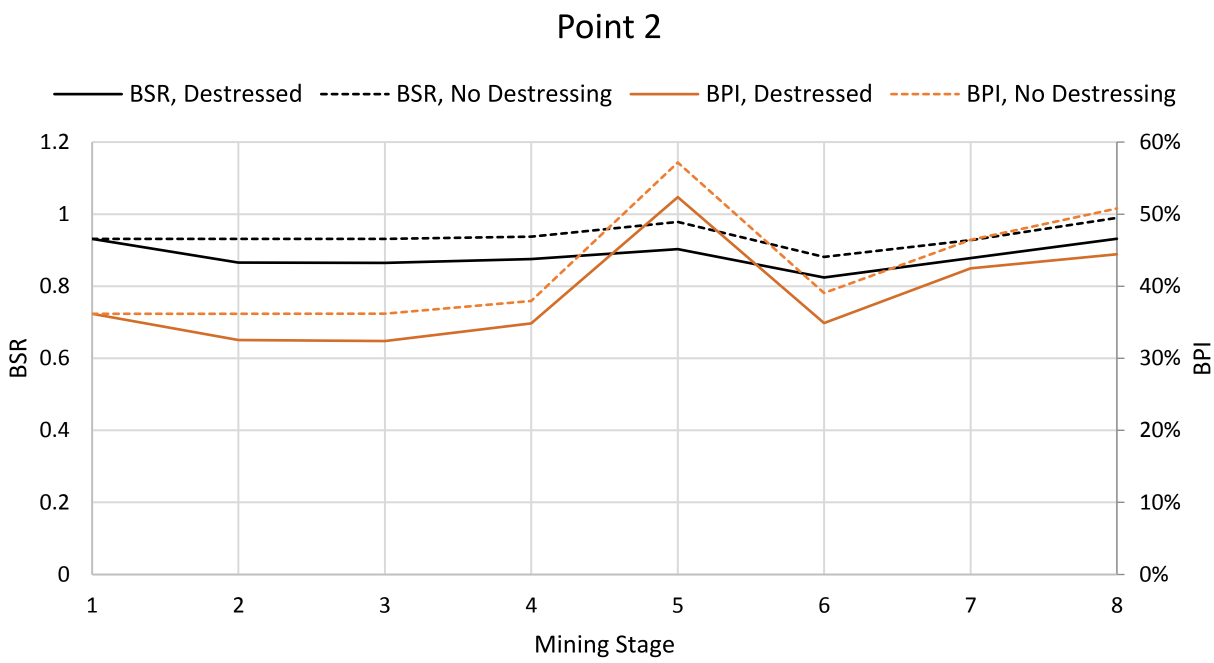

Figure 5.16: BSR and BPI at observation point 2

Ore at risk, defined as ore with a BSR>0.7, is measured at all mining steps for both scenarios. The proportion of ore at risk in stope 9631 before the crown blast is measured at 15.0% with no destressing. The proportion of ore at risk is reduced to 7.7% if the Phase 1 panels are destressed. For the stopes located in the stress shadow of the Phase 1 panels, destressing will decrease the ore at risk from 14.2% to 9.4%.

After extracting stope 9631, the destress blast reduces the proportion of ore at risk in these stopes to from 10.3% to 8.2%. Destressing also reduces the tonnage of ore at risk in the entire pillar over the extraction of stope 9631. Before mining, a BSR cut-off of 0.7 yields 8.3 kt of ore at risk with no destressing. After destressing, the ore at risk tonnage in the pillar is lowered to 8.0 kt. The effect of destressing is more pronounced after the extraction of stope 9631 with a greater reduction of ore at risk in terms of tonnage. The ore at risk tonnage is reduced from 12.5 kt to 10.3 kt.

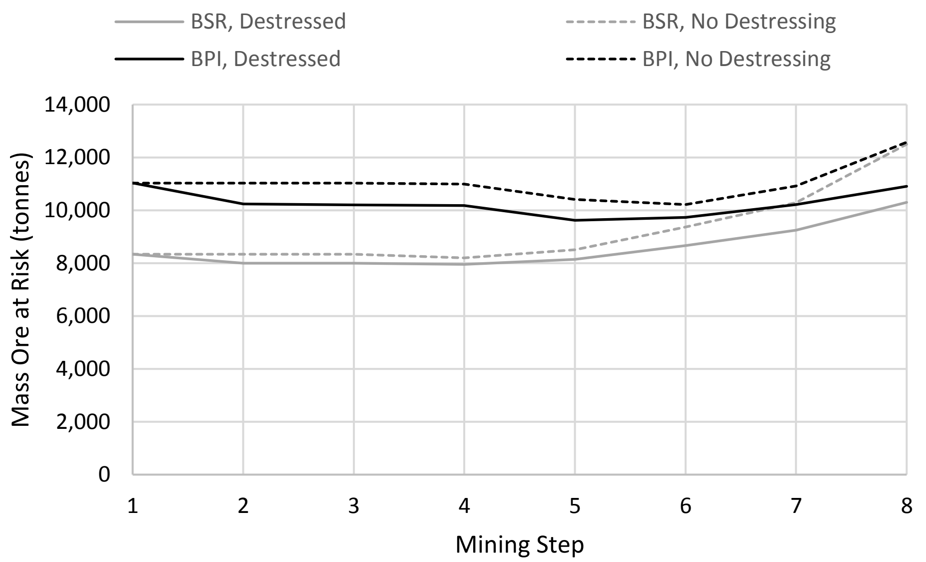

Figure 5.17: Mass of ore at risk in the pillar stopes, excluding 9631.

Ore at risk can also be evaluated with the BPI. To determine a suitable cut-off, the total volume of ore at risk delineated with the BSR at mining step 8 with no destressing is set as a benchmark. It is found that the tonnage of ore at risk obtained with a BPI cut-off of 25% is equal to the tonnage of ore at risk obtained with a BSR cut-off of 0.7 (see Figure 5.17). This BPI cut-off is therefore used to assess ore at risk for all other mining steps and destressing scenarios. The proportion of ore at risk in the pillar over the mining sequence of stope 9631 is plotted in Figures 5.18 and 5.19. With the BPI cut-off of 25%, the destressing step will reduce ore at risk from 8% to 4.4% in stope 9631, and from 8.6% to 6.4% in the combined stress shadow stopes. After extracting 9631, ore at risk in the remaining stress shadow stopes decreases from 7.4% to 6.2%.

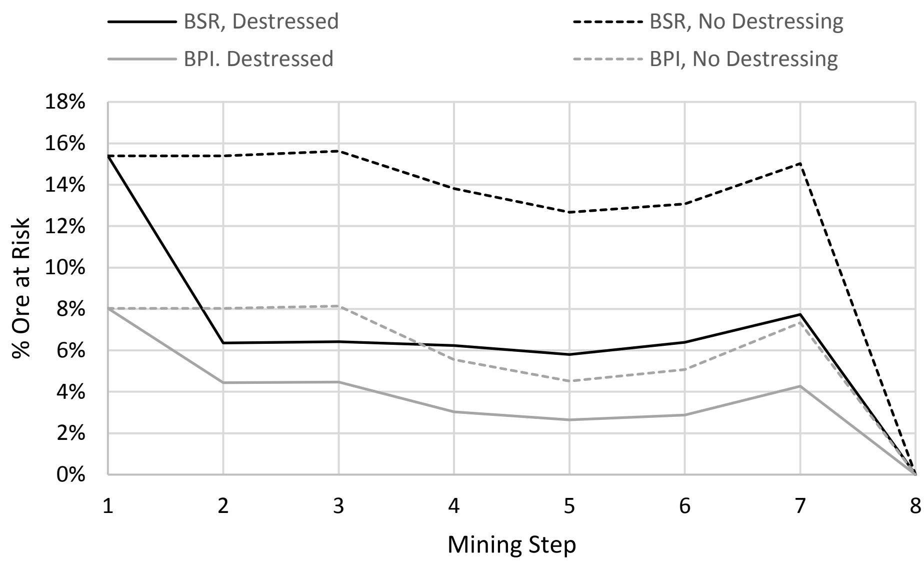

Figure 5.18: Ore at risk in stope 9631 during its extraction. Step 2 is the destressing of the Phase 1 panels.

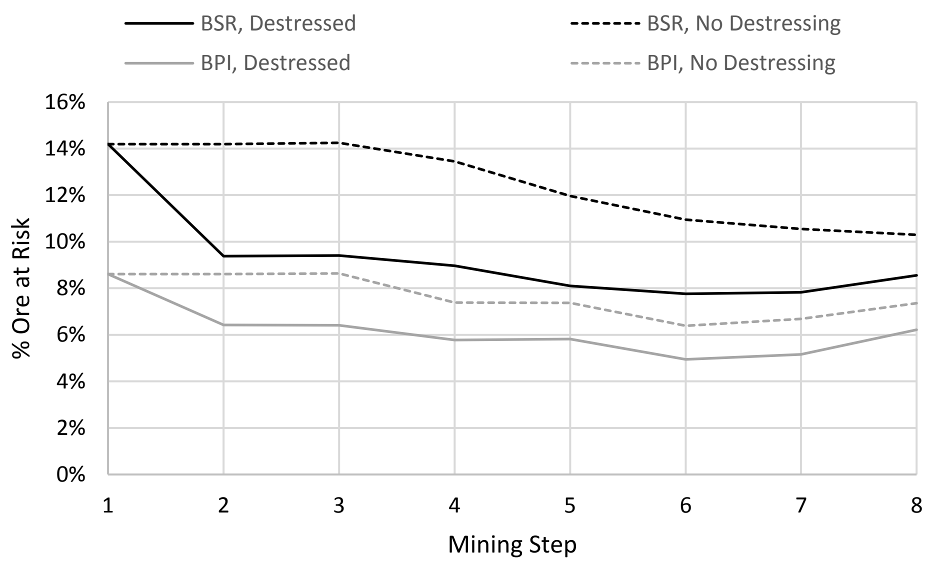

Figure 5.19: Ore at risk in the Phase 1 stress shadow stopes during the extraction of stope 9631. Stress shadow stopes are stopes 9631 sill, 9632 sill, 9631 crown, and 9671 crown.

5.5. Conclusion

In this paper, it is shown that panel destressing is beneficial to stress dissipation in the ore pillar thus enabling more efficient and safe mining. The stress reduction is quantified with an orebody wide numerical model and validated based on measured uniaxial stress change data. Validating the model however requires multiple stress cells, as placement and measurement error can be significant depending on the position of the cell with respect to the panel. In addition, results from single cell can be inconclusive based on its position with respect to the panel, with the same stress decrease being read at the stress cell position in all models. Only by combining results from multiple cells is it possible to conclusively validate the numerical model. Four combinations of α and β were tested and it is shown that the most conforming values are $\alpha = 0.05$ and $\beta = 0.95$. This indicates that the panel was highly damaged, releasing most of the stress. Given these input parameters, the immediate stress change caused by panel blasting provides a beneficial stress decrease in the stress shadow stopes for the Phase 1 blast.

5.6. Acknowledgement

This work is financially supported by a joint grant from MITACS Canada and Vale Canada Ltd, and the MEDA fellowship program of the McGill faculty of Engineering. The authors are grateful for their support. Technical and operational input along with the collaboration in developing these de-stress programs at Vale's Copper Cliff Mine are greatly appreciated.

5.7. References

Andrieux P. Application of rock engineering systems to large-scale confined destress blasts in underground pillars. Vol. Ph.D., Department of Mining, Metallurgical, and Material Sciences. [Quebec]: Laval University; 2005.

Andrieux P, Brummer R, Mortazavi A, Liu Q, Simser BP. Large-Scale panel destress blast at Brunswick Mine. CIM Bull. 2003;(96):78–87.

Brauner G. Rockbursts in coal mines and their prevention. Rotterdam: Baklama; 1994.

Castro LAM, Grabinsky MW, McCreath DR. Damage inititiation through extension fracturing in a moderately jointed brittle shear rock mass. Int J Rock Mech Min Sci. 1997;(34):110–3.

Comeau W, Mitri HS, Mohammed MM, Tang B. World-wide survey of destress blasting practice in deep hard rock mines. In: 25th Annual Conference on Explosives and Blasting Technique. 1999. p. 189–205.

Hoek E, Torres C, Carranza T, Corkum B. Hoek Brown failure criterion - 2002 edition. In: Fifth North American rock mechanics symposium. 2002. p. 267–73.

Konicek P, Saharan MR, Mitri HS. Destress Blasting in Coal Mining – State-of-the-Art Review. Vol. 26. 2011.

Konicek P, Soucek K, Stas L, Singh R. Long-hole destress blasting for rockburst control during deep underground mining. Int J Rock Mech Min Sci. 2013;(61):141–53.

Konicek P, Waclawik P. Stress changes and seismicity monitoring of hard coal longwall mining in high rockburst areas. Tunn Undergr Sp Technol. 2018;(81):237–51.

Liu Q, Ellis B, Chung S. Application of advanced blasting technologies for large scale de-stress blasts at Brunswick mine. CIM Bull. 2005;98(1088).

Martin CD, Kaiser PK. Predicting the depth of stress induced failure around underground excavations in brittle rocks. In: 49th Canadian Geothechnical Conference. St. John's; 1999. p. 105–14.

Mitri HS, Tang B, Simon R. FE modelling of mining-induced energy release and storage rates. J South African Inst Min Metall. 1999;103–10.

Sainoki A, Emad MZ, Mitri HS. Study on the efficiency of destress blasting in deep mine drift development. Can Geotech J [Internet]. 2016;54(4):518–28. Available from: https://doi.org/10.1139/cgj-2016-0260

Shnorhokian S, Mitri HS, Moreau-Verlaan L. Assessement of stope sequence alternatives in a diminishing ore pillar. In: Proceedings of the 7th International Conference on Deep and High Stress Mining. Australian Centre for Geomechanics; 2014. p. 471–84.

Singh R, Mandal PK, Singh AK, Kumar R, Sinha A. Coal pillar extraction at deep cover: With special reference to Indian coalfields. Int J Coal Geol. 2011;86:276–88.

Tang B, Mitri HS. Numerical modelling of rock preconditioning by destress blasting. Gr Improv. 2001;5:1–11.

Vennes I, Mitri HS. Geomechanical Effects of stress shadow created by large scale destress blasting. J Rock Mech Geotech Eng. 2017;9:1085–93.

Wojtecki L, Konicek P, Schreiber J. Effects of torpedo blasting on rockburst prevention during deep coal seam mining in the Upper Silesian Coal Basin. J Rock Mech Geotech Eng. 2017;(9):694–791.

Chapter 6: Validation of Phase 2 and Phase 3 Destress Blasts

6.1 Introduction

Large scale destressing in hard rock mines is implemented to reduce the magnitude of stresses in a critical mining region, in consequence reducing the burst proneness of the rock. This rockburst control strategy was implemented in the mid 2000's at Fraser Mine (Andrieux 2005) and Brunswick Mine (Andrieux et al 2003, Andrieux 2005), and more recently at Copper Cliff Mine. The blast pattern in all these cases was dense, and large diameter holes (>100 mm) were used, yielding explosive energies exceeding 200 kCal/kg. This contrasts with the tactical implementation of destressing for drift development and cut and fill mining where the explosive energy per targeted mass is much lower. The holistic modelling approach established by Tang and Mitri (2001) to destressing was also validated with a back analysis from Copper Cliff Mine (see Chapter 5). The analysis yielded a rock fragmentation factor α of 0.05 and a stress dissipation factor β of 0.95. The validation results indicate that the destress panel is highly fractured, releasing most of the panel's in-situ stresses. The computed stress changes in the stress shadow zone, which are in this case the stopes, confirmed the benefits of destressing. The volume of ore at risk in the stress shadow was reduced significantly. This confirms that part of the benefits of destressing is the lowered stiffness of the panel resulting in stress release.

In this chapter, Tang and Mitri's model is again adopted to simulate Phase 2 and Phase 3 blasts. It is shown that the stress redistribution following Phase 2 blast can be replicated with this model. However, the stress redistribution following the Phase 3 blast could not be explained with the isotropic model, i.e. one value for α, and one value for β in all directions. The anisotropic destressing model hypothesized by Saharan and Mitri (2009) is therefore explored. In his model, Saharan proposed that the degree of stiffness reduction and stress dissipation is influenced by the orientation of the in-situ principal stresses, whereby in the direction of major principal stress, σ_1, the rock fragmentation factor α_1 is likely to be larger than the rock fragmentation factor α_2 in the direction of the minor in situ principal stress. Likewise, the stress dissipation factor β_1 in the major principal stress direction is likely to be less than β_2 in the minor principal stress direction.

Another issue that is examined here is the effect of slight variation of the orientation of the stress cell. The installation of stress cells in the field is tedious and prone to human errors. In this Chapter, variations in stress cell orientation due to possible human error is evaluated. Bearing in mind that the stress cells used in the experimental program are uniaxial, a slight variation in orientation could lead to different stress change results.

This Chapter is divided into 3 sections. In the first section, the isotropic destressing model used in previous chapters is applied to the Phase 2 and Phase 3 blasts. It is shown that the isotropic model can adequately replicate the measured stress changes for the Phase 2 blast. In the second section, the stress change data is analyzed to validate the destressing effects. For Phase 3 blast, the behaviour of stress cell SC3 installed in 9550 sill appears to be unusual showing a stress increase rather than a stress decrease in the shadow zone. This is analyzed in Section 3, where the anisotropic destress model by Saharan and Mitri (2009) is applied to Phase 3 blast. It is shown that after accounting for possible stress cell orientation error of SC3, the anisotropic model is validated for the Phase 3 blast.

6.2. Isotropic Model Validation

6.2.1 Methodology

The holistic simulation method described previously is applied to Phase 2 and Phase 3 blasts. The mining and destressing sequence leading up to these blasts was previously described in Chapter 3. The mining-induced stress tensor and panel stiffness are reduced with the parameters α and β, which range from 0 to 1 (see equations 5.5 to 5.8). The numerical model is then solved, and the stress change contours are calculated and compared to the measured stress changes. The stress cell locations of SC1-SC8 are provided in Chapter 3. Two additional stress cells, SC9 and SC10, were installed prior to Phase 2 blast, as shown in Figure 6.1. The stress changes measured immediately after Phase 2 and Phase 3 blasts are given in Table 6.1.

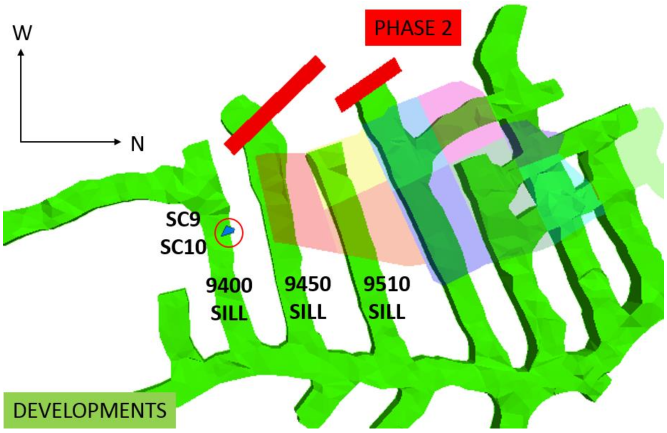

Figure 6.1: Location of SC9 and SC10 with respect to developments on 3710L

Table 6.1: Immediate stress changes measured after Phase 2 and Phase 3 destress blasts

#	Name	Cell orientation	Measured stress change (MPa)	
			Phase 2	Phase 3
SC1	9670-Sill_CN3800_UH-NS	N-S	0.00	N/A
SC2	9670-Sill_CN3801_UH-EW	E-W	+0.08	N/A
SC3	9550-Sill_CN3797_UH-EW	E-W	0.00	+5.85
SC4	9550-Sill_CN3798_UH-NS	N-S	0.00	-1.85
SC5	9550-Sill_CN3802_DH-EW	E-W	+1.94	-6.22
SC6	9550-Sill_CN3804_WH-NS	N-S	-2.05	+0.11
SC7	9590-Sill_CN3799_UH-EW	E-W	0.00	N/A
SC8	9590-Sill_CN3803_DH-EW	E-W	-0.41	N/A
SC9	9400-Sill_CN4187_UH-NS	N-S	+3.02	-0.12
SC10	9400-Sill_CN4188_UH-EW	E-W	-3.70	-0.07

6.2.2 Phase 2 validation

It is postulated that the Phase 2 blast will cause the same level of blasting induced damage to the panels than the Phase 1 blast, due to the similar blast pattern and applied explosive energy. Therefore, the range of tested α and β values will be the same as the range tested in Chapter 5. As such, four numerical models, namely Model 1 to 4 will be analyzed to select the one that provides the best validation with the Phase 2 blast (see Table 6.2.).

Table 6.2: Isotropic parameters for Phase 2 destress blast simulation

Model #	α	β
1	0.05	0.95
2	0.1	0.9
3	0.2	0.8
4	0.3	0.7

After the Phase 2 destress blast, four stress cells detected a major stress change. SC9 and SC10 are located close to the stress shadow of the blast in the adjacent 9400 sill and detected a stress change of +3.02 MPa and -3.70 MPa in the N-S and E-W directions respectively. This is in accordance with the expected behavior of the rock in the stress shadow of a blast. On the other hand, SC5 and SC6, above the Phase 2 panel, detected stress wrapping over the panel. SC5 measured 1.94 MPa increase in the E-W direction and 2.05 MPa decrease in the N-S direction.

The stress cell positions with respect to the stress change shells for Phase 2 blast are shown in Figure 6.2. The spread of values of the distance "D" for each model is given in Figure 6.3. Overall, model 1 ($\alpha = 0.05$, $\beta = 0.95$) yields good conformity with stress cells SC5, SC9, and SC10. For these cells, increasing the destressing effect enlarges the stress change shell closer to the stress cell position. Based on the results shown in Figure 6.3, it appears that the most conforming model for Phase 2 blast is Model 1, where $\alpha = 0.05$, and $\beta = 0.95$. These values are in accordance with the Phase 1 blast. The exception is stress cell 6, which measured a 2.05 MPa decrease in the N-S direction, where changing the destress parameters does little to affect poor model conformity where the distance D is more than 50 m.

	α = 0.05 β = 0.95	α = 0.1 β = 0.9	α = 0.2 β = 0.8	α = 0.3 β = 0.7
Stress Cell 10 9400-Sill_CN4188 Uphole E-W Direction Δσ = -3.70 MPa		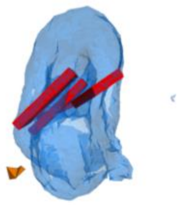	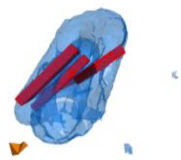	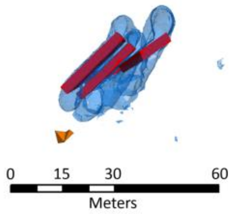
Stress Cell 9 9400-Sill_CN4187 Uphole N-S Direction Δσ = 3.02 MPa	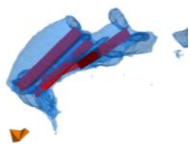	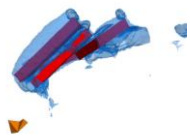	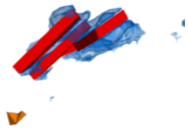	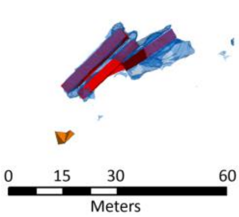
Stress Cell 5 9550-Sill_CN3802 Downhole E-W Direction Δσ = 1.94 MPa	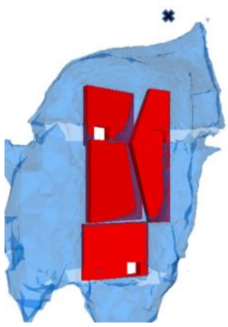	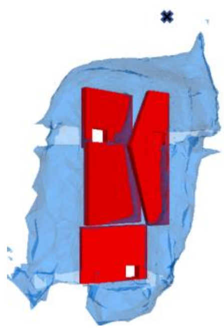	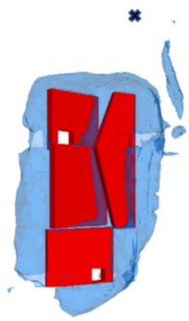	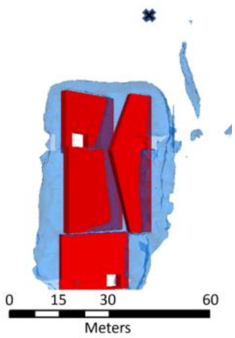

Figure 6.2: Comparison of computed stress change shells and the position of stress cells 10, 9, and 5.

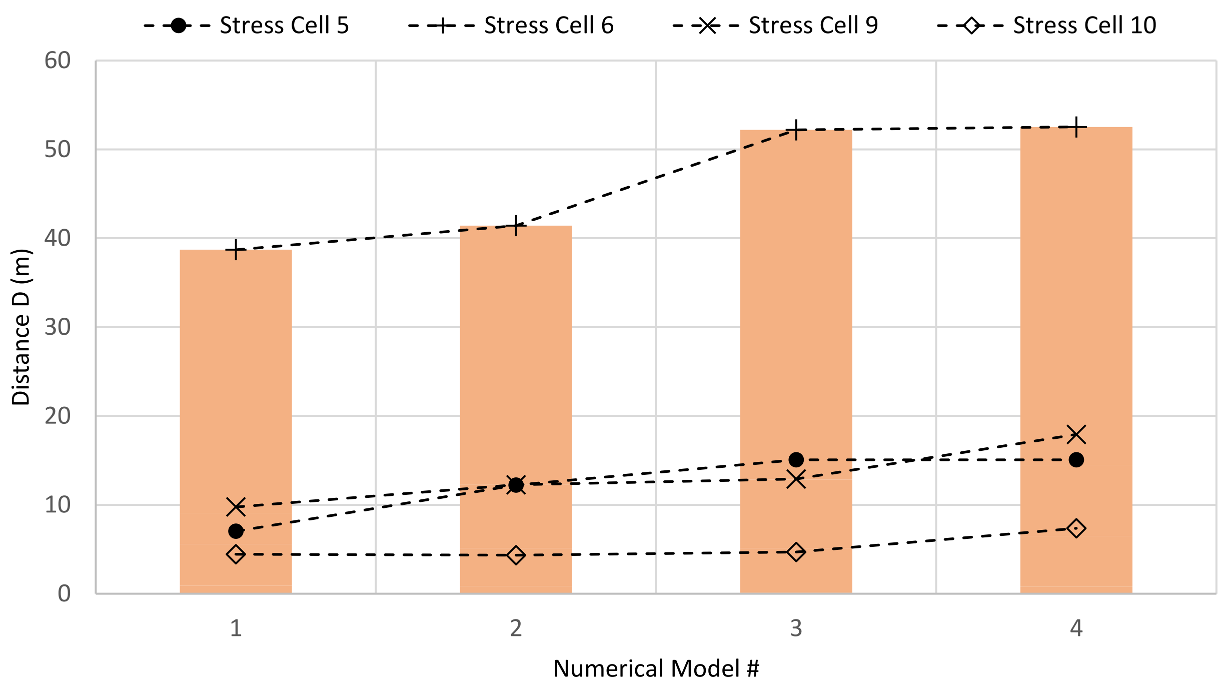

Figure 6.3: Phase 2 validation of models 1-4 based on the distance "D" measured from the stress cell location to the stress change shell boundary. Red bars show the spread of the values of "D" obtained for each model.

Overall, the behavior exhibited by SC9 and SC10 is in accordance with a high stress release and fragmentation effect. Even though the cells were in 9400 sill which is not directly in the panel stress shadow, the computed stress change contours conform with the measured stress change. The measured Phase 2 stress decrease of -3.02 MPa is lower than the measured Phase 1 decrease due to the positioning of the cell rather than the magnitude of the stress release of the panel.

6.2.3 Phase 3 validation

Table 6.3: Validation of destress blasting simulation with isotropic destress blast parameters for Phase 3

Model #	α	β
1	0.05	0.95
2	0.1	0.9
3	0.2	0.8
4	0.3	0.7

Three stress cells, SC3, SC4, and SC5 were in the stress shadow of the Phase 3 panels. SC3, in the shadow of the top panel, detected a stress increase of 6.3 MPa, 10 minutes after the blast. This stress increase was measured in the E-W direction, roughly perpendicular to the destress panel. The same stress cell then measured a slow decrease over the next 7 days, stabilizing at a cumulative stress change of 1.3 MPa with the Phase 3 blast as a base-line. On the other hand, the downhole stress cell SC5, in the shadow of the middle panel, detected a stress decrease of 6.3 MPa, 1 hour and 35 minutes after the blast. This measured stress change remained stable over the following 7 days, as no major seismic event or mining activity occurred the region. Finally, SC4, located next to SC3, detected a stress decrease of 1.8 MPa in the N-S direction, roughly parallel to the destress panel. This stress change also remains stable over the following week.

The validation exercise described in Section 2.3 was repeated for the Phase 3 blast based on these stress measurements. Four combinations of α and β were applied to the Phase 3 panels. Values for D are shown in Figure 6.4. Overall, the best match obtained is where $\alpha = 0.05$ and $\beta = 0.95$. However, the overall spread of D varies little between the 4 models, with poor to good stress cell conformity over all scenarios. The stress shells are therefore compared to the position of the stress cells to elucidate the disparity between the models and the measured results. The obtained stress shells for these 4 models are shown in Figure 6.5.

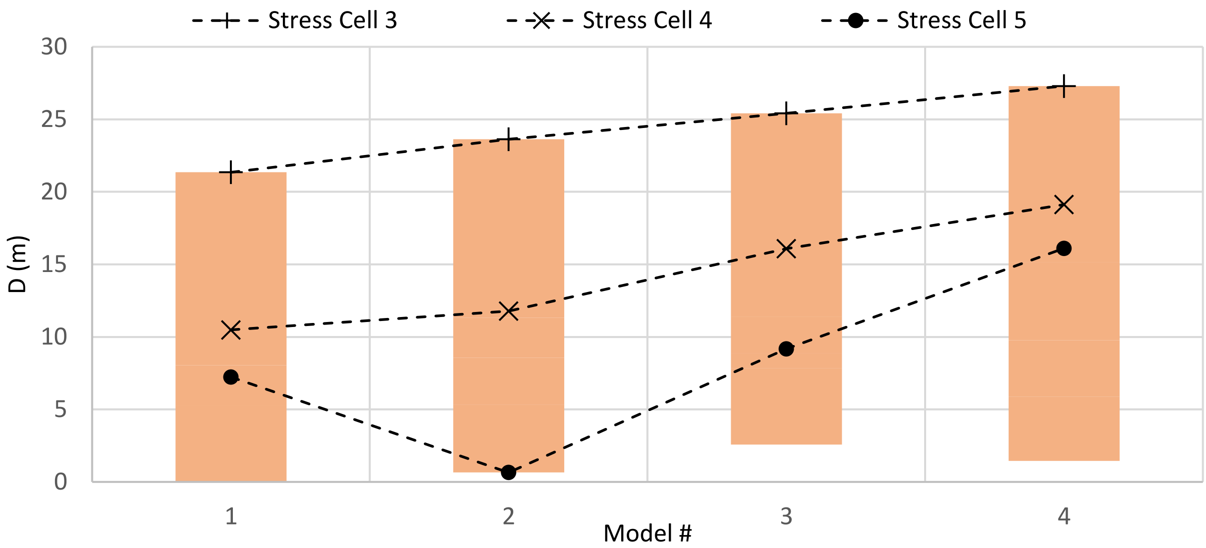

Figure 6.4: Phase 3 validation of models 1-4 based on the distance “D” measured between the stress cell and the stress change shell with the measured stress change. Red bars show the spread of the values of “D” obtained for each model. Poor overall conformity is obtained with all models.

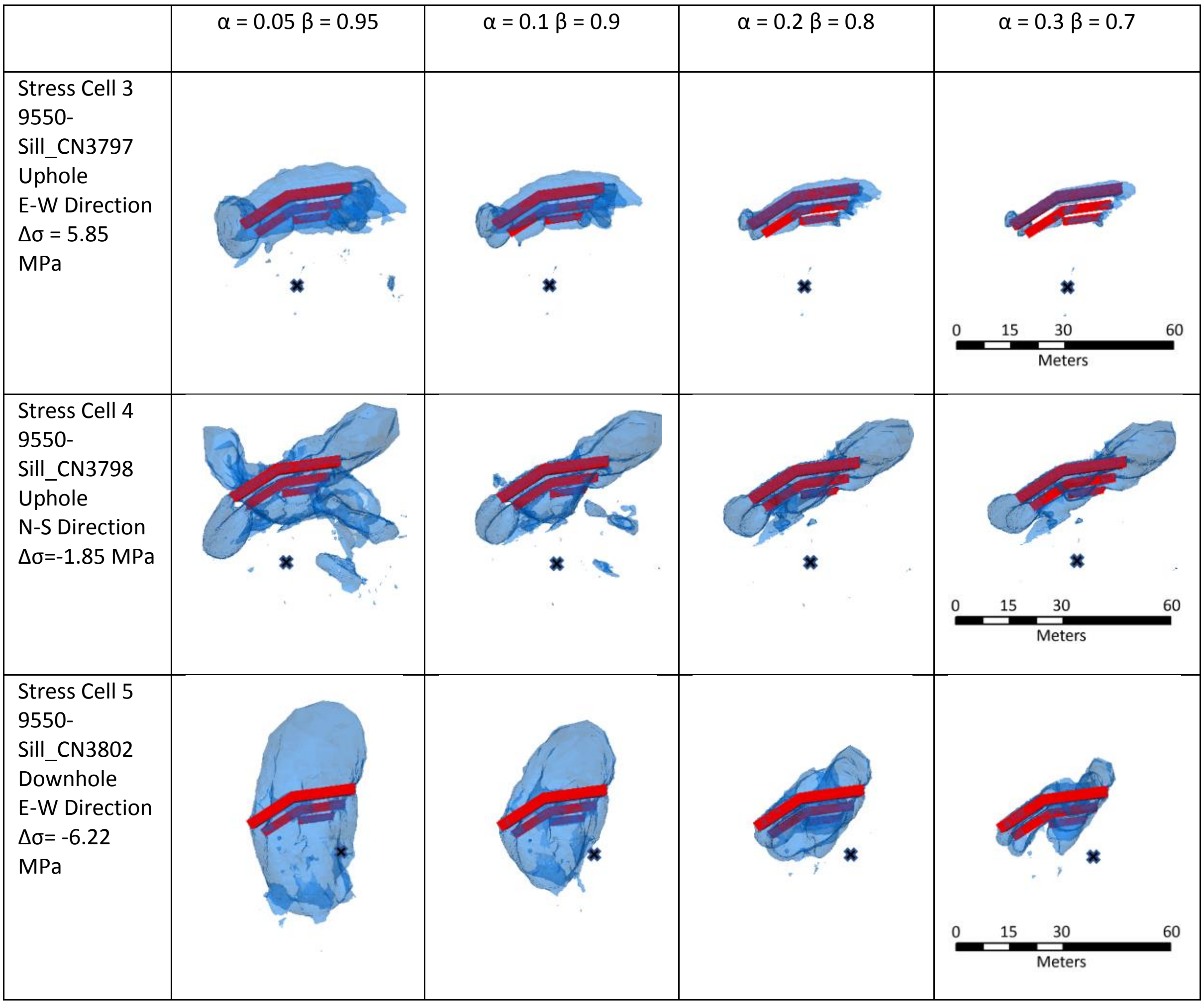

Figure 6.5: Comparison of computed stress change shells and the position of stress cells 3, 4, and 5. The position of SC5 is marked with a black cross. The isotropic model cannot reproduce the measured data from stress cell 3 and 4. However, the results obtained with stress cell 5 can be explained with the isotropic destressing model.

6.2.4 Discussion

For SC5, better conformity between the model results and measured stress is obtained when the rock fragmentation factor is low. SC3 however detects a stress increase in the vicinity of the uppermost panel. Figure 6.6 shows the discrepancy between the results obtained from stress cell 3 and stress cell 5. These stress changes can be interpreted as stress wrapping into the top panel. It is therefore possible that the stiffness of this panel is not reduced, and it is believed that the panel rock could have froze in this portion of the panel. Stress cell orientation error is also a possible cause for poor model conformity, and the effect of this error will be evaluated in Section 6.4.4.2 for SC3, SC4, and Section 6.4.5.1 for SC5.

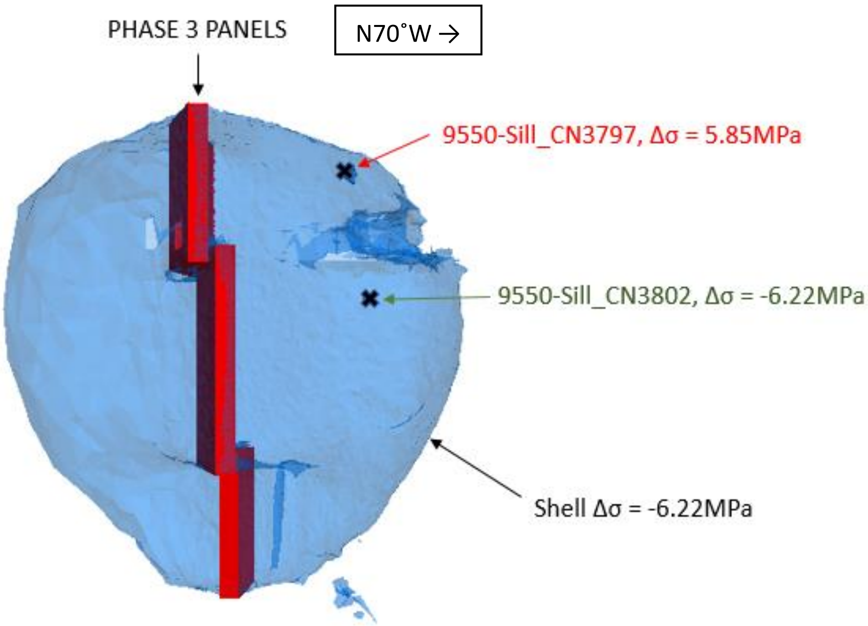

Figure 6.6: Elevation view of the Phase 3 panels, looking N20^{o}E. The stress increase observed at the position of SC5 can be explained with a high destress effect, while the stress increase measured at the position of SC3 cannot.

6.2.5 Evaluation of stress cell orientation error

The effect of stress cell orientation error was evaluated for the isotropic models presented in Table 6.2. The models were validated with stress change contours rotated by 15^{o} in each direction. Based on the discussion in Section 6.3, a corrected stress change measurement of +1 MPa at SC3 was used. The results are shown in Figures 6.7 to 6.9, and the validation exercise shows distinct patterns for each stress cell. For SC3, a good match is obtained with a high destressing effect (α=0.05) and either a +15^{o} or -15^{o} stress cell orientation error. For SC4, a good match is obtained with moderately high destressing (α=0.2), with either orientation error. Finally, SC5 obtains a good match with no error and with high destressing (α=0.1). Overall, the behavior of SC5 is in accordance with good destressing and no orientation error is suggested. The behavior of stress cell 3 and 4 however are not concordant to a single model; the validated destress effect varies with respect to the observed direction. In addition, the measurement concord most with rotated stress change contours. Two conclusions can be drawn: the sill and crown panels should be modelled differently, and the anisotropic destress model should be applied to the crown panel, in accordance with the discussion in section 6.2.4.

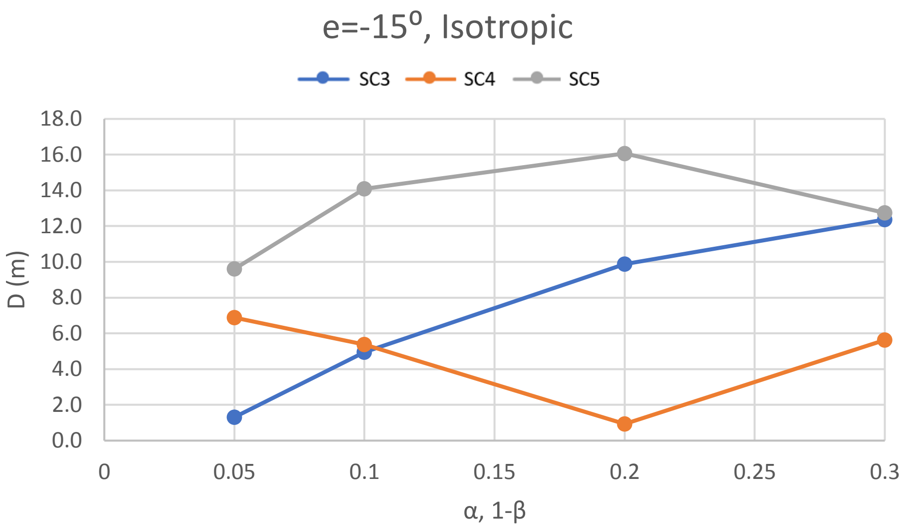

Figure 6.7: “D” with respect to isotropic input parameters, stress cell rotation error of -15⁰

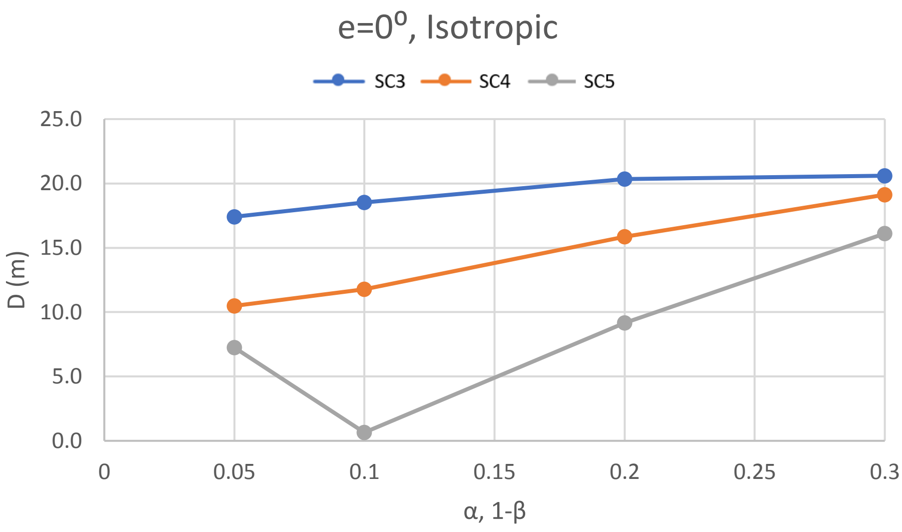

Figure 6.8: “D” with respect to isotropic input parameters, no stress cell rotation error

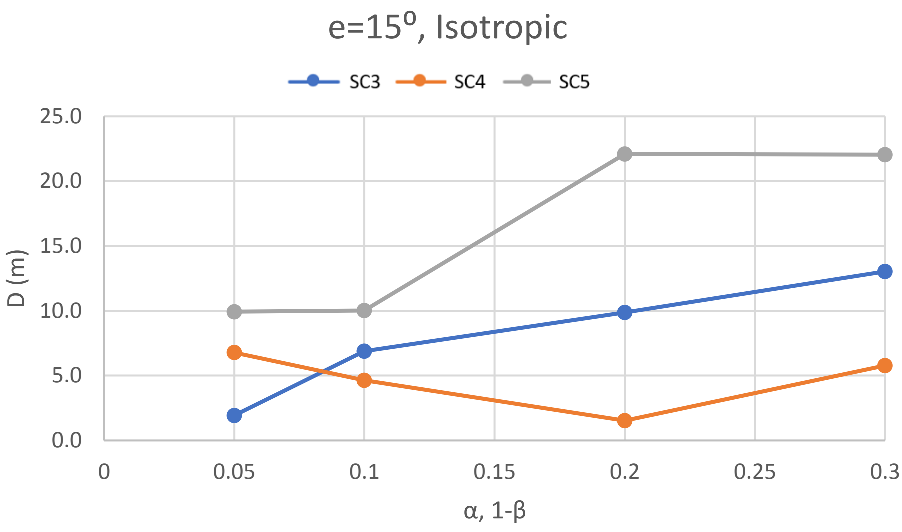

Figure 6.9: “D” with respect to isotropic input parameters, stress cell rotation error of 15^{o}

6.3 Analysis of stress cell data

<u>6.3.1 Rationale of analysis</u>

In this section, all available stress cell data is analyzed to determine if the measured stress changes for Phase 3 are global (at the level of the rock mass) or local (at the level or rock mass blocks). The 10 stress cells logged stress changes over the period between September 21, 2015 and February 2, 2017. Over this period, 3 destress blasts occurred (Phase 1, Phase 2, and Phase 3). In addition, 3 stopes were extracted in the pillar, namely 9631 in the pillar sill, 9511 in the pillar sill, and 9671 in the pillar crown.

It was shown numerically by Sainoki et al. (2016) that local stress concentrations due to the heterogenous nature of a rock mass can explain the fact that rockbursts occur in rock masses where the global stress state does not attain the rock peak properties. This fact was observed by Konicek et al. (2013) in the Lazy colliery with CCBM probes, were the measured in situ stresses in bursting ground were very far from the rock strength. This was also observed at CCM, and a survey of rock burstability criteria computed in the numerical model at the locations of recorded seismic events is provided in Appendix 2.

It is postulated that abnormal stress changes can be attributed to this stress concentration effect. It is therefore important to compare the behavior of adjacent cells to establish if a stress change is global or local before attempting to validate the destress blast model. Stress change data will be also compared to the occurrence of mining and detected micro-seismicity. It is expected that adjacent or nearby stress cells will exhibit the same behavior in terms of stress change magnitude and stress change rate following a seismic event or a mining step if the stress change is global. On the other hand, isolated behavior will indicate either a measurement error or a local change in stresses.

6.3.2 Stress cell behavior over observation period

6.3.2.1 Cumulative stress change: SC1

SC1 (9670-Sill_CN3800_UH-NS) is located in the 9670 sill, uphole along the direction of the assumed minor principal stress. The logged stress changes from SC1 are shown in Figure 6.10. The Phase 1 destress blast caused a 1.2 MPa relaxation. The 9631 Crown blast caused further relaxation to 2.9 MPa. Stress readings at this position are very stable, with little change after immediate stress change, indicates no dynamic effect at its location, with elastic stress redistribution being the sole factor. Stress measurement is also unaffected by seismic events recorded between 9631 crown blast and 9670 stope extraction. Extraction of stope 9670 finally increases the relaxation in the N-S direction to 4.5 MPa, after which the stress cell was lost. Overall, the stress cell detected stable low magnitude stress changes in accordance with the expected redistribution of stresses following stope extraction and destressing.

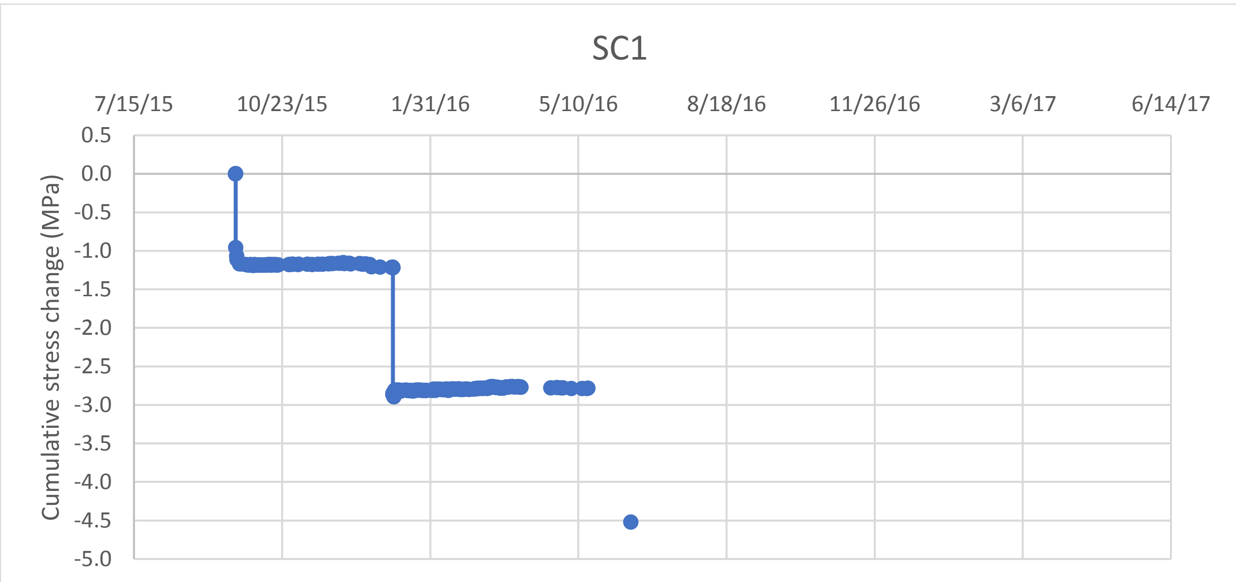

Figure 6.10: Cumulative stress change of SC1 over observation period

6.3.2.2 Cumulative stress change: SC2

SC2 (9670-Sill_CN3801_UH-EW) is also located in 9670 sill, uphole along the direction the major principal stress. The logged stress changes from SC2 are shown in Figure 6.11. The stress cell measured an immediate stress change of -2.7 MPa after the Phase 1 blast, which increased to -3.2 MPa over the next 4 days, and stabilized down to -2.5 MPa over the following 4 months. Extraction of stope 9631 relaxed the stress cell down to -4.4 MPa, which further stabilized to -5.0 MPa. Extraction of stope 9670 caused further destressing down to -6.1 MPa. The cell was lost at the same time as 9670-Sill_CN3800. Stress changes are relatively stable, similar to 9670-Sill_CN3800, with no significant long term stress changes. The behavior is concordant with SC1, and indicates very little stress redistribution in the area. Cumulative stress changes are in accord with elastic model behavior, with relaxation for all mining steps.

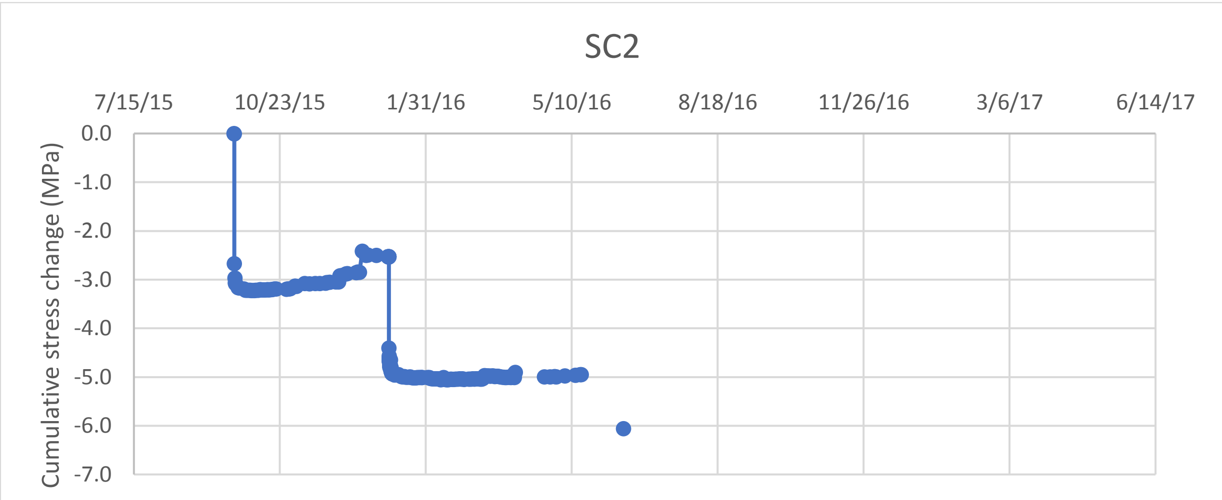

Figure 6.11: Cumulative stress change of SC2 over observation period

6.3.2.3 Cumulative stress change: SC3

SC3 (9550-Sill_CN3797_UH-EW) is installed in 9550-Sill, in crown portion of pillar, close to direction of far field major principal stress. The logged stress changes from SC3 are shown in Figure 6.12. The Phase 1 blast caused an immediate decrease of 0.5 MPa, which accumulated back up to 0.5 MPa. The stope 9631 crown blast caused a high immediate stress increase of 5.5 MPa, accumulating up to 5.9 MPa. The crown blast initiated gradual accumulation of over 2 months, peaking at 46.7 MPa. This stress increase is associated to seismic activity in pillar. A 2.0 MN event, 2.3 MN event, and 1.7 MN events occurred after crown blast. Continued stress increase in region after 9630 crown blast accumulates to about 50 MPa 4 months after the crown blast. Extraction of stope 9670 causes slight increase of cumulative stress from 50.5 MPa to 53.9 MPa, stabilizing to 51.5 MPa over following year. Phase 3 blast caused a cumulative stress to increase to 57.4 MPa, which stabilizes down to 52.8 MPa. The detrimental effect of Phase 3 blast is temporary, with cumulative stress change decreasing over next week from 57.4 MPa to 52.8 MPa. Plastic pillar models demonstrating that the stress accumulation measured by SC3 can not be explained by brittle yielding of the crown excavation damage zone is provided in Appendix 1. It is therefore postulated that the long term stress accumulation at SC3 is local in nature.

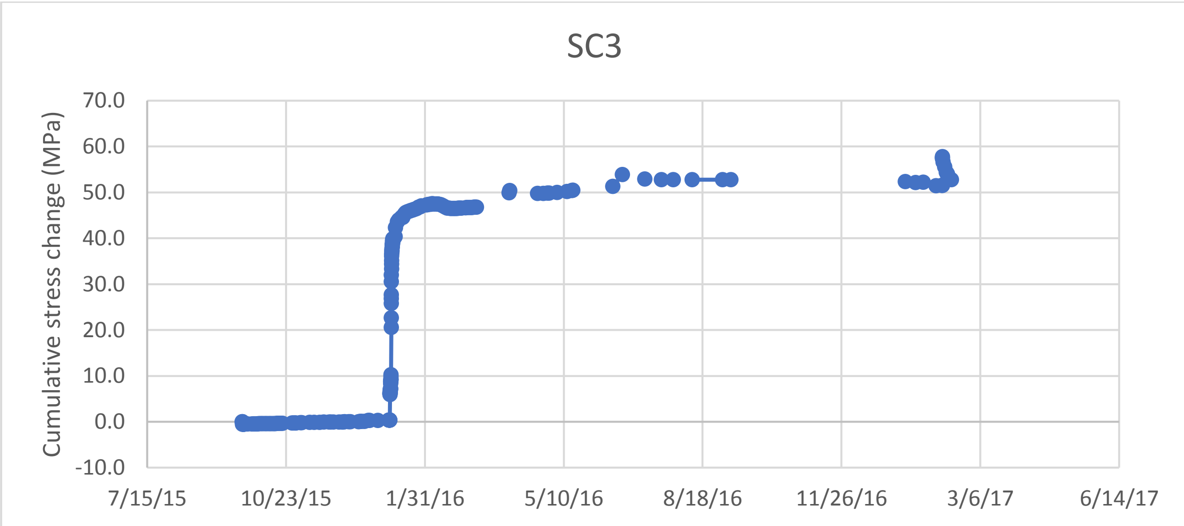

Figure 6.12: Cumulative stress change of SC3 over observation period

<u>6.3.2.4 Cumulative stress change: SC4</u>

SC4 (9550-Sill_CN3798) is in the same position as 9550-Sill_CN3797, but in the N-S direction. The logged stress changes from SC4 are shown in Figure 6.13. The Phase 1 blast caused an immediate stress change of -0.5 MPa which stabilized at a cumulative stress of -0.1. Extraction of stope 9631 causes an additional immediate cumulative stress change of 4.8 MPa. SC4 then experienced a continuous stress increase over period from January 5, 2016 8:00:00 PM to March 8, 2016 6:00:00 AM, where it stabilized at 43.3 MPa. This accumulation is concurrent with multiple seismic events with magnitudes between 1 MN and 2 MN. Extraction of stope 9671 has little effect on this stress cell. Phase 3 blast causes a stable cumulative stress decrease from 43.9 MPa to 42.1 MPa. It exhibits the same high stress concentration effect detected by SC3. As shown in Appendix 1, the stress change magnitude can not be explained by the existence of a yielded excavation damage zone surrounding stope 9631.

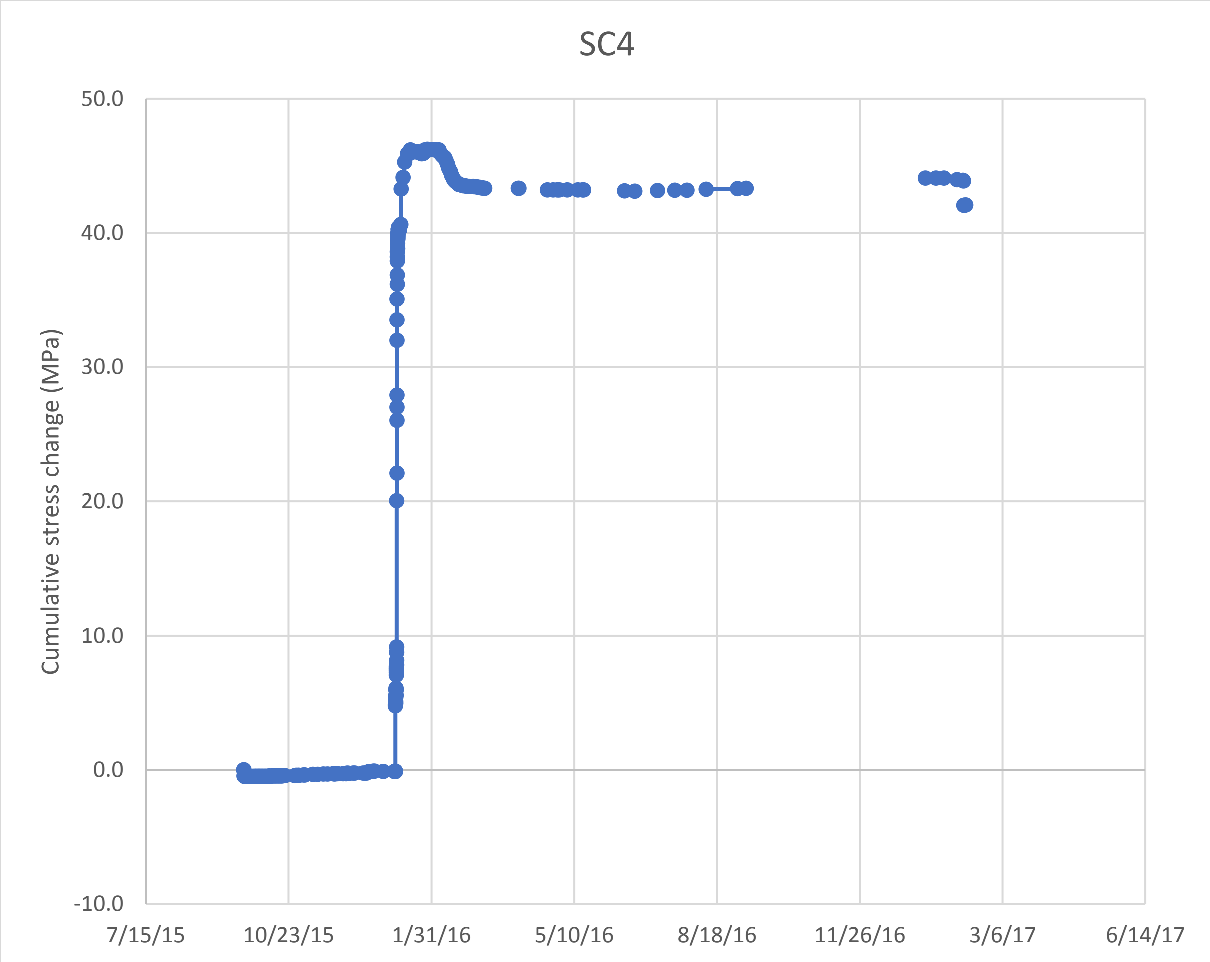

Figure 6.13: Cumulative stress change of SC4 over observation period

6.3.2.5 Cumulative stress change: SC5

SC5 (9550-Sill_CN3802) is installed in sill portion of the pillar, in 9550 sill. It is oriented in the general direction of far field major principal stress. The logged stress changes from SC5 are shown in Figure 6.14. It experienced the expected stable stress decrease following the Phase 1 blast, as it is located directly in the stress shadow. The 9631 crown blast also caused an immediate expected stress increase, which stabilizes to 17.2 MPa over the long term, concurrent with seismic activity in the pillar. Phase 3 blast causes immediate decrease from 20.4 MPa to 14.1 MPa, which stabilized down to 13.1 MPa. As discussed for SC3 and SC4, the high stabilized stress change magnitude can not be fully replicated with a severe excavation damage zone around stope 9631.

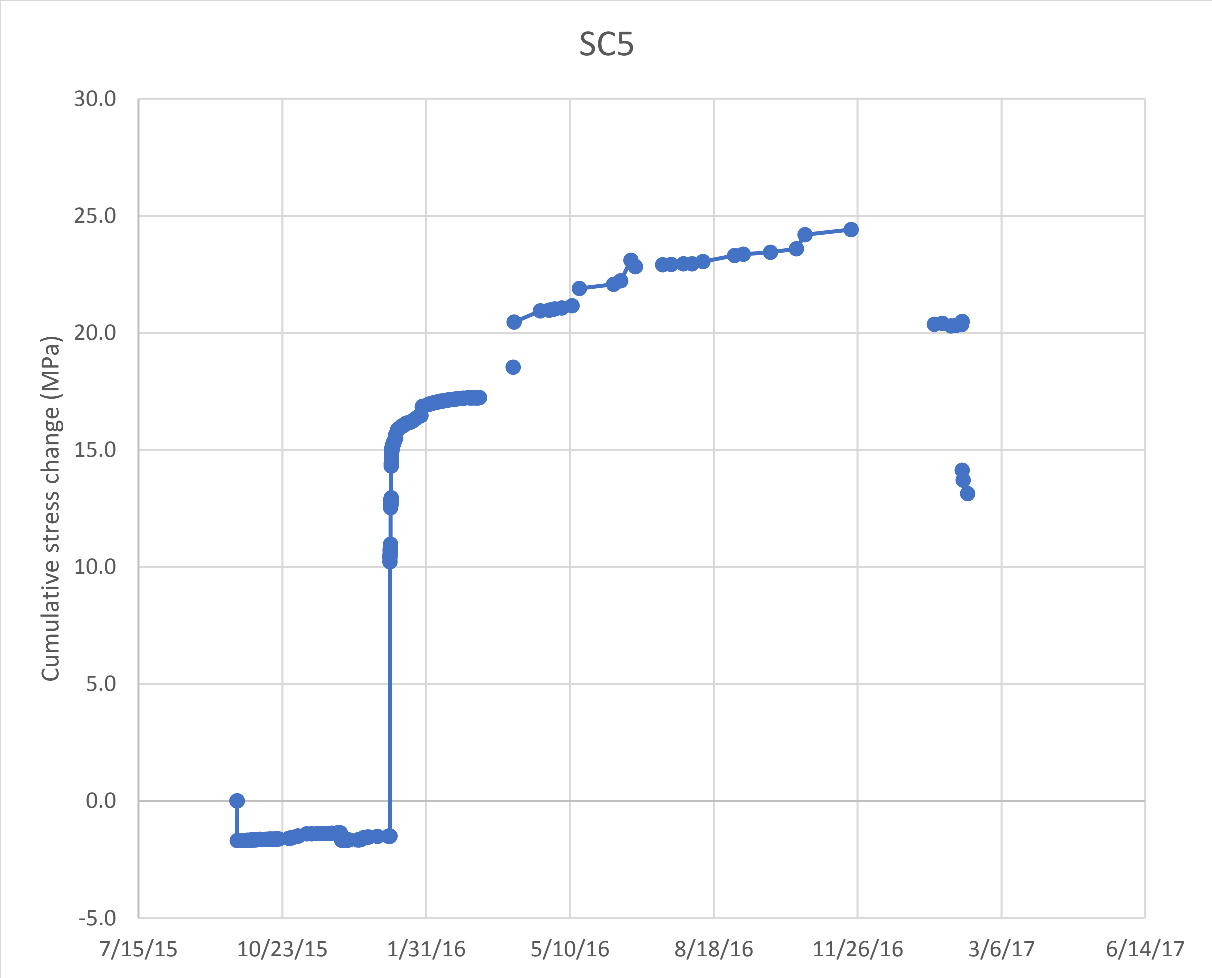

Figure 6.14: Cumulative stress change of SC5 over observation period

6.3.2.6 Cumulative stress change: SC6

SC6 (9550-Sill_CN3804) is installed in sill portion of the pillar, in 9550 sill. It is oriented in general direction of far field intermediate principal stress. The logged stress changes from SC6 are shown in Figure 6.15. It detected a stress change of -0.3 MPa following the Phase 1 blast. Given its relative distance from the blast, the low stress change magnitude is expected. The measured stress oscillated between -0.1 MPa and -0.6 MPa, where stress accumulation can be associated to the extraction of 9631. The 9631 crown blast spiked stress up to 3.7 MPa, stabilizing down to a cumulative 3 MPa stress change. The Phase 2 blast caused a cumulative stress change decrease from 3.5 MPa to 1.4 MPa. As discussed in Section 6.2.2, this stress decrease cannot be explained by elastic stress redistribution following the Phase 2 blast as the stress cell is too distant. Further stress changes are erratic and cannot be directly attributed to mining activity or seismic activity. The Phase 3 blast is not detected by the cell.

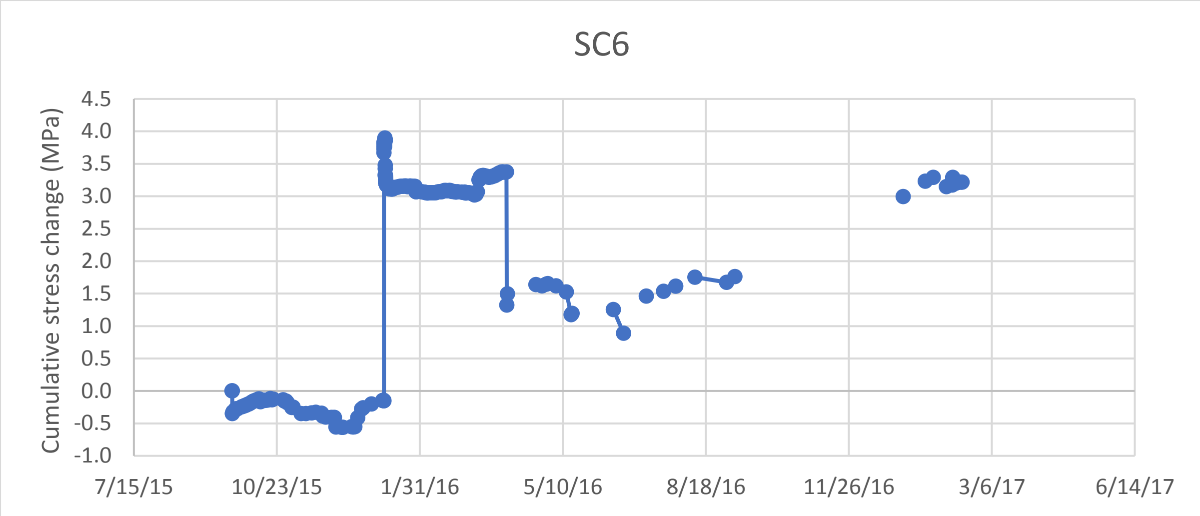

Figure 6.15: Cumulative stress change of SC6 over observation period

6.3.2.7 Cumulative stress change: SC7

SC7 (9590-Sill_CN3799) is installed in the crown portion of the pillar, in the stress shadow of the Phase 1 blast. The logged stress changes from SC7 are shown in Figure 6.16. It is oriented in the E-W direction, which approximates the direction of the far-field major principal stress. The cell detected a major stress decrease of 6.4 MPa in the Phase 1 stress shadow. The elastic stress redistribution back analysis conducted for the Phase 1 blast validated this stress change (see chapter 5). The cell did not detect any further changes following the Phase 1 blast.

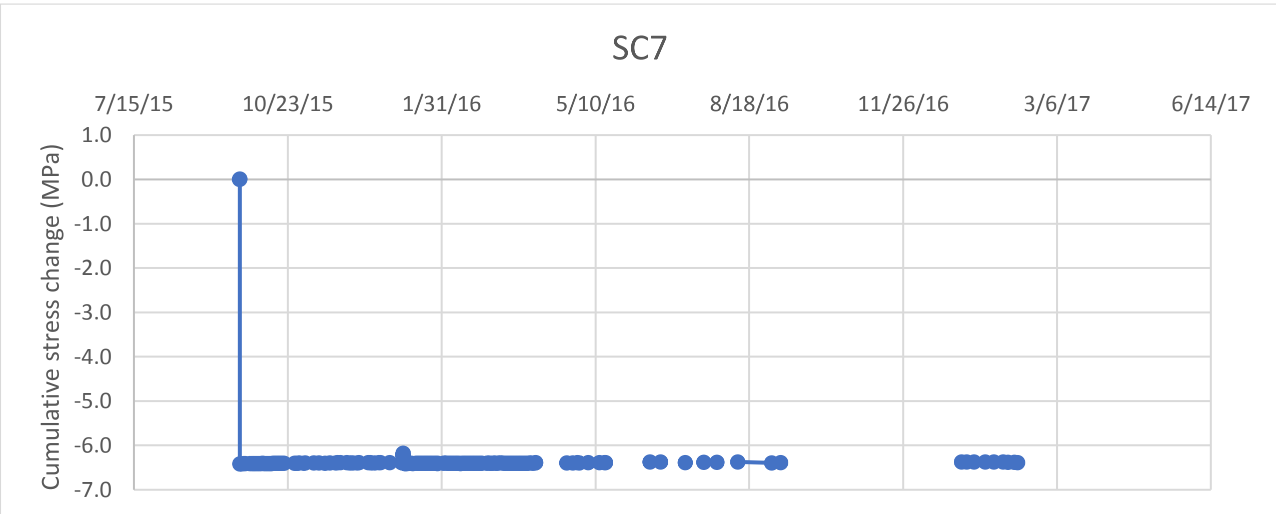

Figure 6.16: Cumulative stress change of SC7 over observation period

6.3.2.8 Cumulative stress change: SC8

SC8 (9590-Sill_CN3803) is installed below SC7, in the sill portion of the pillar. It is also installed in the E-W direction. The logged stress changes from SC8 are shown in Figure 6.17. The cell detected a stress decrease of 1.8 MPa following the Phase 1 blast, which again corroborates with the Phase 1 back analysis conducted in Chapter 5. However, stress re-accumulated back up to a change of -1 MPa between the Phase 1 blast and the stope 9631 crown blast. Unlike SC7, SC8 detected a major stress decrease following the stope 9631 crown blast, with stress decreasing from -1 MPa to -4.5 MPa. Unlike SC4 and SC5 however, the stress stabilized to a realistic level.

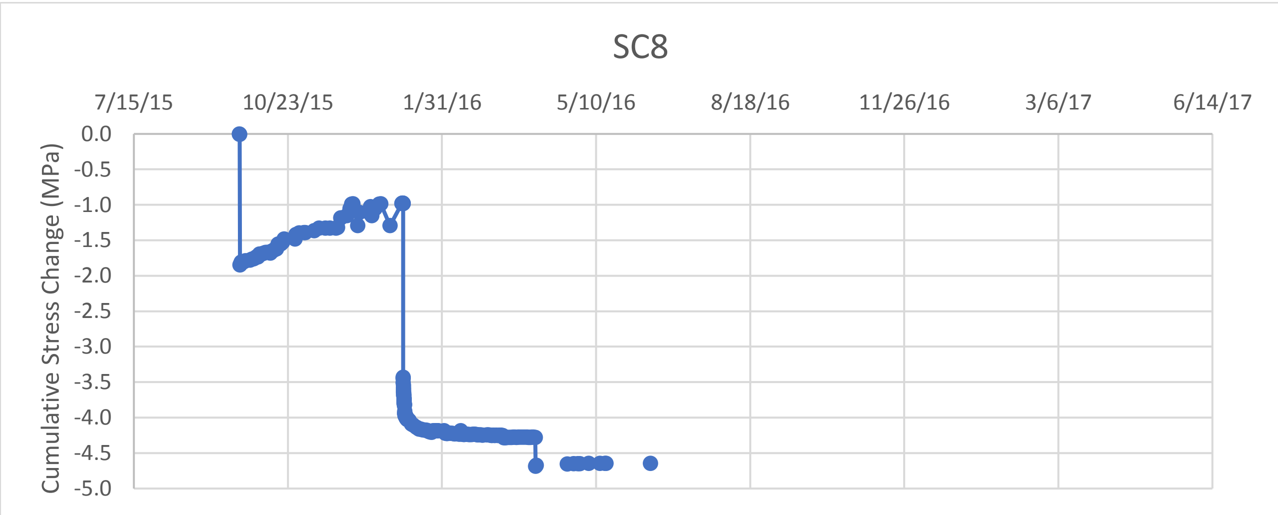

Figure 6.17: Cumulative stress change of SC8 over observation period

6.3.3 Evaluation of 9631 crown blast

Based on the individual assessment of all stress cells in the pillar, it was observed that the high stress accumulation measured by SC3, SC4, and SC5 could be associated to seismic activity in the pillar following the 9631 crown blast.

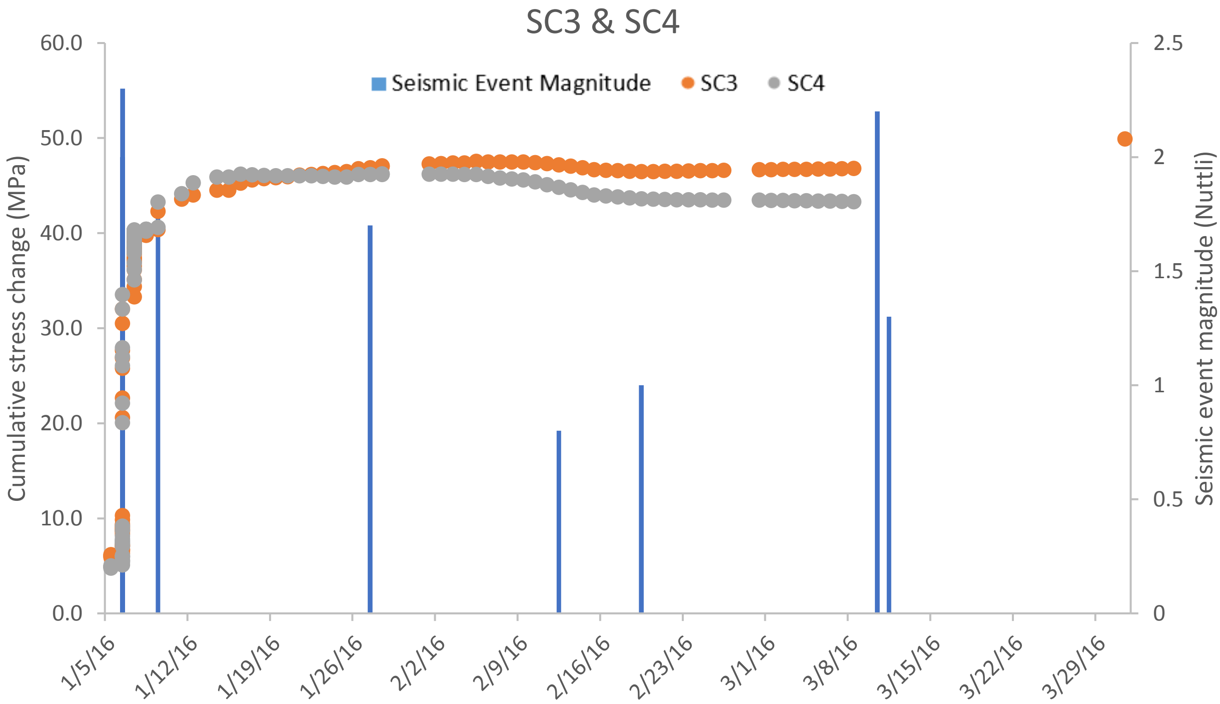

Figure 6.18: Cumulative stress changes measured by SC3 and SC4 overlaid with seismic event magnitudes

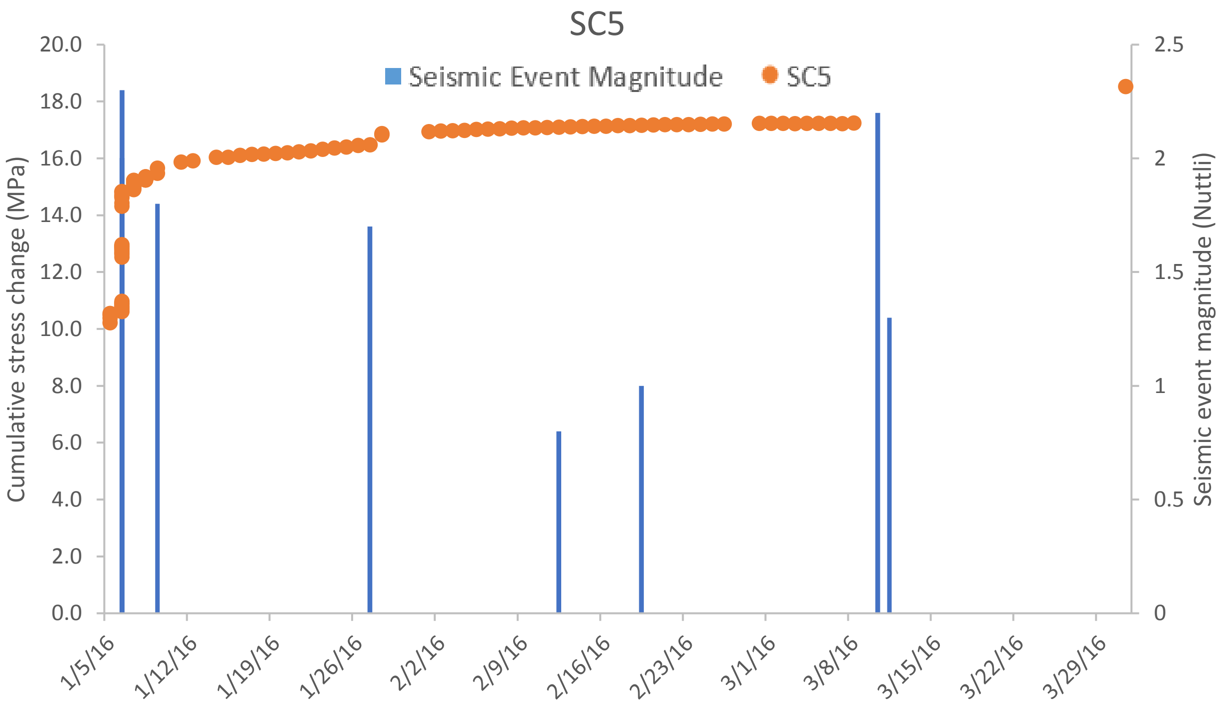

Figure 6.19: Cumulative stress changes measured by SC5 overlaid with seismic event magnitudes

Figures 6.18 and 6.19 show the stress changes measured from the 9590 sill following the stope 9631 crown blast, overlain with the seismic event magnitudes. It shows a partial relationship between measured rapid accumulation or release of stress and nearby seismic activity. Two major seismic events occurred on the same day of the stope 9631 crown blast on January 6, 2016: a 2.3 magnitude event at 8:17, and a 2.3 magnitude event at 18:51. Both of these events triggered an abrupt and permanent increase in E-W stress in the pillar crown and sill, and an abrupt increase in the N-S direction in the pillar crown. On average, the stress accumulated at a rate approximately 1 MPa/hour over the 24 hours following this blast in the pillar crown. In the pillar sill, only the first event triggered stress accumulation at a rate of 0.1 MPa/hr over 24 hours.

This was followed on January 9 by a 1.8 magnitude seismic event at 6:07. This event also caused rapid stress accumulation in the pillar which was detected by SC3 and SC4. The stress accumulated at a rate of roughly 0.5 MPa/hour over 4 hours for both cells in the crown. No abrupt stress change was detected in the sill.

Finally, a 2.2 magnitude event occurred at 11:22 on March 10, 2016, followed by a 1.3 magnitude event at 21:11 on March 11, and can be associated to the increase measured by SC3 and SC5 between March 8 and March 31. However, these stress cells were not logging data during over this period and the rate of stress accumulation could not be calculated. Overall, only 2 events can be definitively associated to a detected change in stress. This can be seen following the stope 9631 crown blast, where the long-term accumulation of stress in the 9590 sill and crown stress cells occurs over a period of consistent micro-seismic activity. However, the effect on stress measurement of low magnitude events is hard to detect. Nonetheless, these results show that high magnitude seismicity cause global stress changes corroborated by multiple stress cells.

6.3.4 Evaluation of Phase 3 blast

No seismic events were detected after the Phase 3 blast in the crown pillar. The absence of micro-seismicity corroborates with the stable stress change measured by SC4. However, a stress reduction rate of 0.08 MPa/hour was measured over 156 hours for SC3. SC5 also detected relaxation, but at a much lower rate. Considering that these stress cells exhibited stress changes that can be directly associated to micro-seismicity in the past, and that these stress changes were global, the absence of seismicity after the Phase 3 blast suggests that the sudden stress increase and gradual stress decrease detected by SC3 is local. The comparison of adjoining cells is further discussed in Section 6.3.5.

6.3.5 Comparison of adjoining stress cell behaviour

In this section, the behaviour of adjoining cells is compared. The main purpose is to validate the data that will be used for the Phase 3 back analysis. However, anomalous behaviour for other stages will also be discussed. Table 6.4 provides the position of all stress cells and the rationale for why they are considered to be adjoining. Table 6.5 provides the stress stabilization rates following each mining and destressing step for comparison between adjoining cells.

Table 6.4: Location of adjoining stress cells

Stress Cell	Elevation	Orientation	Adjoining stress cells
9670-Sill_CN3800	UH	N-S	2 perpendicular UH cells in 9670 sill
9670-Sill_CN3801	UH	E-W	
9550-Sill_CN3797	UH	E-W	2 perpendicular UH cells in 9550 sill, DH cell in 9550 sill
9550-Sill_CN3798	UH	N-S	
9550-Sill_CN3802	DH	E-W	
9550-Sill_CN3804	WH	N-S	
9590-Sill_CN3799	UH	E-W	UH and DH cell in 9590 sill
9590-Sill_CN3803	DH	E-W	

Table 6.5: Behaviour of adjoining cells following stope extraction and destress blasts

		Phase 1	Stope 9631	Phase 2	Stope 9511	Stope 9671 L1	Stope 9671 L2	Phase 3
9670-Sill_CN3800_UH-NS	SC1	L-R	S	N/A	N/A	N/A	N/A	N/A
9670-Sill_CN3801_UH-EW	SC2	M-R	M-R	N/A	N/A	N/A	N/A	N/A
9550-Sill_CN3797_UH-EW	SC3	L-A	H-A	N/A	N/A	N/A	L-R	F-R
9550-Sill_CN3798_UH-NS	SC4	L-A	H-A	N/A	N/A	N/A	S	S
9550-Sill_CN3802_DH-EW	SC5	L-A	M-A	N/A	N/A	N/A	L-R	L-R
9550-Sill_CN3804_WH-NS	SC6	L-A	M-A	N/A	N/A	N/A	S	S
9590-Sill_CN3799_UH-EW	SC7	S	S	N/A	N/A	N/A	S	S
9590-Sill_CN3803_DH-EW	SC8	L-A	L-R	N/A	N/A	N/A	N/A	N/A

* L, M, F: slow, moderate, fast. R, S, A: relaxation, stable, accumulation. Slow stress change rates have a magnitude <0.1 MPa/h. Fast stress change has a magnitude >1.0 MPa/h

There are two occurrences where adjoining stress cell behavior does not match: after the extraction of stope 9631, between stress cells SC1 and SC2 in 9670 sill, and after Phase 3 blast, between SC3, SC4, and SC5 in 9550 sill. In the first case, SC1 measured stable stress in the N-S direction, while nearby SC2 measured a moderately fast relaxation of 0.14 MPa/day over 4 days after the crown blast. In the second case, SC4 installed in the N-S direction detected a stable stress change after the Phase 3 blast in the N-S direction, while SC3 measured a fast decay of stress of 0.77 MPa/day over 6.5-day period after the blast. SC5, installed downhole from the same drift, corroborates with neither, having measured a slow stress release of 0.28 MPa/day over 3.6 days. The cumulative stress changes over this period for SC3, SC4, and SC5 are given in Figure 6.20.

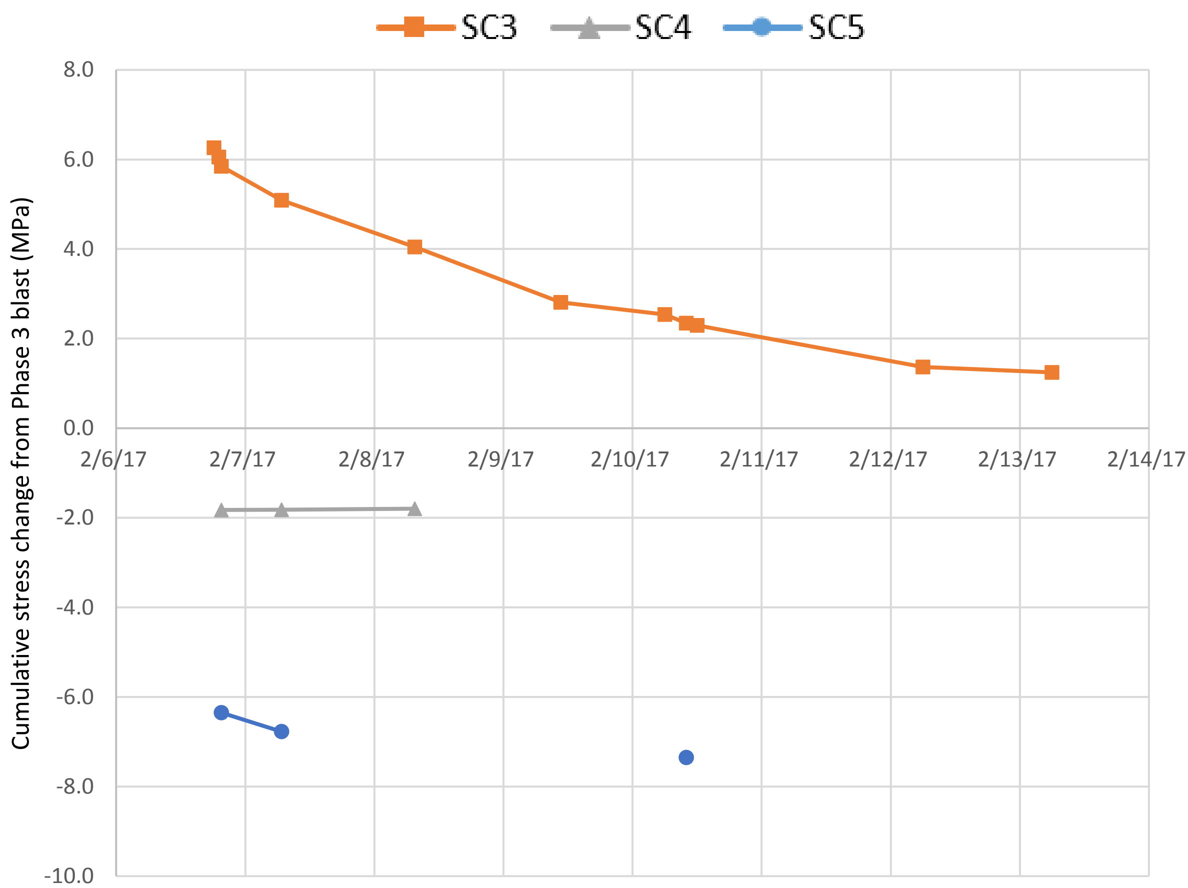

Figure 6.20: Cumulative stress changes for SC3, SC4, and SC5 after the Phase 3 destress blast

Overall, SC3 is in the stress shadow of a sill panel and measured a stress increase in E-W direction. Given the E-W axis is almost normal to the panel, the stress cell data reveals that the crown panel in the Phase 3 blast did not destress stopes in its shadow, regardless of the time the stress change data is acquired. However, the sill panel successfully destressed the sill stopes, as demonstrated by SC5. Stress cell 4 also measured a stress N-S stress relaxation in the pillar crown. There are two mutually exclusive hypotheses that can explain behavior of these stress cells:

- The stress increase following the Phase 3 blast measured by SC3 is local, with a local stress relaxation that stabilizes to global stress change
- The stress measured by SC4 is stable at a local level, and relaxation measured at SC3 and SC5 occurs globally

Since the stress increase magnitude detected by SC3 is too high to replicate, the first hypothesis is deemed more likely than the second. Therefore, it is assumed that the stabilized stress at SC3 (approximately 1 MPa) is the global rock mass response to the Phase 3 blast. The Phase 3 back analysis will therefore use this value for model validation. The corrected stress changes for the stress cells that are used to validate the Phase 3 blast are given in Table 6.6.

Table 6.6: Stress changes used for Phase 3 validation

#	Name	Direction	Measured Stress Change (MPa)
SC3	9550-Sill_CN3797_UH-EW	XX	1.00
SC4	9550-Sill_CN3798_UH-NS	YY	-1.85
SC5	9550-Sill_CN3802_DH-EW	XX	-6.22

6.4. Validation of Phase 3 Destress Blast

6.4.1 Study Parameters

Overall, 5 parameters are varied for the Phase 3 validation:

- Out of plane rock fragmentation factor (α_1)
- In-plane rock fragmentation factor (α_2)
- Elevations where anisotropic model is applied (Anisotropic model elevation cut-off)
- The far field stress magnitude
- Stress cell orientation error

6.4.1.1 Anisotropic parameters (α_1 and α_2)

Given that SC3 measured a stress increase in the stress shadow of the Phase 3 panels, it is hypothesized that the out-of-plane rock fragmentation factor for the crown panel is high. Consequently, high stress will wrap over the well destressed sill panel into the poorly destressed crown panel, resulting in a minor stress increase in the E-W direction. On the other hand, the in-plane rock fragmentation factor will be kept low in accordance with the rock fragmentation factor of the Phase 1 blast. In all, α_1 will be varied between 1.0 and 0.5, while α_2 will be varied between 0.05 and 0.3.

6.4.1.2 Anisotropic model elevation cut-off

As shown in section 6.2.4, it is postulated that the sill portion of the panel is well destressed, while the crown portion is frozen. The elevation where the applied destress blasting model transitions from isotropic to anisotropic is referred to as the anisotropic model elevation cut-off. Two cut-offs are investigated: the floor 3550L and the roof of 3550L.

6.4.1.3 Far-field stress magnitude

The high stress accumulation following the 9631 crown blast is corroborated between multiple stress cells (SC3, SC4, and SC5) and can be directly associated to high magnitude seismic events in the pillar (see Section 6.3.2). Therefore, even though the excavation damage zone models cannot replicate the magnitude of the stress increase, the effect of high deviatoric stress accumulation in the pillar will still be investigated. In the first scenario “FF”, the model far field stresses are calibrated to obtain a stress increase tensor at the position of SC3 that matches the stress change measurements of SC3 and SC4 (51.5 MPa in the E-W direction, and 42.1 MPa in the N-S direction). In the second scenario “FF2”, the model far-field stresses are calibrated to yield a 20.5 MPa stress increase at the location of SC5.

6.4.1.4 Stress cell orientation error

In Section 6.2.5, it is shown that the stress cell orientation error has a significant effect on model conformity in the range of -15^{o} to +15^{o}. The effect of stress cell orientation error will therefore also be implemented to the Phase 3 blast anisotropic models. The range of investigation remains the same at +/-15˚.

6.4.2 Methodology

A damage zone of 16 times the hole diameter is assumed and treated as the targeted panel mass (Andrieux 2005), yielding a 3 m thick panel. To reflect the tendency of fractures to propagate in the direction of the major principal stress, an anisotropic stress reduction factor and rock fragmentation factor is applied. For all models, the stress reduction factor β is calculated from the applied rock fragmentation factor α assuming the relation α = 1-β. To begin, the stress tensor applied to the destress panel zone is calculated as:

$$[\sigma_{123\,destress}] = \begin{bmatrix} \alpha_1\sigma_1 & 0 & 0 \\ 0 & \alpha_2\sigma_2 & 0 \\ 0 & 0 & \alpha_3\sigma_3 \end{bmatrix} \quad [6.1]$$

where α_1 is the rock fragmentation factor in the direction of σ_1, α_2 is the rock fragmentation factor in the direction of σ_2, and α_3 is the rock fragmentation factor in the direction of σ_3. However, it is assumed that the fragmentation and stress release effect is transversely isotropic, with the out-of-plane destress parameter being α_1, and the in-plane parameters α_2 and α_3 being equal. Therefore, for all following equations, α_2 will substitute α_3. The out-of-plane rock fragmentation factor E_1 is expressed as:

$$E_1 = \alpha_1 * E \quad [6.2]$$

where E is the pre-destress rock mass modulus of the panel. The in-plane Poisson's ratio v_{23} is calculated based on the out-of-plane rock fragmentation factor:

$$\upsilon_{23} = \upsilon * (2 - \alpha_1) \quad [6.3]$$

Finally, the in-plane shear modulus G_{23} is calculated as:

$$G_{23} = \frac{E_1}{2(1+\upsilon_{23})} \quad [6.4]$$

The in-plane rock fragmentation factor E_2 is expressed as:

$$E_2 = E_3 = \alpha_2 * E \quad [6.5]$$

The out-of-plane Poisson ratio v_{12} is calculated based on the in-plane rock fragmentation factor:

$$\upsilon_{12} = \upsilon_{13} = \upsilon * (2 - \alpha_2) \quad [6.6]$$

Finally, the out-of-plane shear modulus G_{12} is calculated as:

$$G_{12} = G_{13} = \frac{E_2}{2(1+\upsilon_{12})} \quad [6.7]$$

To reduce application time in the model, the Phase 3 panel is cut in 3 m by 3 m blocks and the average stress tensor is calculated. The average post-destress tensor is then calculated with Equation 6.1 and applied to the respective block. Given that the rock fragmentation does not vary across the panel, the values E_1, E_2, G_{12} and G_{13} calculated with Equations 6.2 to 6.7 are applied to the entire panel.

6.4.3 Models

Overall, 48 models were tested for the Phase 3 blast. Their input parameters are summarized in Table 6.7.

Table 6.7: Phase 3 validation models

Model #	Stress State	Upper extent	α_1	β_1	α_2	β_2	Model Description
1			0.05	0.95	0.05	0.95	Isotropic models
2			0.1	0.9	0.1	0.9	
3			0.2	0.8	0.2	0.8	
4			0.3	0.7	0.3	0.7	
5			0.5	0.5	0.05	0.95	Anisotropic models, anisotropic constitutive models applied to all panels
6					0.1	0.9	
7					0.2	0.8	
8					0.3	0.7	
9			1	0	0.05	0.95	
10					0.1	0.9	
11					0.2	0.8	
12					0.3	0.7	
13		3550L	1	0	1	0	Extreme case models with full extraction of sill panel, extreme variation of crown panel anisotropic parameters
14					0.05	0.95	
15			0.5	0.5	0.05	0.95	Anisotropic models, anisotropic constitutive models applied to crown panel above 3550L
16					0.1	0.9	
17					0.2	0.8	
18					0.3	0.7	
19			1	0	0.05	0.95	
20					0.1	0.9	
21					0.2	0.8	
22					0.3	0.7	
23		3540L	1	0	1	0	Extreme case models with full extraction of sill panel, extreme variation of crown panel anisotropic parameters
24					0.05	0.95	

Table 6.7 (continued): Phase 3 validation models

Model #	Stress State	Upper extent	α1	β1	α2	β2	Model Description
25		3540L	0.5	0.5	0.05	0.95	Anisotropic models, anisotropic constitutive models applied to crown panel above 3540L
26					0.1	0.9	
27					0.2	0.8	
28					0.3	0.7	
29			1	0	0.05	0.95	
30					0.1	0.9	
31					0.2	0.8	
32					0.3	0.7	
33	FF	3540L	0.5	0.5	0.05	0.95	Anisotropic models, anisotropic constitutive models applied to crown panel above 3540L. Far field stress calibrated to match SC3 and SC4 cumulative stress increase
34					0.1	0.9	
35					0.2	0.8	
36					0.3	0.7	
37			1	0	0.05	0.95	
38					0.1	0.9	
39					0.2	0.8	
40					0.3	0.7	
41	FF2	3540L	0.5	0.5	0.05	0.95	Anisotropic models, anisotropic constitutive models applied to crown panel above 3540L. Far field stress calibrated to match SC5 cumulative stress increase
42					0.1	0.9	
43					0.2	0.8	
44					0.3	0.7	
45			1	0	0.05	0.95	
46					0.1	0.9	
47					0.2	0.8	
48					0.3	0.7	

6.4.4. Analysis of SC3 and SC4

Stress cell 3 and stress cell 4 are both installed in the pillar crown from 9590 sill. SC3 measured a stress increase of 1 MPa in what is assumed to be the E-W direction. SC4 measured a stress decrease of 1.85 MPa in the N-S direction. The cells are near each other and will therefore be analyzed in conjunction.

6.4.4.1 Effect of panel anisotropy

The distance "D" was measured for models 5-12, and the procedure described in Section 6.2.5 was used to examine the effect of stress cell orientation error ("e"). The obtained values for

D are plot with respect to the in-plane fragmentation factor α_2, as shown in Figure 6.21 for SC3 and Figure 6.22 for SC4.

If no rotation error is considered, models 1 to 8 conform poorly to the measured stress changes from SC3 and SC4. For SC3, the distance D between the computed stress change contour for an E-W stress increase of 1 MPa and the stress cell ranges between 10.3 m and 22.4 m for all combinations of α_1 and α_2. Similarly, with SC4, the N-S stress decrease contours for 1.85 MPa are 10.7 m to 15.3 m away from the position of SC4. When stress cell position error is considered however, the distance D decrease overall for both SC3 and SC4: down to 1.5 m for SC3 and 1.9 m for SC4.

However, for both stress cells, the observed trend is that a lower in plane rock fragmentation factor (α_2 = 0.05) gives the best results, as shown in Figures 6.21 and 6.22. Changing the out-of-plane rock fragmentation factor from 1 to 0.5 yields no clear trend, but overall the model with best conformity for both SC3 and SC4 is model 1, with factor α_2 = 0.05, and α_2 = 1. However, these holistic parameters are highly unlikely. While blasting induced fracture propagation will tend to extend in the direction of the major principal stress, the overall effect of this phenomenon is likely not as severely anisotropic as the holistic parameters would suggest. Therefore, further investigation is required (see section 6.4.5.4). In addition, it is evident from the results that obtaining an E-W stress increase inside the expected panel stress shadow is not possible with any combination of α_1 and α_2. It is shown however that the measured stress increase at SC3 could instead be stress wrapping around the sides the crown panel, which would be detected if the stress cell is rotated 15 degrees counter clockwise, as shown in Figure 6.23. With a rotation of -15 degrees, the stress cell now intersects stress wrapping around the panel rather than staying within the panel stress shadow.

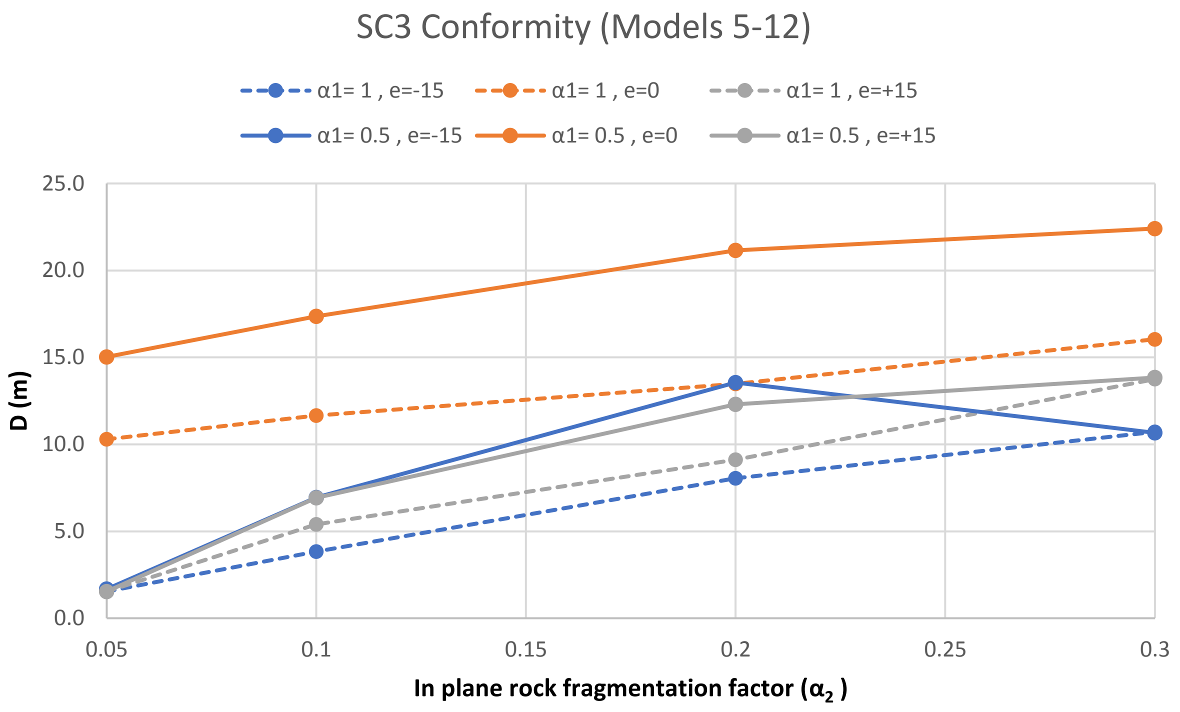

Figure 6.21: SC3 conformity with respect to α2 for models 5-12

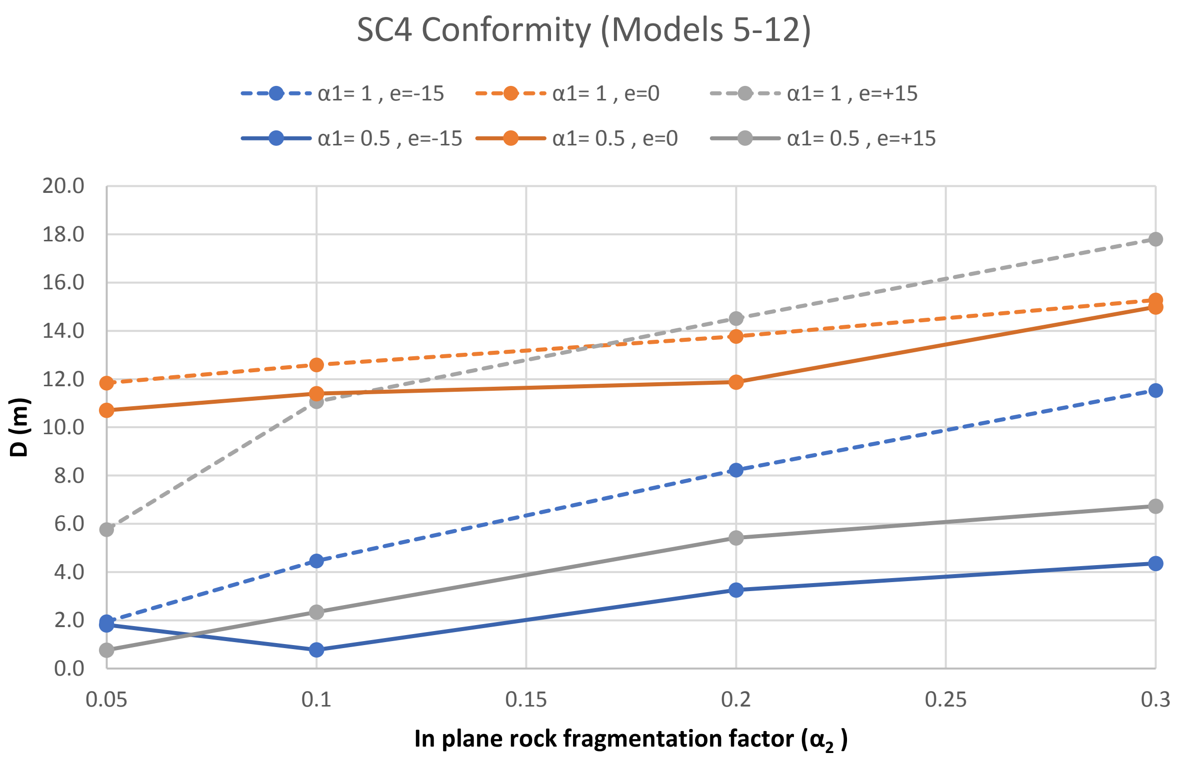

Figure 6.22: SC4 conformity with respect to α2 for models 5-12

6.4.4.2 Effect of stress cell orientation angle (1-12, 15-22, 25-48)

Figure 6.23 aggregates data from all models and demonstrates that higher average model conformity is obtained for SC3 and SC4 when a stress cell orientation error "e" of +/- 15˚ is assumed. The obtained ranges for "D" are plot in red for SC3 and in blue for SC4. Given e = 0, the best "D" obtained for both cells is approximately 10 m. It is therefore postulated that the stress cell is not perfectly oriented along the N-S and E-W axes given that no model can adequately reproduce the measured stress changes along these axes.

These results demonstrate a major shortcoming of uniaxial stress cells. The point of this study is to validate destress blasting by varying the panel input parameters α_1 and α_2. However, "D" is very sensitive to orientation angle of the stress cell. Rotating the stress cell slightly can cause a change in measured stress of equivalent importance to varying the destress blast input parameters. Therefore, e=-15 degrees will be assumed for SC3 and SC4 when investigating the effects of other parameters.

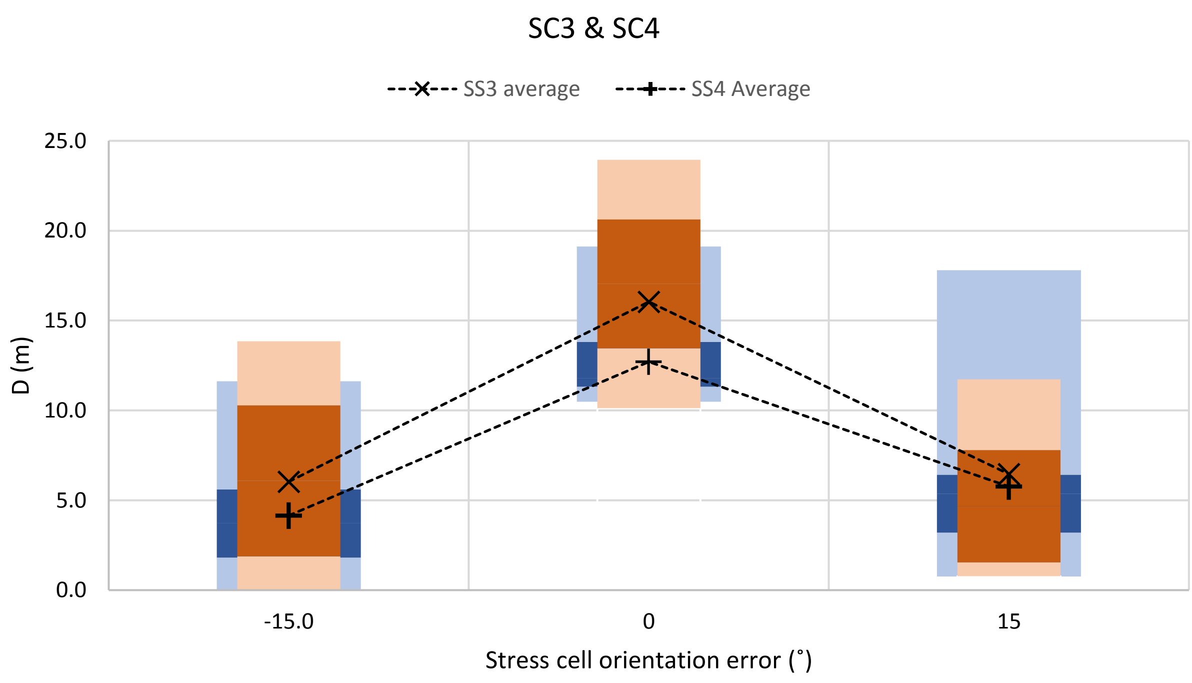

Figure 6.23: Compilation of model conformity with respect to stress cell orientation error (e) for SC3 & SC4. Red bars show the spread of results for "D" obtained SC3. The dark red shows the spread of the middle 50% of the models. Bars in blue show the spread of results for "D" of SC4. The dark blue shows the middle 50% of values for "D" obtained.

6.4.4.3 Effect of the in-plane rock fragmentation factor (α_2) (1-12, 15-22, 25-48)

Figures 6.24 and 6.25 aggregate all model conformity results and plot them with respect to the in-plane rock fragmentation factor. The graphs also compare conformity with no stress cell rotation error (in orange) and with a -15˚ stress cell rotation error (in blue).

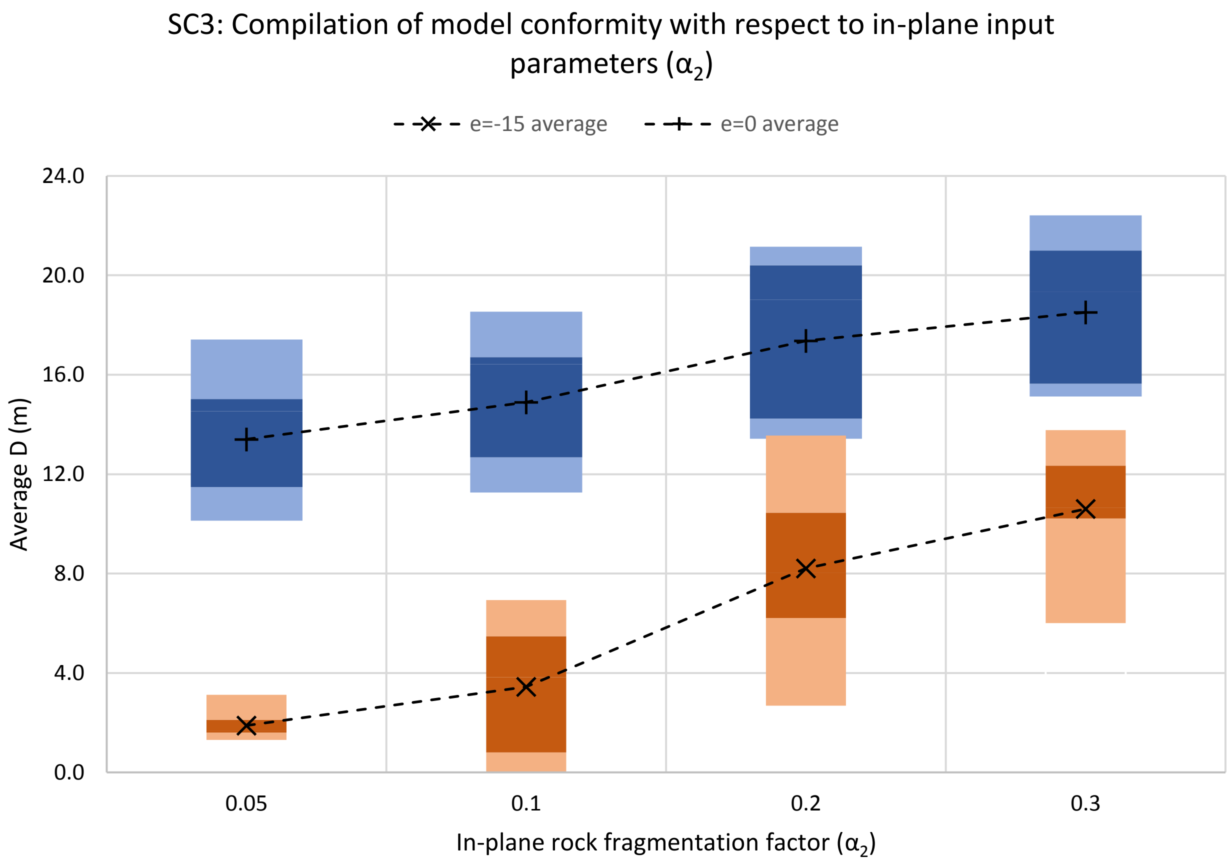

Figure 6.24: Compilation of model conformity for SC3 with respect to In-plane input parameters (α_2). Bars in red show the spread of results for "D" obtained with an error "e" of -15˚. The dark red shows the spread of the middle 50% of the models. Bars in blue show the spread of results for "D" with no orientation error. The dark blue shows the middle 50% of values for "D" obtained. There is no overlap between the bars, showing that for a constant value of α_2, every single measurement of "D" with an error of -15˚ is lower than the measurement of "D" obtained with no orientation error.

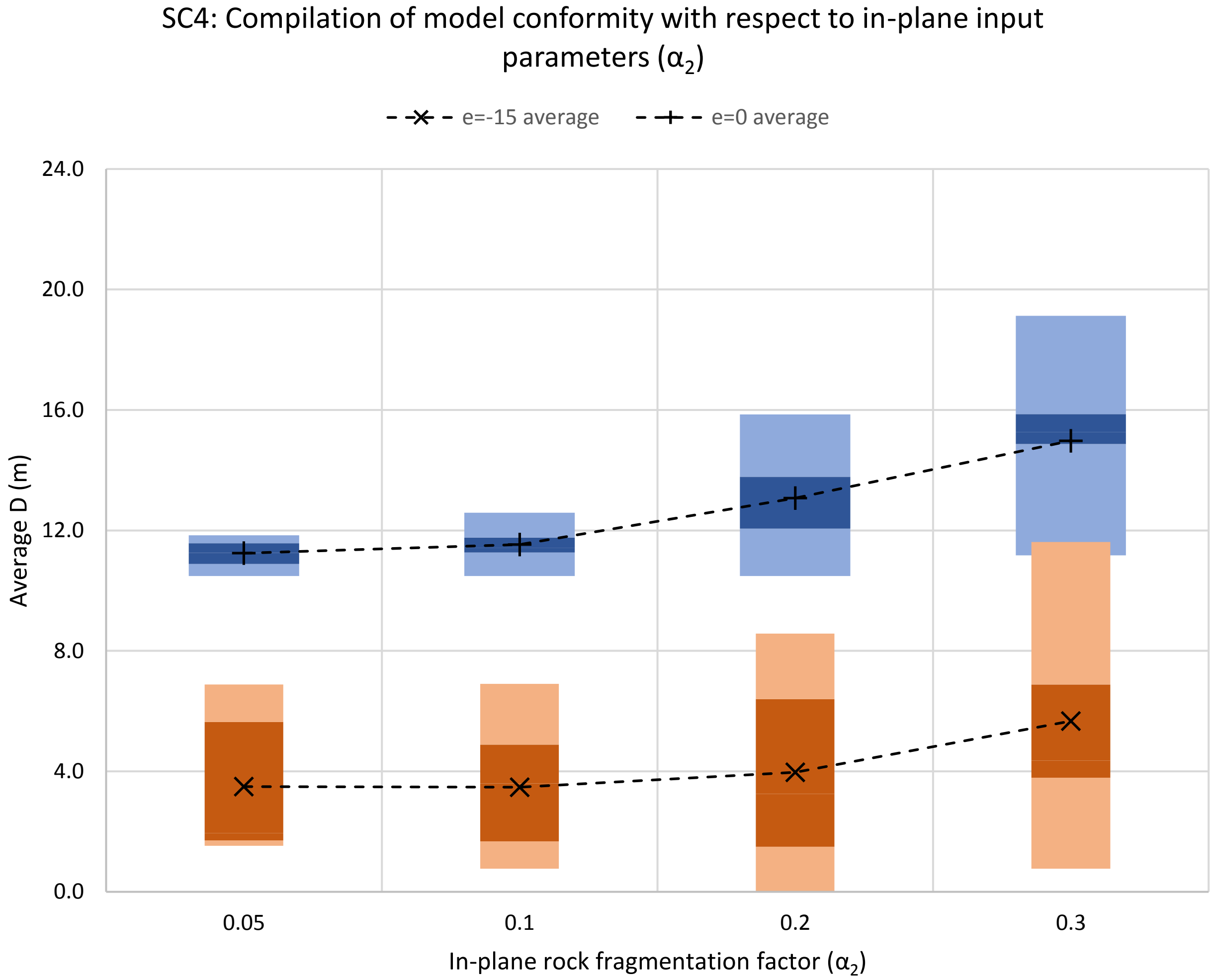

Figure 6.25: Compilation of model conformity for SC4 with respect to in-plane input parameters (α_2). Bars in red show the spread of results for "D" obtained with an error "e" of -15˚. The dark red shows the spread of the middle 50% of the models. Bars in blue show the spread of results for "D" with no orientation error. The dark blue shows the middle 50% of values for "D" obtained. There is very slight overlap between the bars, showing that for a constant value of α_2, almost all measurements of "D" with an error of -15˚ are lower than the measurements of "D" obtained with no orientation error.

It can be seen for both stress cells that there is very little overlap between conformity measurements with no error and with an error of -15˚, in accordance with Figure 6.23. It is also shown that for all models, regardless of the other varied parameters, the orientation error of -15˚ yields distinctly better conformity measurements. For example, the average "D" value with SC3 for all models where α_2 = 0.05 is reduced from 11 m to 3 m when the orientation error is assumed. This increase in average conformity with respect to orientation is observed for both stress cells. In addition, for both SC3 and SC4, the lowest distance "D" is obtained when the in-plane fragmentation factor is very low (α_2 = 0.05). From these results, two points can be established: first, SC3 and SC4 are measuring stress changes -15˚ from the N-S and E-W axes, and secondly, the stress release and rock fragmentation effect in the plane of σ_2 and σ_3 is very high.

6.4.4.4 Effect of out of plane rock fragmentation factor (α_1) (1-12, 15-22, 25-48)

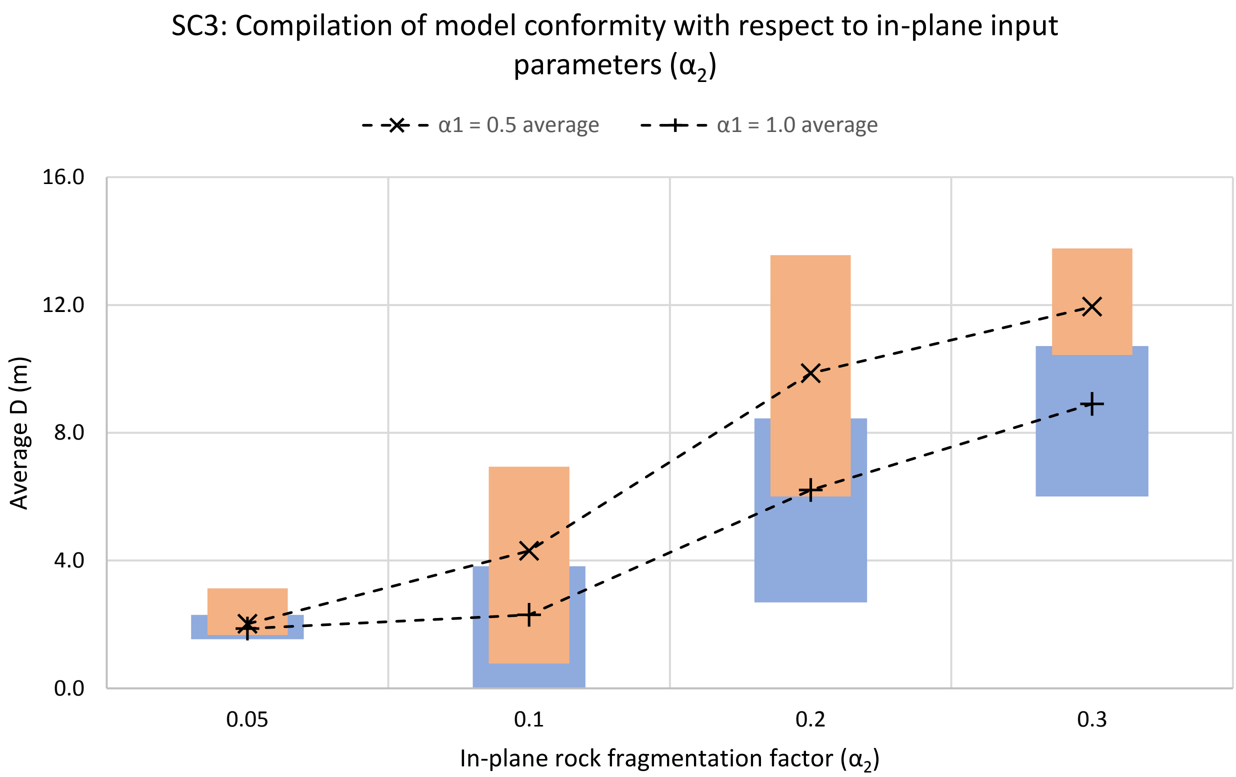

Figure 6.26: Compilation of model conformity for SC3 with respect to in-plane input parameters (α_2). Red bars show the spread of results for "D" obtained with α_1=1.0. Blue bars show the spread of results for "D" with α_1=0.5. There is overlap between the bars, for α_2=0.05. For higher values of α_2, models where α_1 = 1.0 typically give better results.

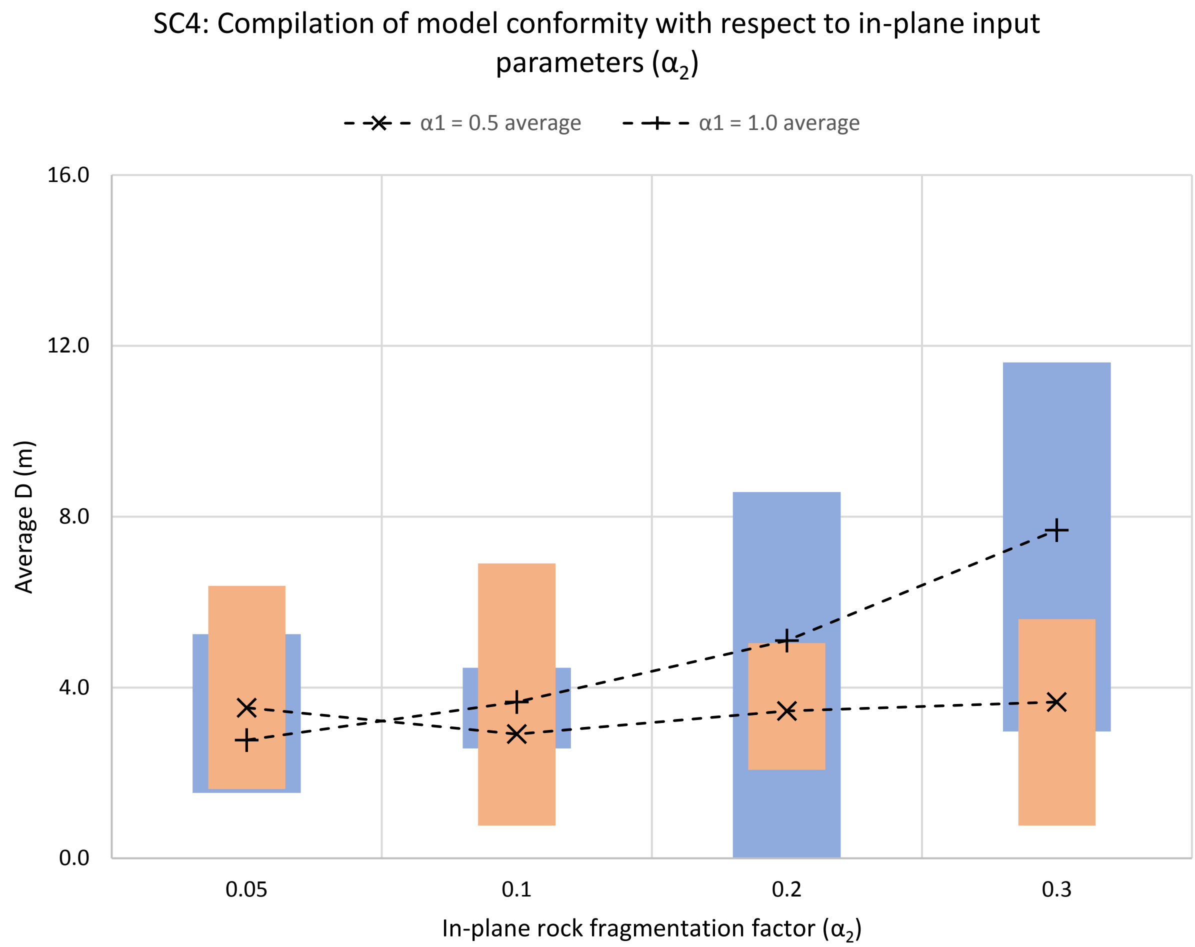

Figure 6.27: Compilation of model conformity for SC4 with respect to in-plane input parameters (α_2). Red bars show the spread of results for "D" obtained with α_1=1.0. Blue bars show the spread of results for "D" with α_1=0.5. There is good overlap between the bars for α_2=0.05. For higher values of α_2, models where α_1 = 0.5 give slightly better results.

Figures 6.26 and 6.27 plot the average conformity of all anisotropic models with respect to the out of plane rock fragmentation factor (α_2). The stress cell error "e" for both figures is -15˚. The spread of "D" values for all models with α_1 = 0.5 is plot in red, while the spread for models where α_1 = 1.0 is plot in blue. Overall, there is considerable result overlap between α_1 = 0.5 and α_1 = 1.0 when the input α_2 is low. This behavior is observed for both SC3 and SC4. Once α_2 is increased however, overlap is lost with one batch of models performing better than the other. However, as shown in the last section, the in-plane fragmentation factor should be low. It is therefore shown that α_1 overall has a smaller effect on model conformity than α_2. The input parameter α_1 = 0.5 is retained for further analysis as it is more realistic than α_1 = 1.0. Overall, the crown cells show low sensitivity to out of plane destress blast parameters, and higher sensitivity to in-plane destress blast parameters.

6.4.5 Analysis of SC5

SC5 detected a major stress decrease of 6.22 MPa, indicating a high destressing effect from the Phase 3 sill panels. Stress change conformity with anisotropic destress input parameters is therefore poor, with D ranging from 9.4 m to 23.4 m across all tested models. Unlike SC3 and SC4, SC5 conformity is far less sensitive to α_2, indicating that the dominant parameter affecting conformity may be α_1. Therefore, it is postulated that the Phase 3 sill panel is well destressed. The aggregated models will therefore not include models where the sill panels in destressed anisotropically.

6.4.5.1 Effect of stress cell orientation angle (15-48)

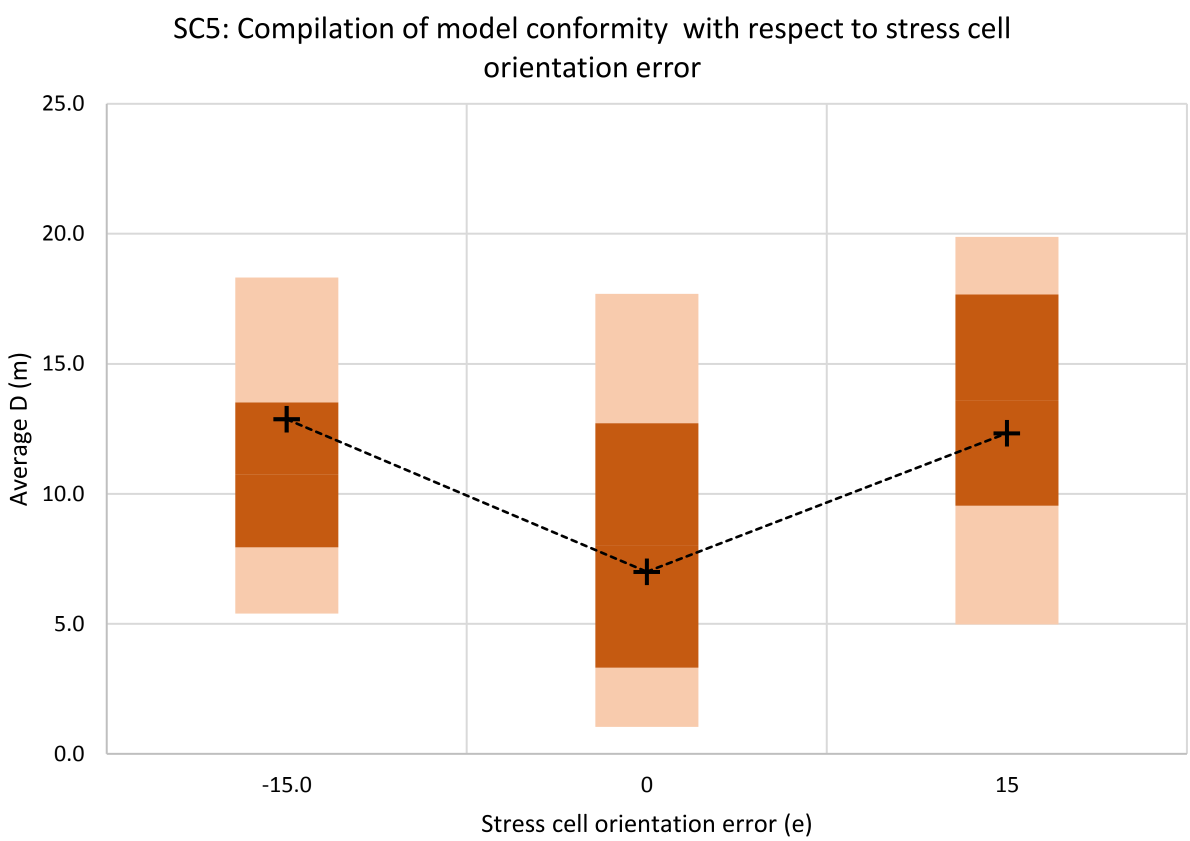

Figure 6.28: Compilation of model conformity for SC5 with respect to stress cell orientation error (e). The red bars show the spread of measurements of “D” obtained for each assumed measurement error. The dark red portion shows the spread of the middle 50% of measurements of “D”.

The SC5 results for "D" from models 15-48 were aggregated to determine the likelihood of stress cell orientation error for SC5. Overall, rotating the stress cell by +/- 15˚ yields higher values for D as shown in Figure 6.28. Given this trend, it is assumed that SC5 is correctly oriented and stress cell orientation error will not be considered in the remaining analysis of results.

6.4.5.2 Effect of anisotropic elevation cut-off (5-12, 15-22, 25-32)

The destress blast input parameters for the sill portion of the pillar, if isotropic, were kept constant at $\alpha = 0.05$, $\beta = 0.95$, based on past experience with the Phase 1 and Phase 2 destress blasts. However, the destressing effect in the crown panel will have an effect on the stress shadow at the level of the sill panel. A poor destressing effect in the crown will shrink the stress shadow, while a high destressing effect in the crown will increase it. The values for "D" for SC5 are therefore plot with respect to the input parameter of the crown panels. Figure 6.29 shows that good conformity is obtained for SC5 if the in-plane fragmentation factor is low, and if the out-of-plane fragmentation factor is equal to 0.5. This corroborates with Section 4.3.4, where α_1 in the crown panel was determined to be 0.5 rather than 1.0. In addition, setting the anisotropic model cut-off in the roof of 3550L rather than the floor yields better results.

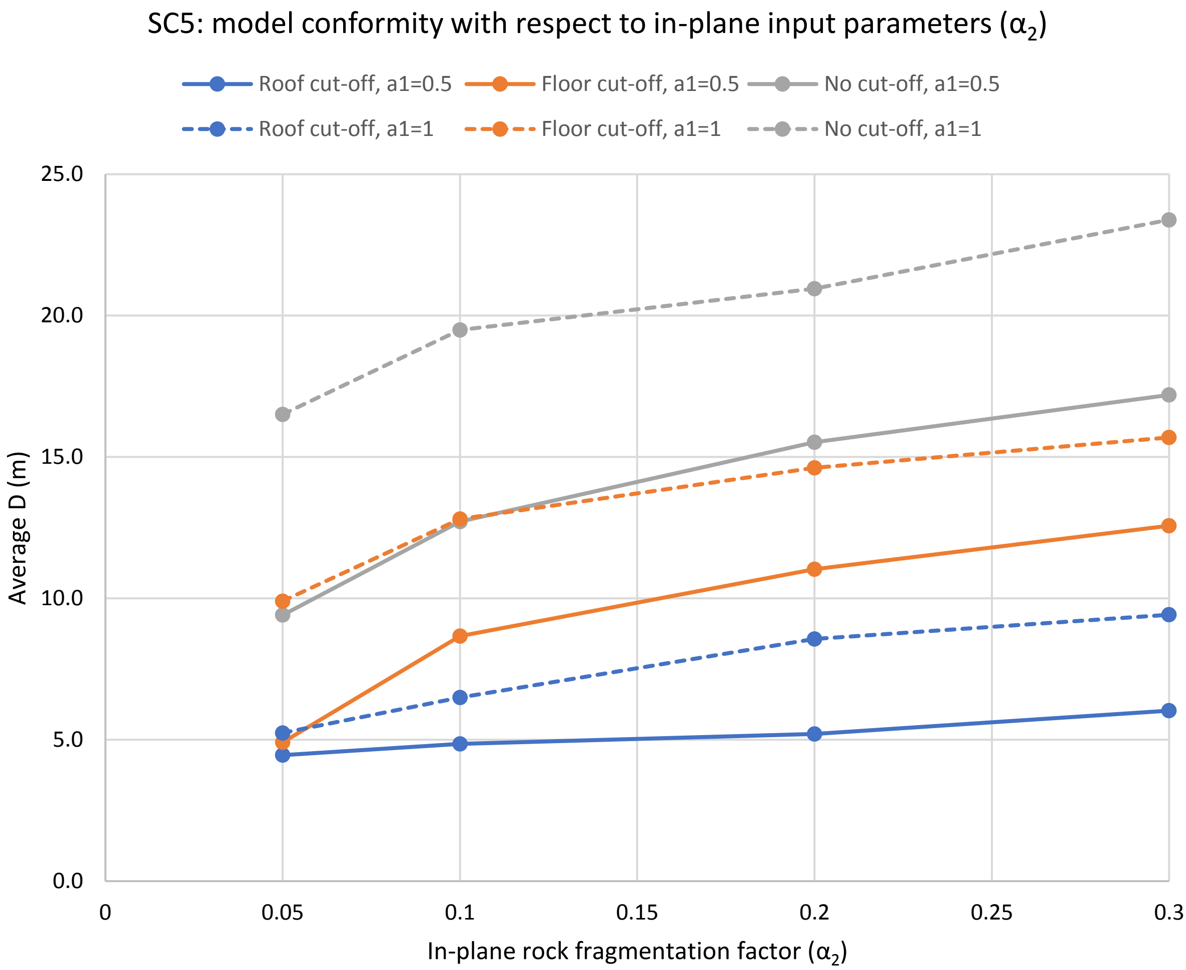

Figure 6.29: Model conformity for SC5 with respect to in-plane input parameters (α_2)

6.4.5.3 Effect of far-field stress calibration (25-48)

Comparing results from models 25-48 shows that increasing the far field stresses proportionally increases the stress drop in the stress shadow. Therefore, better conformity is obtained overall as the stress shadow with the base model is too small even with a severe isotropic destressing effect. However, it is not proven that the high stress accumulation detected by SC3, SC4, and SC5 is global or local. Therefore, the moderate increase in conformity obtained for SC5 does not warrant the assumption that the stress increase measured after the 9631 crown blast is global.

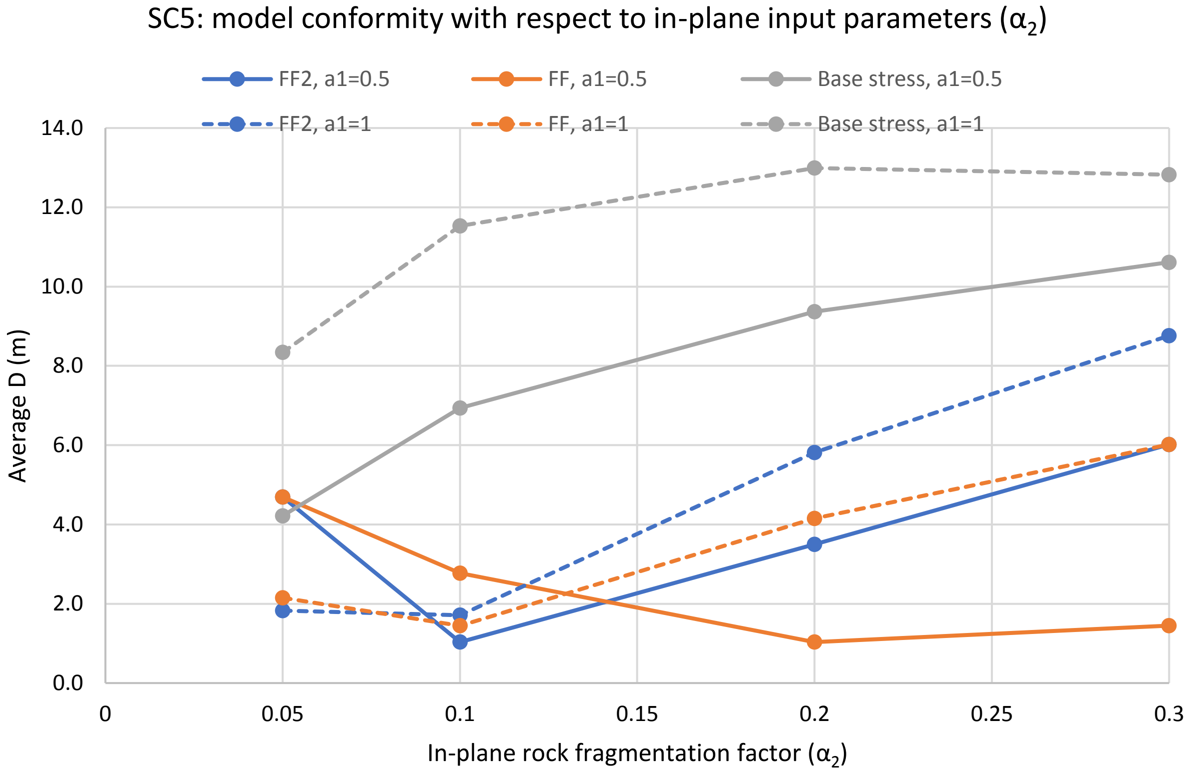

Figure 6.30: Model conformity for SC5 with respect to in-plane input parameters (α_2)

<u>6.4.5.4 Quantification of the Stress wrapping effect (13,14,23,24)</u>

The models 1, 9, and 17 were compared to quantify the stress increase in the crown caused by stress wrapping around a well destressed sill panel. The fully anisotropic model 1 showed poor conformity in the E-W direction (D = 10.3 m). While the model with good destressing in the sill pillar (9) obtained slightly better results in the crown (D = 10.1 m), the model with good destressing in the sill panel and crown sidewalls (17) showed poorer conformity (D = 11.2 m). The best conformity for all heterogenous scenarios was obtained with $\alpha = 0.05$ and $\beta = 0.95$ normal to the major principal stress for the crown panel.

Overall, even with a severely anisotropic crown panel with no stress release in the major principal stress direction, and with a completely destressed sill panel, the stress wrapping effect detected in the crown is very minor. The extreme stress wrapping effect was modelled with models 13, 14, 23, and 24. The sill panel was modelled as a void, and the crown panel was either left intact or given an α_1 value of 1. The results for "D" are given in Table 6.8. The models showed better results with good conformity assuming no stress cell orientation error. However, the significance of the input parameters does not match field observations.

Table 6.8: Results for models 13, 14, 23, 24, compared to model 25. Stress cell orientation error e = 0.

	Cut-off	Sill α	Crown α_1	Crown α_2	SC3	SC4	SC5
13	3450L	null	1	1	3.8	9.5	9.3
14			1	0.05	6.5	10.2	9.0
23	3440L	null	1	1	1.3	10.8	6.8
24			1	0.05	4.4	10.8	8.2
25	3440L	0.05	0.5	0.05	15.1	10.7	4.2

Therefore, the stress wrapping hypothesis must be discarded, as it was observed in the field that both panels were destressed, and the voided sill panel model does not conform with measured stress changes in the pillar sill. In addition, the conformity is poor with SC4. In accordance with section 6.4.4, examination of the stress change contours showed that the combination of stress wrapping around crown pillar and stress cell orientation error is the most likely explanation for the measured stress increase.

6.4.6 Conclusions

Overall, the following conclusions can be drawn from the results of the numerical models 1-48

- A rock fragmentation factor α_2 of 0.05 is most likely very low.
- The stress cells SC3 and SC4 are not sensitive to changes in the rock fragmentation factor α_1. The most realistic value for α_1 is 0.5, which is therefore retained.
- A slight variation in the stress cell orientation (due to possible human error during installation) can explain the measured stress increase at SC3.
- The results from SC5 suggest good destressing in the sill panel.
- Best conformity for SC5 is obtained when the model cut-off is set at the roof of 3540L.
- SC5 conformity is better with increased far field stress, but not enough to warrant the assumption of a global stress increase in the pillar.
- The hypothesized stress wrapping effect cannot explain by itself the measured stress increase in the sill.

Based on these conclusions, model 25 is deemed to be the most likely representation of the Phase 3 blast. The values for “D” are shown in Table 6.9 with respect to the stress cell and the error “e”. Model input parameters are listed in Table 6.10.

Table 6.9: Conformity results for model 25

	e=-15	e=0	e=15
SC3	1.7	15.1	3.1
SC4	1.8	10.7	0.9
SC5	7.8	4.2	13.5

Table 6.10: Model 25 input parameters

Model #	25
field stress	base
cut-off	3540L
isotropic α	0.05
α_1	0.05
α_2	0.5

Chapter 7: Conclusions and Recommendations

This chapter is divided in 3 sections. To begin, the overall conclusions of the thesis will be outlined. Then, the limitations of the study will be discussed, followed by the scope of future research.

7.1 Conclusions

The scope of this work is large scale destress blasting in deep hard rock mines, which aims to reduce stress in the burst-prone mining region, consequently reducing the risk of strainbursts. The mine of interest is Copper Cliff Mine (CCM). The work focused on the back analysis of destress blasts conducted at CCM. A numerical model of the 100/900 Orebody of CCM has been built. The destress blasts are simulated using the holistic constitutive models developed by Tang and Mitri (2001) and Saharan and Mitri (2009). With these models, the effect of the stress state prior to destress blasting, fracture propagation in the direction of the major principal stress, and instantaneous stress release due to fracture propagation were examined. With a quantified destressing effect, the safety of mining the pillar was assessed in the model.

Destress blasting is used as a last resort, when burst prone structures cannot be avoided by changing the mining sequence or geometry. Based on the review of case studies, it was found that destress blasting is applied in two general mining scenarios: for the development of drifts, raises, or shafts, where high stress occur at the advancing face, and for the extraction of highly stressed diminishing ore pillars. The practice can further be divided into two types, which are tactical and strategic destressing. Tactical destressing involves directly pre-conditioning burst prone rock that is to be extracted, while strategic destressing aims is to reduce the burst proneness of an entire mining region by damaging rock at its periphery. The case study Copper Cliff Mine is an example of a strategic destress blasting program, comparable in scale and strategy to the Fraser Mine and Brunswick Mine case studies.

Copper Cliff Mine is a deep hard rock mine, where a large-scale panel destressing program was applied to reduce the burst proneness of the 100OB diminishing ore pillar. The purpose of the study is to quantify the destressing effect of these destress panels with a numerical modelling back analysis based on measured stress changes in the diminishing pillar. Ten stress cells were installed in the pillar and periodically recorded stress changes over 2 years of mining and destressing. During that period, three destress blasting Phases were conducted and three stopes in the stress shadow zone were mined.

The parametric study presented in Chapter 4 was conducted before building the pillar model. The aim was to verify if the large-scale panel destressing strategy can yield a beneficial stress drop in the diminishing pillar. The potential for burst of the ore was estimated with the Brittle Shear Ratio (BSR). The ore at risk in the pillar was defined as the volume of rock with a BSR exceeding 0.7. This was compared between destressing scenarios. Destress simulation was applied holistically to the panels with the rock fragmentation factor (α) and the stress reduction factor (β). The Fraser and Brunswick Mine case studies both provided stress change data that could be used to evaluate probable values for α and β at Copper Cliff Mine. It was found that comparable stress changes were obtained in the model with a rock fragmentation factor α of 0.2 and a stress reduction factor β of 0.8. The immediate reduction in BSR computed in the model is significant, validating the methodology that is to be used in the pillar model.

Chapter 5 discussed the validation of the Phase 1 blast at CCM with the pillar model. The α and β holistic model validated in the parametric study (Chapter 4) was adopted to simulate the destress blast. Conformity between the stress cells measurements and the numerical model is measured with the distance "D" between the stress cell and the stress change contours computed in the model. It is shown that the best correlation between the numerical model and field measurements is obtained when the combination of α and β represents high fragmentation (α =0.05) and high stress release (β =0.95) in the destress panel. It is demonstrated that the burst proneness of the ore blocks in the panel stress shadow is reduced in terms of the brittle shear ratio (BSR) and the burst potential index (BPI). It is also concluded that proper model validation requires multiple stress cells, as placement and measurement error can be significant depending on the position of the cell with respect to the panel. In addition, results from single cell can be inconclusive based on its position with respect to the panel, with the same stress decrease being read at the stress cell position regardless of the destress blasting input parameters.

In Chapter 6, the Phase 2 blast is successfully validated with the methodology outlined in Chapter 5. It was found that the most valid rock fragmentation factor and stress reduction factor are α = 0.05 and β = 0.95 respectively. However, the stress changes measured after the Phase 3 blast could not be replicated with this model. In brief, a stress increase was detected in the expected stress shadow of the crown panel, while a stress decrease was measured in the shadow of the pillar sill. Therefore, it is believed the high mining induced stress accumulated in the pillar crown has caused the crown panel to freeze. The anisotropic destressing model hypothesized by Saharan and Mitri (2009) was therefore adopted for the crown panel. With this model, Saharan proposed that the degree of stiffness reduction and stress dissipation is influenced by the orientation of the in-situ principal stresses, which can explain why the stress did not decrease in the crown panel stress shadow. Another issue that was examined is the effect of slight variation of the orientation of the stress cell. Overall, a slight variation in the stress cell orientation (due to possible human error during installation) must be accounted for to explain measured stress in the crown. It was also determined that crown panel fragmentation factor in the orientation of σ_1 was much higher than the rock fragmentation factor in the σ_2-σ_3 plane, with a value of α_1 of 0.5 and a value of α_2 of 0.05. Therefore, the anisotropic stress release and fragmentation effect due to preferential fracture propagation was quantified, where the stress release and fragmentation normal to σ_1 is almost double the effect in the orientation of σ_1.

In all, a methodology to quantify the geomechanical effect of destress blasting was developed. The holistic destressing model was validated based on this methodology with Phase 1, Phase 2, and Phase 3 blasts. Phase 1 and Phase 2 blast completely fractured the rock and released most of the stresses (α = 0.05, β = 0.95). For Phase 3 blast, the sill panels were also successfully destressed. However, the crown panel did not exhibit a behavior that could be explained with the isotropic model. The anisotropic destressing model was adopted and partially replicated the measured stress changes. Stress cell orientation error was also considered, and adequately explained the discrepancies between the model and the measured stress changes. Table 7.1 summarizes the α and β that provided the best correlation.

Table 7.1: Summary of validation results

<table>
<tr><td></td><td colspan="2">α</td><td colspan="2">β</td></tr>
<tr><td>Phase 1</td><td colspan="2">0.05</td><td colspan="2">0.95</td></tr>
<tr><td>Phase 2</td><td colspan="2">0.05</td><td colspan="2">0.95</td></tr>
<tr><td rowspan="2">Phase 3</td><td>Crown</td><td>Sill</td><td>Crown</td><td>Sill</td></tr>
<tr><td>α_1=0.5, α_2=0.05</td><td>0.05</td><td>β_1=0.5, β_2=0.95</td><td>0.95</td></tr>
</table>

7.2 Limitations of the Study

1. The linear-elastic model can only replicate the immediate elastic redistribution of stresses after each mining step. Time dependent stress changes associated with the progressive failure of the pillar are detected by the stress cells but not captured in the elastic model. As demonstrated in Appendix 1, the linear-elastic model and plastic excavation damage zone models could not adequately reproduce the time dependent accumulation of stress in the pillar associated with recorded high seismicity after the 9631-crown blast. Consequently, the mining induced stress state of Phase 3 blast was unknown at the time of Phase 3 blasts. The validated destress parameters are thus applied to a stress tensor that is likely lower than the stress tensor in the field. The parametric values are therefore systematically under-estimated. This effect is partially demonstrated in Chapter 6, where better model conformity was obtained under higher model far-field stress for the Phase 3 sill panel.

2. As shown in Chapter 6, it is not clear if the long term stress changes detected by the stress cells are local or not, given the heterogenous nature of the in-situ rock mass. A local stress change may be attributed to time-dependent slip between joints in the rock mass. Even if multiple stress cells corroborate, it is still not apparent which proportion of the measured change could be replicated with a homogenous plastic numerical model. This was especially apparent after the 9631-crown blast, where a 50 MPa stress increase was detected in the pillar crown and a 20 MPa increase in the pillar sill after prolonged seismicity. Therefore, the analysis is limited to validation based on immediate stress changes only. All numerical analysis can therefore be done in a linear-elastic model, where only the immediate redistribution of stresses can be studied.

3. Stress cell orientation is also a major factor in the validation process. The uniaxial stress cells are very sensitive to observation direction of the cell. For Phase 3 blast, a change in orientation of 15° would affect the distance of correlation "D" by the same margin as varying the destress blast constitutive model parameters. It was also shown in Chapter 5 that it is possible for a uniaxial stress cell to provide totally inconclusive results if it is oriented parallel to the stress change contours. It is therefore important to have multiple cells available to validate the model.

4. The panel thickness was kept constant throughout the entire study. It is shown in Appendix 4 that the stress change effect of panel thickness variation can be replicated by changing the panel destressing parameters. Therefore, the validated parameters can only be interpreted holistically until the assumed panel thickness is validated. In addition, damage was only simulated in the panel itself, with no disturbed rock at the periphery of the panel. Therefore, the quantified destressing effect is likely overestimated as the total damage zone is limited to the panel volume.

7.3 Scope of future research

This study lays a foundation for future research into quantifying the effects of destress blasting as an effective means for rockburst control. However, all validations were done based on immediate stress changes in a linear-elastic homogenous medium. The scope of future research discussed in this section partially addresses these limitations.

7.3.1 Investigation of seismic source parameters and energy analysis

The literature review revealed that most case studies of destress blasting evaluate the success of a destress blast based on the seismic response to destress blasting. Given the widespread use of seismic networks in mining, cross-examination of the stress change effect on the seismic response more rigorously would enhance the understating of the effect of destress blasting.

7.3.2 Development of new brittle failure burst potential criteria

In the study it is demonstrated that with a BSR threshold of 0.7, the destress blast stress shadow provides a significant decrease in ore at risk. However, as can be seen from the results in

Appendix 2, the computed BSR values obtained from the linear elastic model for seismic source locations are well below the threshold of 0.7. Therefore, a more robust rock mass modelling, e.g. discrete element modelling, is required to derive a new brittle failure criterion taking into consideration the presence of structural discontinuities in the rock mass. The same can be said about the BPI, which was shown to predict burst zones only at and near the pillar boundaries, and not where seismic source locations were detected by the microseismic network.

7.3.3 Blast damage models

In all applications of the constitutive model, it was assumed that $\alpha + \beta = 1$. However, it is not possible with the methodology used in this study to distinguish between different combinations of α and β that cause the same stress change at a point outside the panel. In view of the limited number of destress blasts, it is not possible for example to conclude that the stiffness of the in-situ rock was reduced by half when the destress parameter α=0.5. The holistic destress blast models are simple and easy to use in any numerical modelling software. It is important however to validate the assumption that $\alpha + \beta = 1$ through further investigations, preferably with other case studies in different stress and geologic environments.

Chapter 8: References

Andrieux P. Application of rock engineering systems to large-scale confined destress blasts in underground pillars. Vol. Ph.D., Department of Mining, Metallurgical, and Material Sciences. [Quebec]: Laval University; 2005.

Andrieux P, Brummer R, Mortazavi A, Liu Q, Simser BP. Large-Scale panel destress blast at Brunswick Mine. CIM Bull. 2003;(96):78–87.

Aubertin M, Gill DE. A methodology for asessing the potential for rockbursts in Abitibi Mines. Colloq sur le Control Terrain. 1988;47–77.

Blake W. Destressing test at the Galena Mine. Trans SME-AIME. 1972;252(1):294–9.

Boler FM, Swanson PL. Seismicity and Stress Changes Subsequent to Destress Blasting at the Galena Mine and Implications for Stress Control Strategies. Report of Investigations 9448. U.S Department of the Interior Bureau of Mines; 1993.

Brauner G. Rockbursts in coal mines and their prevention. Rotterdam: Baklama; 1994.

Brown ET. Rockbursts: prediction and control. Tunnels and Tunnelling. 1984.

Castro LAM, Grabinsky MW, McCreath DR. Damage inititiation through extension fracturing in a moderately jointed brittle shear rock mass. Int J Rock Mech Min Sci. 1997;(34):110–3.

Comeau W, Mitri HS, Mohammed MM, Tang B. World-wide survey of destress blasting practice in deep hard rock mines. In: 25th Annual Conference on Explosives and Blasting Technique. 1999. p. 189–205.

Cook NGW. Design of underground excavations. In: 8th US Rock Mechanics Symposium. Minnesota; 1967. p. 167–93.

Cook NGW. An industry guide to the amelioration of hazards of rockbursts and rockfalls. Chamber of Mines of South Africe; 1978.

Hakami H, Kankunnen J, O'Flaherty T, Olsson M. Destress Blasting Experiments at the Pyhasalmi

Mine, Finland. SveDeHo; 1990.

Hanson D, Quesnel W, Hong R. Destressing a Rockburst Prone Crown Pillar: Macassa Mine. CANMET; 1987.

Hedley DGF. Rockburst Handbook for Ontario Mines. CANMET Special Report SP92-1E. Mining Research Laboratories; 1992.

Herget G. Stress assumptions for underground excavations in the Canadian Shield. Int J Rock Mech Min Sci Geomech Abstr. 1987;24(1):95–7.

Hoek E, Torres C, Carranza T, Corkum B. Hoek Brown failure criterion - 2002 edition. In: Fifth North American rock mechanics symposium. 2002. p. 267–73.

Itasca. Kubrix [Internet]. 2016. Available from: http://www.itascacg.com/software/kubrix

Karwoski WJ, McLaughin WC. Rock pre-conditioning to prevent rockbursts - report on a field demonstration. United States Department of the Interior, Bureau of Mines; 1975.

Klaus WJ. Civil engineering approach to evaluate the strength and deformability of regularly jointed rock. In: Rock Mechanics Theory and Practice, 11th Symposium. New York; 1970. p. 69–80.

Knoteck S, Matusek Z, Skrabis A, Janas P, Stas B. Research of geomechanics evaluation of rock mass due to geophysical methods. VVUU Ostrava; 1985.

Konicek P, Saharan MR, Mitri HS. Destress Blasting in Coal Mining – State-of-the-Art Review. Vol. 26. 2011.

Konicek P, Soucek K, Stas L, Singh R. Long-hole destress blasting for rockburst control during deep underground mining. Int J Rock Mech Min Sci. 2013;(61):141–53.

Konicek P, Waclawik P. Stress changes and seismicity monitoring of hard coal longwall mining in high rockburst areas. Tunn Undergr Sp Technol. 2018;(81):237–51.

Lightfoot N, Kullman DH, Toper AZ, Stewart RD, Gronder M, Rensburg ALJ van, et al.

Preconditioning to Reduce the Incidence of Face Bursts of Highly Stressed Faces. CSIR: MININGTEK; 1996.

Liu Q. Design and general practice of mass blast in underground open stoping method. In: A.K G, A J, editors. Blasting in Mines - New Trends. Taylor & Francis Group; 2013. p. 11–20.

Liu Q, Ellis B, Chung S. Application of advanced blasting technologies for large scale de-stress blasts at Brunswick mine. CIM Bull. 2005;98(1088).

Ma GW, An XM. Numerical simulation of blasting-induced rock fractures. Int J Rock Mech Min Sci. 2008;45(6):966–75.

Makuch A, Neumann M, Hedley DGF, Blake W. Destress Blasting at Campbell Red Lake Mine. Canada/Ontario/industry Rockburst Research Project. CANMET, Elliot Lake Laboratory; 1987.

Martin CD, Kaiser PK. Predicting the depth of stress induced failure around underground excavations in brittle rocks. In: 49th Canadian Geothechnical Conference. St. John's; 1999. p. 105–14.

McNeel. Rhino. 5th ed. Robert McNeel and Associates; 2015.

Mitri HS. Practitioner's Guide to Destress Blasting in Hard Rock Mines. 2nd ed. Department of Mining and Metallurgical Engineering, McGill University; 2001.

Mitri HS, Tang B, Simon R. FE modelling of mining-induced energy release and storage rates. J South African Insitute Min Metall. 1999;:103–10.

Moruzi GA, Paseika AR. Evaluation of a blasting technique for destressing ground subject to rockbursting. In: 6th US Rock Mechanics Symposium. Rolla, Missouri; 1964. p. 185–204.

O'Donnell JDP. The use of destress blasting at Inco's Creighton Mine. In: MASSMIN 92. Johannesburg: SAIMM; 1992. p. 71–4.

Oliver P, Wiles T, MacDonald P, O'Donnel D. Rockburst control measures at Inco's Creighton

Mine. In: 6th Conference on Ground Control in Mining. West Virginia; 1987.

Ortlepp WD. Invited Lecture: The design of support for the containement of rockburst damage in tunnels - an engineering approach. In: Kaiser PK, McCreath DR, editors. Rock Support and Underground Construction. Balkema; 1992. p. 593–609.

Peng Z, Wang Y. Griffith theory and the criteria of rockburst. Chinese J Rock Mech Eng. 1996;(1):491–5.

Roux AJA, Leeman ER, Denkhaus HG. Destressing: a means of ameliorating rock-burst conditions. J South African Inst Min Metall. 1957;(58):104–46.

Saharan MR, Mitri HS. Simulations for rock fracturing by destress blasting, as applied to hard rock mining conditions. Saarbrucken: VDM Verlag; 2009.

Sainoki A, Emad MZ, Mitri HS. Study on the efficiency of destress blasting in deep mine drift development. Can Geotech J [Internet]. 2016a;54(4):518–28. Available from: https://doi.org/10.1139/cgj-2016-0260

Sainoki A, Mitri HS, Chinnasane D. Characterization of Aseismic Fault-Slip in a Deep Hard Rock Mine Through Numerical Modelling: Case Study. Rock Mech Rock Eng. 2017;50(10):2709–29.

Sainoki A, Mitri HS, Yao M, Chinnasane D. Discontinuum Modelling Approach for Stress Analysis at a Seismic Source: Case Study. Rock Mech Rock Eng. 2016b;49(12):4749–65.

Salamon MDG. Rock mechanics of underground excavations. Advances in rock mechanics. In: Third Conference of the International Society of Rock Mechanics. 1974. p. 951–1099.

Shnorhokian S, Mitri HS, Moreau-Verlaan L. Assessement of stope sequence alternatives in a diminishing ore pillar. In: Proceedings of the 7th International Conference on Deep and High Stress Mining. Australian Centre for Geomechanics; 2014. p. 471–84.

Shnohorkian S, Mitri HS, Moreau-Verlaan L. Stability assessment of stope sequence scenarios in a diminishing ore pillar. Int J Rock Mech Min Sci. 2015;(59).

Singh R, Mandal PK, Singh AK, Kumar R, Sinha A. Coal pillar extraction at deep cover: With special reference to Indian coalfields. Int J Coal Geol. 2011;86:276–88.

Tang B. Rockburst control using destress blasting. PhD Thesis. McGill University; 2000.

Tang B, Mitri HS. Numerical modelling of rock preconditioning by destress blasting. Gr Improv. 2001;5:1–11.

Vennes I, Mitri HS. Geomechanical Effects of stress shadow created by large scale destress blasting. J Rock Mech Geotech Eng. 2017;9:1085–93.

Wojtecki L, Konicek P, Schreiber J. Effects of torpedo blasting on rockburst prevention during deep coal seam mining in the Upper Silesian Coal Basin. J Rock Mech Geotech Eng. 2017;(9):694–791.

Wu Y, Zhang W. Prevention of rockburstsin coal mines in China. In: Gibowicz S., editor. Rockbursts and Seismicity in Mines. Krakow: Baklama; 1997. p. 361–6.

Yang LY, Ding CX. Fracture mechanism due to blast-imposed loading under high static stress conditions. Int J Rock Mech Min Sci [Internet]. 2018;107(April):150–8. Available from: https://doi.org/10.1016/j.ijrmms.2018.04.039

Yang R, Wang Y, Ding C. Laboratory study of wave propagation due to explosion in a jointed medium. Int J Rock Mech Min Sci [Internet]. 2016;81:70–8. Available from: http://dx.doi.org/10.1016/j.ijrmms.2015.10.014

Zhu Z, Mohanty B, Xie H. Numerical investigation of blasting-induced crack initiation and propagation in rocks. Int J Rock Mech Min Sci. 2007;44(3):412–24.

Appendix 1: Excavation damage zone for 9631 Stope

Table A.1: Measured stress changes following Stope 9631 extraction

Stress Cell	Stress change (MPa)		
	Immediate Cumulative	Immediate Crown Blast	Stabilised Cumulative
9670-Sill_CN3800_UH-NS	-1.67	-1.64	-1.63
9670-Sill_CN3801_UH-EW	-1.21	-1.88	-1.83
9550-Sill_CN3797_UH-EW	5.97	5.34	46.76
9550-Sill_CN3798_UH-NS	5.03	4.70	46.35
9550-Sill_CN3802_DH-EW	11.27	11.19	17.98
9550-Sill_CN3804_WH-NS	3.75	3.82	3.23
9590-Sill_CN3799_UH-EW	0.18	0.16	0.00
9590-Sill_CN3803_DH-EW	-1.90	-2.47	-2.63

Table A.2: Failure envelope and post peak properties for ore zones

Ore Behaviour	#	Failure Envelope				Residual		
		m_b	s	a	UCS (MPa)	m_r	s_r	Strength Reduction (MPa)
Elasto-plastic	4	25	1	0.5	140	25	0	140
Softening	3	25	1	0.5	140	15	0	24
Intermediate	2	25	1	0.5	140	7.5	0	12
Brittle	1	25	1	0.5	140	5	0	12
Elastic	5	N/A	N/A	N/A	N/A	N/A	N/A	N/A

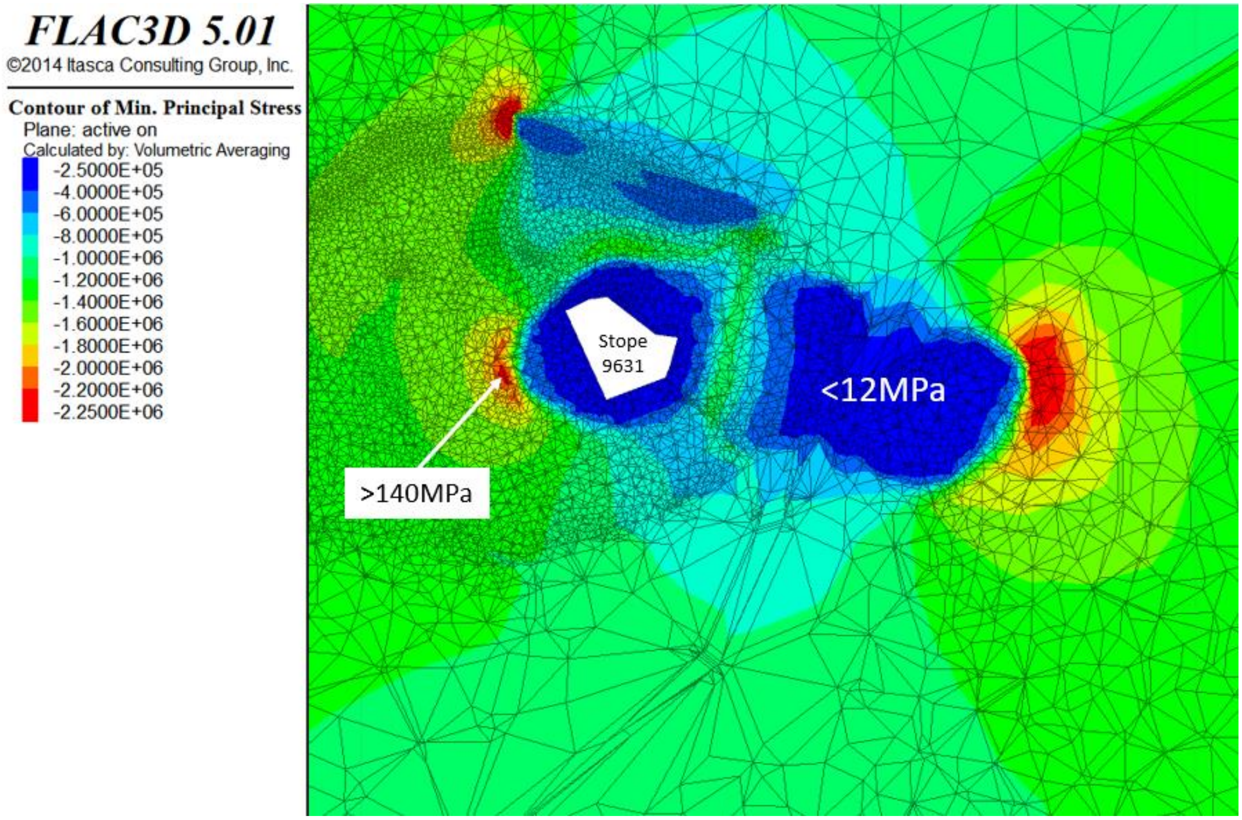

Figure A.1: Excavation damage zone around stope 9631 after crown blast in brittle failure model

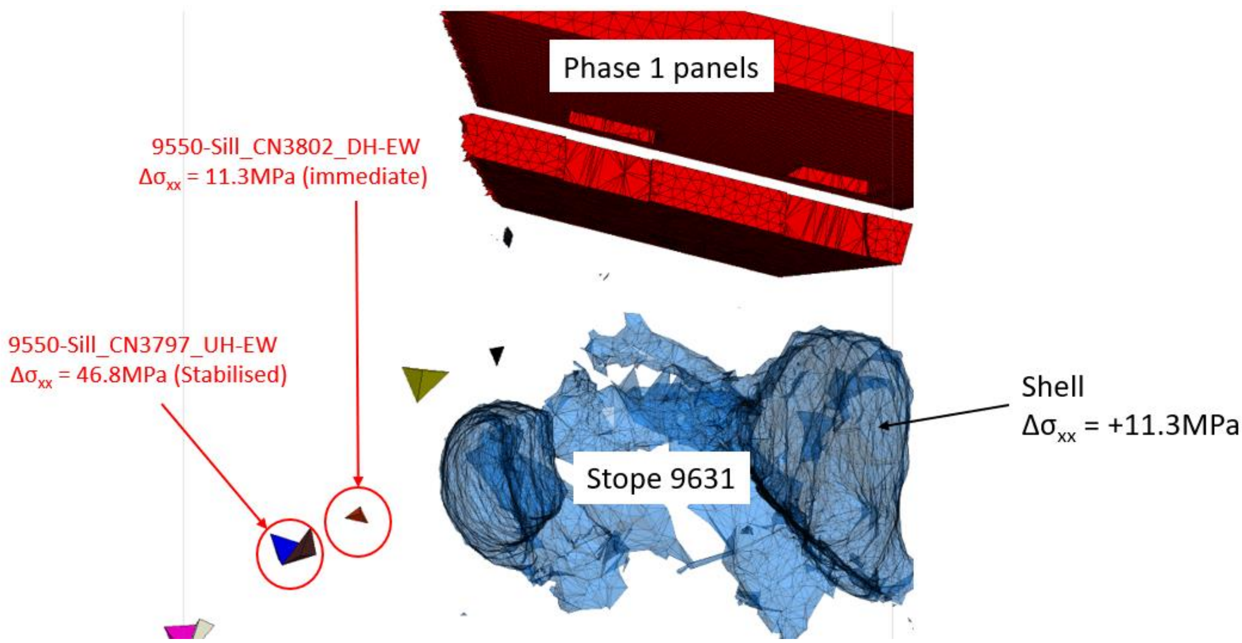

Figure A.2: Comparison of stress change shell for in brittle post peak behaviour model after 9631 crown blast. SC5 detected an 11.3 MPa immediate stress change after the crown blast.

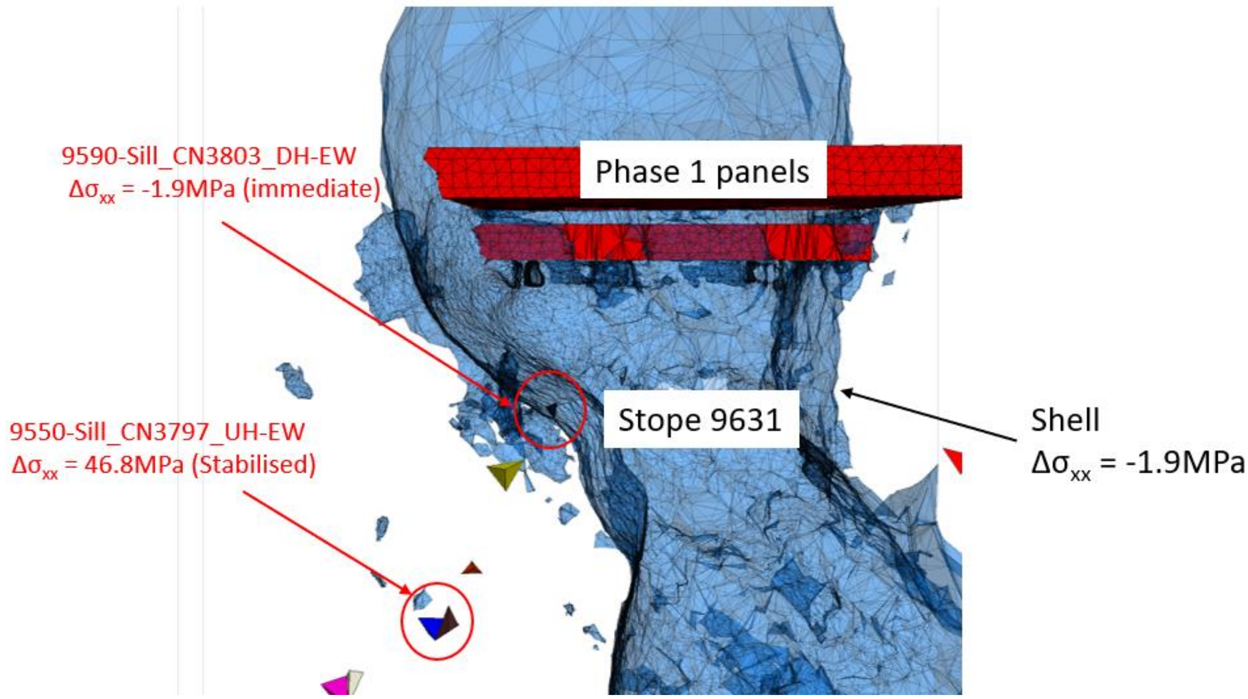

Figure A.3: Immediate stress change comparison for brittle post peak behaviour model after 9631 crown blast. SC8 detected an immediate stress change of -1.9 MPa

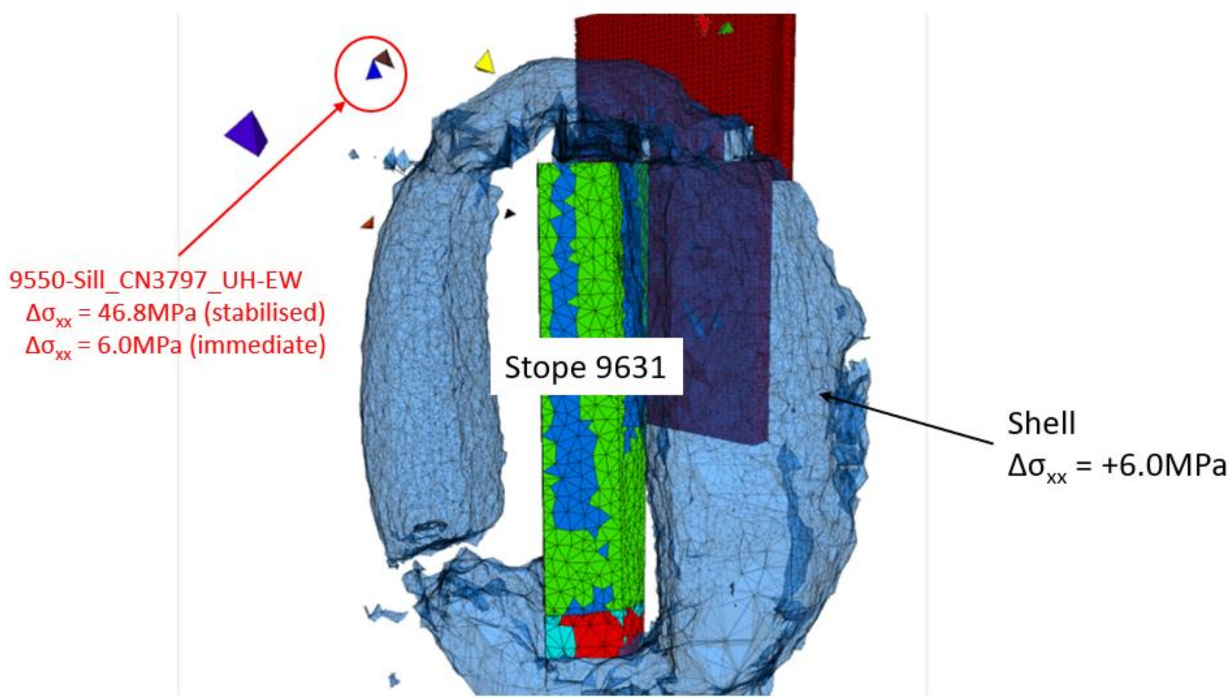

Figure A.4: Brittle failure model, immediate stress change can be replicated, but not the stabilized stress increase. SC3 detected an immediate stress change of +6.0 MPa

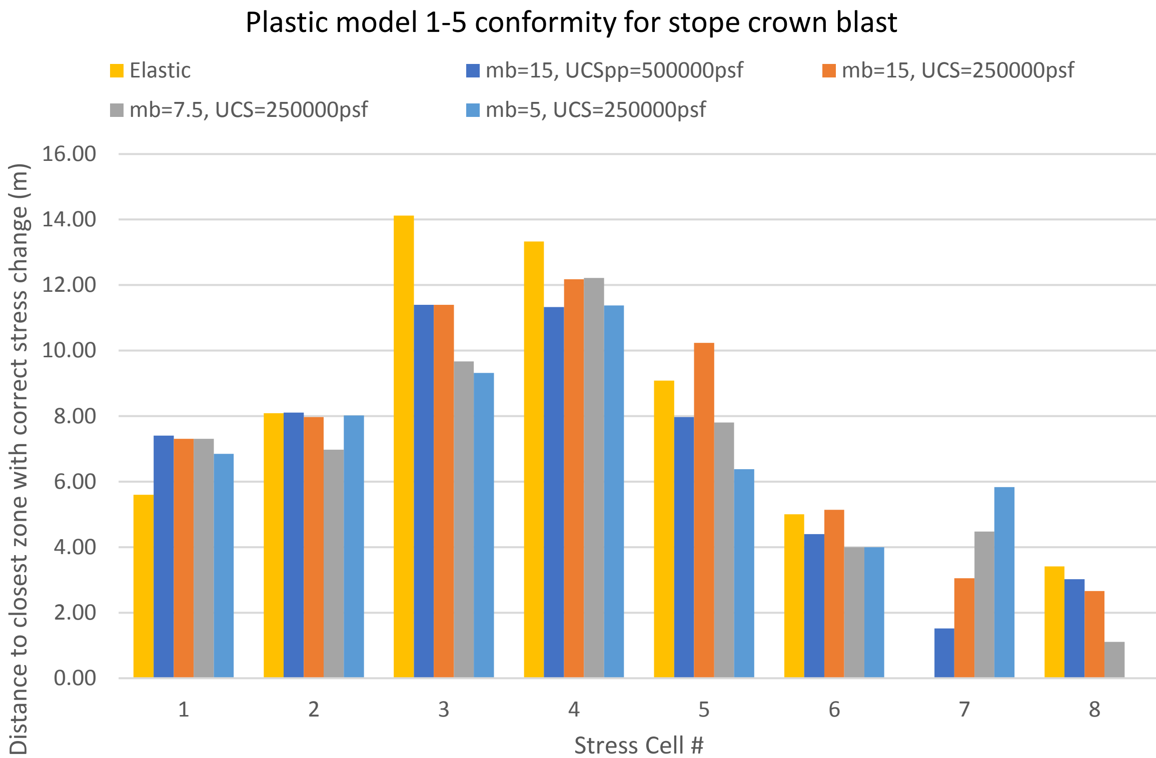

Figure A.5: Validation of ore post peak properties based measured immediate stress changes. Model conformity generally better with decreased post peak properties

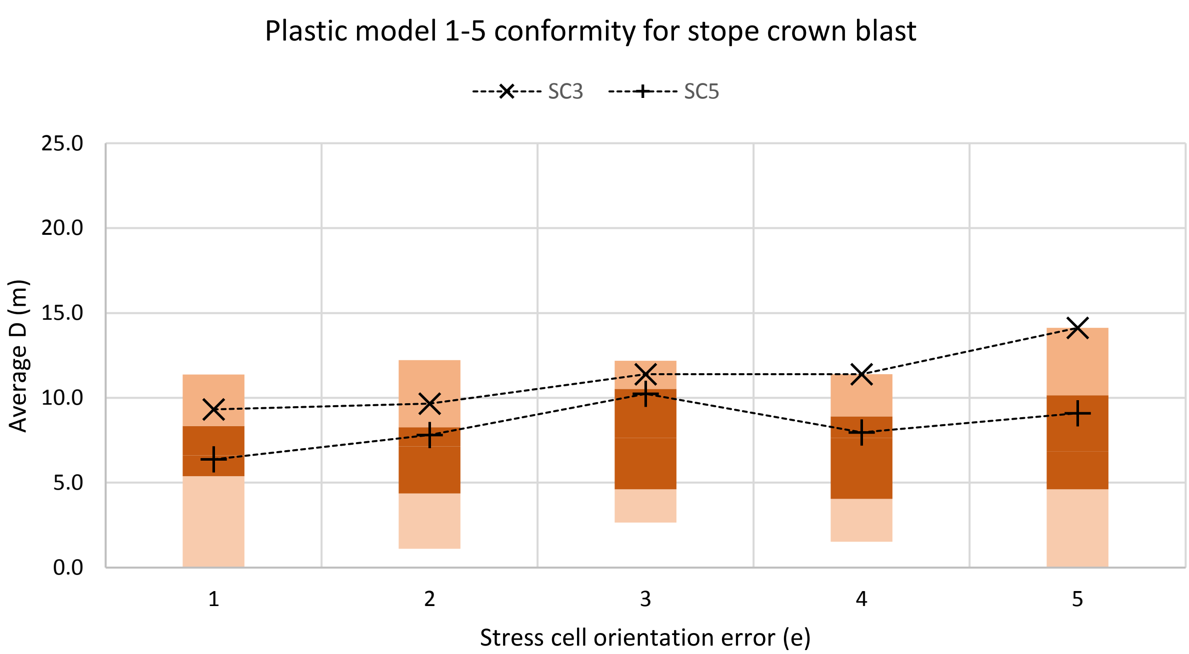

Figure A.6: Variation of distances "D" for models 1 to 5. Model 5 is the linear elastic model

Appendix 2: BSR of Seismic Source Locations

Table A.3: Source locations of large magnitude seismic events

Time	Magnitude (Nuttli)	X	Y	Z	BSR	Observations (CCM)	Analysis	Annotation
Mar 4, 2017	2.4	23886	23568	7375	0.33	Minor surface damage to the wall support in the 9460 sill on 3550L. Associated with drift blast in the 9510 sill.	High minor principal stress	D.1., C.3.
Apr 7, 2017	1.7	23905	23741	7311	0.31	No damage. Associated with production blast in the 9591 stope.	In pillar, high minor principal stress	D.1., C.3.
Apr 14, 2017	2.2	23882	23701	7418	0.29	Minor damage at the leading edge (bulking only) of the freshly blasted drift round in the 9510 sill on 3550L. Associated with drift blast in the 9510 sill on 3550L.	In pillar, high minor principal stress	D.1., C.3.
Apr 20, 2017	2.6	23887	23678	7396	0.29	Major damage at two locations and bulking at three locations on 3550L. Not associated with any type of blasts.	In pillar, high minor principal stress	D.1., C.3.
April 20, 2017	1.6	23882	23713	7396	0.31	Not evident damage observed. Not associated with any type of blasts.	In pillar, high minor principal stress	D.1., C.3.

Table A.4: Rockburst Damage on 3550L

Rockburst damage on 3550L	X	Y	Z	BSR	Observations (CCM)	Analysis	Annotation
Location 1	23791	23679	7445	0.60	Severe damage to the dynamic support system (Approximately 70 tons displaced from the back/shoulders in the 9550 sill)	Close to free surface, low BSR	H.1
Location 2	23789.4	23637.9	7445.8	0.28	Minor damage to the previously installed dynamic support system at the leading edge (Approximately 150 tons displaced from the unsupported back in the 9510 sill)	High confinement, leading to low BSR	C.2, B.1, H.2

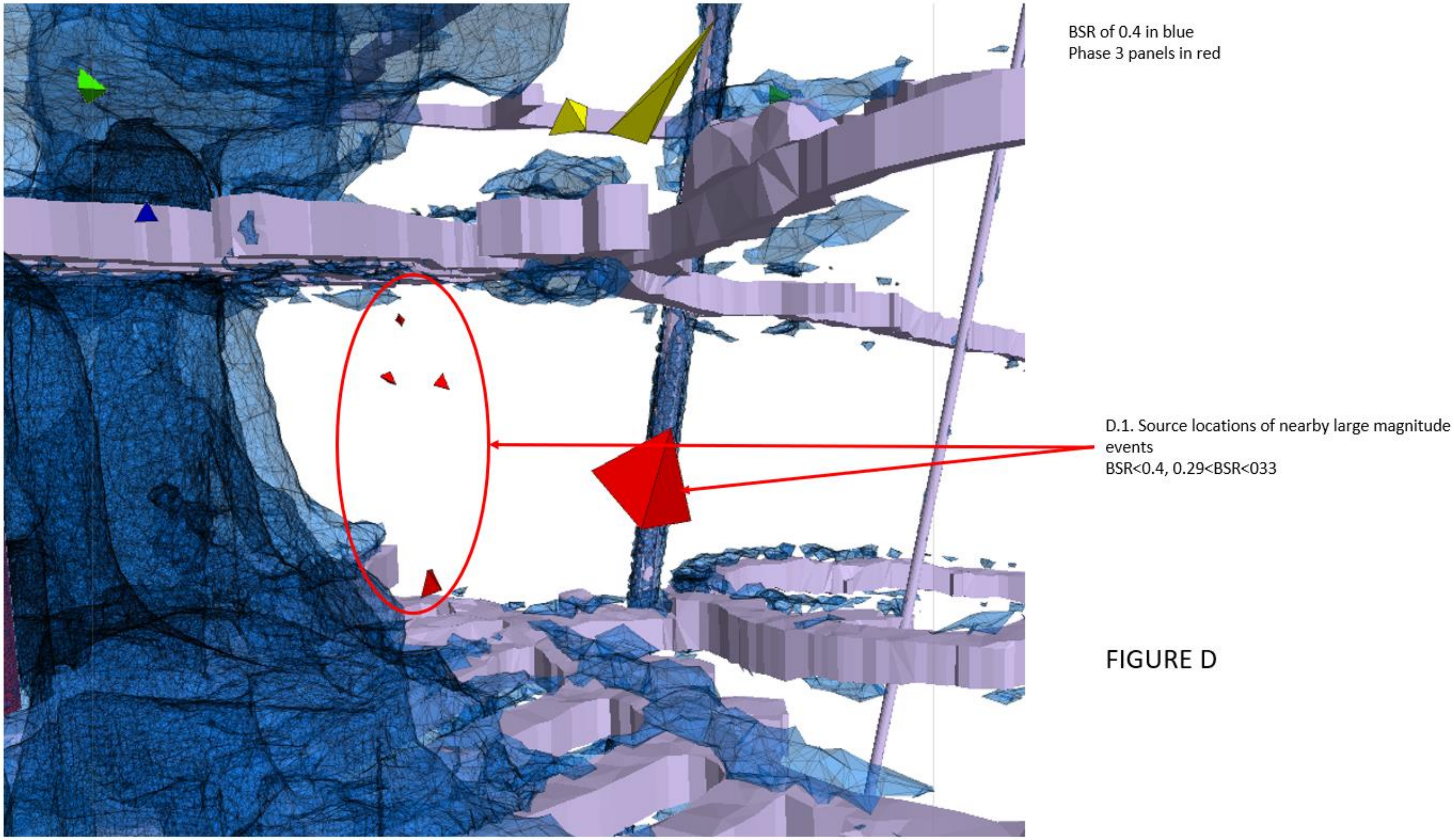

Figure A.7: Seismic source locations of large magnitude events between March 4, 2017, and April 20, 2017

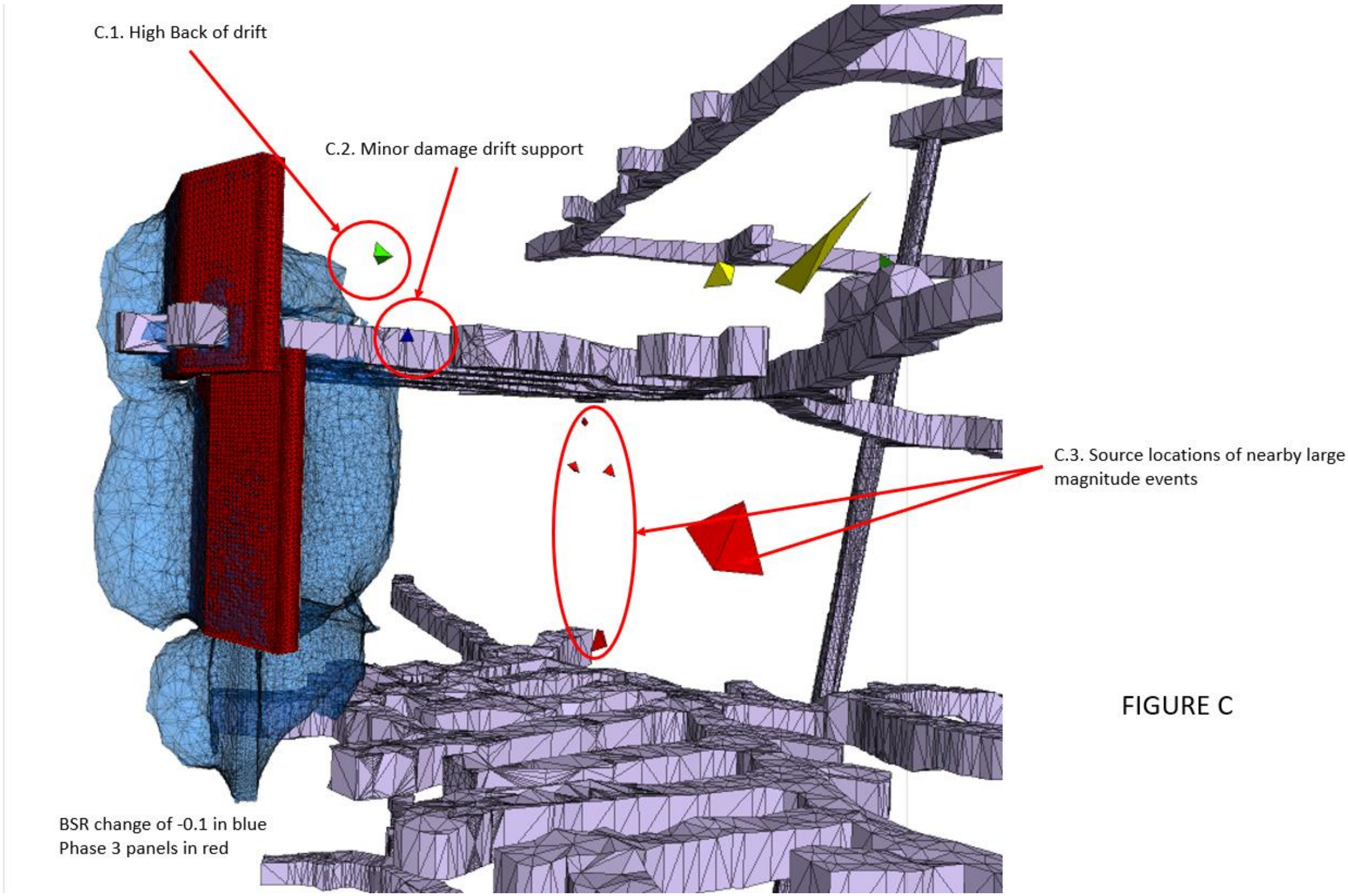

Figure A.8: Seismic source locations of large magnitude events between March 4, 2017, and April 20, 2017

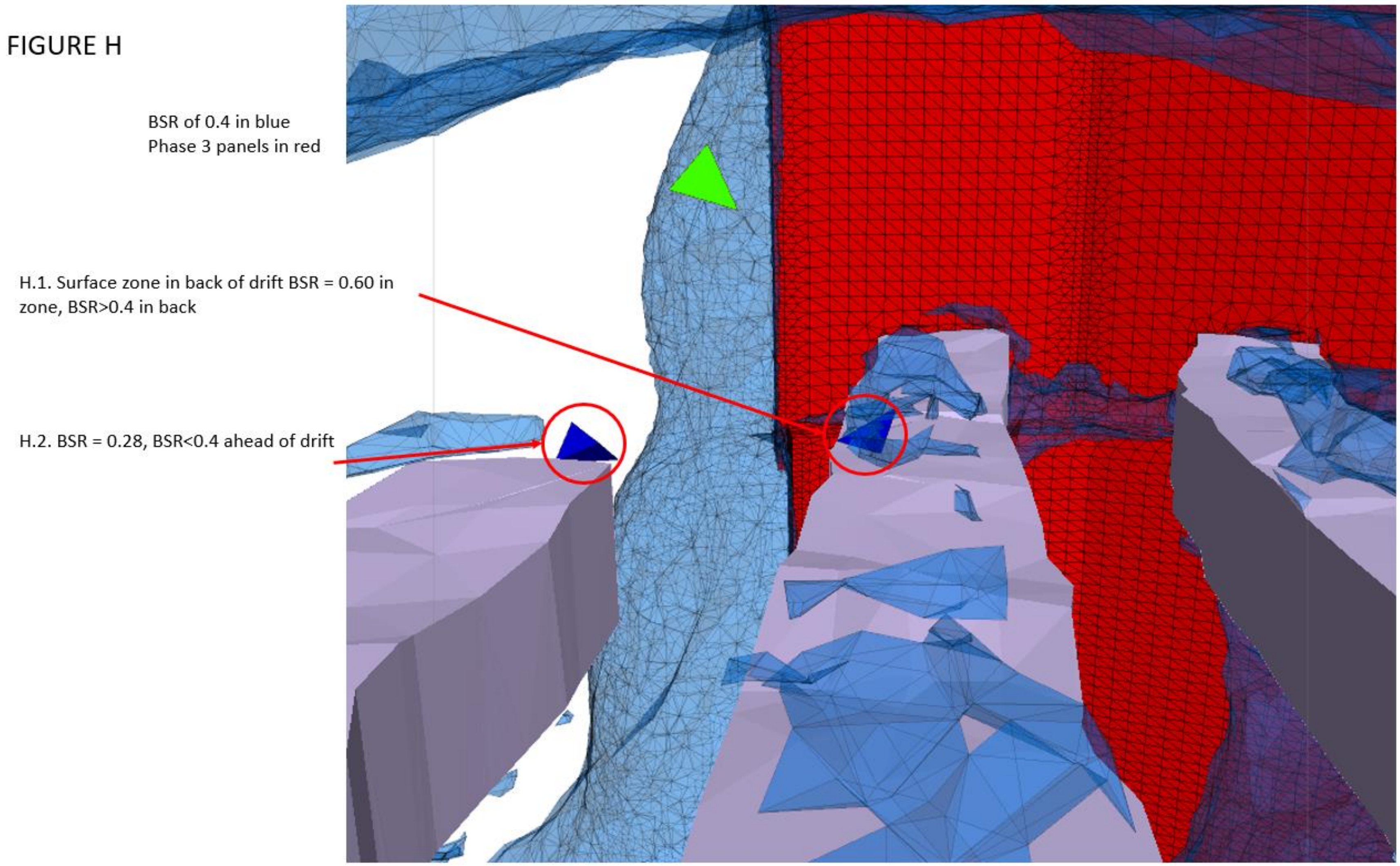

Figure A.9: Seismic source locations of large magnitude events between March 4, 2017, and April 20, 2017

Appendix 3: Ore at Risk over Diminishing Pillar Extraction

Table A.5: Ore at risk over pillar extraction with no destressing

	3	4	5	6	7	8	9	10	11	12	13	14	15	16	17	18	19	20
9631 SILL	3.98%	4.03%	3.71%	6.16%	6.21%	6.78%	7.24%	7.07%	2.99%	3.25%	3.30%	3.57%	3.57%	3.73%	3.85%	3.92%	3.97%	4.03%
9511 SILL	7.56%	0.00%	0.00%	0.00%	0.00%	0.00%	0.01%	0.01%	0.01%	0.01%	0.01%	0.01%	0.01%	0.00%	0.00%	0.00%	0.00%	0.00%
9671 CROWN	0.00%	0.00%	0.00%	0.00%	0.00%	0.00%	0.00%	0.00%	0.00%	0.00%	0.00%	0.00%	0.00%	0.00%	0.00%	0.00%	0.00%	0.00%
9512 SILL	7.56%	0.00%	0.00%	0.00%	0.00%	0.00%	0.01%	0.01%	0.01%	0.01%	0.01%	0.01%	0.01%	0.00%	0.00%	0.00%	0.00%	0.00%
9591 SILL	9.86%	10.14%	8.85%	0.00%	0.00%	0.00%	0.00%	0.00%	0.01%	0.00%	0.00%	0.00%	0.00%	0.00%	0.00%	0.00%	0.00%	0.00%
9632 SILL	14.33%	14.35%	14.72%	16.14%	16.56%	0.00%	0.00%	0.00%	0.00%	0.00%	0.00%	0.00%	0.00%	0.00%	0.00%	0.00%	0.00%	0.00%
9551 SILL	3.13%	3.10%	3.02%	9.82%	10.52%	11.68%	0.00%	0.00%	0.00%	0.00%	0.00%	0.04%	0.04%	0.05%	0.05%	0.04%	0.01%	0.01%
9631 CROWN	5.38%	7.14%	7.97%	10.59%	10.76%	13.02%	14.25%	0.00%	0.00%	0.01%	0.01%	0.01%	0.01%	0.01%	0.01%	0.01%	0.01%	0.01%
9592 SILL	1.34%	1.39%	0.90%	1.23%	1.22%	2.90%	3.67%	3.72%	0.00%	0.00%	0.00%	0.00%	0.00%	0.00%	0.00%	0.00%	0.00%	0.00%
9591 CROWN	0.27%	0.32%	0.04%	2.94%	3.59%	4.22%	5.97%	12.58%	11.71%	0.00%	0.00%	0.00%	0.00%	0.00%	0.00%	0.00%	0.00%	0.00%
9552 SILL	0.59%	0.63%	0.53%	0.54%	0.49%	0.53%	0.48%	0.43%	0.92%	0.77%	0.00%	0.00%	0.00%	0.00%	0.00%	0.00%	0.00%	0.00%
9511 SILL	0.83%	1.70%	2.13%	2.52%	2.57%	2.72%	9.76%	10.20%	11.35%	11.64%	10.28%	0.00%	0.00%	0.00%	0.00%	0.00%	0.00%	0.00%
9592 CROWN	0.33%	0.33%	0.31%	0.97%	0.97%	1.34%	2.59%	2.51%	2.81%	3.47%	3.64%	4.16%	0.00%	0.00%	0.00%	0.00%	0.00%	0.00%
9512 SILL	1.09%	1.41%	1.86%	2.51%	2.55%	2.84%	3.61%	3.72%	3.81%	3.84%	4.43%	1.34%	1.45%	0.00%	0.00%	0.00%	0.00%	0.00%
9551 CROWN	0.02%	0.02%	0.00%	0.03%	0.08%	0.08%	1.14%	1.48%	1.23%	5.28%	5.57%	8.51%	7.09%	6.32%	0.00%	0.00%	0.00%	0.00%
9461 SILL	0.01%	0.05%	0.07%	0.07%	0.07%	0.09%	0.18%	0.18%	0.20%	0.21%	0.26%	12.78%	13.49%	12.04%	13.19%	0.00%	0.00%	0.00%
9552 CROWN	0.01%	0.01%	0.01%	0.02%	0.02%	0.02%	0.54%	0.25%	0.43%	0.22%	0.17%	0.48%	2.49%	3.35%	4.18%	4.11%	0.00%	0.00%
9511 CROWN	0.01%	0.01%	0.00%	0.01%	0.01%	0.00%	0.01%	0.01%	0.01%	0.01%	0.01%	1.47%	1.49%	1.26%	3.93%	10.97%	11.06%	0.00%

Table A.6: Ore at risk over pillar extraction with destressing (assuming Phase 1 blast input parameters)

	3	4	5	6	7	8	9	10	11	12	13	14	15	16	17	18	19	20
9631 SILL	4.22%	4.24%	4.24%	6.31%	6.31%	6.80%	7.24%	7.09%	3.36%	3.45%	3.52%	3.88%	3.83%	3.89%	4.02%	4.14%	4.22%	4.25%
9511 SILL	8.05%	0.00%	0.00%	0.00%	0.00%	0.00%	0.01%	0.01%	0.01%	0.01%	0.01%	0.01%	0.01%	0.00%	0.00%	0.00%	0.00%	0.00%
9671 CROWN	0.00%	0.00%	0.00%	0.00%	0.00%	0.00%	0.00%	0.00%	0.00%	0.00%	0.00%	0.00%	0.00%	0.00%	0.00%	0.00%	0.00%	0.00%
9512 SILL	8.05%	0.00%	0.00%	0.00%	0.00%	0.00%	0.01%	0.01%	0.01%	0.01%	0.01%	0.01%	0.01%	0.00%	0.00%	0.00%	0.00%	0.00%
9591 SILL	16.63%	17.05%	17.05%	0.00%	0.00%	0.00%	0.00%	0.01%	0.01%	0.00%	0.00%	0.00%	0.00%	0.00%	0.00%	0.00%	0.00%	0.00%
9632 SILL	15.33%	15.42%	15.42%	17.64%	17.64%	0.00%	0.00%	0.00%	0.00%	0.00%	0.00%	0.00%	0.00%	0.00%	0.00%	0.00%	0.00%	0.00%
9551 SILL	3.34%	3.26%	3.26%	16.85%	16.85%	19.47%	0.00%	0.00%	0.00%	0.00%	0.00%	0.03%	0.03%	0.04%	0.04%	0.04%	0.01%	0.01%
9631 CROWN	9.27%	11.66%	11.66%	16.25%	16.25%	17.93%	20.40%	0.00%	0.00%	0.01%	0.01%	0.01%	0.01%	0.01%	0.01%	0.01%	0.01%	0.01%
9592 SILL	2.11%	2.25%	2.25%	1.38%	1.38%	3.22%	3.79%	3.78%	0.00%	0.00%	0.00%	0.00%	0.00%	0.00%	0.00%	0.00%	0.00%	0.00%
9591 CROWN	0.97%	1.01%	1.01%	7.24%	7.24%	7.86%	12.06%	20.99%	19.27%	0.00%	0.00%	0.00%	0.00%	0.00%	0.00%	0.00%	0.00%	0.00%
9552 SILL	1.05%	1.25%	1.25%	1.03%	1.03%	1.29%	0.77%	0.73%	1.34%	1.19%	0.00%	0.00%	0.00%	0.00%	0.00%	0.00%	0.00%	0.00%
9511 SILL	2.30%	2.82%	2.82%	4.19%	4.19%	4.74%	20.70%	22.40%	24.51%	25.61%	20.76%	0.00%	0.00%	0.00%	0.00%	0.00%	0.00%	0.00%
9592 CROWN	0.45%	0.44%	0.44%	1.53%	1.53%	2.20%	4.66%	2.98%	3.66%	3.71%	4.03%	4.42%	0.00%	0.00%	0.00%	0.00%	0.00%	0.00%
9512 SILL	1.57%	3.88%	3.88%	5.12%	5.12%	5.87%	6.73%	6.95%	7.35%	7.58%	6.78%	2.31%	2.37%	0.00%	0.00%	0.00%	0.00%	0.00%
9551 CROWN	0.04%	0.04%	0.04%	0.18%	0.18%	0.20%	3.12%	3.88%	3.73%	14.79%	15.22%	21.80%	17.48%	14.26%	0.00%	0.00%	0.00%	0.00%
9461 SILL	0.17%	0.37%	0.37%	0.71%	0.71%	0.73%	1.24%	1.29%	1.38%	1.48%	1.66%	24.25%	24.74%	25.66%	27.81%	0.00%	0.00%	0.00%
9552 CROWN	0.01%	0.01%	0.01%	0.02%	0.02%	0.04%	0.80%	0.43%	0.96%	0.31%	0.27%	0.67%	3.10%	4.45%	4.49%	4.32%	0.00%	0.00%
9511 CROWN	0.01%	0.01%	0.01%	0.02%	0.02%	0.02%	0.09%	0.10%	0.10%	0.10%	0.11%	3.90%	3.74%	3.05%	9.03%	23.27%	23.57%	0.00%

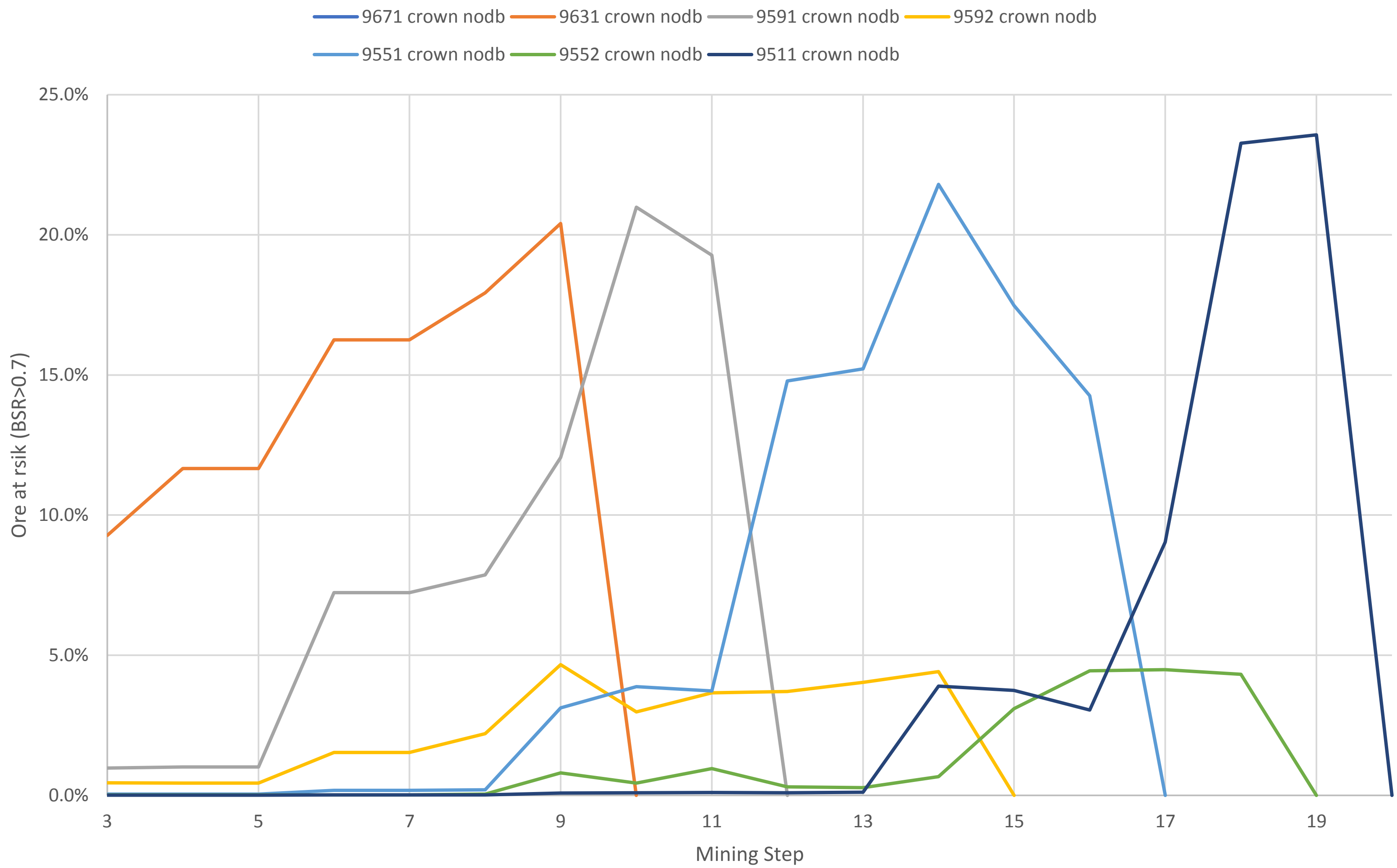

Figure A.10: Ore at risk over pillar extraction with no destressing for crown stopes

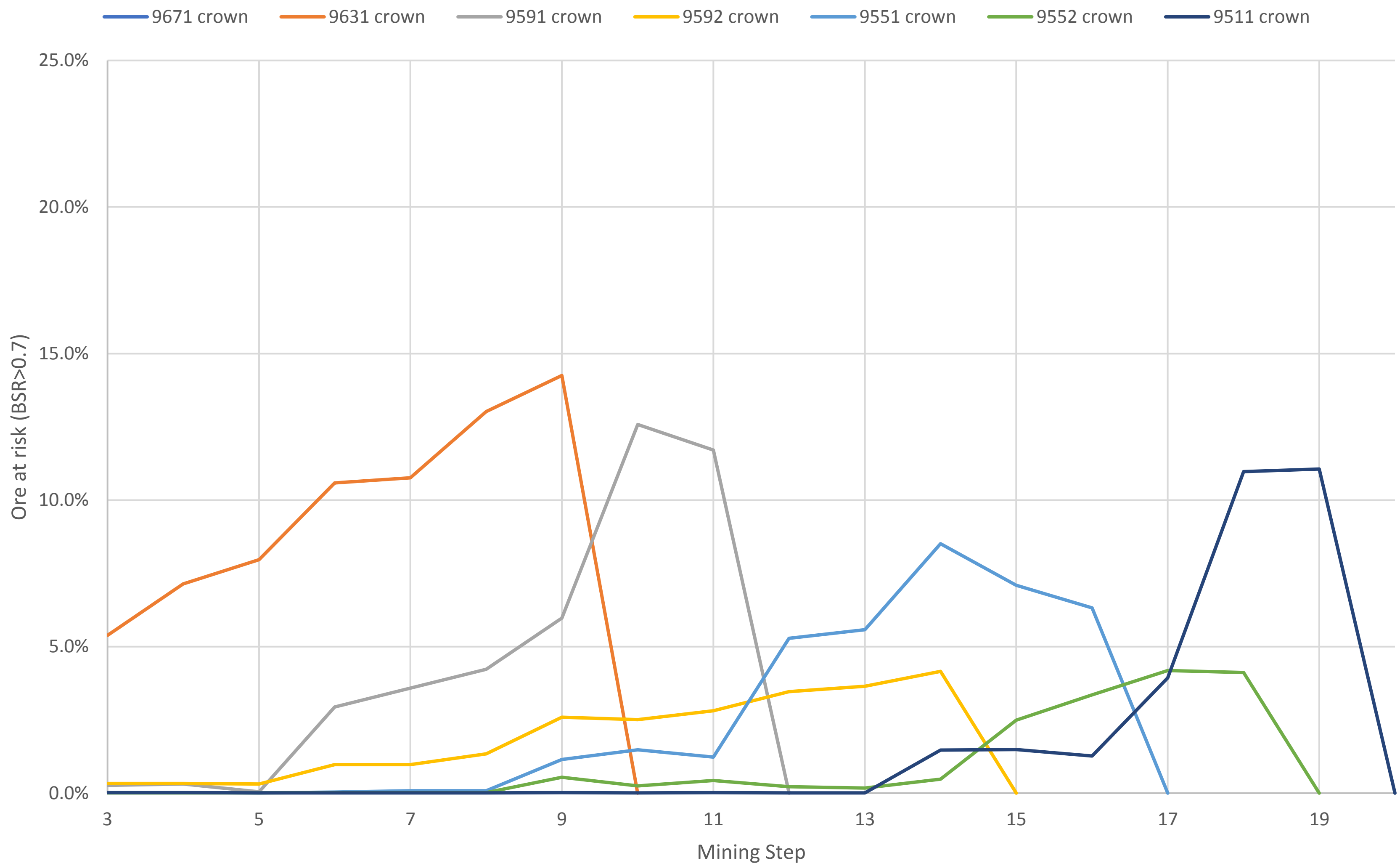

Figure A.11: Ore at risk for crown stopes

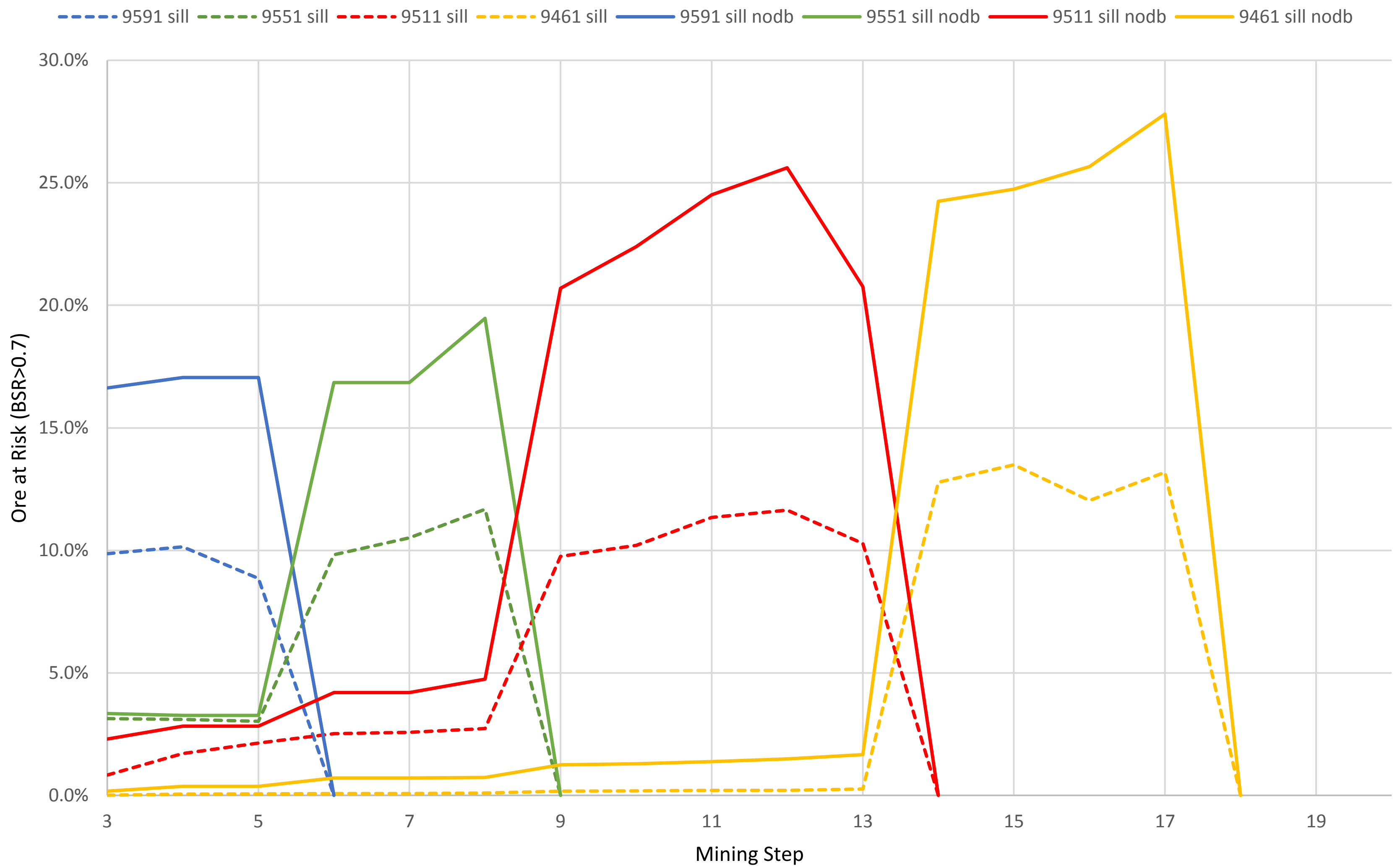

Figure A.12: Ore at risk comparison for critical stopes in pillar crown for destressing and no destressing scenarios

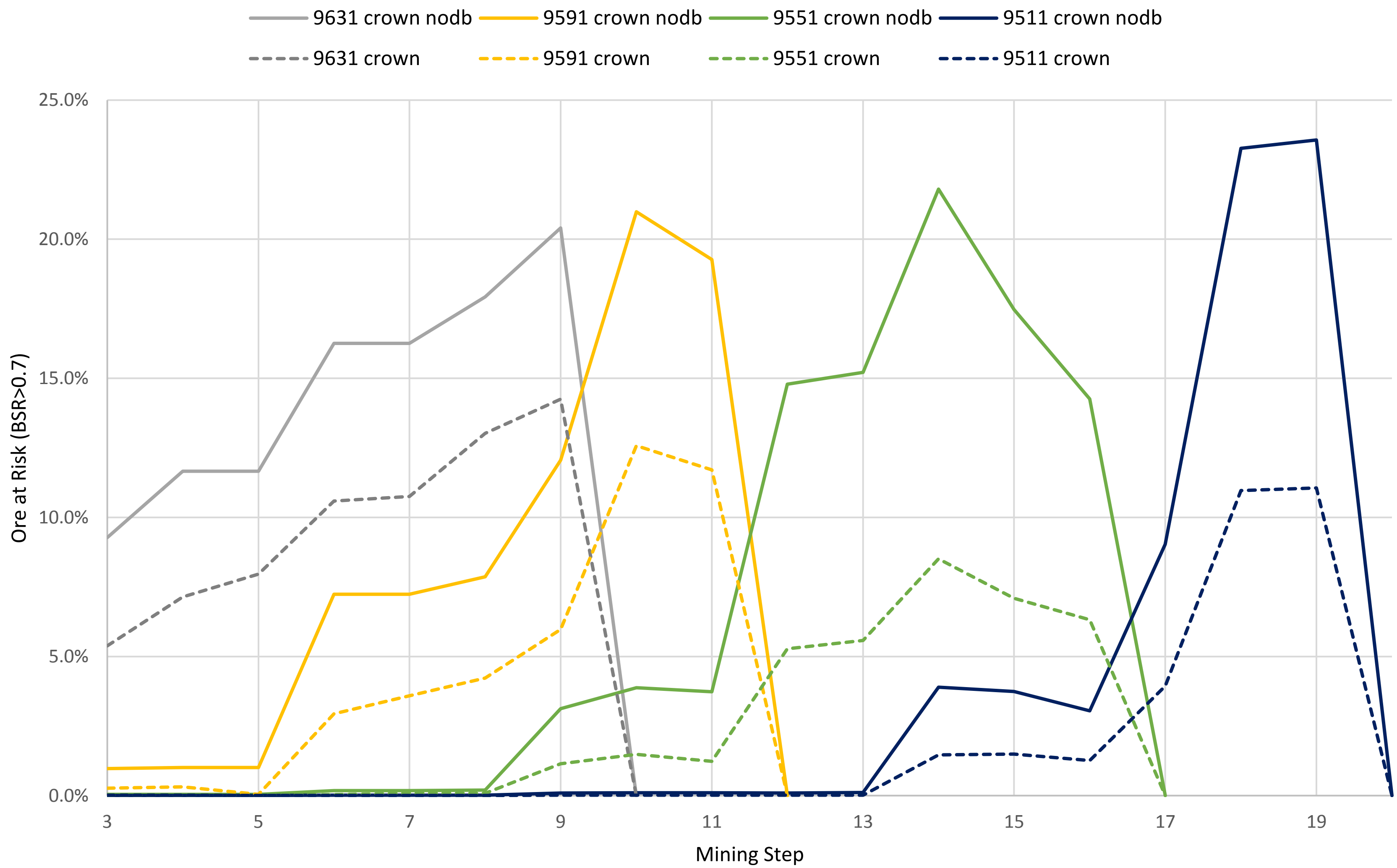

Figure A.13: Ore at risk comparison for critical stopes in pillar sill for destressing and no destressing scenarios

Table A.3: Model external loading work for each mining step

MINING STEP	CUMULATIVE BOUNDARY WORK (DESTRESSING)	CUMULATIVE BOUNDARY WORK (NO DESTRESSING)	INCREMENTAL BOUNDARY WORK (DESTRESSING)	INCREMENTAL BOUNDARY WORK (NO DESTRESSING)
1	1.666E+10		1.666E+10	
2	2.797E+10	1.695E+10	1.131E+10	1.695E+10
3	3.199E+10		4.020E+09	
4	4.313E+10	2.730E+10	1.114E+10	1.035E+10
5	4.512E+10	2.798E+10	1.985E+09	6.790E+08
6	4.644E+10	2.922E+10	1.323E+09	1.237E+09
7	6.294E+10		1.650E+10	
8	7.133E+10	4.624E+10	8.389E+09	1.702E+10
9	7.604E+10		4.703E+09	
10	8.641E+10	5.448E+10	1.038E+10	8.245E+09
11	9.726E+10	6.865E+10	1.084E+10	1.417E+10
12	9.643E+10	6.878E+10	-8.255E+08	1.314E+08
13	1.028E+11	7.555E+10	6.347E+09	6.769E+09
14	1.078E+11	8.017E+10	5.000E+09	4.621E+09
15	1.088E+11	8.235E+10	9.923E+08	2.175E+09
16	1.206E+11	9.699E+10	1.188E+10	1.465E+10
17	1.201E+11	9.646E+10	-5.228E+08	-5.330E+08
18	1.215E+11	9.786E+10	1.330E+09	1.394E+09
19	1.239E+11	1.014E+11	2.417E+09	3.594E+09
20	1.350E+11	1.155E+11	1.115E+10	1.401E+10
21	1.347E+11	1.142E+11	-3.675E+08	-1.310E+09
22	1.339E+11	1.154E+11	-7.195E+08	1.206E+09

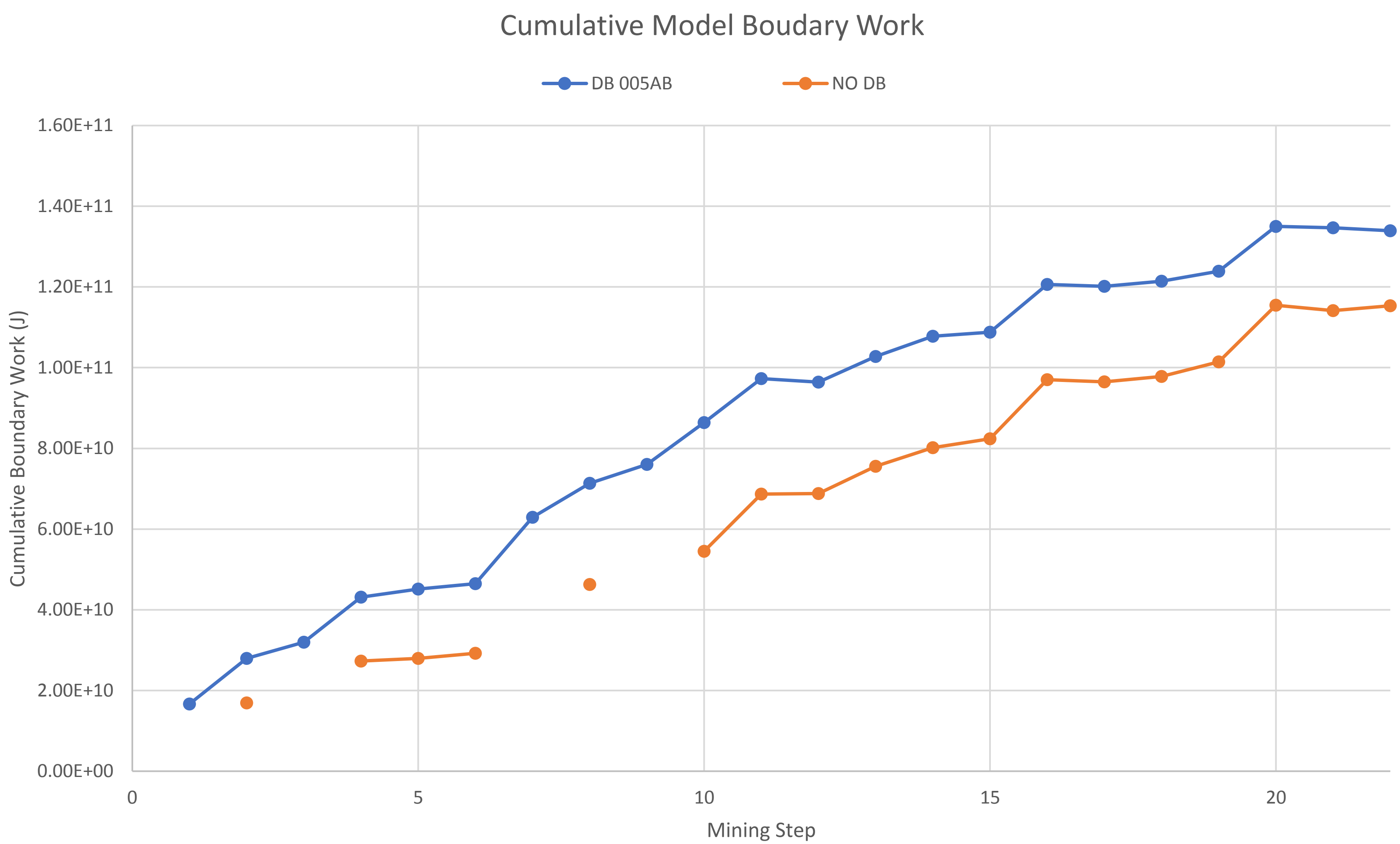

Figure A.14: Comparison of model boundary work over pillar extraction between model with destressing (blue) and model with no destressing (orange)

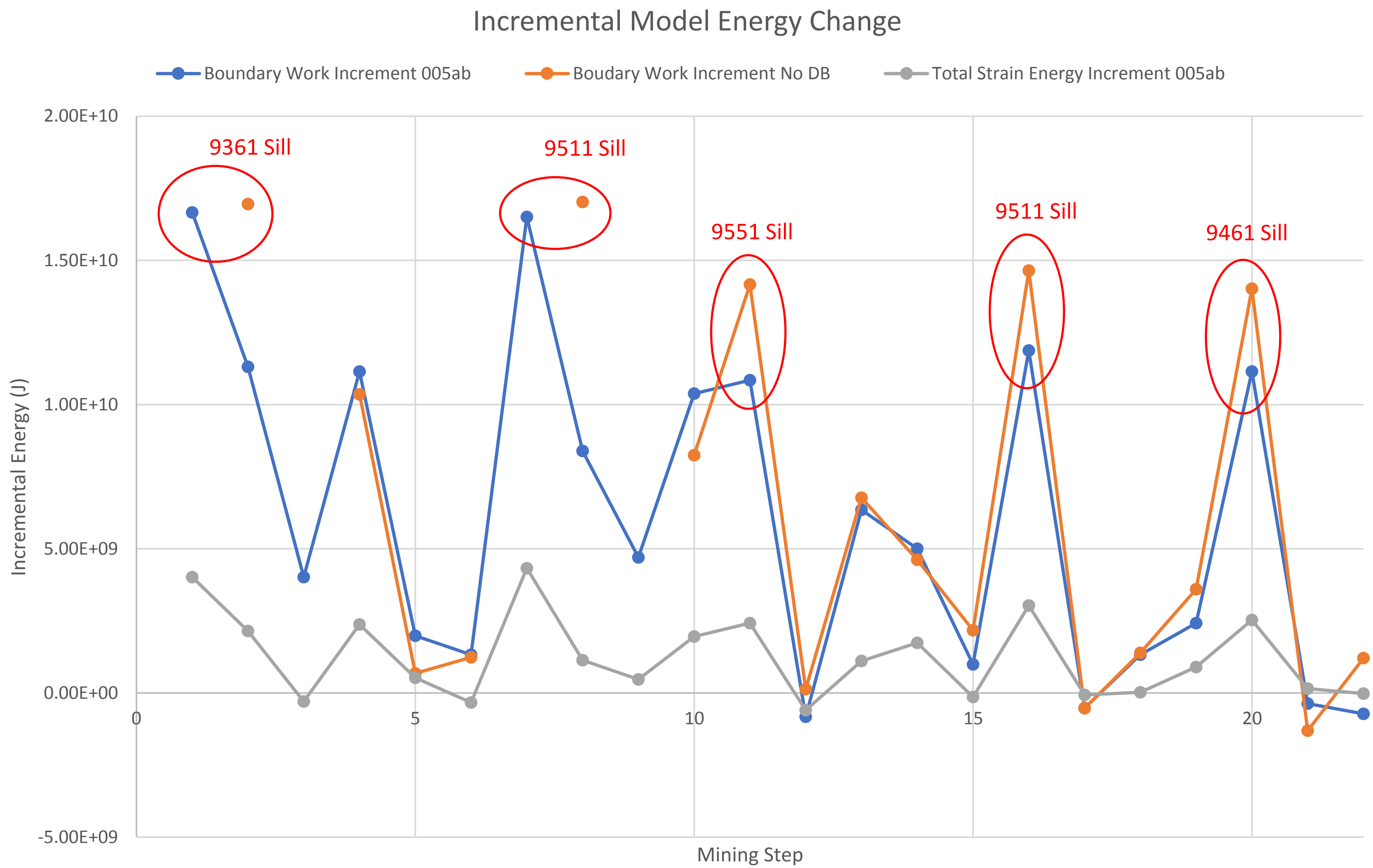

Figure A.15: Comparison of model boundary work increments per mining step between model with destressing (blue) and model with no destressing (orange)

Appendix 4: Panel Volume Parametric Study

The effect of panel thickness in conjunction with the destress blast input parameters was evaluated in a small-scale simplified panel model. The panel is 4 units high and 4 units wide. The thickness was varied between 0.2 and 0.8. The stiffness is set to 1000 units and the stress is isotropic at 1 unit. The destress blasting holistic model proposed by Tang and Mitri (2001) was applied to the panel. The rock fragmentation factor α was set at 0.1, 0.2, 0.4, and 0.8. The corresponding stress reduction factor β for each tested value of α was calculated with the equation $\alpha + \beta = 1$. The boundary work increment of each model after the destressing step is also evaluated to quantify the overall effect on the model energy following destressing. Overall, the stress change effect of panel thickness can be replicated by changing the parameters α and β in the panel. Panel thickness can therefore be kept constant in the CCM back analysis.

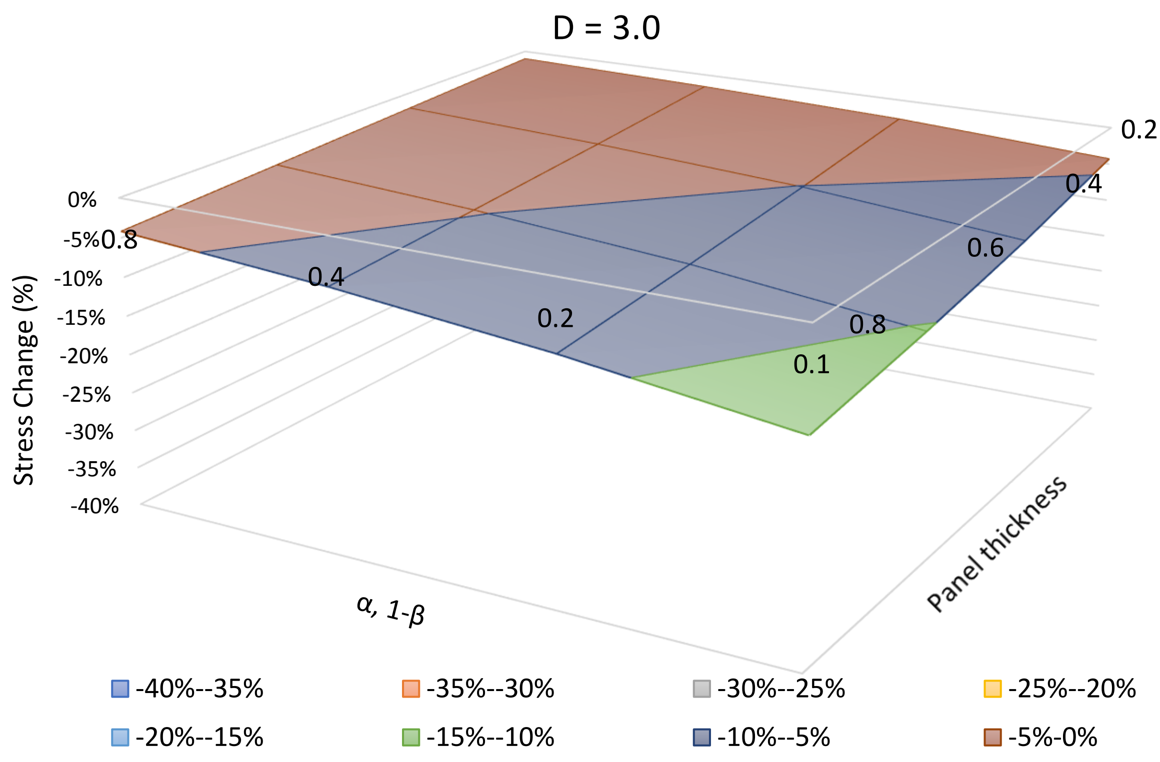

Figure A.16: Stress change % at point 3.0 unit lengths away from the panel. Colored bands show combinations of panel thicknesses and destressing input parameters which provide the same stress decrease range.

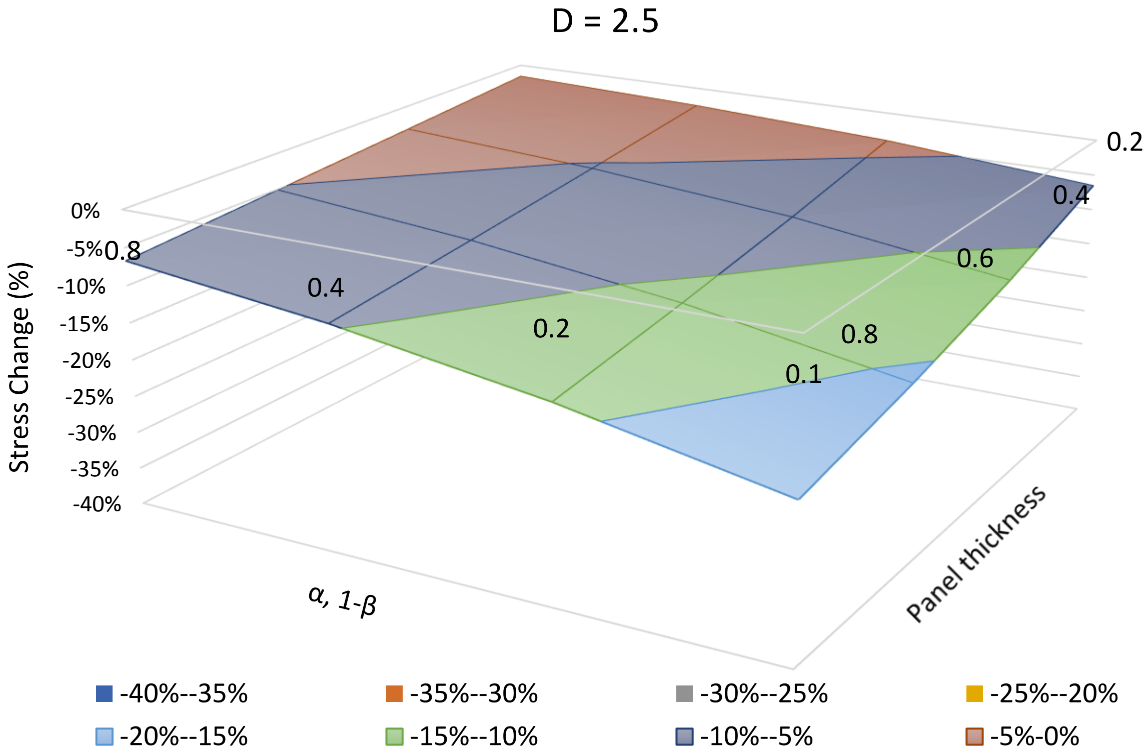

Figure A.17: Stress change % at point 2.5 unit lengths away from the panel

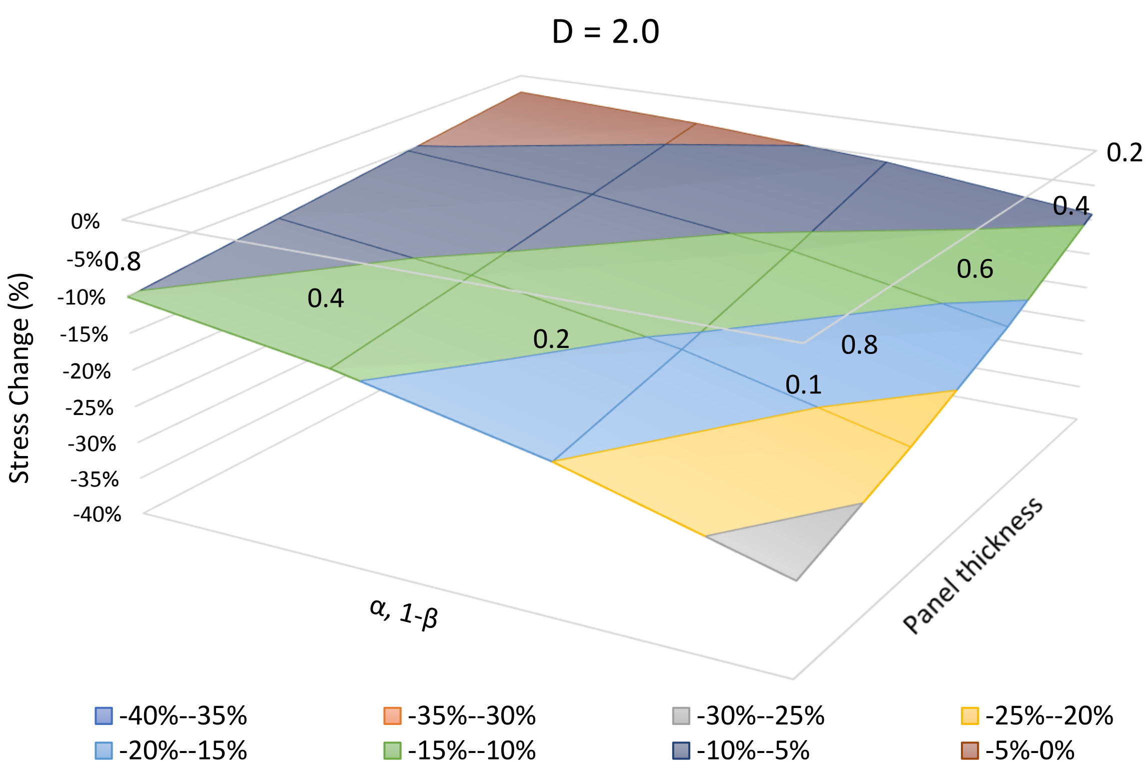

Figure A.18: Stress change % at point 2.0 unit lengths away from the panel

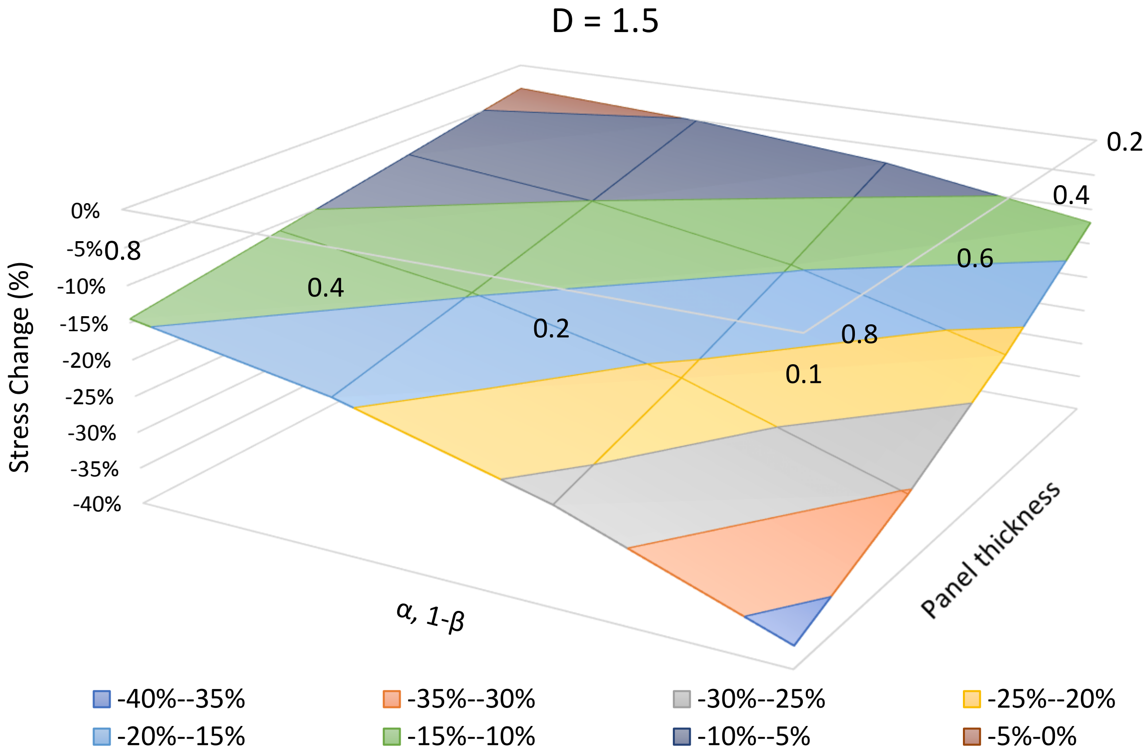

Figure A.19: Stress change % at point 1.5 unit lengths away from the panel

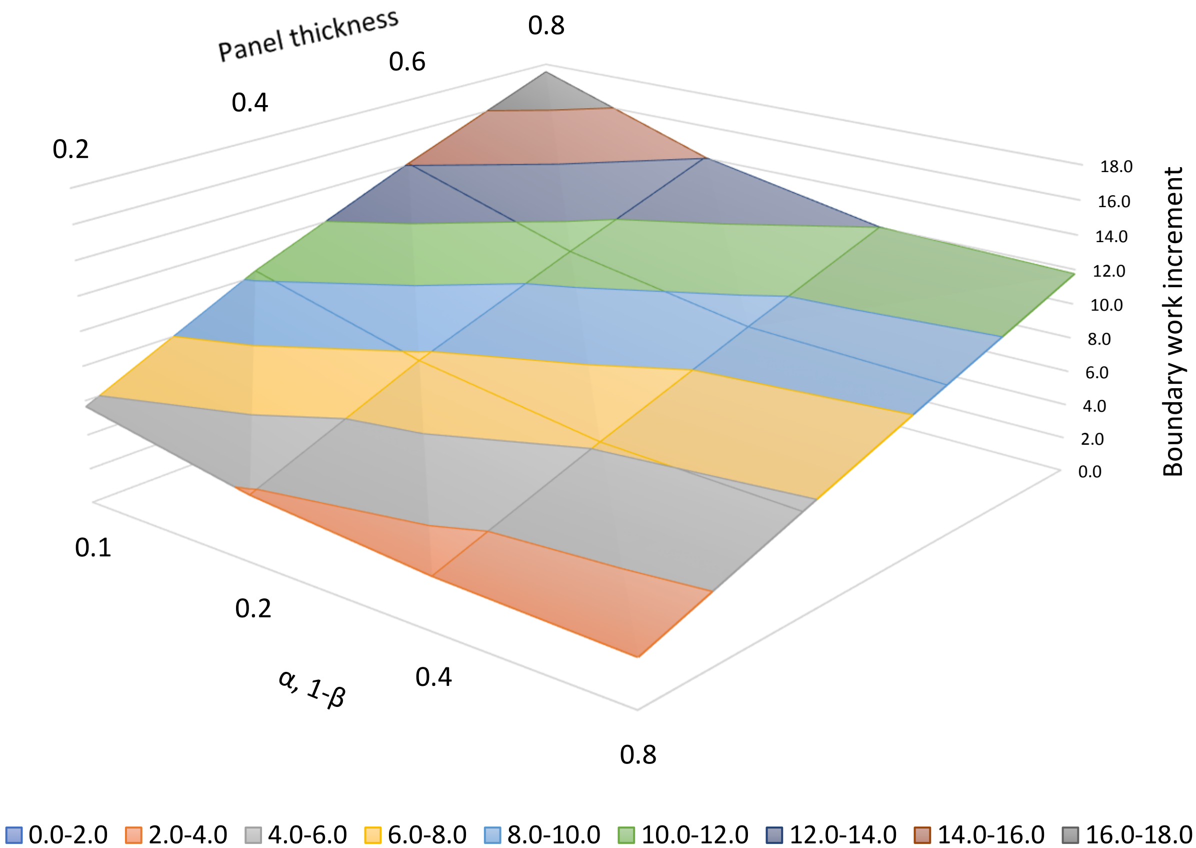

Figure A.20: Boundary work increment